Rosana Maria Alves Dias **Micro-g MEMS Accelerometer Based on Time Measurement**

UMinho | 2013

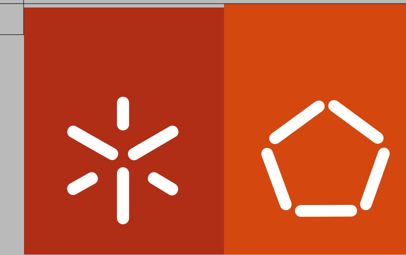

Universidade do Minho
Escola de Engenharia

Rosana Maria Alves Dias

Micro-g MEMS Accelerometer Based on Time Measurement

Março de 2013

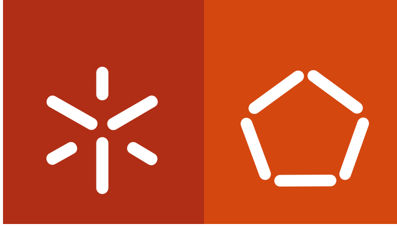

Universidade do Minho
Escola de Engenharia

Rosana Maria Alves Dias

Micro-g MEMS Accelerometer Based on Time Measurement

Programa Doutoral em Engenharia Electrónica e de Computadores

Trabalho realizado sob a orientação do
Professor Doutor Luis Alexandre Machado da Rocha
e do
Professor Doutor José Higino Gomes Correia

Março de 2013

DECLARAÇÃO

Nome
Rosana Maria Alves Dias

Título tese
Micro-g MEMS Accelerometer Based on Time Measurement

Orientadores:
Professor Doutor Luis Alexandre Machado da Rocha
Professor Doutor José Higino Gomes Correia

Ano de conclusão: 2013

Designação do Doutoramento:
Programa Doutoral em Engenharia Electrónica e de Computadores

É AUTORIZADA A REPRODUÇÃO INTEGRAL DESTA TESE APENAS PARA EFEITOS DE INVESTIGAÇÃO, MEDIANTE DECLARAÇÃO ESCRITA DO INTERESSADO, QUE A TAL SE COMPROMETE;

Universidade do Minho, 26 de Março, 2013

Assinatura: ____

ACKNOWLEDGEMENTS

I consider myself privileged, since I had the opportunity to study some time abroad, join different lab groups, meet great people and visit amazing places. This was a wonderful 4-year experience from which I've grown a better researcher and a better person.

Firstly, I must acknowledge my supervisor, Professor Luis Rocha, without whom this work had not been possible. This is obvious. What is not obvious, is how thankful I am for the opportunity I've been given, for his guidance and for the faith he deposited in me. I'm glad I had a supervisor that provided close attention to my path, recognized my efforts, and even showed me the good side of what I sometimes was considering failure. And for his great ideas, of course!

I'd like to thank Professor Higino Correia, for his support and prompt availability to help whenever I needed. In fact, I have many people at the Department of Industrial Electronics to say thank you to, from lab colleagues to employees, secretaries and lab technicians, who were so kind and helped me so much in many stages of my PhD, especially Carlos e Sr. Joel.

I'm indebted to Professor Reinoud Wolffenbuttel and Ger de Graaf from Delft University of Technology, for their collaboration, discussions and ideas that proved very fruitful. I thank also my lab colleagues, for the nice moments spent outside the laboratory, especially Arvin, Bere and Wen.

I'm grateful to Dr. Edmond Cretu for his help and research ideas, and my friends at UBC, Mrigank, Miguel, Elie, Hussein and Amy who made my stay in Vancouver very enjoyable.

Although the work at INL is not featured here, (anyway, I spent a large part of the time there writing this thesis) I'd like to thank my colleagues and co-workers, especially João Gaspar and Hélder who tutored me in the clean-room. And of course, Cátia; it's great to have a true friend working right next to you!

I want to thank my colleagues at the University for the nice moments we've shared during these years, from Alexandre, whom I know since I went to the University and was always very kind and helpful whenever needed; to more recent "acquisitions" such as Filipe whom, besides being great to work with, I own a great deal of results as he programmed the FPGA; not forgetting David, João, João Paulo, Macedo, Manuel e Miguel.

Finalmente, quero agradecer aos meus amigos, porque a vida não é apenas trabalho e os bons momentos passados com eles são imprescindíveis. Agradeço muito à minha família, em especial aos meus pais, por todo o apoio que sempre senti. O que consegui devo-o a eles. E ao Pedro, por tanto que nem dá para enumerar.

The author, Rosana Maria Alves Dias, was supported by Portuguese Foundation for Science and Technology (SFRH/BD/46030/2008).

ABSTRACT

Micro-g MEMS Accelerometer Based on Time Measurement

The MEMS sensor market has experienced an amazing growth on the last decades, with accelerometers being one of the pioneers pushing the technology into widespread use with its applications on automotive industry. Since then, accelerometers have been gradually replacing conventional sensors due mainly to its lower cost. As the performance of MEMS accelerometers improves, the applications range where they replace conventional accelerometers increases. Nowadays, there is still a large range of applications for which suitable MEMS accelerometers are yet to be developed.

This work focuses on the development of a high performance accelerometer taking advantage of the high sensitivity of a non-linear phenomenon that occurs in electrostatically actuated movable capacitive microdevices: electrostatic *pull-in*. Although the pull-in effect has been known for more than 40 years, it is usually avoided when dealing with movable microstructures as it leads to a region of instability, where the position of movable parts cannot be fully controlled. In the last decade, the pull-in displacement profile of 1-DOF parallel-plates devices has been the subject of research that revealed the presence of a so-called meta-stability. This meta-stability occurs in specific damping and voltage actuation conditions and translates as a non-linear displacement profile, rather than simple time-of-flight. This feature makes the pull-in time duration significantly longer, and it happens to be extremely sensitive to intervenient forces, such as external acceleration. Basically, measuring the pull-in time of specifically designed microstructures (while maintaining the other parameters constant) allows the measurement of the external acceleration that acts on the system. Using a pull-in time measurement rather than direct capacitance/displacement/acceleration transduction presents several advantages. The most important is the fact that time can be measured very accurately with technology readily available. For instance, if one uses a 100MHz clock on the time counting mechanism, which corresponds to a time measurement resolution of 100 ns, given the 0.26 μs/μg sensitivity of the accelerometer developed in this work, an acceleration resolution of 0.38 μg could be achieved.

One of the main challenges of the time based accelerometer development is the damper design, as damping is of outmost importance in defining the accelerometer performance parameters, namely sensitivity and noise. A new squeeze-film damper geometry design has been presented and studied. It consists of flow channels implemented on the parallel-plates that relieve

the squeeze-film damping pressures generated when the device is moving. This geometry has proved to be very effective in increasing the capacitance/damping ratio in parallel-plates, which was up to now a great challenge of in-plane parallel-plates design.

This work reports the development of an open-loop accelerometer with 0.26 μs/μg sensitivity and 2.7 μg /√Hz noise performance. The MEMS structures used for its experimental implementation were fabricated using a commercially available SOI micromachining process. The main drawbacks of this accelerometer were the low system bandwidth and non-linearity. Closed-loop approaches using electrostatic feedback were explored in this work in order to overcome these limitations, and the dynamic range was successfully extended to 109 dB along with improvements on the linearity.

From the thorough damping study performed in this work, a new application for the pull-in time using the same microstructures was developed. It consists of a gas viscosity sensing application. At the low frequencies operated, damping is directly proportional to the viscosity of the gas medium. The experimental results obtained with gases with viscosities ranging from 8 μP to 18 μP have shown a sensitivity of 2 ms/μP, making the pull-in time viscosity sensor a very promising approach.

Keywords: Pull-in, MEMS, accelerometer, noise, parallel-plates, damping, electrostatic feedback, gas viscosity.

RESUMO

Acelerómetro MEMS para a gama de micro-g, baseado em medição de tempo

Nas últimas décadas assistiu-se a um imenso crescimento no mercado de sensors MEMS, tendo os acelerómetros sido uma das maiores forças impulsionadoras desse crescimento devido às suas aplicações na indústria automóvel. Desde então, a gama de aplicações destes sensores expandiu-se multidirecionalmente, novas aplicações emergiram e acelerómetros convencionais em aplicações já existentes foram substituídos por acelerómetros MEMS. Isto deve-se essencialmente ao seu baixo custo e pequenas dimensões. Há no entanto, aplicações para as quais o desempenho dos acelerómetros MEMS ainda não é suficiente.

O objectivo deste trabalho é desenvolver um acelerómetro de elevado desempenho tirando partido da elevada sensibilidade do efeito de *pull-in* a forças externas tais como a aceleração. O efeito de pull-in, descrito pela primeira vez há mais de 40 anos, ocorre em dispositivos capacitivos com partes móveis. Este é um efeito não-linear geralmente evitado/indesejado, uma vez que se traduz numa instabilidade que dificulta o controlo da posição das partes móveis. Na última década foi dedicada alguma investigaçao científica a este fenómeno, tendo sido descoberta a existência de um perfil de deslocamento particular, denominado meta-estabilidade, em determinadas condições de amortecimento e de actuação electrostática. Esta característica do pull-in torna a sua duração extremamente sensível a variações nas forças intervenientes, incluindo aceleração externa. Assim sendo, a medição do tempo de pull-in de micro-estruturas especificamente concebidas para o efeito pode ser utilizada para medir aceleração. Esta abordagem apresenta vantagens significativas em comparação com a transdução direta de capacidade para aceleração (caso da generalidade dos acelerómetros capacitivos). Nomeadamente, a variável tempo pode ser medida com elevada precisão com relativa facilidade e sem necessidade de desenvolvimentos tecnológicos (o que não é o caso da medição de capacidade). Por exemplo, o uso de uma frequência de relógio de 100 MHz no mecanismo de contagem de tempo permite uma resolução de 100 ns na medição de tempo, o que corresponde, considerando a sensibilidade de 0.26 µs/µg do acelerómetro desenvolvido neste trabalho, a uma resolução na medição de acceleração de 0.38µg.

Um dos maiores desafios do desenvolvimento de um acelerómetro baseado no tempo de pull-in é o desenho do amortecedor, pois a sensibilidade e o ruído/resolução do sensor final dependem do nível de amortecimento. Uma nova geometria para o amortecedor (estabelecido por

um mecanismo de *squeeze-film*) é apresentada e estudada neste trabalho. Esta consiste em abrir canais nas placas paralelas facilitando assim o fluxo de ar quando as placas se movem. Ficou provado que esta geometria é eficaz na redução da razão capacidade/amortecimento, o que constituía um problema recorrente no desenho de dispositivos de placas paralelas *in-plane*.

Neste trabalho é descrito o desenvolvimento de um acelerómetro em malha aberta com uma sensibilidade de 0.26 µs/µg e 2.7 µg /√Hz de ruído. As estruturas MEMS utilizadas na sua implementação foram fabricadas num processo de microfabrico SOI comercial. As principais desvantagens desta abordagem são pequena gama dinâmica devido à não-linearidade da resposta. Neste trabalho foram exploradas abordagens em malha fechada, usando *feedback* electrostático, de modo a ultrapassar estas limitações, tendo sido alcançado um aumento da gama dinâmica para 109 dB, com grandes melhoria na linearidade.

Uma nova aplicação para o tempo de pull-in foi também desenvolvida: medição de viscosidade de gases. Uma vez que as microstruturas utilizadas são operadas a baixas frequências, o amortecimento é proporcional à viscosidade. O estudo efectuado mostra que o tempo de pull-in é muito sensível ao amortecimento e portanto a variações de viscosidade. Os resultados experimentais obtidos com gases e misturas de gases com viscosidades entre 8 µP e 18 µP mostraram uma sensibilidade de 2 ms/µP, confirmando o potencial da utilização de tempo de pull-in na medição de viscosidade

Palavras chave: *Pull-in*, *MEMS*, acelerómetro, placas-paralelas, amortecimento, *feeback* electrostático, viscosidade de gas.

TABLE OF CONTENTS

ACKNOWLEDGEMENTS iii
ABSTRACT v
RESUMO vii
TABLE OF CONTENTS ix
LIST OF FIGURES xv
LIST OF TABLES xxi
LIST OF ACRONYMS xxiii
1. Introduction 1
1.1. Conventional versus MEMS accelerometers 4
1.2. State-of-the-art high performance MEMS accelerometers 5
1.2.1. Open-loop capacitive accelerometers 7
1.2.2. Closed-loop capacitive accelerometers using ΣΔ modulators 8
1.2.3. Pull-in accelerometers 9
1.2.3.1. Pull-in voltage accelerometer 11
1.2.3.2. Pull-in time accelerometer 11
1.2.3.3. Pull-in time accelerometer with metastability 11
1.3. Motivation and goals 13
1.4. Organization of the thesis 15
References 18
2. Electromechanical coupling analysis 23
2.1. One degree-of-freedom MEMS device 25
2.2. Pull-in of capacitive 1-DOF parallel-plates – Static analysis 28
2.2.1. Comb-like structures 31
2.3. Dynamic analysis of pull-in 33
2.3.1. Metastable region – sensitivity to acceleration 38
2.4. Conclusions 42

References 43
3. Fabrication of devices 45
3.1. SOIMUMPs micromachining process 46
3.2. Fabricated MEMS structures 50
3.2.1. MEMS structures description 50
3.2.2. Elastic spring model 56
3.3. Fabricated capacitive readout circuit 57
3.4. Conclusions 60
References 61
4. Squeeze-film damper design 63
4.1. Parallel-plates MEMS design 64
4.1.1. Conventional plate configuration 64
4.1.2. Improved damper geometry – channels 66
4.2. Squeeze-film damping analytic model 68
4.2.1. Squeeze-film damping 68
4.2.2. Analytic model with rarefaction and compressibility effects 69
4.2.3. Border effects 71
4.2.4. Inertial effects 72
4.2.5. Damping in parallel-plates with channels 72
4.3. Fabricated devices damper analysis 73
4.4. CFD modeling 75
4.4.1. Parallel-plates with channels – CFD 78
4.5. Experimental procedure and results 83
4.6. Channels geometry parameters – preliminary assessment 90
4.7. Pull-in accelerometer damper considerations 92
4.8. Conclusions 93

References 95

5. Open-loop accelerometer operation and characterization 97

5.1. Open-loop operation description 98

5.2. Microstructure design and dynamic behavior simulation 100

5.3. Noise analysis 103

5.3.1. Mechanical-thermal (Brownian) noise 104

5.3.2. Readout circuit noise 105

5.3.1. Actuation voltage source noise 105

5.3.1. Total noise 106

5.4. Experimental evaluation 106

5.4.1. Experimental setup 106

5.4.2. Results 107

5.4.3. Readout noise 110

5.4.4. Actuation voltage noise 111

5.4.5. External noise 112

5.4.6. Discussion 113

5.5. Conclusions 114

References 115

6. Closed-loop operation 119

6.1. Open loop response limitations 119

6.2. Electrostatic feedback compensation 121

6.2.1. Constant pull-in critical displacement 122

6.2.2. Constant pull-in time 124

6.2.2.1. Keeping $V_{step} = \alpha\, V_{PI,n}$, changing V_{EF} 124

6.2.2.2. Other possibilities 125

6.2.3. Model study conclusions 125

6.3. Sensitivity verification over an extended operation range 126

6.3.1. Experimental verification 126

6.3.2. Discussion 129

6.4. Closed-loop real time operation 130

6.4.1. Control algorithm 130

6.4.2. Experimental setup 133

6.4.3. Results 134

6.5. Conclusions 138

References 139

7. Gas viscosity sensing based on pull-in time 141

7.1. Viscosity measurement 142

7.1.1. General viscosity measurement techniques 142

7.1.2. Viscosity measurement based on MEMS techniques 143

7.1.3. Application areas for gas viscosity sensors 145

7.1.4. Gas viscosity theory 145

7.2. Principle of operation of the viscosity sensor based on pull-in time 146

7.2.1. Damping coefficient viscosity dependence 148

7.2.2. Pull-in time viscosity dependence 149

7.3. Experimental setup 150

7.3.1. Microstructure electrostatic operation and readout 150

7.3.2. Gas testing experimental setup 151

7.4. Test procedure 153

7.4.1. H_2-N_2 mixtures 153

7.4.2. Pure gas viscosity measurements 154

7.4.3. CH_4-N_2 and CH_4-N_2-CO_2 mixtures 155

7.4.4. Actuation voltage dependence 156

7.4.5. Performance discussion and future improvements 157

7.5. Conclusions 158

References 159

8. Conclusions 163

8.1. Conclusions 163

8.2. Future work 165

References 167

ANNEX 1 – LIST OF PUBLICATIONS 169

LIST OF FIGURES

Figure 1.1: General accelerometer structure and its mechanical lumped model. 4
Figure 1.2: Open-loop operation diagram. 6
Figure 1.3: Closed-loop operation diagram. 7
Figure 1.4: Typical pull-in dynamic characteristic of an overdamped microdevice. 12
Figure 1.5: Open-loop pull-in time accelerometer operation. 13
Figure 1.6: Fabricated MEMS structure SEM pictures and detail of damper, springs and stoppers. 14
Figure 1.7: Electrostatic counter actuation of parallel-plate structure. 14
Figure 1.8: New damper geometry used to decrease squeeze-film damping between parallel-plates. 15
Figure 1.9: Main steps involved in the accelerometer development. 16
Figure 2.1: Actuator schematic. 25
Figure 2.2: Bode plot of different quality factor devices. 27
Figure 2.3: Step response of different quality factor devices. 28
Figure 2.4: Normalized forces. 29
Figure 2.5: Normalized forces for increasing voltage values. 30
Figure 2.6: Typical in-plane parallel-plate device geometry. 31
Figure 2.7: Normalized pull-in critical displacement as a function of the normalized second gap dimension. 32
Figure 2.8: Simulink block diagram. 33
Figure 2.9: Pull-in dynamic transition. 35
Figure 2.10: Forces acting during a pull-in dynamic transition of an overdamped device. 36
Figure 2.11: Pull-in time variation with quality factor for a) α=1.01 and b) α=1.001. 37
Figure 2.12: Pull-in time variation with actuation voltage. 38
Figure 2.13: Pull-in time variation with external acceleration forces. 39
Figure 2.14: Simulated pull-in time changes with voltage step amplitude and external acceleration. 40
Figure 2.15: Simulated pull-in time variation with external acceleration and different quality factors. 41

Figure 2.16: Calculated pull-in time changes with voltage step amplitude and external acceleration, using equation (2.24). ... 42
Figure 3.1: SOIMUMPs process flow diagram. ... 47
Figure 3.2: SOIMUMPs process steps. ... 48
Figure 3.3:Trench and silicon beams features for manual subdicing. ... 50
Figure 3.4: Picture of a die as provided by MEMSCAP and two smaller pieces already subdiced from another die. ... 51
Figure 3.5: Optical microscope picture of microstructure S0 showing the comb beams for actuating (on the extremities of the movable mass) and for sensing (the more numerous plates in the central area, with top and bottom already connected on the die), and detail of one bi-folded spring. ... 52
Figure 3.6: Optical microscope picture of microstructure S1. ... 52
Figure 3.7: Optical microscope picture of microstructure S2. ... 53
Figure 3.8: SEM picture of microstructure S2 showing the damper channels detail. ... 53
Figure 3.9: SEM picture of microstructure S0 detail showing spring and stoppers. ... 54
Figure 3.10: Applied force on beam with one fixed and one guided end. ... 57
Figure 3.11: Sensing capacitance variation of microstructure S0 with displacement from rest position. ... 58
Figure 3.12: Displacement detection circuit with charge amplifier and AM demodulation stage. 59
Figure 3.13: Readout circuit output as a function of sensed differential capacitance. ... 60
Figure 4.1: Change in damping coefficient as function of number of parallel-plates in a 1 pF total capacitance. ... 65
Figure 4.2 : Example of two sets of parallel-plates (dampers) of an in-plane device without substrate, with a sensing gap of 2 μm. ... 66
Figure 4.3: Design of square damping reducing holes on parallel plate moving out-of plane. ... 67
Figure 4.4: Proposed improved geometry for parallel-plates dampers: schematic of a flow channel in a parallel-plate. ... 67
Figure 4.5: (a) Symmetrical and (b) nonsymmetrical outlets on parallel-plates. ... 71
Figure 4.6: Microscope pictures of the fabricated structures (a) S1 and (b) S2 with detail showing air channels, folded spring and stoppers. ... 74
Figure 4.7: Knudsen number as a function of gap for the geometry of S1. ... 75
Figure 4.8: a) Schematic of the damper highlighting the volume of air modeled by CFD and b) 3D CFD meshed model. ... 76

Figure 4.9: 3D CFD model with 10 air channels (channels are included both on the moving and fixed arms).. 79
Figure 4.10: Pressure distribution on the gas medium for a) normal and b) improved geometry. 80
Figure 4.11: CFD modeled flow velocity profiles in cross sections (indicated in Figure 4.10) of a) conventional parallel-plates and b) parallel-plates with air channels. 81
Figure 4.12: Capacitance and damping coefficient (normalized to the maximum values) changes with air channels at a 1.5 µm gap. 82
Figure 4.13: Capacitive readout circuit calibration results. 84
Figure 4.14: Comparison between damping coefficients obtained from experimental measurements, analytic (equations (4.14) and (4.16)) and CFD modeling for structures a) S1 and b) S2. 86
Figure 4.15: SEM picture of the structure S1, evidencing the vertical misalignment. 87
Figure 4.16: Comparison between S1 damping measurements with damping values obtained by analytic modelling with correction for deflection. 88
Figure 4.17: Damping coefficient results comparison, for the structures with conventional damper and with air channels. 89
Figure 4.18: Variation of the brownian noise and the sensitivity with the quality factor of a pull-in accelerometer. 93
Figure 5.1: Microaccelerometer block diagram. 99
Figure 5.2: Simulated pull-in dynamic transition using α = 1.01. 102
Figure 5.3: Simulated pull-in time variation with α. 102
Figure 5.4: Pull-in time variation with external acceleration, for α = 1.01. 103
Figure 5.5: Picture of the Polytec microsystem analyzer MSA-500, the setup used for frequency analysis. 107
Figure 5.6: Experimental setup a) overview and b) detail of the microstructure mounted on the front-end readout circuit. 107
Figure 5.7: Bode analysis performed with MSA-500 using sinusoidal actuation of amplitude 1 V and 1 V offset. 108
Figure 5.8: Simulated and experimental nominal (0 g) pull-in time. 109
Figure 5.9: Simulated and experimental pull-in time values for different values of α ($\alpha = V_{step}/V_{PI}$). 109

Figure 5.10: a) Simulation and experimental results of pull-in time variation with external acceleration and b) accelerometer response to ±3 mg external acceleration (6 mg_{p-p}) applied at 1 Hz. 110

Figure 5.11: Measured t_{PI} rms noise using actuation voltages with added rms noise. The data was fitted excluding the actuation voltage rms noise values below 30 mV and yielded a correlation factor R^2= 0.987. 112

Figure 5.12: Comparison between normalized experimental and modeled results for pull-in time noise as a function of the actuation voltage noise. 113

Figure 6.1: Accelerometer model response using $V_{step} = \alpha V_{PI,n}$ and $V_{step} = \alpha V_{PI,a}$. 120

Figure 6.2: Pull-in accelerometer setup with electrostatic counter-actuation. 122

Figure 6.3: Simulation pull-in time results when actuating with $V_{step} = \alpha V_{PI,xPI}$ and $V_{EF,xPI}$ and corresponding voltages, over large DC acceleration range and ± 4 mg. 123

Figure 6.4: Simulation pull-in time results when actuating with constant $V_{step} = \alpha V_{PI,n}$ and $V_{EF} = f(a_{ext})$ and corresponding voltages, over large DC acceleration range and - 1 mg - 4 mg. 125

Figure 6.5: Photograph of the experimental setup used and detail of the accelerometer mounted on the PCB readout circuit. 127

Figure 6.6: Pull-in time results for AC acceleration values of ± 1 to ± 4 mg, at 1 Hz, over a 200 mg DC acceleration. 128

Figure 6.7: Pull-in voltages results and electrostatic compensation voltage applied. 128

Figure 6.8: Accelerometer response to ± 4 mg AC acceleration, with DC accelerations compensated electrostatically, and resulting sensitivity. 129

Figure 6.9: Closed-loop pull-in accelerometer setup. 130

Figure 6.10: Response of proportionality constant (50) algorithm. 131

Figure 6.11: Control algorithm response to acceleration steps of 10, 50 100 and 300 mg. 132

Figure 6.12: Control algorithm response to sinusoidal acceleration of amplitude 10, 50 100 and 300 mg. 133

Figure 6.13: Photograph of the accelerometer and the readout circuit PCB mounted on the elevator structure. 134

Figure 6.14: Photograph of the accelerometer and the readout circuit PCB mounted on the shaker. 134

Figure 6.15: Experimental pull-in time and V_{EF} results under (left) an AC acceleration of 8 mg_{p-p} at 1 Hz, over a 13 mg offset and (right) an AC acceleration of 2 mg_{p-p} at 1 Hz, over a 110 mg offset. 135
Figure 6.16: Experimental pull-in time and V_{EF} results under an increasing AC acceleration of 26 mg_{p-p} over a 14 mg offset. 135
Figure 6.17: Experimental V_{EF} results under an increasing AC acceleration of 66 mg_{p-p} maximum over a 14 mg offset. 136
Figure 6.18: Electrostatic feedback voltage results for 125 mg_{p-p} acceleration, at 1 Hz, over a 14 mg offset. 136
Figure 6.19: Electrostatic feedback voltages for the different external accelerations applied. ... 137
Figure 7.1: Beam-supported, mass-loaded plate, Pyrex substrate and gas-flow cap comprising the test structure [7.3]. 143
Figure 7.2: Basic topology of the viscosity sensor. 147
Figure 7.3: a) Schematics and b) picture of the fabricated sensor housing. 152
Figure 7.4: Sensor in housing connected to gas supply of the EDGaR installation. 152
Figure 7.5: Pull-in times measured for different N2-H2 compositions. 154
Figure 7.6: tPI measurement results for pure gases. 154
Figure 7.7: All the pull-in times measured. Those of mixtures with methane are inside the circle. 156
Figure 7.8: Pull-in time variation as a function of the actuation voltage, for the different pure gases tested. 157

LIST OF TABLES

Table 1.1: Acceleration sensor application grades [1.12]. 3
Table 1.2: Overview of commercial and state-of-the-art high-resolution accelerometers found in literature. 10
Table 3.1: Main modeled (analytic model) design parameters of the structures S0, S1 and S2. .. 55
Table 3.2: S2 air channel damper geometry values. 56
Table 4.1: Measured velocities, corresponding frequencies (for 1 nm oscillation amplitude), and cut-off frequencies, at different gaps for both structures S1 and S2. 85
Table 4.2: Channel parameters (in µm) and results of the 25 simulations performed. 91
Table 4.3: Rank results according to the Taguchi analysis. 91
Table 6.1: Main accelerometer parameters. 138
Table 7.1: Physical constants of a few common gases at standard conditions (1 atm and T= 293 K) [7.17], [7.19], [7.24], [7.30], [7.31]. 148
Table 7.2: Comparison between damping coefficient sensitivity to viscosity and mean free path changes, using different gases and taking in account a 1.5 µm damper width, at standard conditions (1 atm and T= 293 K) [7.17], [7.24], [7.30], [7.31]. 149
Table 7.3: Pure gas and mixture calculated viscosities and pull-in time results. 153
Table 7.4: Compositions of natural and synthetic gases reported in literature [7.34]–[7.37]. 155
Table 7.5: t_{PI} results for different gas mixtures. 155

LIST OF ACRONYMS

AC – Alternate current

AHRS – Attitude heading reference system

BOX – Buried oxide

BS – Backside

CAD – Computer-aided design

CFD – Computational fluid dynamics

DAC – Digital to analog converter

DAQ – Data acquisition board

DC – Direct current

DOF – Degree-of-freedom

DRIE – Deep reactive ion etching

FEM – Finite element modelling

FPGA – Field Programmable Gate Array

FS – Frontside

IC – Integrated circuits

ICP – Inductively coupled plasma

IMU – Inertial measurement unit

MEMS – Microelectromechanical systems

PCB – Printed circuit board

PSG – Phosphosilocate glass

RIE – Reactive ion etching

RMS – Root mean square

SEM – Scanning electron microscope

SI – International system

SNG – Synthetic natural gas

SOI – Silicom-on-insulator

UV – Ultra-violet

1.

Introduction

The acronym MEMS – MicroElectroMechanical Systems was introduced in the late 1980s, and refers to a wide range of concepts. Commonly, it can refer to a system, i.e., a combination of components with dimensions in the range of micrometers and with functionality in the mechanical and electrical domains (and others). MEMS can refer simply to a structure with micro dimensions fabricated on a silicon wafer, or a whole system containing sensors, actuators and electronic circuits. In a nutshell, a MEMS product is a miniature system with one or more micromachined components [1.1]. The techniques used to fabricate such systems, micromachining techniques, evolved from the IC (Integrated Circuits) industry, and are generally grouped in two categories: bulk and surface micromachining. Although micromachining has been demonstrated in a variety of materials such as glasses, polymers and metals, silicon is strongly associated with MEMS [1.1]. Since the MEMS industry evolved from the silicon-based IC industry, design tools are available, and the material properties, especially electrical, are very well characterized. In addition, low-cost batch fabrication is enabled by the use of silicon, which has desirable mechanical properties [1.1].

Microelectromechanical structures and systems are today present in many application areas, especially automotive, medical, consumer, industrial, and aerospace. The MEMS technology relies on a large toolbox of design and fabrication processes (many borrowed from the IC industry). MEMS development is an inherently interdisciplinary process, that requires understanding of both the toolbox and end application [1.2].

Pressure sensors were responsible for the first big leap in the MEMS world. These were the first MEMS products to be technically and economically successful, produced by bulk

micromachining in the late 1970s [1.3]. Pressure sensors still represent a large and important part of the MEMS component industry [1.4]. Surface micromachining emerged later in the mid-1980s and it was used for the fabrication of accelerometers and other electromechanical structures [1.3]. The first micromachined accelerometer was reported by Roylance et al. in 1979 [1.5]. It used bulk micromachining and wafer bonding techniques. A silicon bulk micromachined proof mass was bonded between two glass wafers and its displacement was detected using a piezoresistive transduction mechanism [1.5]. Approximately 10 years after, piezoresistive accelerometers were commercially available [1.6]–[1.8], but it was only in 1993 that accelerometer production became successful at large scale, with Analog Devices' accelerometer ADXL50, used to deploy airbags [1.9]. Since then, micromachined acceleration sensors have been the subject of intensive research, with work published on several types of MEMS accelerometers, and with the applications expanding from the automotive industry (the initial major driver) to an immensely broad range of fields. Accelerometers are included in the larger group of the inertial sensors, together with gyroscopes. A good review of the history, applications and types of MEMS inertial sensors is provided by Yazdi [1.10]. Accelerometers are used in biomedical applications for activity monitoring; consumer applications, such as mobile phones for picture orientation, in laptops to prevent hard disc damage when shock occurs, in video game controllers to detect three dimensional movement; in industrial applications such as vibration monitoring; military applications, including impact and void detection; and many others. High-sensitivity accelerometers specifically, are essential components in navigation and guidance systems (IMU-Inertial Measurement Units and AHRS-Attitude Heading Reference Systems), seismometry for oil exploration and earthquake prediction, and microgravity measurements in space [1.10].

Within the MEMS market, modern inertial sensors – accelerometers and gyroscopes - have gained a considerable share, reaching 28 % of the 10.2 billion dollars MEMS market in 2011 [1.11]. According to Yole Développement, in the last three years the MEMS accelerometer market value grew 78% [1.11]. Accelerometers for consumer and automotive applications only, exceed one billion dollars of the expected 11.5 billion dollars total MEMS market value in 2012 [1.11].

Consumer applications in general have very low requirements for accelerometer specifications while other applications can be very demanding, as is the case of inertial navigation systems (requiring a few micro-g resolution), seismic disturbances detection and gravity gradients measurement (nano-g range) [1.12]. Although the SI unit (International System

of Units) of acceleration is m/s^2 (meters per square second), *g* ("*gee*") is the unit generally used in the accelerometers market and research field, (1 g = 9.80665 m/s^2 [1.13]).

A very wide range of accelerometer accuracies is available, and accelerometers can be classified according to the application grade for which their accuracy is best suited, as shown in Table 1.1. High performance accelerometers can be segmented into several categories: tactical grade, navigation grade and military grade each characterized by an order of magnitude improvement on bias stability, linearity and noise.

Table 1.1: Acceleration sensor application grades [1.12].

Application grade	Accelerometer performance
Consumer/Commercial	>50 mg
Tactical	~1 mg
Navigation	25 µg
Strategic	~1 µg

Accelerometers can detect the effect of acceleration in several different ways, but most of them can be grouped into proof-mass displacement monitoring or resonance frequency shift detection. The most common type of accelerometers are based on monitoring the displacement of a proof mass suspended by compliant beams anchored to a fixed frame (Figure 1.1). This can be done electronically using capacitive, piezoresistive or piezoelectric electronic circuits. Some devices also use a tunneling current transduction mechanism that employs a tunneling tip attached to a movable inertial mass to detect its displacement. Optical and magnetic transduction mechanisms are also found in accelerometers. The devices that use resonating elements (beams or membranes) rely on the resonance frequency shift of a beam caused by loading of a proof mass attached to the beam or the beam mass itself.

Additionally, there are also accelerometers that use thermal convection as the transduction mechanism. Thermal flux can be used to measure the distance between a fixed heater and a movable heat-sink (these accelerometers fall into the first movable proof-mass monitoring group), but gas convection can also be used to sense acceleration using all-fixed heater and heat-sink structures (making up a whole different way of measuring acceleration without requiring proof-masses) [1.14]–[1.16].

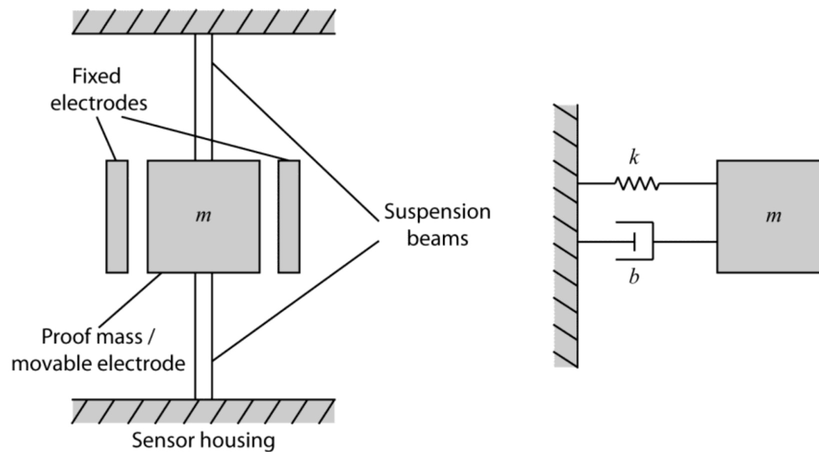

Figure 1.1: General accelerometer structure and its mechanical lumped model.

Optical technologies have also been proposed for the realization of accelerometers, with potential for very high sensitivities. Optical accelerometers use an optical readout of the effect of acceleration on a physical structure. Examples of studies concerning fiber-optic and fiber Bragg grating accelerometers are [1.17] and [1.18]. The accelerometer described in [1.19] comprises a Fabry-Perot interferometer monolithically integrated with a photodiode. Despite highly sensitive, optical accelerometers developed so far haven't reached much commercial success since other characteristics limit their performance [1.12].

1.1. Conventional versus MEMS accelerometers

The most accurate accelerometer developed so far, which is at laboratory demonstration stage, is the light force accelerometer. It is based on the laser levitation of a dielectric proof mass and is estimated to have the potential of resolving 5 ng [1.12].

Innalabs Ltd. commercializes a quartz accelerometer with 1 μg resolution and a large input range of ± 50 g, INN-202 [1.20]. The applications of these high performance accelerometers are inertial navigation and orientation systems for aerial and maritime circulation and also orientations systems for oil drilling industry [1.20].

Honeywell [1.21] offers a high accuracy micromachined resonant accelerometer, the quartz resonating beam accelerometer RBA500, with 1 μg resolution. It has a piezoelectric frequency readout coupled with well-established and robust oscillator circuit concepts [1.22]. The quartz material is high-purity single crystal. This kind of systems are sometimes called QMEMS, quartz MEMS, due to their small dimensions, but despite having some of the advantages of (Si) MEMS, these are still very expensive to manufacture.

Although MEMS accelerometers are already available with sub-µg noise characteristics, these still cannot compete with the state-of-the-art conventional accelerometer in terms of input range, DC (Direct Current) bias and thermal coefficient [13], [16].

MEMS technology offers many benefits such as size reduction, batch production and cost reduction, power reduction and robustness. However, the size reduction creates challenges in respect to performance. For instance, smaller inertial masses translate to higher thermal-mechanical noise. MEMS accelerometers have enabled many new applications in the last decades, and continue to replace conventional accelerometers as higher performance MEMS accelerometers become available.

1.2. State-of-the-art high performance MEMS accelerometers

High sensitivity accelerometers have been given a lot of attention by the MEMS community in the last years [1.24]–[1.41]. The motivation is the development of high-resolution MEMS accelerometers that are needed in a large number of applications, including inertial navigation, space microgravity measurement and earthquake prediction. MEMS accelerometers are based on the detection of small movements of a proof mass due to the acceleration force and the resolution of the accelerometer is limited by the mechanical-thermal noise of the sensor (given by the damping coefficient and the mass of the structure) and by the readout electronics (which is usually the limitating factor).

Microfabricated tunneling accelerometers have been demonstrated, resolving 20 ng/√Hz over 5 Hz to 1.5 kHz (i.e., a maximum resolution of 0.5 µg, at 5 Hz) with a closed-loop dynamic range of more than 90 dB but limited to a measurement range of approximately 1 mg [1.42]. The tunneling accelerometer reported in [1.43] have a 15 ng/√Hz over 1 to 100 Hz (i.e., resolution threshold of 15 ng at 1 Hz).

Capacitive and piezoresistive methods are the most common MEMS accelerometer readouts. Piezoresistive accelerometers offer as main advantages the simplicity of their structure and fabrication process, as well as of their readout circuitry [1.10]. A capacitive readout is usually more complex, but using capacitance change as the transduction effect offers some benefits in comparison to piezoresistive methods. The changes of the gaseous/air dielectric constant with temperature are very small, and, although capacitance gap changes with temperature due to thermal expansion of the walls material (silicon), the thermal coefficient of capacitance can be up to two orders of magnitude smaller than the thermal coefficient of

resistivity of doped silicon [1.10], [1.44]. Therefore, capacitance sensing has the potential to provide a wider temperature range of operation, without compensation, than piezoresistive sensing. In respect to the accelerometers that use piezoelectric transduction mechanisms, these require a dynamic input of a minimum frequency to generate a response, presenting limitations for near DC frequencies, while capacitive methods can be used to sense DC accelerations [1.44], [1.45]. The advantages described allow the capacitive accelerometers to be used in a wider range of applications and is also the reason why there is so much research on capacitive MEMS accelerometers.

Accelerometers can also be classified according to their type of operation: open-loop or closed-loop. An example of an open-loop operated accelerometers is simply the displacement measurement of a proof-mass using the capacitance variation that the displacement causes (displacement is proportional do acceleration) (Figure 1.2). A common closed-loop operation consists of maintaining the proof mass in the rest position using electrostatic force. The mass displacement is measured as in the open-loop approach, but a feedback mechanism is present, i.e., a control mechanism applies an electrostatic force to counterbalance the acceleration effect (Figure 1.3).

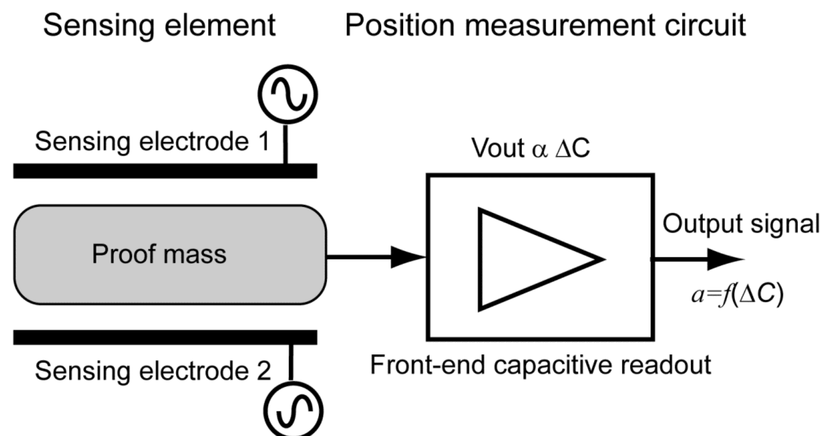

Figure 1.2: Open-loop operation diagram.

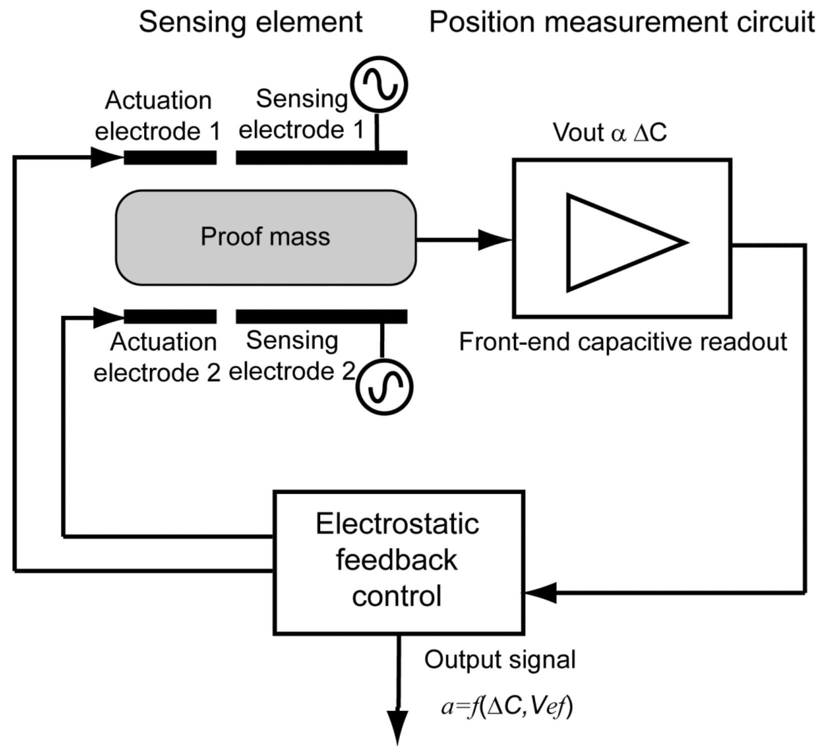

Figure 1.3: Closed-loop operation diagram.

In the case of open-loop operation, the required interface circuitry is much simpler than the circuits required for closed-loop operation, but closed-loop operation provides a better control over the electrostatic forces interaction and presents less sensitivity to changes in the system parameters and thus improved accelerometer performance [1.46]. Despite the advantages of closed-loop operation (improvement of the overall sensor performance, such as linearity, dynamic range and bandwidth), the closed-loop operated devices described in literature present higher noise level characteristics.

1.2.1. Open-loop capacitive accelerometers

Initial approaches to deliver high-resolution accelerometers were based on open-loop configurations [1.24]–[1.27] using capacitive transduction mechanisms. Chae et al. report a high-resolution accelerometer with a 120 dB dynamic range using an open-loop configuration and with a total noise floor of 1.6 µg/√Hz, fabricated using a complex doubled-sided bulk micromachining fabrication process mixed with surface micromachining [1.24]. In [1.25] an SOI (Silicon-On-Insulator) based process with a 50 µm layer is used. The works in [1.26] and [1.27] also use SOI-based fabrication processes. In [1.26] a high-aspect ratio polysilicon and single-crystal silicon process is used.

State-of-the-art capacitive parallel-plates accelerometers have already demonstrated sub-μg resolution, with the total noise floor threshold being currently set on 230 ng√Hz by the device described in [1.27]. This device is open-loop operated and has a 5 Hz bandwidth. It is fabricated using a modified and dedicated micromachining procedure to allow keeping a portion of the SOI handle wafer attached to the proof mass.

A common characteristic of these open-loop approaches is the high demanding specifications of the electronic readout circuits. All these accelerometers require readout circuits with capacitance resolutions below 10 aF with very low noise characteristics and good stability. In addition, the complexity of the fabrication processes requires technological improvements for large scale production. Regarding long-term stability, almost no data is available and open-loop systems tend to have poor long-term performance since any small change on the system directly affects the output.

The described approaches require modified fabrication processes as well as highly sensitive low noise readout circuits (with resolutions on the order of attofarads). Still, there are open-loop accelerometers commercially available, namely Silicon Designs' accelerometers, with up to 5 μg/√Hz noise for a ± 2 g input range.

1.2.2. Closed-loop capacitive accelerometers using ΣΔ modulators

A second approach used to deliver high-resolution accelerometers is based on closed-loop systems using high-order ΣΔ modulators [1.28]–[1.33] (which has become the dominant line of research). The benefits of closed-loop control are the increase in dynamic range, linearity and bandwidth. Moreover, sigma-delta conversion is expected to effectively reduce noise and improve overall performance. Nevertheless, when compared to open-loop accelerometers, closed-loop ΣΔ accelerometers are much more complex. The initial works on closed-loop ΣΔ accelerometers [1.28]–[1.30] were mainly focusing on proving the concept of ΣΔ accelerometers. In [1.28], [1.47] a total noise floor above 0.85 μg/√Hz is reported. More recently, the work presented in [1.31]–[1.33] has been focusing on long-term stability and improvements on the fabrication process have yielded a system with bias stability of 100 μg for 24 hours and bias thermal coefficient of 200 μg/ºC.

Changes to the traditional ΣΔ modulator have been recently proposed in order to improve the accelerometer performance [1.34]–[1.36]. Similarly to the open-loop accelerometers, ΣΔ closed-loop systems require very good readout electronic circuits along with stable actuation

voltages. The control systems are very complex and process variations during fabrication of the MEMS structure can degrade the accelerometer performance.

Table 1.2 presents a summary of the main parameters of different accelerometers found in scientific literature, commercially available, and also the pull-in time approach studied in this thesis.

1.2.3. Pull-in accelerometers

Electrostatic pull-in occurs in electrostatically actuated movable capacitors where one or more electrodes are connected to a spring. Considering a parallel-plate capacitor with a 1-DOF plate, if a voltage higher than a threshold (pull-in voltage) is applied between the plates, an electrostatic force with a value higher than the mechanical counter force is generated. In these conditions, the movable plate is accelerated towards the fixed one until it is stopped by mechanical contact (or the actuation voltage is turned off). This phenomenon is called pull-in. Generally, measures are taken to prevent short-circuiting between the electrodes, such as placing physical stoppers limiting displacement or protecting the fixed plate/electrode with an isolating material.

The pull-in effect occurs in voltage driven, electrostatically actuated microstructures and it is commonly avoided during operation since it leads to a region of instability where the position of the movable structure cannot be fully controlled. Yet, some acceleration sensing applications were already proposed, based on pull-in voltage measurement and pull-in time.

Table 1.2: Overview of commercial and state-of-the-art high-resolution accelerometers found in literature.

Reference	Sensitivity	Dynamic range	Noise density	Bias instability	Technology
Open-loop					
J Chae, H Kulah and K Najafi 2004 [1.24]	0.49 µV/µg (5.6 pF/g)	-	1.6 µg/√Hz	-	Double-sided process developed in-house (combined surface and bulk micromachining technology)
BV Amini and F Ayazi 2005 [1.25]	0.75 µV/µg	102 dB	11 µg/√Hz	-	In-house SOI process with active layer of 50 µm
P Monajemi and F Ayazi 2006 [1.26]	0.25 µV/µg	126 dB	0.95 µg/√Hz	-	High-aspect ratio polysilicon and single-crystal silicon process
R Abdolvand, BV Amini and F Ayazi 2007 [1.27]	105 µV/µg(35 pF/g)	-	0.21 µg/√Hz	8 µg (for 3h)	In-house SOI process with extra proof mass Specifically developed micromachining process
Silicon Designs Inc. (commercial) [1.44]	2 µV/µg		5 µg/√Hz		In-house, non-disclosed process
Closed-loop					
Y Dong, M Kraft, et al 2005 [1.28]	16 pF/g	-	1 µg/√Hz	-	Silicon on Glass process with active layer of 60 µm
H Kulah, J Chae, N Yazdi and K Najafi 2006 [1.29]	0.96 µV/µg		10 µg/√Hz	-	Double-sided process developed in-house (combined surface and bulk micromachining technology)
BV Amini, R Abdolvand and F Ayazi 2006 [1.30]	30 µV/µg	95 dB	4 µg/√Hz	8 µg (for 12h)	In-house SOI process with extra proof mass
P Zwahle, Y Dong, M Pastre et al 2009-11 [1.31]–[1.33]	-	132 dB	1.7 µg/√Hz	100 µg (for 24h)	In-house bulk micromachining and bonding of three wafers
B Almutairi and M Kraft 2010-2011 [1.34], [1.35]	0.65 V/g	-		-	In-house SOI process with active layer of 50 µm
U Sonmez, H Kulah and T Akin 2011 [1.36]	-	128 dB	6 µg/√Hz	6.4 µg (not specified)	In-house SOI process with active layer of 35 µm
Colibris SA (commercial) [1.23]	1.2 µV/µg		0.3 µg/√Hz		In-house bulk micromachining and bonding of three wafers
Open-loop Time based					
In this work [1.37], [1.38]	0.26 µs/µg	77 dB	2.7 µg/√Hz	-	Commercially available SOI process with active layer of 25 µm
Closed-loop Time based					
In this work [1.40]	31 V^2/g 0.26 µs/µg	109 dB	2.7 µg/√Hz	-	Commercially available SOI process with active layer of 25 µm

1.2.3.1. Pull-in voltage accelerometer

In the pull-in voltage measurement approach, as acceleration yields displacement of a proof-mass (movable electrode), the gap between the movable and fixed electrodes is changed and consequently also the pull-in voltage. Continuous measurement of the pull-in voltage (actuating with a voltage ramp) allows detection of pull-in voltage changes that are proportional to external acceleration [1.48].

The claimed advantage of this approach is the digital output of the sensor. The accelerometer performance can also be improved by differential measurement of bilateral pull-in voltages of a symmetrical capacitive structure (such as the one depicted in Figure 1.1) [1.48]. If this is done alternately, the difference in the pull-in voltages gives the measure of the external acceleration the device is experiencing. The use of this differential scheme improves the linearity and cancels out any drift in time of the pull-in voltage or changes with temperature, which means that no calibration is needed. This is an interesting approach but no reports on actual implementation are available.

1.2.3.2. Pull-in time accelerometer

In [1.49] the use of the pull-in time, t_{PI} as the acceleration sensing mechanism has been proposed. In this approach, voltage pulses are alternately applied to the electrodes of a symmetrical capacitor, and two pull-in times (one to each side) are measured. The central movable electrode (proof mass) is prevented from touching the fixed electrodes by mechanical stoppers placed between the electrodes (nearer to the fixed ones). If no acceleration is present the time-of-flight t_{PI} of the structure is the same for both sides, while if acceleration is present, differing pull-in times are observed. The t_{PI} difference, Δt_{PI}, is hence proportional do external acceleration. Since Δt_{PI} is a pulse-width-modulated signal it can be measured with a digital circuit, giving immediately a digital output. A limitation of this approach is the bandwidth, since bandwidths higher than 14% of the structure resonance are difficult to achieve [1.49]. More recently, a sensitivity of 5 μs / 1 g has been reported on fabricated devices using this approach, which is quite low in comparison to state-of-the-art accelerometers discussed so far [1.50].

1.2.3.3. Pull-in time accelerometer with metastability

In [1.51], a detailed study of the pull-in dynamic transition revealed the existence of a meta-stable region during the pull-in transition in overdamped micromechanical devices. In

certain actuation and damping conditions (that are later discussed in Chapter 2), the pull-in displacement profile presents a plateau characterized by relative slow motion of the structure near the critical pull-in deflection, defined as meta-stability [1.51] (Figure 1.4), with translates to a significantly longer pull-in event duration.

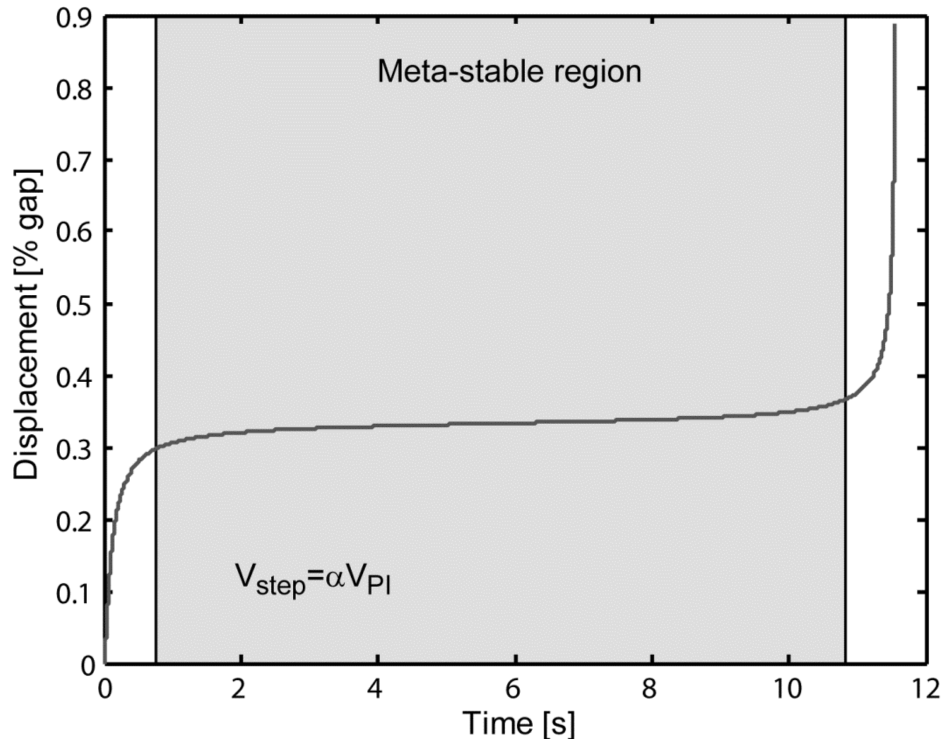

Figure 1.4: Typical pull-in dynamic characteristic of an overdamped microdevice.

The time duration of this metastable region is very sensitive to the intervenient forces, including external accelerations. In [1.51], [1.52] it has already been suggested that the high sensitivity of the meta-stable region could be used to measure small external accelerations. The first publications featuring the pull-in time accelerometer based on the metastable region were [1.53] and [1.54]. Although there were some previous reports featuring devices to measure acceleration using pull-in, these did not use the meta-stability feature, but rather relied on the measurement of the pull-in voltage [1.48] or the time-of-flight with no meta-stability occurring [1.49].

Repeatedly bringing a microstructure to pull-in, while measuring the pull-in time, enables the measurement of the external acceleration (Figure 1.5). Since a time measurement is performed, rather than a capacitive measurement, high resolutions are possible. High resolution capacitive readout circuits are difficult to accomplish but the resolution of the time measurement can be made very high. As the non-mechanical noise is set primarily by measurement resolution, the only noise source of the system will be the mechanical thermal noise. The time-based

accelerometer low-noise and the low requirements for the capacitive sensing circuit are clear advantages of this approach. The main disadvantage is the increase in the system complexity and the low system bandwidth.

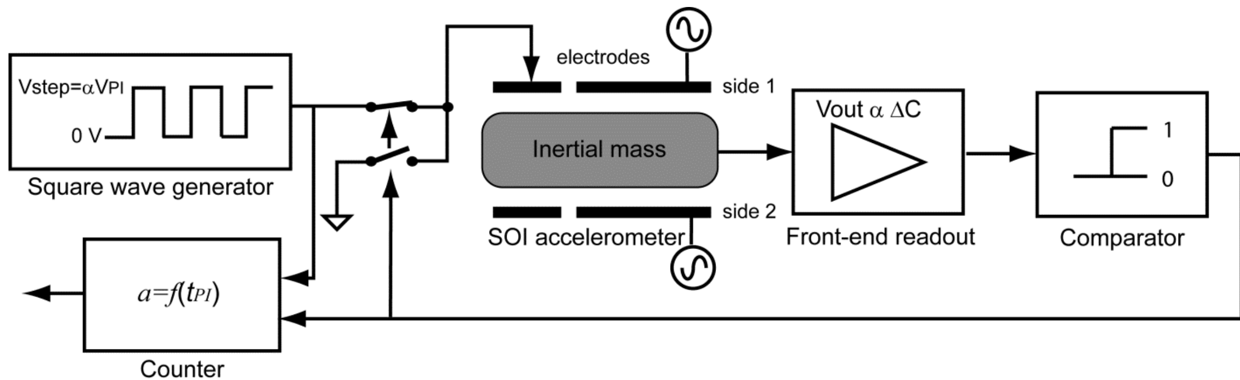

Figure 1.5: Open-loop pull-in time accelerometer operation.

1.3. Motivation and goals

A considerable amount of researched is dedicated to MEMS accelerometers and despite the efforts, there are still high resolution applications for which there are no suitable micromachined accelerometers available. Several accelerometer applications require resolutions better than 5 µg: inertial navigation, seismic activity monitoring, space microgravity measurements [1.1], and these applications typically demand a dynamic range of at least ±1 g (120 dB if 1 µg resolution is considered).

The main goal of this thesis is to develop a high resolution accelerometer taking advantage of the high sensitivity of the pull-in phenomenon to external forces. Rocha in [1.53] in 2005 provided the necessary knowledge concerning the pull-in nonlinearities, and also presented the idea of a pull-in time accelerometer based on the metastable region for the first time. As will be demonstrated in the following chapter, a tight equilibrium between the forces acting on an electrostatically actuated microstructure can be achieved, making the structure's behavior very sensitive to small changes in the intervenient forces including the external acceleration. This behavior is explored in this thesis to fabricate a very sensitive accelerometer with very high resolution capabilities. One of the main advantages of this approach is that a time measurement is performed rather than direct capacitance/displacement transduction into acceleration. In this approach, capacitance is only used to detect the pull-in event (the full travel gap is used). The time measurement can be performed with very high resolution with technology readily available (no improvements are required on the capacitance detection performance) and therefore, the noise

performance will not be limited by the measurement resolution, but by the mechanical-thermal noise of the microsystem.

Achieving the proposed goal involves modeling, designing and fabricating the microstructures (Figure 1.6) to be used for the accelerometer implementation, while aiming to maximize resolution, readout capabilities and pull-in time sensitivity to external acceleration. New closed-loop operation approaches (Figure 1.7) must also be developed to overcome performance limitations such as non-linearity and short dynamic range.

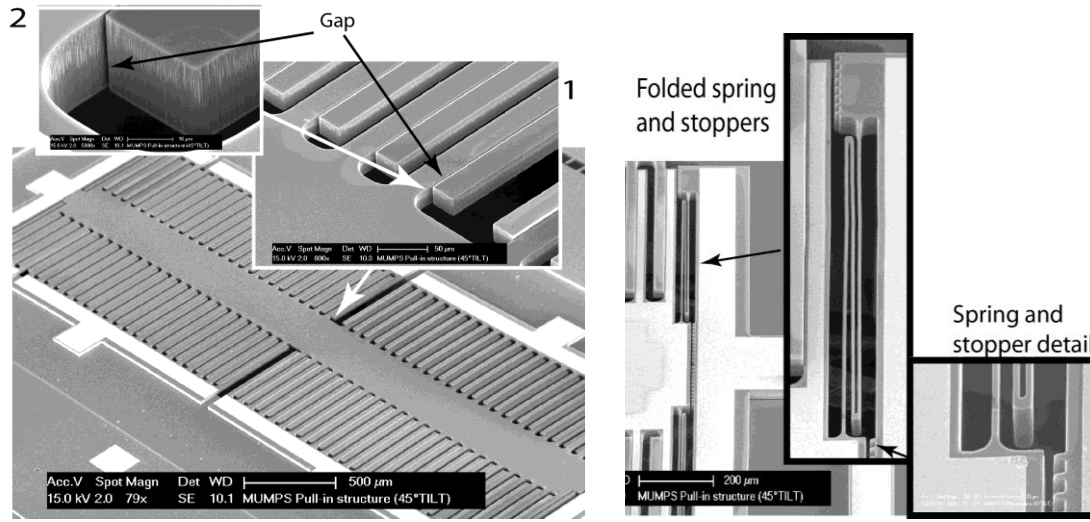

Figure 1.6: Fabricated MEMS structure SEM pictures and detail of damper, springs and stoppers.

Figure 1.7: Electrostatic counter actuation of parallel-plate structure.

One of the main challenges of the microstructure design is the damper design (a thorough damping study must be performed). New geometries (Figure 1.8) can be used to address existing capacitance/damping design conflicts. The damping of the system (established through a squeeze-film damping mechanism) will determine not only the dynamic behavior of the system, but also the mechanical-thermal noise, ultimately defining the resolution limit. A thorough

analysis of the noise sources must also be performed, as the low noise characteristic is one of the main claims regarding this acceleration sensing approach.

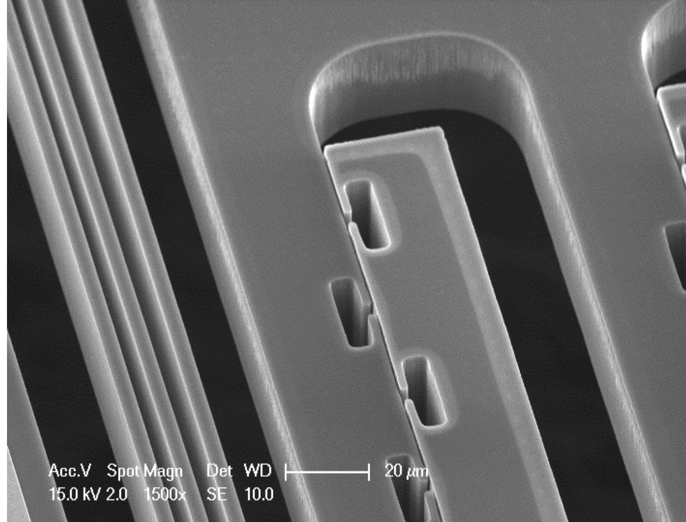

Figure 1.8: New damper geometry used to decrease squeeze-film damping between parallel-plates.

1.4. Organization of the thesis

A scheme showing the main steps that helped to fulfill the proposed objective is shown in Figure 1.9. Firstly it was necessary to study the theory behind the pull-in phenomenon and its sensitivity to the involved parameters. This knowledge, together with the microfabrication rules and constraints, allowed defining realistic accelerometer specifications. Modeling techniques were extensively used at this stage (analytical, finite element modeling and computation fluid dynamics), and the microstructures were designed and fabricated. New damper geometries were developed and characterized. Next, open and closed-loop operation methods were explored, to improve sensor performance. A thorough analysis of the noise sources involved was also performed.

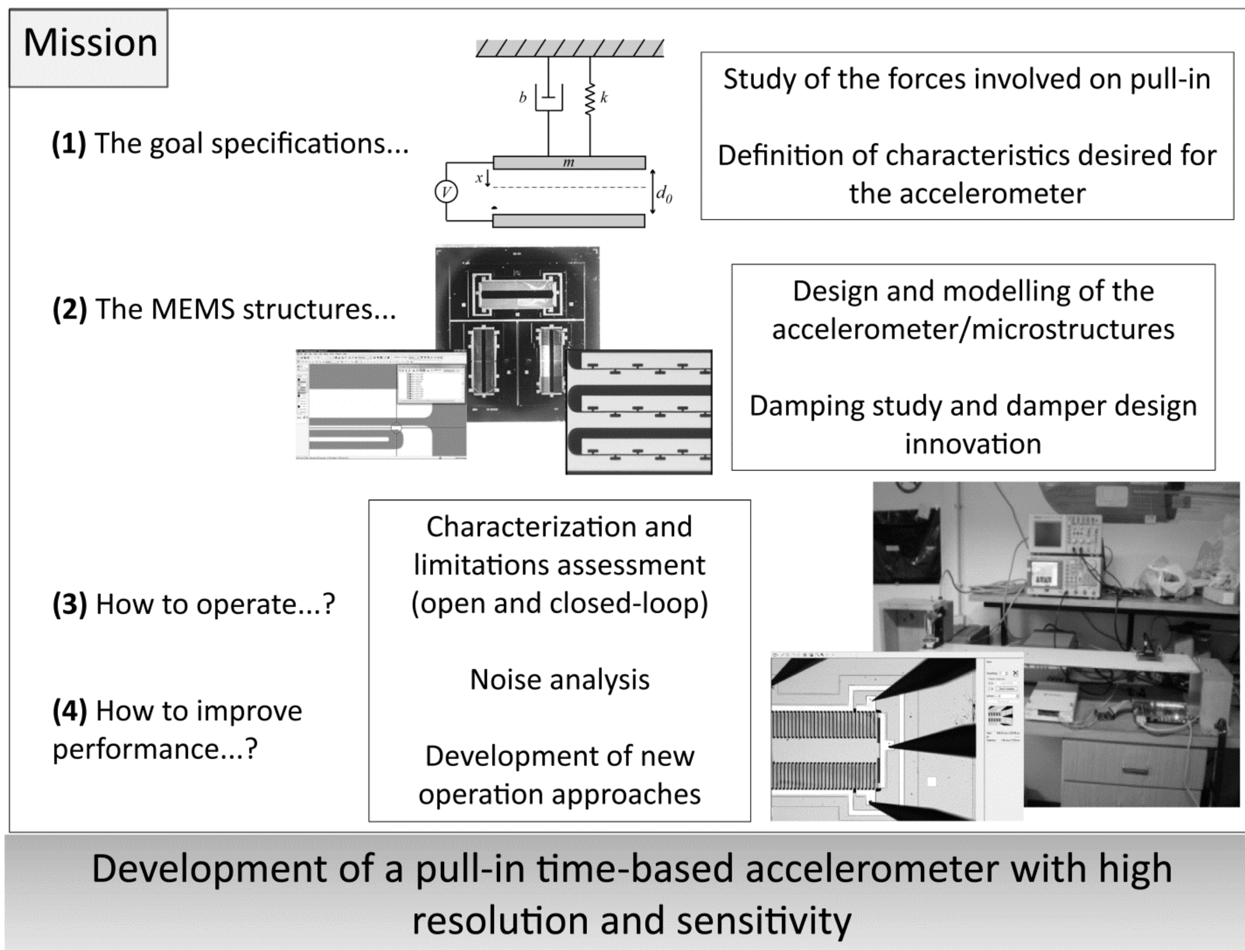

Figure 1.9: Main steps involved in the accelerometer development.

From this work, a new application also arose, using the same microstructures. As pull-in time is very sensitive to the damping conditions, and damping is very dependent on the viscosity of the gas medium, a gas viscosity sensor application was explored.

The thesis is organized around 8 chapters. This first chapter, Introduction, presented the state-of-the-art concerning high-resolution MEMS accelerometers, with particular emphasis on accelerometers with capacitive readouts; the motivation for fabricating MEMS sensors instead of the conventional macrosystems, and how these are being replaced; and also the motivations for the development of the pull-in time accelerometer. The next chapter features the review of the principle behind the measurement of acceleration using pull-in, namely the pull-in behavior theory and the origin of the metastable region and its sensitivity to external acceleration.

The structures used throughout this work for experimental verification and the technology used to fabricate them are described in Chapter 3. The SOIMUMPs surface micromachining process was used for fabrication of the devices designed and used throughout the work. As the

front-end capacitive readout circuit is also common to all the studies presented in the subsequent chapters, it is also described in this intermediate chapter.

The starting point of this work was designing and fabricating the MEMS structures for the actual implementation of the accelerometer concept. This task required, in parallel with the geometry design, analytical modeling of the springs, the damper, the pull-in voltage and the overall dynamic behavior of the structure. While the fabricated structures are described in Chapter 3, the modeling results are only presented in the following chapters where the microstructures are used, and where they are also compared with the respective experimental results.

Damping is crucial for MEMS design and particularly for the pull-in-based approach. In Chapter 4 the methodology adopted for damping modeling is described. When designing capacitive parallel-plates devices, a conflict between capacitance and damper design becomes evident. Both are proportional to the number of parallel-plates implemented but while it is desirable to increase capacitance (increasing readout capabilities), damping is a noise source and for most applications it must be kept as low as possible. In Chapter 4 an improved damper geometry is also presented, which addresses the capacitance/damper design conflict by allowing increasing the capacitance/damping ratio in comparison to traditional geometries. It consists of implementing flow channels on the parallel-plates, effectively decreasing the squeeze-film damping effect, at the same time yielding only a very small capacitance reduction. Analytic modeling and extensive computational fluid dynamic simulations were used to validate the solution. Microstructures have been fabricated specifically for the validation of this approach and the experimental results are presented in this chapter.

Chapter 5 presents the modeling and experimental results of the open-loop operation of the accelerometer while Chapter 6 focuses on closed-loop operation, with experimental results also being presented. The open-loop characterization shows the limitations of this approach, but it is of major importance to understand the behavior of the device as well as validate the modeling approach. In the closed-loop approach those open-loop limitations are addressed and a new mode of operation is proposed in which the transduction method is not only the pull-in time, but the electrostatic feedback voltage required to keep pull-in time constant at the nominal value.

Chapter 7 features the new application that arose from the damping study, the viscosity sensor. The theoretical basis for the viscosity sensing is presented, as well as simulations and experimental results obtained using the same MEMS structures as in the accelerometer testing. In the last chapter, the main conclusions regarding this work are presented.

References

[1.1] S. Beeby, G. Ensell, M. Kraft, and N. White, *Mems Mechanical Sensors*. Norwood: Artech House, Inc., 2004.

[1.2] N. Maluf and K. Williams, *An introduction to microelectromechanical systems engineering*, 2nd ed. Norwood: Artech House, Inc., 2004.

[1.3] S. D. Senturia, *Microsystem Design*. Dordrecht: Kluwer Academic Publishers, 2001.

[1.4] Y. Rosen and N. Elman, *Biomaterials Science: An Integrated Clinical and Engineering Approach*. Boca Raton: CRC Press, 2010.

[1.5] L. M. Roylance and J. B. Angell, “A batch-fabricated silicon accelerometer,” *IEEE Transactions on Electron Devices*, vol. ED-26, no. 12, pp. 1911–1917, 1979.

[1.6] P. W. Barth, F. Pourahmadi, R. Mayer, J. Poydock, and K. Petersen, “A monolithic silicon accelerometer with integral air damping and overrange protection,” in *Solid-State Sensor and Actuator Workshop*, 1988, pp. 35–38.

[1.7] F. Pourahmadi, L. Christel, and K. Petersen, “Silicon accelerometer with new thermal self-test mechanism,” in *IEEE Solid-State Sensor and Actuator Workshop, 5th Technical Digest*, 1992, pp. 122–125.

[1.8] H. V. Allen, S. C. Terry, and D. W. De Bruin, “Accelerometersystems with self-testable features,” *Sensors and Actuators*, vol. 20, no. 1–2, pp. 153–161, 1989.

[1.9] Analog Devices Inc., “ADXL50-monolithic accelerometer with signal conditioning, Datasheet,” 1993.

[1.10] N. Yazdi, F. Ayazi, and K. Najafi, “Micromachined inertial sensors,” *Proceedings of the IEEE*, vol. 86, no. 8, pp. 1640–1659, 1998.

[1.11] Eric Mournier (Yole Developpement), “MEMS Markets & Applications 2011-2017, an Overview,” in *Proceedings of dMEMS*, 2012.

[1.12] N. M. Barbour, “Inertial Navigation Sensors,” in *RTO-ENSET-116(2011)*, vol. 116, NATO Research and Technology Organisation, 2011, pp. 1–28.

[1.13] NIST, *The International System of Units (SI)*. National Institute of Standards and Technology, 2008.

[1.14] L. A. Rocha, C. S. Silva, M. F. Cerqueira, J. F. Ribeiro, L. M. Goncalves, A. J. Pontes, and J. C. Viana, “A microinjected 3-axis thermal accelerometer,” *Procedia Engineering*, vol. 25, pp. 607–610, Jan. 2011.

[1.15] J. Bahari and A. M. Leung, "Micromachined three-axis thermal accelerometer with a single composite heater," *Journal of Micromechanics and Microengineering*, vol. 21, no. 7, pp. 1–13, Jul. 2011.

[1.16] X. B. Luo, Y. J. Yang, F. Zheng, Z. X. Li, and Z. Y. Guo, "An optimized micromachined convective accelerometer with no proof mass," *Journal of Micromechanics and Microengineering*, vol. 11, no. 5, pp. 504–508, Sep. 2001.

[1.17] T. Wang and S. Zhang, "Silicon micromechanical accelerometer using an optical fiber," in *Proceedings of SPIE*, 2002, vol. 4928, pp. 264–266.

[1.18] S. R. K. Morikawa, A. S. Ribeiro, R. D. Regazzi, L. C. G. Valente, and A. M. B. Braga, "Triaxial bragg grating accelerometer," in *15th Optical Fiber Sensors Conference Technical Digest*, 2002, pp. 95–98.

[1.19] R. Waters, T. Jones, and J. Kim, "Micro-Electro-Mechanical-Systems (MEMS) navigation grade Electro-Optical Accelerometer (EOA)," in *NATO SET-104*, NATO Research and Technology Organisation, 2007.

[1.20] "Innalabs Ltd." [Online]. Available: http://www.innalabs.com/. [Accessed: 09-Nov-2012].

[1.21] "Honeywell Accelerometers." [Online]. Available: http://www.inertialsensor.com/. [Accessed: 09-Nov-2012].

[1.22] S. Becka, M. Novack, S. Slivinsky, and M. Paul, "A high reliability solid-state accelerometer for ballistic missile inertial guidance," *AIAA GN&C, Honolulu, HI*, 2008.

[1.23] Colibrys SA, "SF1600S accelerometer datasheet," 2012.

[1.24] J. Chae, H. Kulah, and K. Najafi, "An in-plane high-sensitivity, low-noise micro-g silicon accelerometer with CMOS readout circuitry," *Journal of Microelectromechanical Systems*, vol. 13, no. 4, pp. 628–635, 2004.

[1.25] B. V. Amini and F. Ayazi, "Micro-gravity capacitive silicon-on-insulator accelerometers," *Journal of Micromechanics and Microengineering*, vol. 15, no. 11, pp. 2113–2120, Nov. 2005.

[1.26] P. Monajemi and F. Ayazi, "Design optimization and implementation of a microgravity capacitive HARPSS accelerometer," *IEEE Sensors Journal*, vol. 6, no. 1, pp. 39–46, 2006.

[1.27] R. Abdolvand, B. V. Amini, and F. Ayazi, "Sub-micro-gravity in-plane accelerometers with reduced capacitive gaps and extra seismic mass," *Jounal of Microelectromechanical Systems*, vol. 16, no. 5, pp. 1036–1043, 2007.

[1.28] Y. Dong, M. Kraft, C. Gollasch, and W. Redman-White, "A high-performance accelerometer with a fifth-order sigma–delta modulator," *Journal of Micromechanics and Microengineering*, vol. 15, no. 7, pp. S22–S29, Jul. 2005.

[1.29] H. Kulah, J. Chae, N. Yazdi, and K. Najafi, “Noise analysis and characterization of a sigma-delta capacitive microaccelerometer,” *IEEE Journal of Solid-State Circuits*, vol. 41, no. 2, pp. 352–361, 2006.

[1.30] B. V. Amini, R. Abdolvand, and F. Ayazi, “A 4.5-mW Closed-Loop ΔΣ Micro-Gravity CMOS SOI Accelerometer,” *IEEE Journal of Solid-State Circuits*, vol. 41, no. 12, pp. 2983–2991, 2006.

[1.31] M. Pastre, M. Kayal, P. Zwahlen, A. Nguyen, Y. Dong, H. Schmid, and A. Huber, “A 300Hz 19b DR capacitive accelerometer based on a versatile front end in a 5th-order ΔΣ loop,” in *Proceedings of ESSCIRC*, 2009, pp. 288–291.

[1.32] P. Zwahlen, A.-M. Nguyen, Y. Dong, F. Rudolf, M. Pastre, and H. Schmid, “Navigation grade MEMS accelerometer,” in *Proceedings of MEMS*, 2010, pp. 631–634.

[1.33] Y. Dong, P. Zwahlen, A.-M. Nguyen, R. Frosio, and F. Rudolf, “Ultra-high precision MEMS accelerometer,” in *Proceedings of Transducers*, 2011, pp. 695–698.

[1.34] B. Almutairi and M. Kraft, “Comparative study of multi stage noise shaping and single loop sigma–delta modulators for MEMS accelerometers,” *Procedia Engineering*, vol. 5, pp. 512–515, Jan. 2010.

[1.35] B. Almutairi and M. Kraft, “Multi stage noise shaping sigma-delta modulator (MASH) for capacitive MEMS accelerometers,” *Procedia Engineering*, vol. 25, pp. 1313–1316, Jan. 2011.

[1.36] U. Sonmez, H. Kulah, and T Akin, “A fourth order unconstrained ΣΔ capacitive accelerometer,” in *Proceedings of Transducers*, 2011, no. 1, pp. 707–710.

[1.37] R. A. Dias, L. Mol, R. F. Wolffenbuttel, E. Cretu, and L. A. Rocha, “Design of a time-based micro-g accelerometer,” *IEEE Sensors Journal*, vol. 11, no. 8, pp. 1677–1683, 2011.

[1.38] R. A. Dias, E. Cretu, R. Wolffenbuttel, and L. A. Rocha, “Pull-in-based μg-resolution accelerometer: Characterization and noise analysis,” *Sensors and Actuators A: Physical*, vol. 172, no. 1, pp. 47–53, Dec. 2011.

[1.39] V. Rajaraman, B. S. Hau, L. A. Rocha, R. A. Dias, K. A. A. Makinwa, and R. Dekker, “A novel SOI-MEMS ‘ micro-swing’ time-accelerometer operating in two time-based tranduction modes for high sensitivity and extended range,” in *Proceedings of Transducers*, 2011, pp. 2066–2069.

[1.40] R. A. Dias, R. F. Wolffenbuttel, E. Cretu, and L. A. Rocha, “Sensitivity linearization technique for a time based MEMS accelerometer,” in *Proceedings of Transducers*, 2011, pp. 715–718.

[1.41] V. Rajaraman, B. S. Hau, L. A. Rocha, P. J. French, and K. A. A. Makinwa, “Design and modeling of a flexible contact-mode piezoresistive detector for time-based acceleration sensing,” *Procedia Engineering*, vol. 5, pp. 1063–1066, Jan. 2010.

[1.42] C. Liu and T. Kenny, “A high-precision, wide-bandwidth micromachined tunneling accelerometer,” *IEEE Journal of Microelectromechanical Systems*, vol. 10, no. 3, pp. 425–433, 2001.

[1.43] H. Dong, Y. Hao, S. Shen, L. He, and J. Lei, “A novel out-of-plane MEMS tunneling accelerometer with excellent low frequency resolution,” in *2006 1st IEEE International Conference on Nano/Micro Engineered and Molecular Systems*, 2006, pp. 821–825.

[1.44] “Silicon Designs Inc.” [Online]. Available: http://www.silicondesigns.com/tech.html. [Accessed: 09-Nov-2012].

[1.45] N. Yazdi, H. Kulah, and K. Najafi, “Precision readout circuits for capacitive microaccelerometers,” *Proceedings of IEEE Sensors*, no. 2, pp. 28–31, 2004.

[1.46] B. Borovic, A. Q. Liu, D. Popa, H. Cai, and F. L. Lewis, “Open-loop versus closed-loop control of MEMS devices: choices and issues,” *Journal of Micromechanics and Microengineering*, vol. 15, no. 10, pp. 1917–1924, Oct. 2005.

[1.47] Y. Dong, M. Kraft, and W. Redman-White, “Force feedback linearization for higher-order electromechanical sigma–delta modulators,” *Journal of Micromechanics and Microengineering*, vol. 16, no. 6, pp. S54–S60, Jun. 2006.

[1.48] W. C. Tang, “Digital Capacitive Accelerometer,” U.S. Patent US Patent 53536411994.

[1.49] H. Lang, L. S. Pakula, and P. J. French, “A novel pull-in accelerometer,” in *Proceedings of Eurosensors XVII*, 2003, pp. 204–207.

[1.50] L. Pakula and P. French, “A pull-in operation mode accelerometer,” in *Proceedings of IEEE Sensors*, 2006, pp. 1127–1130.

[1.51] L. A. Rocha, E. Cretu, and R. F. Wolffenbuttel, “Behavioural analysis of the pull-in dynamic transition,” *Journal of Micromechanics and Microengineering*, vol. 14, no. 9, pp. S37–S42, 2004.

[1.52] L. A. Rocha, E. Cretu, and R. F. Wolffenbuttel, “Pull-in dynamics: analysis and modeling of the transitional regime,” in *Proceedings of MEMS*, 2004, pp. 249–252.

[1.53] L. A. Rocha, “Dynamics and nonlinearities of the electro-mechanical coupling in inertial MEMS,” Delft University of Technology, 2005.

[1.54] L. A. Rocha, L. Mol, R. F. Wollfenbuttel, and A. Lage, “A time based micro-g accelerometer,” in *Proceedings of Eurosensors XXII*, 2008, pp. 1565–1568.

2.

Electromechanical coupling analysis

A characteristic of MEMS devices is the strong coupling between the various domains involved. The coupling between electrical and mechanical domains is not exclusive of the MEMS field, but due to how the different forces scale, there are characteristics that are unique in MEMS. When the characteristic dimensions of the elements decrease from the macroscale level to the micrometer size, the effects related to the device volume, such as gravity become negligible as compared to surface effects such as adhesive and friction effects [2.1].

Electrical and mechanical coupling can be observed in electrical motors, air compressors and RMS-DC converters. In an electrostatic voltmeter (based on RMS-DC conversion), the electrostatic forces (originated by the voltage being measured) between two parallel plates cause movement of one of the plates, which can be detected using a micrometer. Hence, the coupling between the mechanical and electrical domains enables the measurement of an electrical parameter (RMS –Root Mean Square value) through the measurement of a mechanical variable (displacement). Due to the construction and material properties, operation of the macro device is limited to very small displacements. Moreover, at high voltage levels, voltage breakdown occurs across the capacitor.

The uniqueness of the μ-domain results from the fact that device operation is not limited by electrostatic breakdown, but rather by *pull-in* of the microstructure. The electrostatic breakdown voltage of parallel-plates (given by Paschen's law), increases for narrow (a few

microns) gaps. Typical values for the necessary electric field are around 180 MV/m for a 2 μm wide gap (~350V) [2.2]. Considering this value for breakdown voltage and the dimensions of a typical microstructure, breakdown is unlikely to take place at the μ-domain.

Several new phenomena are enabled or become relevant at the MEMS scale. (e.g. Brownian noise or Paschen's effect [2.3]). The tighter interaction between the electrical and mechanical domains in miniaturized devices gives rise to the occurrence of the pull-in nonlinear phenomenon. It was first reported in 1967 [2.4] when a resonant gate transistor (RGT) exploring the electro-mechanical coupling had to deal with this nonlinearity. Assuming a parallel-plate actuator (where one of the plates is movable and anchored by a spring while the other is fixed), if a voltage V is applied, an electrostatic force between the two electrodes is generated. Since the electrostatic force in a vertical field is inversely proportional to the square of the deflection and the restoring elastic force is, in a first approximation, linear with deflection, an unstable system results in case of a deflection, x, beyond a critical value, x_{PI}. The *pull-in voltage*, V_{PI}, is defined as the voltage that is required to reach the critical deflection. This unique MEMS characteristic has been subject of several studies [2.5]–[2.12]. In [2.5]–[2.7] the pull-in has been analyzed from the application perspective while in [2.8]–[2.11] the fundamental underlying mechanisms behind the nonlinear pull-in phenomenon have been studied.

In this chapter the basic principles behind the pull-in time accelerometer are presented. A mathematical description of the pull-in phenomenon is provided along with the equations that govern this non-linear transition, evidencing the role of each of the intervenient forces.

The pull-in effect is analyzed both static and dynamically. Static pull-in has been modeled and experimentally verified in the scientific literature [2.12]–[2.15]. A static analysis assumes a quasi-static regime, i.e. it is a simplified approach where the variation of the applied voltage is considered slow enough so that it is possible to reach static equilibrium at any moment in time. In such quasi-static conditions inertia and damping are neglected, and thus the static analysis consists basically in finding equilibrium between electrostatic and elastic forces that act in opposite directions.

It is important to distinguish between static and dynamic analysis: the first assumes a quasi-static regime, which does not apply when the voltage changes rapidly. When the aim is to analyze the dynamic behavior, i.e., to describe the motion of the structure (displacement versus time), the static analysis is not helpful, and damping and inertia need to be considered.

The dynamic pull-in behavior of a device is governed by non-linear equations, and accurate prediction of the device's position in time cannot be performed analytically. In this case,

all the forces acting on the system must be accounted for as they may significantly change the pull-in voltage threshold and the critical pull-in deflection. To describe the dynamic transition simulation tools must be employed. In this work, a Simulink™ model is used to solve the dynamic equilibrium problem. External acceleration is included in the dynamic model and the sensitivity of the pull-in time to acceleration is observed. For the simulations used in this chapter the damping coefficient is considered constant, although this is not accurate; this subject will be addressed later as damping is the main focus of Chapter 4. The origin of the metastable behavior when pull-in occurs in overdamped structures is demonstrated here.

2.1. One degree-of-freedom MEMS device

The system considered for the analysis is a gap-varying parallel-plate capacitor with one movable plate. The movable plate has 1-DOF *(*Degree Of Freedom*)* and when voltage is applied across the parallel-plates, the inter-plate distance changes (Figure 2.1). The capacitance between two parallel-plates is defined as [2.16]:

$$C_0 = \varepsilon \frac{A}{d_0} \tag{2.1}$$

where ε is the dielectric constant of the material between the plates (usually air), A is the overlapping area of the plates and d_0 is the distance between the plates. If one plate moves towards the other, decreasing the inter-plate gap, the capacitance increases. Including the displacement of the device as the variable x, the new capacitance is:

$$C_x = \varepsilon \frac{A}{d_0 - x} = C_0 \frac{d_0}{d_0 - x} \tag{2.2}$$

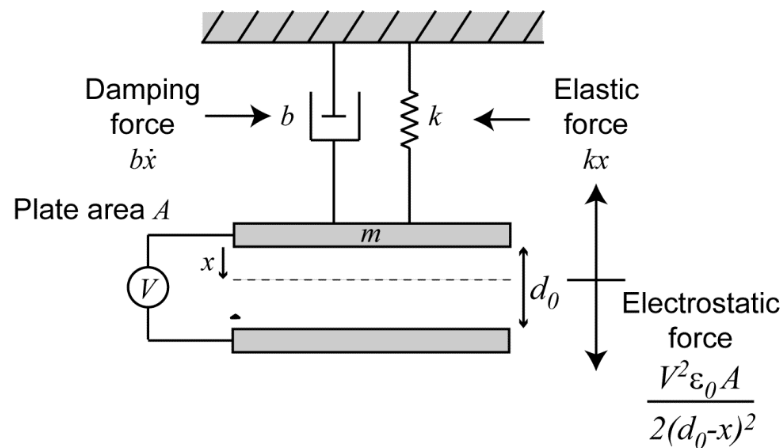

Figure 2.1: Actuator schematic.

When a voltage V is applied between the parallel-plates of the capacitor, an electrostatic force is generated that attracts the two plates together. If one of the plates is movable (attached to a spring), then the movable plate moves towards the fixed one. As the gap decreases, the capacitance and electrostatic force increases as:

$$F_{elect} = \frac{1}{2}V^2\frac{C_x}{d_0 - x} = \frac{1}{2}V^2\frac{C_0 d_0}{(d_0 - x)^2} \quad (2.3)$$

Assuming the movable plate is anchored by a spring with stiffness k, the elastic force increases for decreasing gap, contrary to the movement direction, $F_{elas} = -kx$.

When the plate moves, at a certain velocity, a damping force is generated due to the flow resistance (viscosity) of the fluid that fills the gap, usually air. In the case of gap-changing parallel-plate systems (movement normal to the plate plane), when the gap dimension is just a few microns and small in comparison to the plate's width and length, a damping mechanism called squeeze-film damping is established. This force contrary to the plate movement is denominated viscous damping force, and is directly proportional to the plate velocity, $F_b = -b\frac{dx}{dt}$. b is the damping coefficient, which depends on the fluid properties and the physical dimensions of the structure (gap size and plate geometry).

Another force that arises from the plate (with mass m) movement is inertia $F_i = -m\frac{d^2x}{dt^2}$. Additionally, external forces such as acceleration ($F_a = ma_{ext}$) may be present. When an object moves through a fluid, drag forces (pressure and friction drag) are also originated. These depend on the properties of the fluid, the geometry of the object and the Reynolds number. When present, squeeze-films produce damping forces several orders of magnitude higher than drag. The devices considered in this work are based on parallel-plates geometry, with movement normal to the plates which creates squeeze-film damping, hence drag forces are not considered in this study.

The equilibrium of the forces acting on the system can then be expressed as:

$$F_{elect} + F_{elas} + F_b + F_i + F_a = 0 \quad (2.4)$$

Equation (2.4) can be rewritten as:

$$\frac{1}{2}V^2 C_0\frac{d_0}{(d_0 - x)^2} - kx - b\frac{dx}{dt} - m\frac{d^2x}{dt^2} + ma_{ext} = 0 \quad (2.5)$$

If no voltage is applied to the system it can be simplified into equation (2.6), evidencing that the structure can be represented mechanically as a second order system:

$$m\frac{d^2x}{dt^2} + b\frac{dx}{dt} + kx = ma_{ext} \tag{2.6}$$

At this stage, the damping coefficient is considered linear for the sake of performing a qualitative analysis, although this is not correct as the damping coefficient depends on the changing gap dimension, velocity (compressibility) and gas medium inertial effects, $b = f\left(x, \frac{dx}{dt}\right)$. A thorough analysis of the squeeze-film damping coefficient is presented later in Chapter 4.

In a second order mechanical system, the natural resonant frequency of the system is defined as $\omega_0 = \sqrt{\frac{k}{m}}$, and the quality factor (a measure of the losses in the system) is $Q = \frac{\sqrt{km}}{b}$. Equation (2.6) can be again reformulated to emphasize these parameters that characterize the system dynamics:

$$\frac{d^2x}{dt^2} + \frac{\omega_0}{Q}\frac{dx}{dt} + {\omega_0}^2 x = a_{ext} \tag{2.7}$$

The system is considered overdamped if *Q<0.5*, underdamped if *Q>0.5* and critically damped if *Q=0.5*. An underdamped system is characterized by an oscillatory behavior, while in overdamped conditions no oscillations are present Figure 2.1 and Figure 2.3).

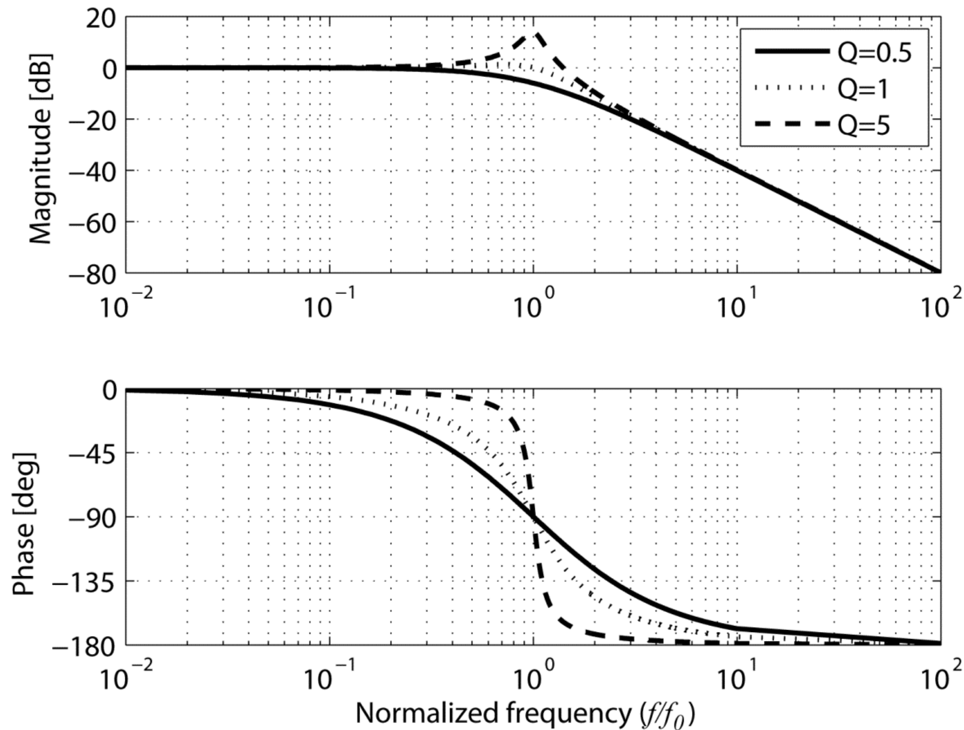

Figure 2.2: Bode plot of different quality factor devices.

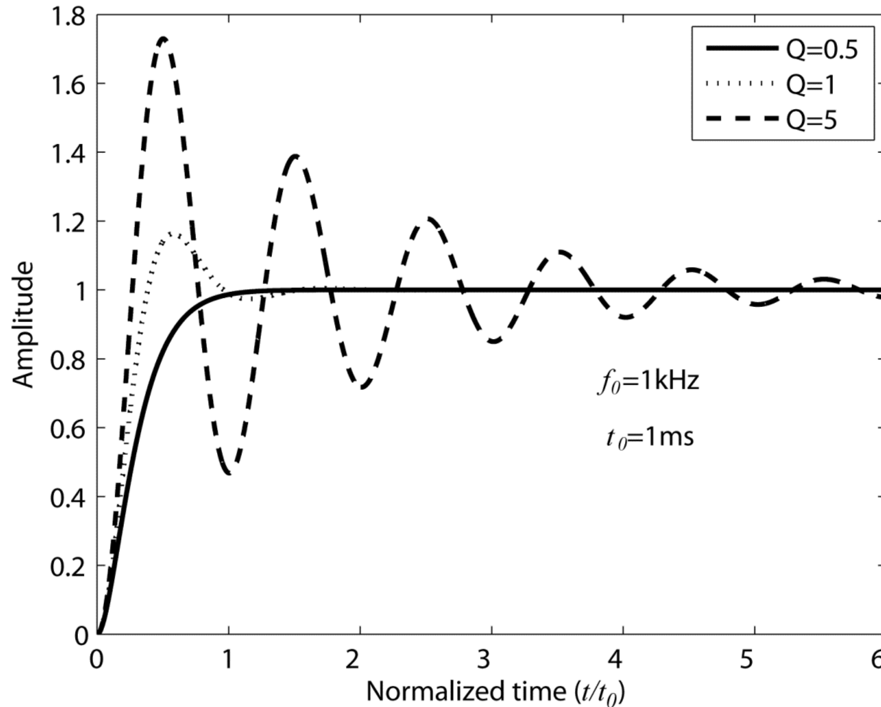

Figure 2.3: Step response of different quality factor devices.

2.2. Pull-in of capacitive 1-DOF parallel-plates – Static analysis

A physical system in static equilibrium is either at rest – the relative positions of subsystems do not vary over time, or moves at constant velocity. When the voltage applied to the 1-DOF capacitor system is increased beyond a critical value, it is impossible to reach static equilibrium and an electrostatic force exists that cannot be compensated by the mechanical force. At this point the movable plate is accelerated towards the fixed electrode until it is stopped mechanically. Basically, the pull-in phenomenon is defined as this loss of stability of the equilibrium position. A stability study allows the computation of the equilibrium points as voltage is increased and the voltage at which stability is lost. For the static analysis of pull-in, only the electrostatic and elastic forces are considered. Damping and inertia are disregarded since in static (no movement) conditions these forces are zero (damping is a function of velocity and inertia a function of acceleration).

Figure 2.4 shows the computed values of electrostatic (for a voltage lower than the pull-in voltage) and elastic forces, normalized to the maximum elastic force, as a function of displacement (note that these two forces act in opposite directions). Two equilibrium solutions can be observed, x_1 and x_2, but only x_1 is stable. While small perturbations on the displacement around x_1 give rise to larger restoring force than push-away force, the opposite happens in the

vicinity of x_2 where the push-away force is larger. For instance, a small increment of displacement near x_1 corresponds to an elastic force (which acts against displacement – restoring force) higher than the electrostatic (acting towards increasing displacement – push-away force). On the other hand, near x_2 a small increment of displacement increases the electrostatic force (push-away force) to a value higher than the elastic force (restoring force), so the displacement will increase even further away from the unstable equilibrium point.

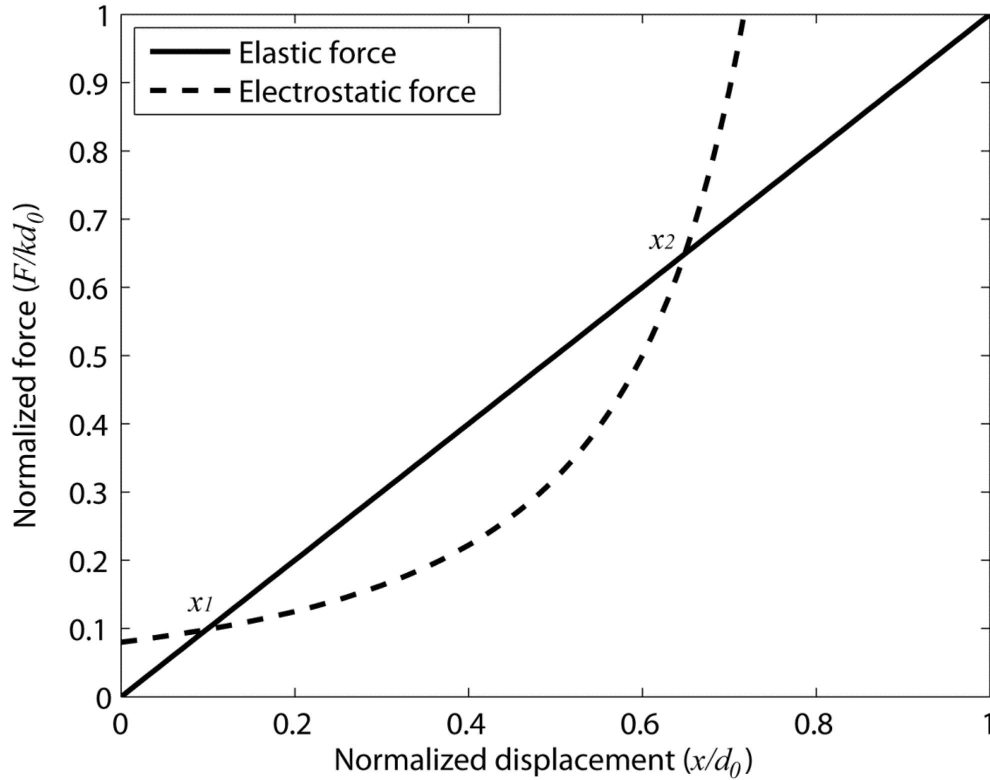

Figure 2.4: Normalized forces.

For small input voltages, equilibrium is possible, but beyond a certain voltage value, no stable equilibrium point exists (Figure 2.5). The threshold voltage at which stability is possible can be calculated analytically. As inertia and damping forces are neglected on the static analysis, the sum of the forces can be expressed as:

$$F_{total} = F_{elect} + F_{elas} = \frac{1}{2}V^2 C_0 \frac{d_0}{(d_0 - x)^2} - kx. \quad (2.8)$$

And differentiated in respect to x:

$$\frac{dF_{total}}{dx} = V^2 C_0 \frac{d_0}{(d_0 - x)^3} - k. \quad (2.9)$$

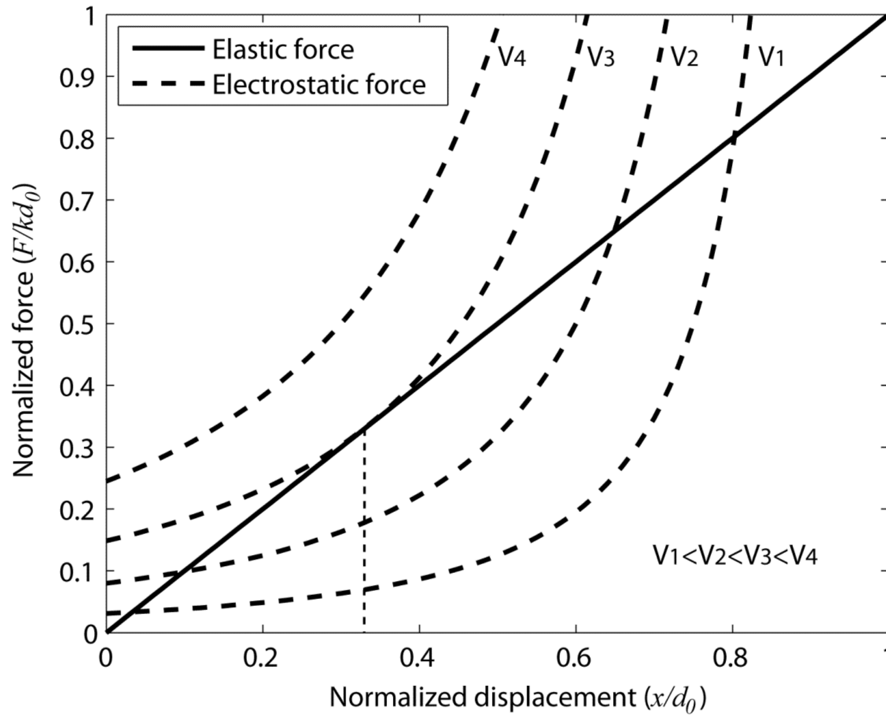

Figure 2.5: Normalized forces for increasing voltage values.

For a given applied voltage *V*, equilibrium positions exist when elastic force balances the electrostatic one: $|F_{elas}| = |F_{elect}|$. Stability requires that at the equilibrium point $\frac{d|F_{elas}|}{dx} > \frac{d|F_{elect}|}{dx}$, so the restoring force is higher than the push-away force.

The threshold of stability occurs at the maximum displacement x where these conditions can be met, or mathematically, when $\frac{d|F_{elas}|}{dx} = \frac{d|F_{elect}|}{dx}$.

Solving the equation system:

$$\begin{cases} |F_{elas}| = |F_{elect}| \\ \dfrac{d|F_{elas}|}{dx} = \dfrac{d|F_{elect}|}{dx} \end{cases} \tag{2.10}$$

in respect to *x* yields the critical pull-in displacement $x_{PI} = \frac{1}{3}d_0$.

The critical pull-in voltage can be found by inserting the critical pull-in displacement into equation $|F_{elas}| = |F_{elect}|$, which yields the pull-in voltage:

$$V_{PI} = \sqrt{\frac{8}{27}\frac{{d_0}^2 k}{C_0}} \tag{2.11}$$

If the voltage applied is higher than the nominal pull-in voltage, the elastic force can no longer compensate the generated electrostatic force, and pull-in occurs, i.e., stability is lost and the movable plate snaps against the counter electrode causing short-circuiting (unless a mechanical stopper is present or the voltage is turned off).

2.2.1. Comb-like structures

It is usually the case of in-plane capacitive parallel-plate microdevices that the fixed parallel-plates are intertwined with the movable plates forming two comb-like structures (Figure 2.6). Hence, besides the main gap d_0, there is a larger second gap $d_{2,0}$ where electrostatic force is also generated, $F_{2,elect} = \frac{1}{2}V^2 C_{2,0} \frac{d_{2,0}}{(d_{2,0}+x)^2}$, acting opposite to displacement.

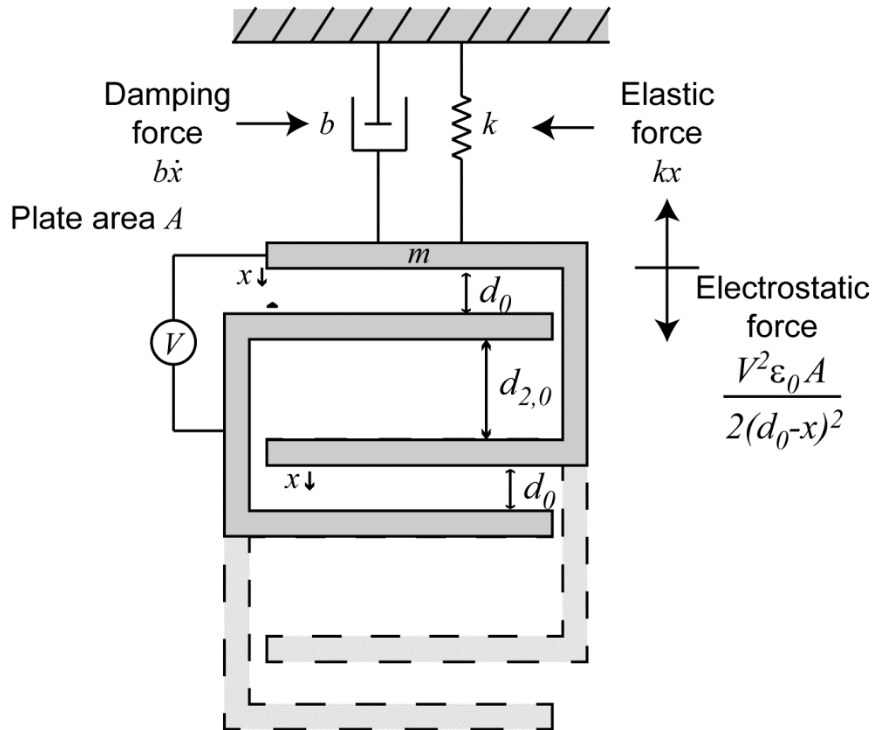

Figure 2.6: Typical in-plane parallel-plate device geometry.

Similarly to the two-plate case, stable equilibrium points are found by solving the system of equations:

$$\begin{cases} |F_{elas} + F_{2,elect}| = |F_{elect}| \\ \frac{d|F_{elas} + F_{2,elect}|}{dx} = \frac{d|F_{elect}|}{dx} \end{cases} \quad (2.12)$$

In this case an exact solution cannot be found but a simplified equation can be achieved that relates the pull-in displacement and the two initial gaps:

$$\frac{d_0 - 3x_{PI}}{(d_0 - x_{PI})^3} - \frac{d_{2,0} + 3x_{PI}}{\left(d_{2,0} + x_{PI}\right)^3} = 0 \tag{2.13}$$

Normalizing the variables to d_0 and assuming $d_{2,0}$ is proportional to d_0, with proportionality constant K ($d_{2,0}=Kd_0$), the equation can be rewritten as:

$$\frac{1 - 3\frac{x_{PI}}{d_0}}{(1 - \frac{x_{PI}}{d_0})^3} - \frac{K + 3\frac{x_{PI}}{d_0}}{\left(K + \frac{x_{PI}}{d_0}\right)^3} = 0 \tag{2.14}$$

Equation (2.14) shows that when K tends to infinity, $\frac{x_{PI}}{d_0}$ tends to $\frac{1}{3}$, i.e. $x_{PI} = \frac{1}{3}d_0$, as previously demonstrated. Figure 2.7 show the variation of $\frac{x_{PI}}{d_0}$ as a function of K. For a second gap 10 times larger than the main gap, the critical pull-in displacement occurs at $0.3323d_0$, i.e., $x_{PI} \approx \frac{1}{3}d_0$.

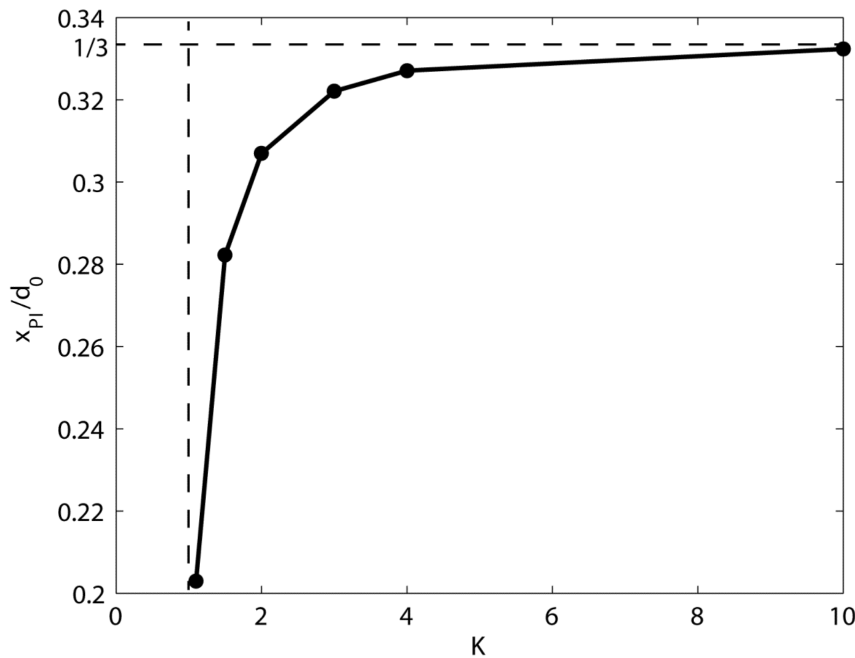

Figure 2.7: Normalized pull-in critical displacement as a function of the normalized second gap dimension.

These results show that when designing comb-like capacitors, leaving a secondary distance approximately 10 times larger than the main capacitor gap is usually enough to disregard the effect of this extra electrostatic force.

2.3. Dynamic analysis of pull-in

An analysis of the dynamic behavior of a structure pulling-in cannot be performed using analytical methods as in the static analysis. All the forces acting on the system must be considered which results in a non-linear differential equation. This equation can be analyzed using simulations tools. In this section, a method for modeling parallel-plates MEMS dynamics, using Simulink™, is presented.

Dynamic pull-in behavior is determined by the interaction between the forces acting on the system such as elastic force, electrostatic force, damping, inertia, and externally applied forces. The pull-in is a very sensitive phenomenon and small changes in the intervenient forces, such as external acceleration, greatly affects the overall duration of the event.

If the notation $\dot{x} = f(x, V)$ is adopted, equation (2.4) can be rewritten as:

$$\dot{x} = y$$
$$\dot{y} = a_{ext} + \frac{1}{m}\left(\frac{C_0 d_0 V^2}{2(d_0 - x)^2} - kx - by\right) \tag{2.15}$$

This system of equations is very useful when one wants to solve differential equations using simulation tools. Implementing these equations in Simulink™ results in the model depicted in Figure 2.8.

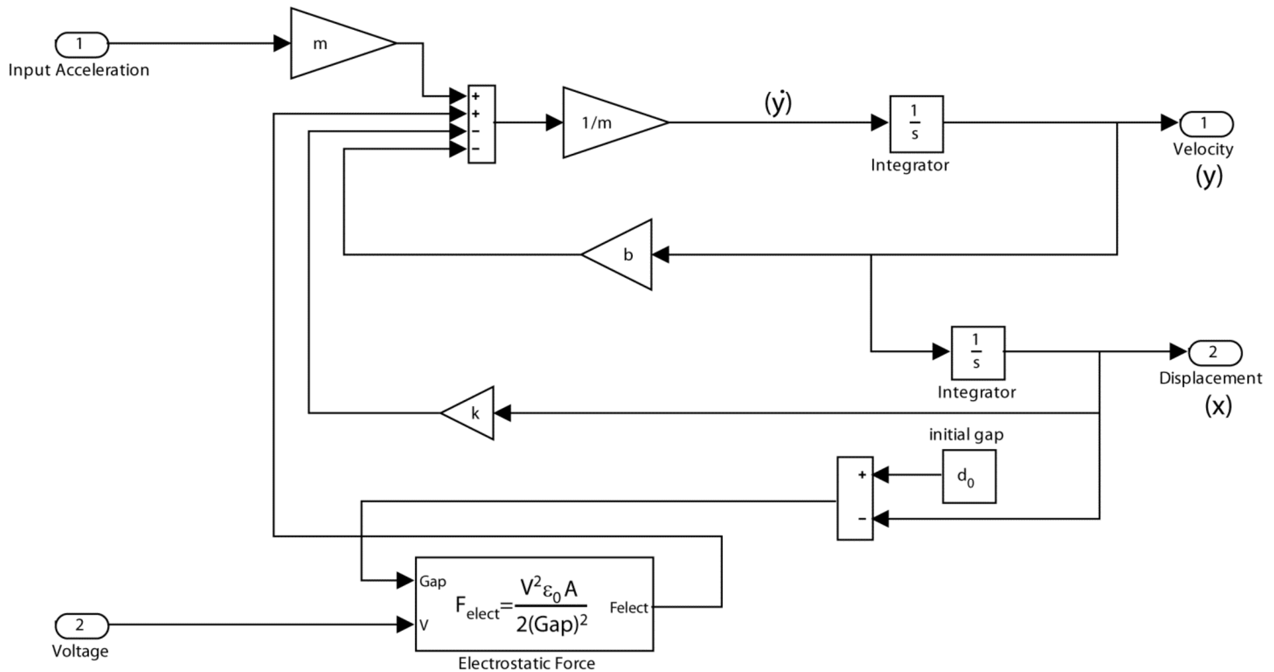

Figure 2.8: Simulink block diagram.

The dynamics of the device can be re-written as the nonlinear differential equation:

$$\frac{1}{2m}V^2C_0\frac{d_0}{(d_0-x)^2}-\omega_0{}^2x-\frac{\omega_0}{Q}\frac{dx}{dt}-\frac{d^2x}{dt^2}+a_{ext}=0 \quad (2.16)$$

Using again the notation $\dot{x}=f(x,V)$, this can be rewritten as:

$$\dot{x}=y$$

$$\dot{y}=a_{ext}+\frac{V^2C_0d_0}{2m(d_0-x)^2}-\omega_0{}^2x-\frac{\omega_0}{Q}y \quad (2.17)$$

The state variables *x* and *y* represent displacement and velocity, respectively. A general analysis of the system can be performed, irrespective of the numerical values of the parameters involved, by implementing a model in Simulink™ with normalized state variables. The displacement is normalized to the maximum displacement d_0, $x_n\equiv\frac{x}{d_0}$, and the velocity and acceleration are automatically normalized to $y_n\equiv\frac{y}{d_0}$ and $a_n\equiv\frac{a_{ext}}{d_0}$. The voltage is normalized to the nominal pull-in voltage $V_n\equiv\frac{V}{\sqrt{\frac{8}{27}\frac{d_0{}^2k}{C_0}}}$ and the electrostatic force using the normalized variables is expressed as:

$$F_{elect}=\frac{1}{2}V^2\frac{C_0d_0}{(d_0-x)^2}=\frac{1}{2}\left(\sqrt{\frac{8}{27}\frac{d_0{}^2k}{C_0}}V_n\right)^2\frac{C_0d_0}{(d_0-d_0x_n)^2}=\frac{4}{27}V_n{}^2\frac{d_0k}{(1-x_n)^2} \quad (2.18)$$

With the normalized forces, equation 2.4 can be expanded to:

$$\frac{4}{27}V_n{}^2\frac{k/m}{(1-x_n)^2}-k/mx_n-b/my_n-\dot{y_n}+a_n=0 \quad (2.19)$$

Reformulating to evidence system parameters gives:

$$\frac{4}{27}V_n{}^2\frac{\omega_0{}^2}{(1-x_n)^2}-\omega_0{}^2x_n-\frac{\omega_0}{Q}y_n-\dot{y_n}+a_n=0 \quad (2.20)$$

The normalized equation of motion thus becomes:

$$\dot{x_n}=y_n$$

$$\dot{y_n}=\frac{4}{27}V_n{}^2\frac{\omega_0{}^2}{(1-x_n)^2}-\omega_0{}^2x_n-\frac{\omega_0}{Q}y_n+a_n \quad (2.21)$$

Implementing these equations in Simulink™ allows to study the dynamics of pull-in of a generic device with resonant frequency ω_0 and quality factor Q.

When the system is at rest and a voltage is applied, higher than the threshold pull-in voltage, stability is lost and the movable parallel-plate moves towards the counter electrode. The travel time of the device from rest position (zero-displacement) to maximum displacement (full gap travel) is called pull-in time.

The profile of the pull-in displacement over time can be significantly different depending whether the system is underdamped or overdamped. Figure 2.9 shows the pull-in displacement profile of a critically damped system ($Q=0.5$) and that of an underdamped system ($Q=5$), when a step voltage higher than the pull-in voltage is applied $V_{step}=\alpha V_{PI}$, $\alpha=1.01$.

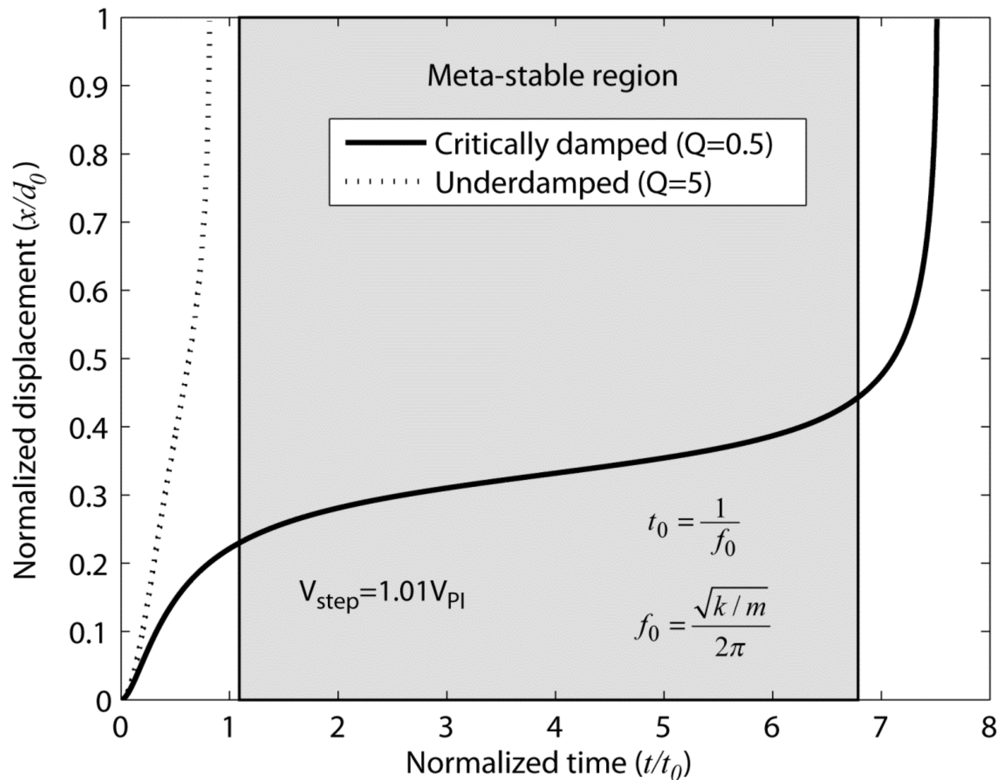

Figure 2.9: Pull-in dynamic transition.

An underdamped device moves fast until it reaches the counter electrode, presenting an approximately linear displacement profile. In the overdamped case the structure does not move linearly. In fact, the displacement profile can be divided in three distinct regions. In a first region, the structure moves rapidly until it approaches the static pull-in displacement ($x_{PI}=d_0/3$). In the vicinity of this critical deflection, it moves slowly creating what can be defined as a *metastable* region. Finally, after passing this area, it moves fast again snapping against the counter-electrode.

Figure 2.10 presents the plot of the normalized intervenient forces. Note that the electrostatic force acts in the direction of displacement while the other forces act opposite to displacement. In the first region, the initial imposed electrostatic force is compensated by inertia but as the structure starts to move inertia quickly decreases and damping becomes the main component opposing electrostatic force (limiting displacement forced by electrostatic actuation). As deflection increases the elastic force equilibrates the electrostatic one and damping force reduces becoming almost negligible.

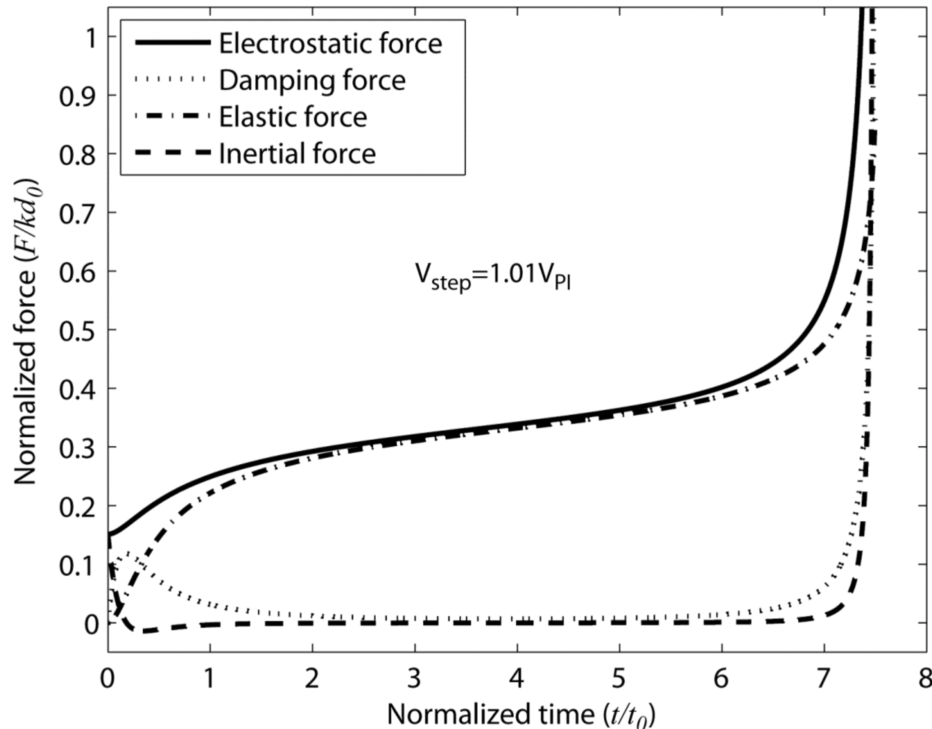

Figure 2.10: Forces acting during a pull-in dynamic transition of an overdamped device.

In the second meta-stable region, which is near the critical deflection, the elastic force value is very close to the electrostatic force one, which translates to a sort of meta-stable equilibrium characterized by very slow motion of the structure.

In the third region the elastic force can no longer compensate the electrostatic one and the structure is accelerated towards the fixed parallel-plate. As velocity increases and acceleration is positive, damping force and inertia also increase.

Despite the fact that the damping force during the metastable region is very small in comparison to the electrostatic and elastic ones, damping has a decisive role in the duration of the metastable region. Figure 2.11 shows the pull-in profile changes with the quality factor (which is a measure of the damping of the system). As the damping coefficient increases (and the quality factor decreases) the pull-in time increases.

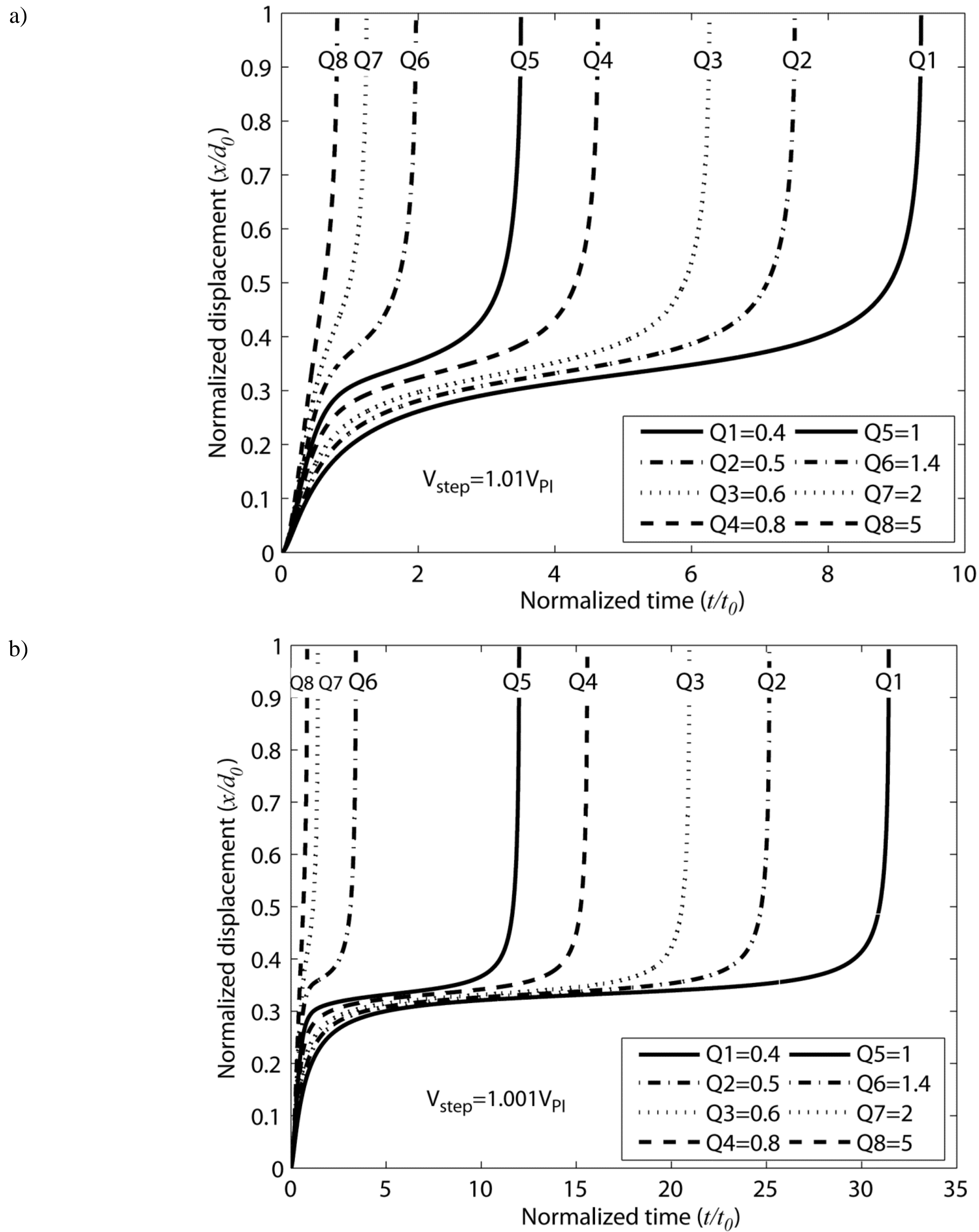

Figure 2.11: Pull-in time variation with quality factor for a) α=1.01 and b) α=1.001.

Although the pull-in time decrease is gradual, a threshold value of Q can be defined above which the metastable region is not easily delimited, approximately $Q \approx 1.5$ for α = 1.001 and $Q \approx 1.2$ for α = 1.01. Figure 2.12 shows the different simulated pull-ins as V_{step} is changed. Similarly, it can be seen that when step voltages higher than approximately 1.01 times the pull-in voltage are used, the metastable region can hardly be defined. If higher quality factors are

considered, this threshold decreases (for instance, for $Q = 2$, $\alpha < 1.0002$ is required for the metastable region to be clearly visible).

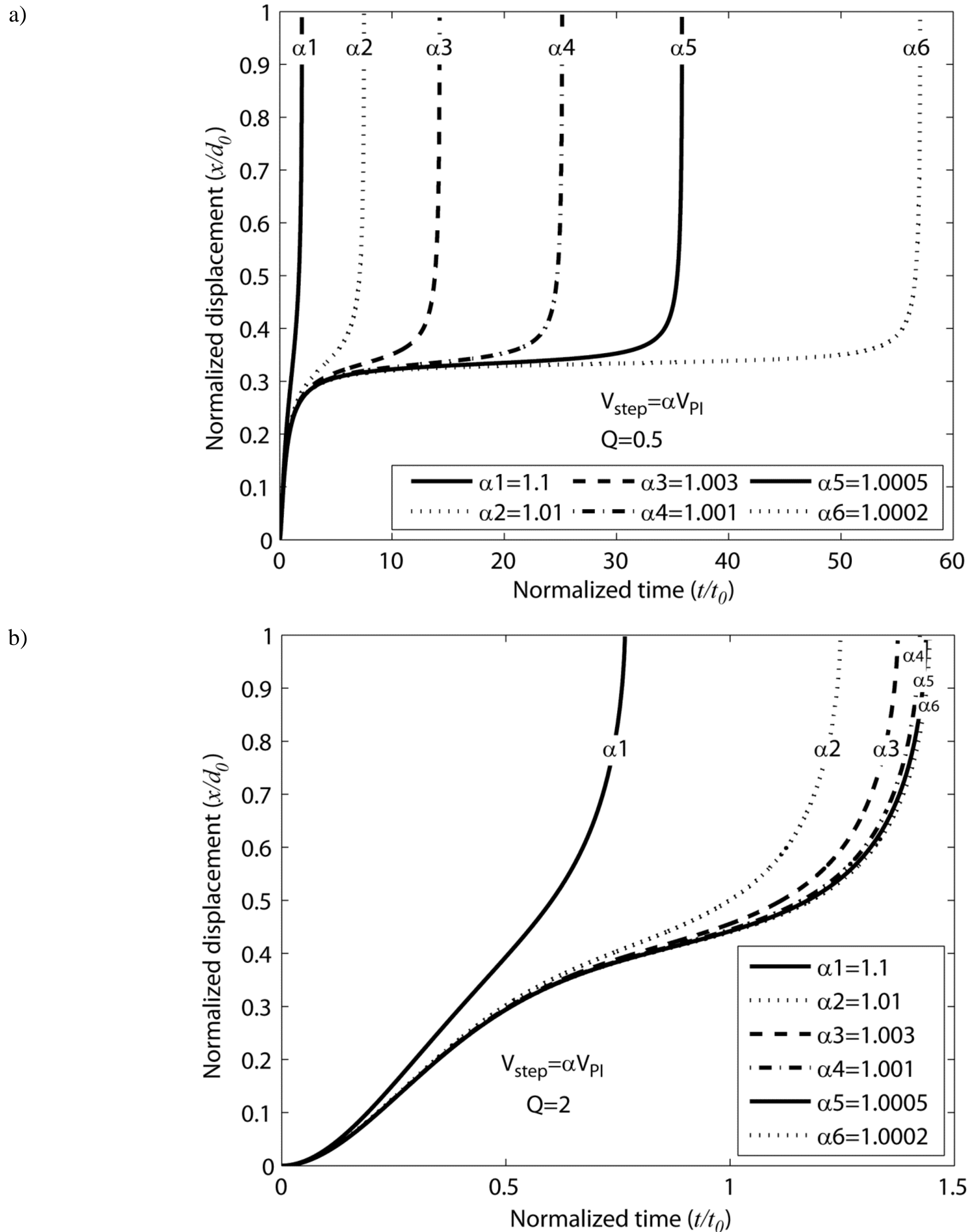

Figure 2.12: Pull-in time variation with actuation voltage.

2.3.1. Metastable region – sensitivity to acceleration

External acceleration changes the pull-in voltage. If an external acceleration is considered, the following equation system results:

$$\begin{cases} |F_{elas}| = |F_{elect} + F_a| \\ \dfrac{d|F_{elas}|}{dx} = \dfrac{d|F_{elect} + F_a|}{dx} \end{cases} \tag{2.22}$$

Solving the equation system in respect to x yields the critical pull-in displacement $x_{PI,a} = \frac{d_0 k + 2ma}{3k}$.

The critical pull-in voltage can be found by inserting the critical pull-in displacement into equation $|F_{elas}| = |F_{elect} + F_a|$, which yields:

$$V_{PI,a} = \sqrt{\frac{8}{27}\frac{d_0 k - ma}{k}}\sqrt{\frac{d_0 k - ma}{d_0 C_0}} \tag{2.23}$$

It can be observed that if the external acceleration is in the direction of the pull-in displacement (positive acceleration value), the new threshold pull-in voltage is lower than the nominal pull-in voltage (in the absence of acceleration). If the same voltage step, α times the nominal (without acceleration) pull-in voltage, is used to actuate the structure, the pull-in time will be shorter as this scenario is equivalent to increasing α. Similarly, if external acceleration is in the direction opposite to pull-in, the overall pull-in time will be longer as an additional force that opposes pull-in is present (Figure 2.13).

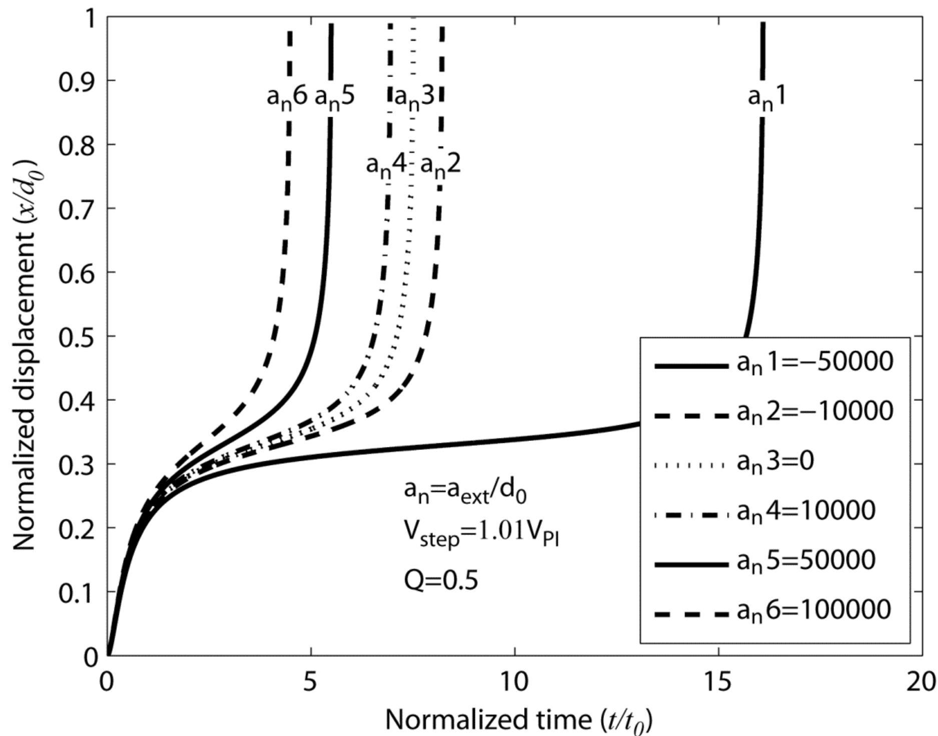

Figure 2.13: Pull-in time variation with external acceleration forces.

As demonstrated in the previous section, the existence of metastability implies that both low Q and low α (in $V_{step} = \alpha\ V_{PI}$) have to be used. Moreover, the metastable region is characterized by a tight equilibrium between electrostatic and elastic forces. Any small interference on the meta-stable equilibrium affects the duration of this transition and therefore the overall pull-in time. The changes in the pull-in time for different external accelerations and step voltage amplitudes (different values of α, ranging between 1.001 and 1.1) were simulated for a critically damped ($Q = 0.5$) generic device and the results are presented in Figure 2.14.

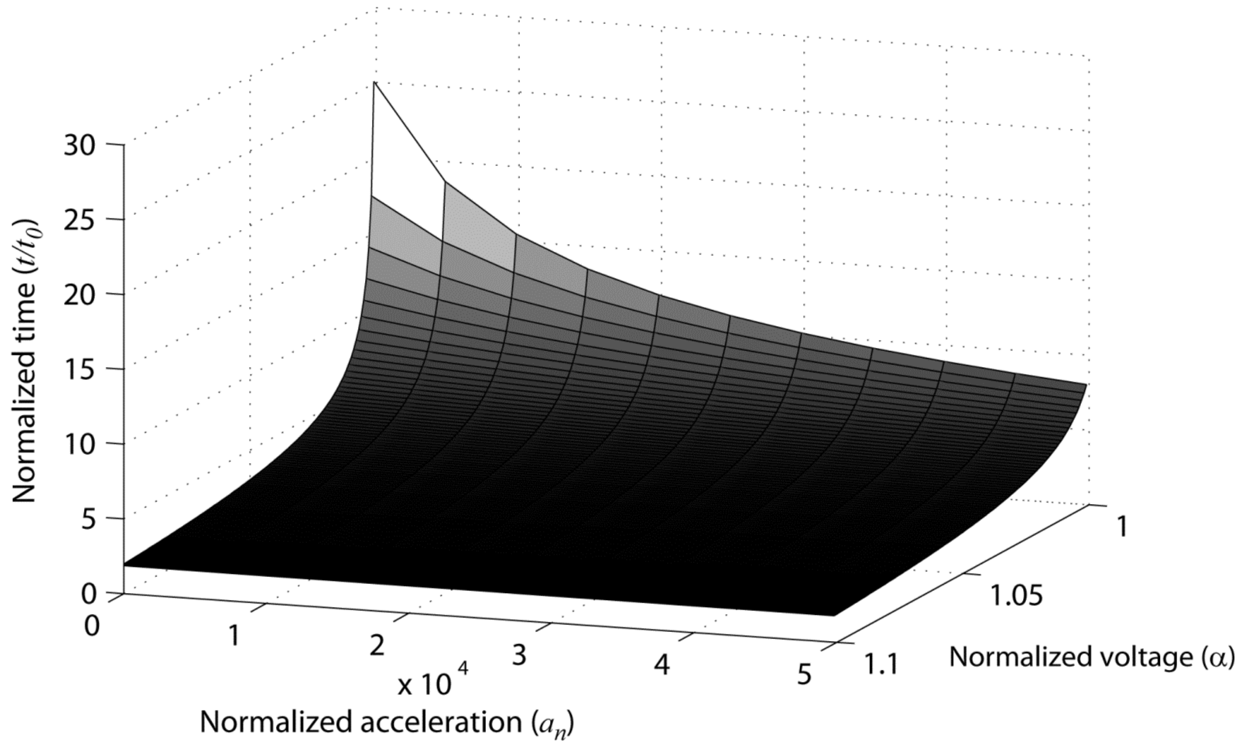

Figure 2.14: Simulated pull-in time changes with voltage step amplitude and external acceleration.

Note that the acceleration values featured in the chart are normalized to the maximum displacement. Taking into account that the typical gap values of MEMS devices are a few microns, the corresponding absolute acceleration values are actually quite small. In this graph, high sensitivity of the transition time to external acceleration is observed, and higher sensitivity is observed for smaller α values. This is due to the intrinsic behavior of the metastable region. Since this region is best described by an equilibrium of forces, any small change acts as a perturbation to the meta-stable equilibrium, thus providing the means to achieve very high sensitivity in the time domain.

Pull-in time variation with external acceleration was also simulated for quality factor values ranging between 0.1 and 5, keeping the actuation voltage constant with α=1.01. The

results (presented in Figure 2.15) show that the pull-in time sensitivity increases with decreasing quality factor, as expected in accordance with Figure 2.11.

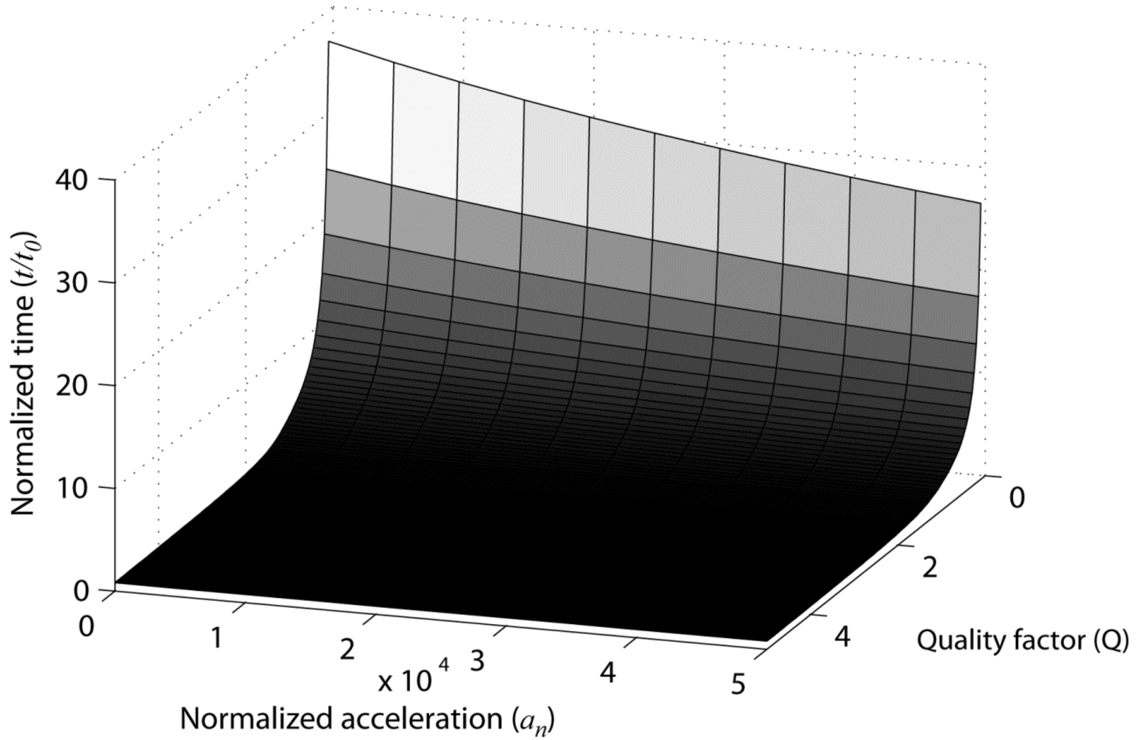

Figure 2.15: Simulated pull-in time variation with external acceleration and different quality factors.

In [2.13], [2.17], [2.18], an expression for the time spent at the metastable region was found by analytically solving a linearized differential equation of the device's displacement near the critical pull-in deflection x_{PI}. Assuming that the structure spends 85% of the time in the metastable region an expression for the pull-in time was found:

$$t_{PI} = \frac{2\ ln\left[1 + \dfrac{3{\omega_0}^2(\alpha^2 - 1)\dfrac{\Delta z}{d_0}}{3a_n + {\omega_0}^2(\alpha^2 - 1)}\right]}{-\dfrac{\omega_0}{Q} + \sqrt{\left(\dfrac{\omega_0}{Q}\right)^2 - 4{\omega_0}^2(1 - \alpha^2)}} \times \frac{1}{0.85} \quad (2.24)$$

where Δz is the small displacement around x_{PI} during metastability. Although useful for a qualitative analysis, this formula is quite limited since it is only valid for low Q devices, assumes that metastability comprises 85% of the total pull-in time and one must choose/know beforehand a suitable value of displacement around x_{PI} during the metastable transition Δz. The pull-in time was computed using this equation for different actuation voltages and external accelerations ($\Delta z/d_0=0.05$, $f_0=500$ Hz and $Q=0.5$) and the results are presented in Figure 2.16.

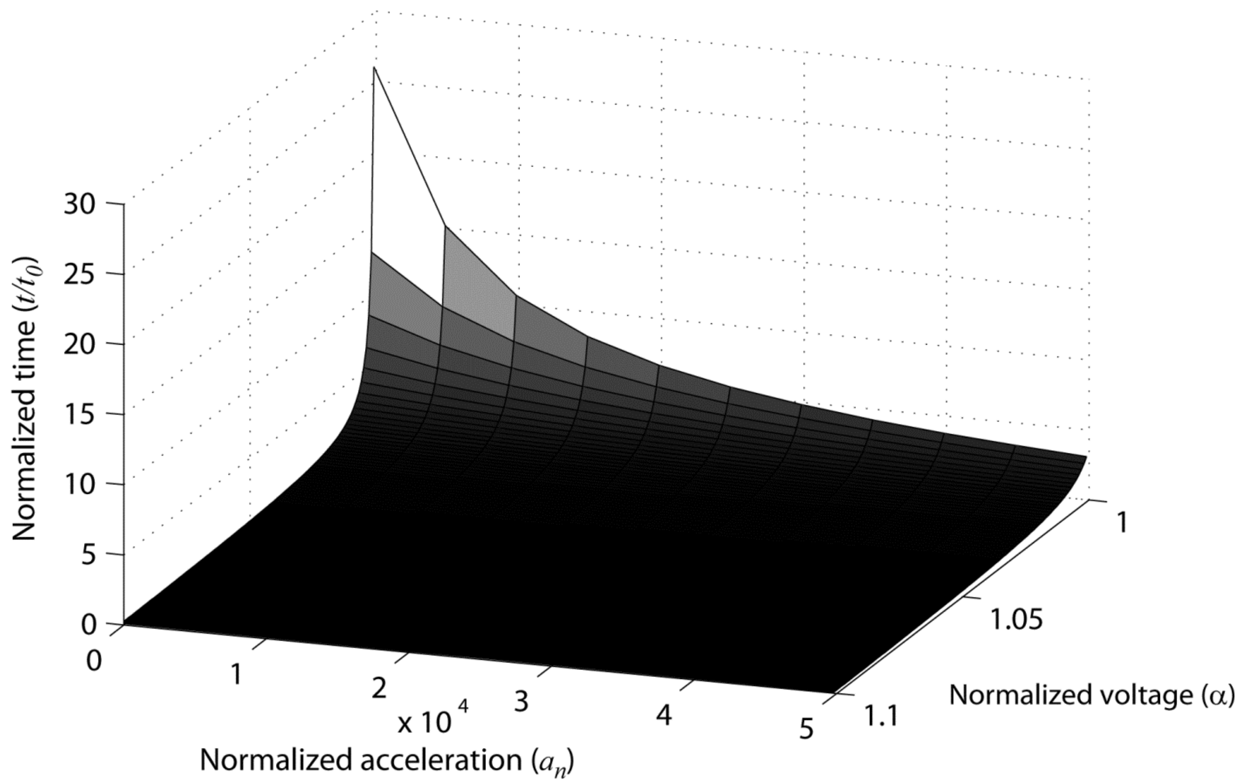

Figure 2.16: Calculated pull-in time changes with voltage step amplitude and external acceleration, using equation (2.24).

When comparing the results presented in Figure 2.14 and Figure 2.16, it can be seen that the trend of pull-in time changes with acceleration and voltage is the same, and the absolute values for the largest pull-in times are quite similar, but for shorter pull-in times, significant deviations are observed. For the smallest pull-in times, the errors exceed 100%. Despite the accuracy and applicability limitations of the linear model obtained in equation (2.24), it can be very useful to tackle pull-in time in a first approach when designing MEMS pull-in devices, and to analyze the behavior of pull-in with changes in the intervenient parameters – actuation voltage, acceleration, and structural parameters (quality factor, resonance frequency).

2.4. Conclusions

In this chapter, the operation principle behind the pull-in time accelerometer has been described. The origins of the electrostatic pull-in in 1-DOF capacitors have been demonstrated as well as the role on the non-linear behavior of each of the intervenient forces acting on the device. The pull-in instability arises from an imbalance between the pull-in electrostatic force that increases non-linearly with displacement and the restoring elastic force that increases linearly with displacement. For a given microstructure, a well-defined voltage, necessary to induce

pull-in, exists, named pull-in voltage. It depends basically on the geometry and materials of the microstructure, which define its capacitance, zero-displacement gap and elastic spring stiffness coefficient. The pull-in behavior is also associated with a critical displacement/deflection beyond which it is impossible to attain equilibrium between electrostatic and elastic force. This pull-in displacement is also well-defined, and through a static analysis found it to be located at 1/3 of the initial gap, for parallel-plate devices.

The pull-in behavior has been analyzed from a dynamic perspective using a Simulink model. The occurrence of a meta-stable behavior during the dynamic pull-in transition has been discussed. Meta-stability occurs under well-defined actuation and damping conditions. Generally, a microstructure with higher damping coefficient spends more time in the vicinity of the critical pull-in deflection when it is pulled-in and the movable electrodes travel towards the fixed ones. This behavior translates to an extended pull-in travel time. The same is observed when actuating with voltages closer to the pull-in voltage (smaller α in $V_{step}=\alpha V_{PI}$, $\alpha>1$).

In respect to the pull-in time sensitivity to external acceleration, which is the transduction principle of the pull-in time accelerometer, it has been observed to be greater for longer nominal pull-in times, i.e, increases with damping coefficient (decreases for higher quality factors) and with decreasing actuation voltage (as long as it is not lower than the voltage required for pull-in to occur).

References

[2.1] M. Wautelet, “Scaling laws in the macro-, micro- and nanoworlds,” *European Journal of Physics*, vol. 22, no. 6, pp. 601–611, Nov. 2001.

[2.2] T. Ono, D. Y. Sim, and M. Esashi, “Micro-discharge and electric breakdown in a micro-gap,” *Journal of Micromechanics and Microengineering*, vol. 10, no. 3, pp. 445–451, Sep. 2000.

[2.3] J. J. Allen, *Micro Electro Mechanical System Design*. Boca Raton: CRC Press, 2005.

[2.4] H. C. Nathanson, W. R. Newell, R. A. Wickstrom, and J. R. Davis, “The resonant gate transistor,” *IEEE Transactions on Electron Devices*, vol. ED-14, no. 3, p. 117, 1967.

[2.5] P. M. Osterberg and S. D. Senturia, “M-test: A test chip for mems material property measurement using electrostatically actuated test structures,” *Journal of Microelectromechanical Systems*, vol. 6, no. 3, pp. 286–286, Sep. 1997.

[2.6] R. K. Gupta and S. D. Senturia, “Pull-in time dynamics as a measure of absolute pressure,” in *IEEE Workshop on Micro Electro Mechanical Systems*, 1997, pp. 290–294.

[2.7] H. Lang, L. S. Pakula, and P. J. French, “A novel pull-in accelerometer,” in *Proceedings of Eurosensors XVII*, 2003, pp. 204–207.

[2.8] H. A. C. Tilmans and R. Legtenberg, “Electrostatically driven vacuum-encapsulated polysilicon resonators: Part II. Theory and performance,” *Sensors and Actuators A: Physical*, vol. 45, no. 1, pp. 67–84, Oct. 1994.

[2.9] M. H. H. O. Nijhuis, T. G. H. Basten, Y. H. Wijnant, H. Tijdeman, and H. A. C. Tilmans, “Transient non-linear response of ‘pull-in MEMS devices’ including squeeze film effects,” in *Proceedings of Eurosensors XIII*, 1999, no. 2, pp. 729–732.

[2.10] L. A. Rocha, E. Cretu, and R. F. Wolffenbuttel, “Dynamics of pull-in: analysis of the meta-stable regime,” in *Proceedings of MME*, 2003, pp. 57–60.

[2.11] L. M. Castaner and S. D. Senturia, “Speed-energy optimization of electrostatic actuators based on pull-in,” *Journal of Microelectromechanical Systems*, vol. 8, no. 3, pp. 290–298, 1999.

[2.12] L. A. Rocha, E. Cretu, and R. F. Wolffenbuttel, “Analysis and analytical modeling of static pull-in with application to MEMS-based voltage reference and process monitoring,” *Journal of Microelectromechanical Systems*, vol. 13, no. 2, pp. 342–354, 2004.

[2.13] L. A. Rocha, “Dynamics and nonlinearities of the electro-mechanical coupling in inertial MEMS,” Delft University of Technology, 2005.

[2.14] E. Cretu, “Inertial MEMS devices, modeling, design and applications,” Delft University of Technology, 2003.

[2.15] Z. Xiao, W. Peng, R. F. Wolffenbuttel, and K. R. Farmer, “Micromachined variable capacitor with wide tuning range,” *Sensors and Actuators A: Physical*, vol. 104, no. 3, pp. 299–305, 2003.

[2.16] L. K. Baxter, *Capacitive Sensors: Design and Applications*. New York: John Wiley & Sons, 1996.

[2.17] L. A. Rocha, E. Cretu, and R. F. Wolffenbuttel, “Analytical model for the pull-in time of low-Q MEMS devices,” in *Proceedings of Nanotech*, 2004, vol. 2, pp. 271–274.

[2.18] L. A. Rocha, E. Cretu, and R. F. Wolffenbuttel, “Measuring and interpreting the mechanical–thermal noise spectrum in a MEMS,” *Journal of Micromechanics and Microengineering*, vol. 15, no. 7, pp. S30–S38, Jul. 2005.

3.

Fabrication of devices

For the realization of the accelerometer prototypes used throughout this work, several sets of microelectromechanical devices were designed and fabricated. These devices have been fabricated using SOIMUMPs micromachining process [3.1], from the company MEMSCAP Inc. It is based on a Silicon-On-Insulator (SOI) wafer with a 25 µm active layer thickness. This service is commercially available within the framework of Europractice multi-project wafer (MPW) runs [3.2].

The design of in-plane movable capacitive structures is a common approach amongst users of SOI processes [3.3]. Thick active layers can also be achieved by epitaxial polysilicon growth. The relatively thick active layers provide sufficient sidewall area for the design of large capacitance required for electrostatic actuation and readout, so the design of gap-changing parallel-plates MEMS structures is commonplace [3.3]. The large sidewall areas together with the thin gaps allowed by the SOIMUMPs process enable the design of an effective squeeze-film damper.

The SOIMUMPs process was selected in detriment to the other SOI process available through Europractice – MEMSOI [3.4], due to lower cost and simplicity (it requires less masks at the expense of not providing vacuum chip encapsulation). On the MEMSOI process, there is a substrate present underneath the movable structures, which is an additional source of damping. The MEMSOI process however, would allow designing an even larger proof mass as the devices are fabricated using SOI wafers with a 60 µm-thick active layer.

The requirements for micromachining process selection were a well-established process where the deviations between the designed and fabricated geometries are known and acceptable.

For the high-sensitivity time based accelerometer, a process enabling large masses and high aspect ratio features is desirable. Maximizing the proof-mass allows decreasing Brownian noise. High aspect ratio capabilities are required for designing thin gaps, to obtain large capacitances and low pull-in voltages, and also thin silicon features to allow designing compliant springs.

The design of a microstructure is a nontrivial task that evolves from the actual geometry design, using some kind of CAD (computer-aided design) software, and simultaneous device's behavior simulations. In other words, the structure dimensions must be defined considering the micromachining process limitations/rules and characteristics, and aiming to obtain the desired device behavior. The dynamic behavior modeling approach has been presented in the previous chapter for a generic device. In short, microstructures have been fabricated aiming to maximize pull-in time sensitivity to acceleration, minimize mechanical-thermal noise and maximize readout capacitance (among other goals). The different micromachined structures, used in the experimental work throughout this thesis, are herein described, although the reasons behind the choice of the several parameters and dimensions are not the subject of this chapter (refer to Chapter 5, where the dynamic behavior of one of the fabricated structures is simulated).

As the displacement of the devices is detected capacitively, a capacitive readout was also designed and implemented, with suitable sensitivity for the capacitance variation range. In this chapter, the commercial surface micromachining process used is described and the fabricated devices are presented. The front-end capacitive readout circuit is also described since it is common to several experimental tests described in the following chapters.

3.1. SOIMUMPs micromachining process

The main characteristic of the SOIMUMPs process is that it allows fabricating free-standing structures on a 25 μm thick silicon layer, with minimum feature size and gap between silicon features of 2 μm. It allows patterning and etching both sides of the SOI wafer up to the buried oxide, enabling through-holes and movable structures suspended in the air. This process uses microtechnologies such as deep reactive ion etching (DRIE). Including those for metal patterning (to build bond pads and connections), a total of 4 masks are used. Figure 3.1 presents an overview of the fabrication process flow. The process steps requiring a mask are depicted in dark gray. Next, a description of each of the process steps is provided.

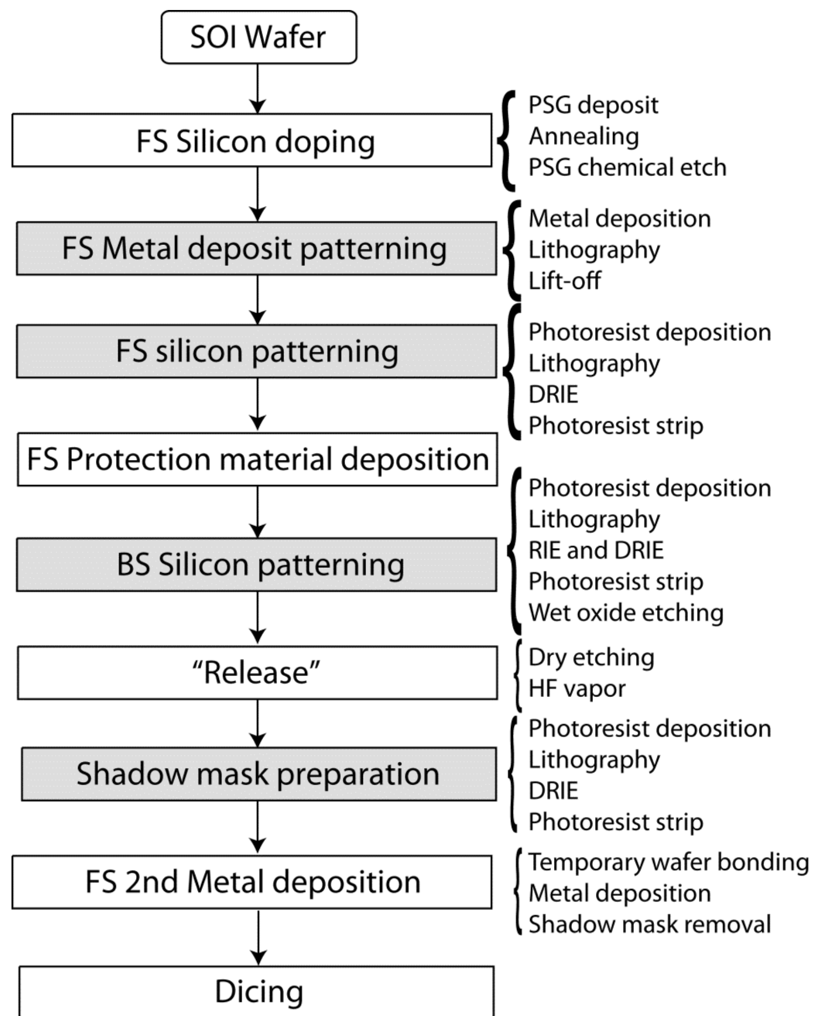

Figure 3.1: SOIMUMPs process flow diagram.

The SOIMUMPs process starts with a 6 inch (150 mm) n-type double-side polished SOI wafer, which consists of a stack of a handle wafer (substrate layer, 400 µm-thick), a 2 µm-thick buried oxide (BOX) layer, and the 25 µm-thick device layer (Figure 3.2a). A 10 µm-thick device layer option is also available in this process but was not used in this work. The device layer is also called SOI or active layer since it is where the active, movable structures are defined. A back side (BS) oxide layer is also initially present (the device layer side is considered the front and the handle the back side.)

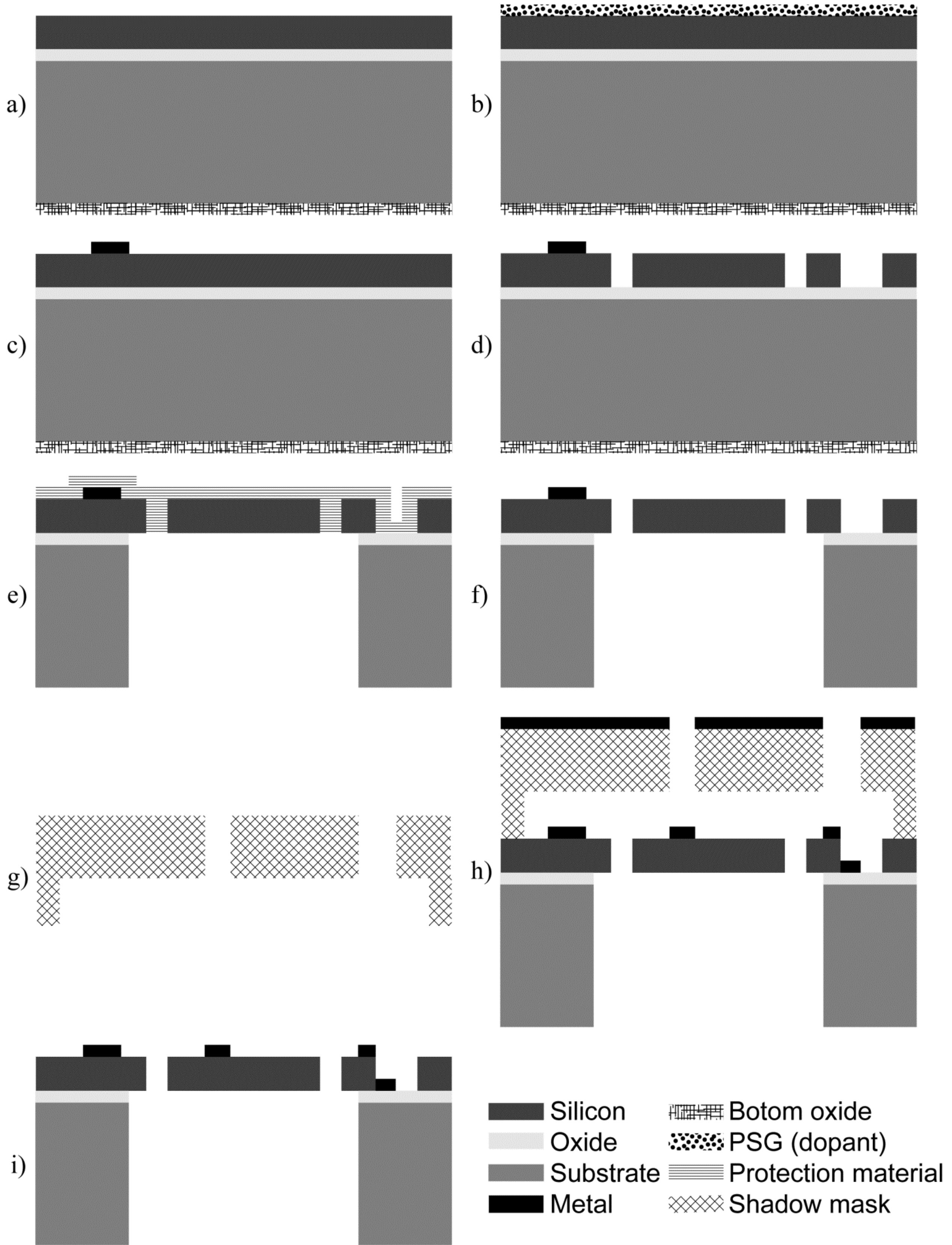

Figure 3.2: SOIMUMPs process steps.

An initial doping step is performed on the front-side (FS) (Figure 3.2b). A phosphosilicate glass (PSG) layer is deposited, and the wafer is annealed at 1050 ºC for 1 hour in Argon to drive the phosphorous dopant into the top surface of the SOI layer. The PSG layer is subsequently removed by wet chemical etching.

The second step consists of FS metal patterning (Figure 3.2c), using lithography and lift-of techniques, using the first designer-defined mask, *Pad Metal*. The wafer is coated with negative photoresist and lithographically patterned by exposing the photoresist with light through the mask and then developing it. A metal stack consisting of 20 nm of chrome and 500 nm of gold is deposited over the photoresist pattern by e-beam evaporation. The photoresist is then dissolved to leave behind metal in the opened areas (lift-off).

The third step consists on the patterning of the SOI layer (Figure 3.2d). The front-side is coated with UV-sensitive positive photoresist which is lithographically patterned by exposing the photoresist to UV (ultra-violet) light through the *SOI* mask. Next, the photoresist is developed. The photoresist in exposed areas is removed, leaving behind a patterned photoresist etching mask. Deep reactive ion etching (DRIE) is then used to etch the silicon down to the BOX layer. This etching step uses Inductively Coupled Plasma (ICP) technology and special recipe to reduce undercutting of the silicon layer. After etching, the photoresist is chemically stripped.

In the fourth step the back side is processed to etch-through the handle wafer (Figure 3.2e). Firstly, a frontside protection material is applied to the patterned active layer. Next, the backside of the wafer is coated with photoresist and the *Trench* mask is lithographically patterned. Reactive ion etching (RIE) is used to pattern the bottom oxide layer (used as hard mask for DRIE) prior to DRIE etch of the full handle, stopping on the BOX. After etching is completed, the photoresist is removed. Finally, a wet oxide etch process is used to remove the buried oxide layer in the regions defined by the *Trench* mask.

Structures are then release on the fifth step (Figure 3.2f). The frontside protection material is stripped using a dry etch process, thus “freeing” any mechanical movable structures in the silicon layer that are located over through-holes defined in the substrate layer. The remaining “exposed” oxide is also removed from the top surface using a vapor HF process, allowing for an electrical contact to the handle silicon, and providing an oxide layer undercut.

A separate double-side polished silicon wafer is used to fabricate a shadow mask (Figure 3.2g) for the second metal deposition step. “Standoffs” are pre-fabricated into the shadow mask so that it does not come into contact with patterned features in the active layer of the SOI wafer. The shadow mask wafer is then coated with photoresist and lithographically patterned using the

Blanket Metal mask. DRIE silicon etching is used to etch completely through the shadow mask wafer, producing holes for the metal to be evaporated through. After etching is completed, the photoresist is removed.

The shadow mask is aligned and temporarily bonded to the SOI wafer. The second metal layer, consisting of 50 nm Cr + 600 nm Au, is deposited through the shadow mask (Figure 3.2h), and the shadow mask is removed, leaving a patterned metal layer on the SOI wafer (Figure 3.2i).

At the MEMSCAP foundry, the multi-project wafer is diced in 11.15 × 11.15 mm^2 chips. A method for subdicing is allowed by the SOIMUMPs process with consists in the design of trenches below thin silicon features, which are easily torn apart by the user (Figure 3.3). The available design area is 9×9 mm^2.

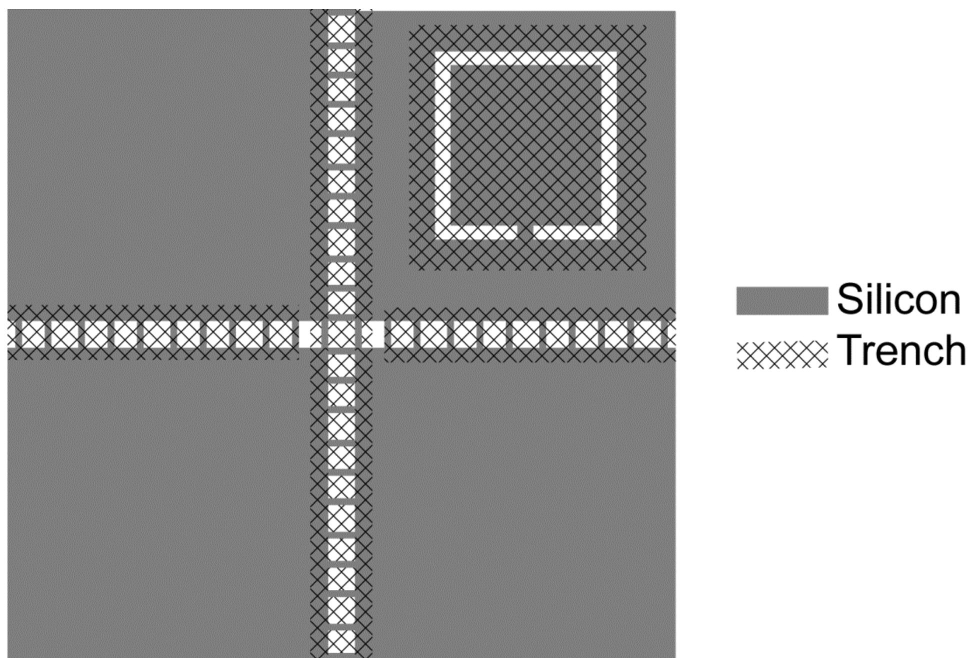

Figure 3.3:Trench and silicon beams features for manual subdicing.

In this work, three different microstructures were placed in the same chip. The three structures are described in the following section.

3.2. Fabricated MEMS structures

3.2.1. MEMS structures description

The MEMS structures used throughout this work were fabricated using the SOIMUMPs process. Three distinct microstructures were designed in the same 11.15 × 11.15 mm^2 die, and were later separated using the subdicing technique described in the previous section. Figure 3.4 shows a picture of one fabricated chip and how it is subdiced.

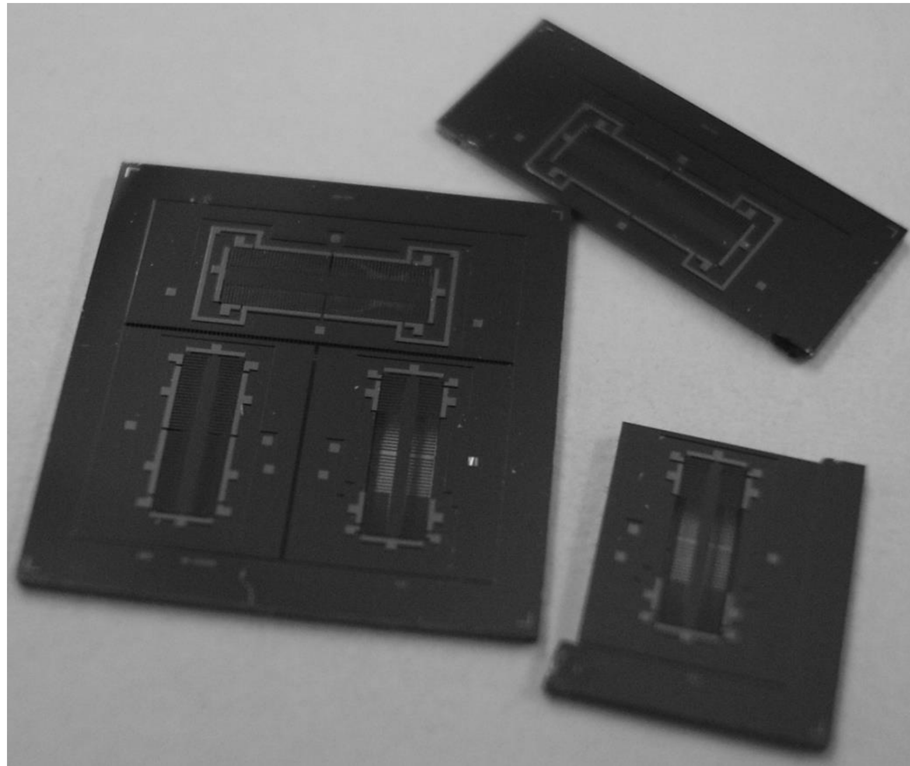

Figure 3.4: Picture of a die as provided by MEMSCAP and two smaller pieces already subdiced from another die.

All the devices are in-plane movable structures, i.e., the movement is in the direction parallel to the die plane. The devices use parallel-plate capacitors: the movable proof-mass has comb-like features (array of beams) which together with fixed comb-like structures form parallel-plate capacitors. The capacitance area is defined by the height of the beams, which is the thickness of the SOI layer, and the overlapping length. Each set of two adjacent parallel-plates/electrodes (one movable and one fixed) is both a capacitor (for sensing or for actuation) and a damper.

One of the structures (structure S0) was designed to take maximum advantage of the SOIMUMPs capabilities, i.e., large proof-mass dimensions and large actuation and sensing capacitances. This structure (Figure 3.5) is the largest of the three fabricated structures and was the one used for the general study of the time-based accelerometer approach. Other two microstructures, S1 and S2 (Figure 3.6 and Figure 3.7), were designed to study the effects of a different damper geometry. These two structures have the same dimensions, but while S1 uses a conventional damper geometry S2 has vertical channels implemented on the dampers (Figure 3.8). They also have different number of dampers (S2 has twice the number of dampers of S1). The study of the squeeze-film dampers is presented in Chapter 4.

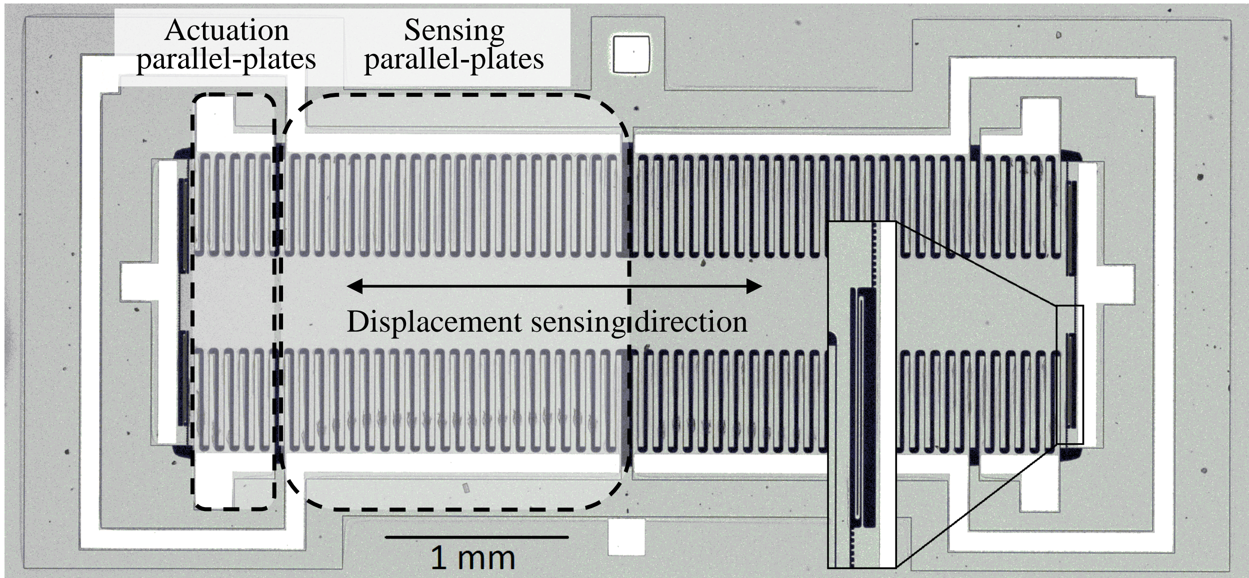

Figure 3.5: Optical microscope picture of microstructure S0 showing the comb beams for actuating (on the extremities of the movable mass) and for sensing (the more numerous plates in the central area, with top and bottom already connected on the die), and detail of one bi-folded spring.

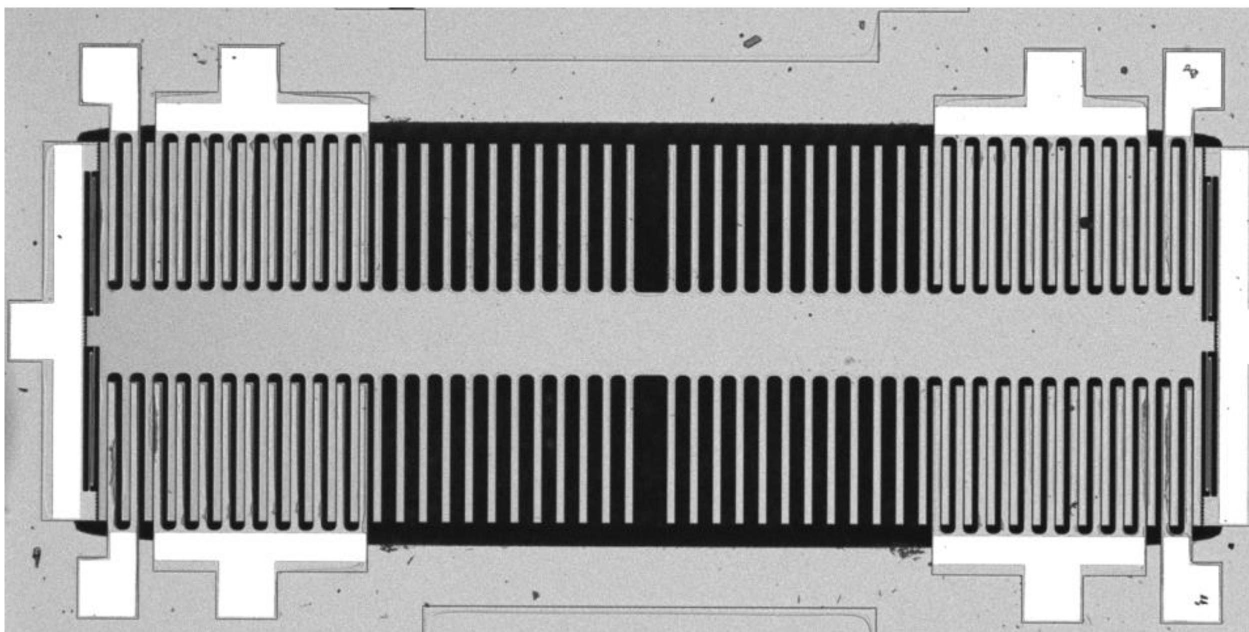

Figure 3.6: Optical microscope picture of microstructure S1.

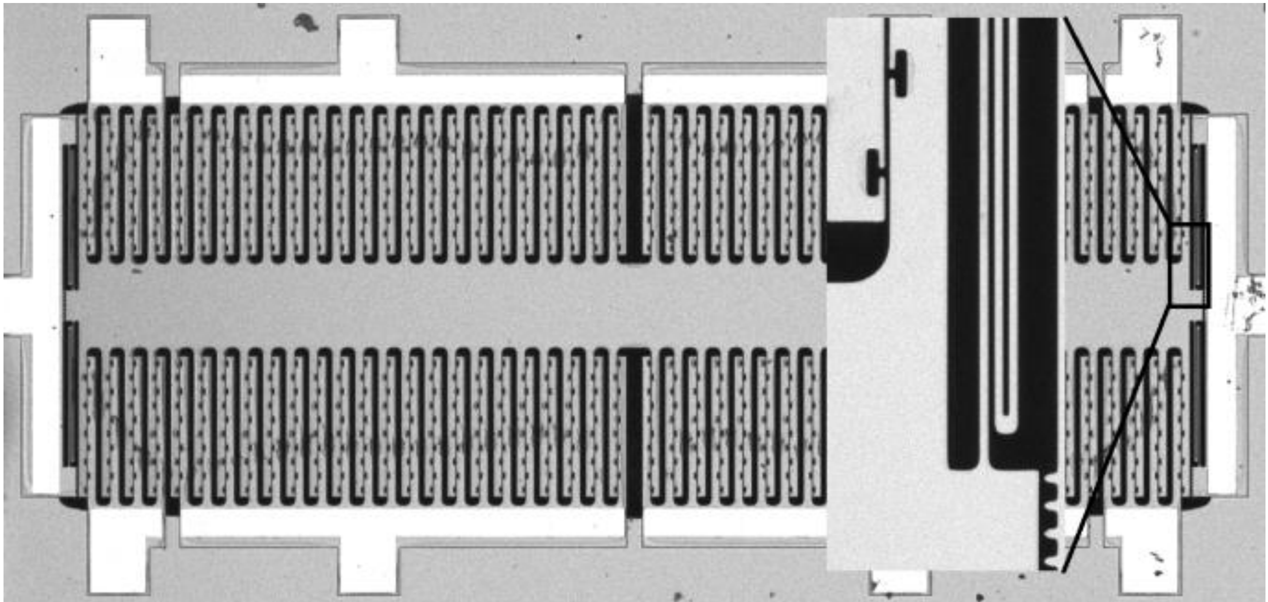

Figure 3.7: Optical microscope picture of microstructure S2.

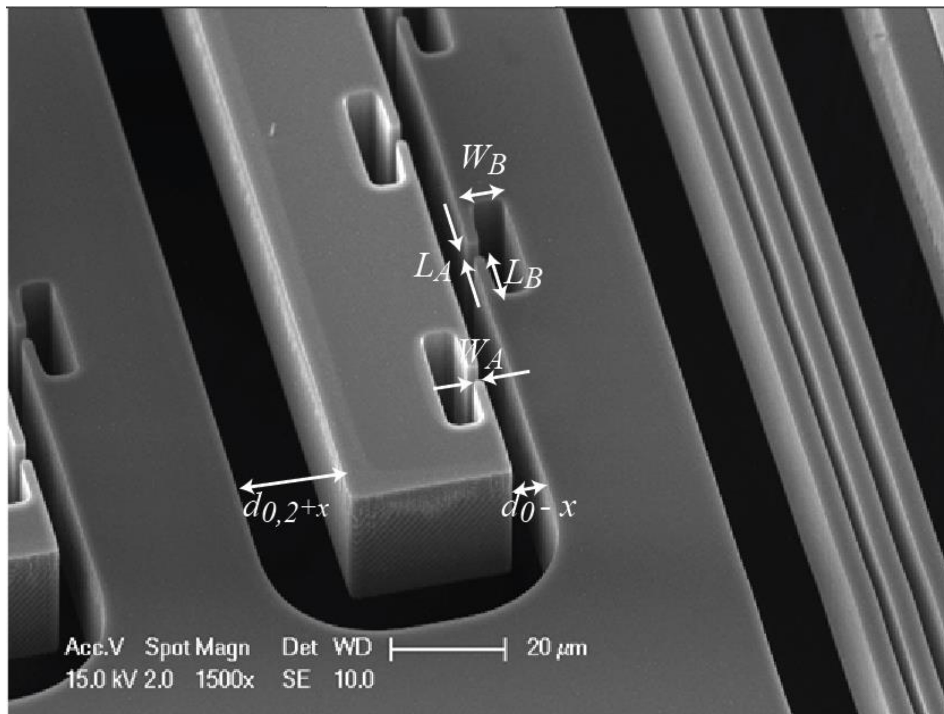

Figure 3.8: SEM picture of microstructure S2 showing the damper channels detail.

The minimum feature size and the minimum spacing allowed between silicon features recommended in the SOIMUMPs process is 2 µm. While the minimum feature size was not used on the fabricated devices (the smaller features are the folded springs of S0 with a width of 4 µm), the minimum distance was used for designing the stoppers that limit device displacement and prevent contact between the movable and fixed parallel-plates. As the pitch of the SOI mask design is 0.25 µm [3.1], the gaps between the parallel-plates were designed 2.25 µm-wide, and

the stoppers 2 μm apart from the movable mass. In this way, the proof mass can move 2 μm to each side (gap variation between 0.25 and 4.25 μm) without contact occurring between the movable and fixed electrodes. The stoppers are at the same voltage potential as the movable mass.

The designed structures are symmetrical in the two plane axis. All the structures comprise different sets of parallel-plate capacitors for sensing and for actuation, symmetrically placed in each direction. Ideally, to avoid additional wire bonding and connections outside the chip, the fixed actuating comb structures that act on the same direction should be connected on-chip. Due to space constraints, only the sensing comb structures of structure S0 were connected in the die. Designing additional routes would render them too close to each other and create parasitic capacitances that could compromise the electronic readout capabilities.

Each of the proof-masses is suspended on four flexible bi-folded beams, acting as springs. Details of one of the springs and stoppers are present in Figure 3.5 and Figure 3.9. The suspensions define the dominant degree-of-freedom of the mass displacement as the direction parallel to the mass length, i.e. perpendicular to the plane of the parallel-plates capacitors. For well-designed springs, the displacement in other directions is negligible and the device can be considered as 1-DOF device. In order to obtain compliant enough springs while at the same time respecting the minimum recommended feature size, a bi-folded (“N” shaped) design of opted for.

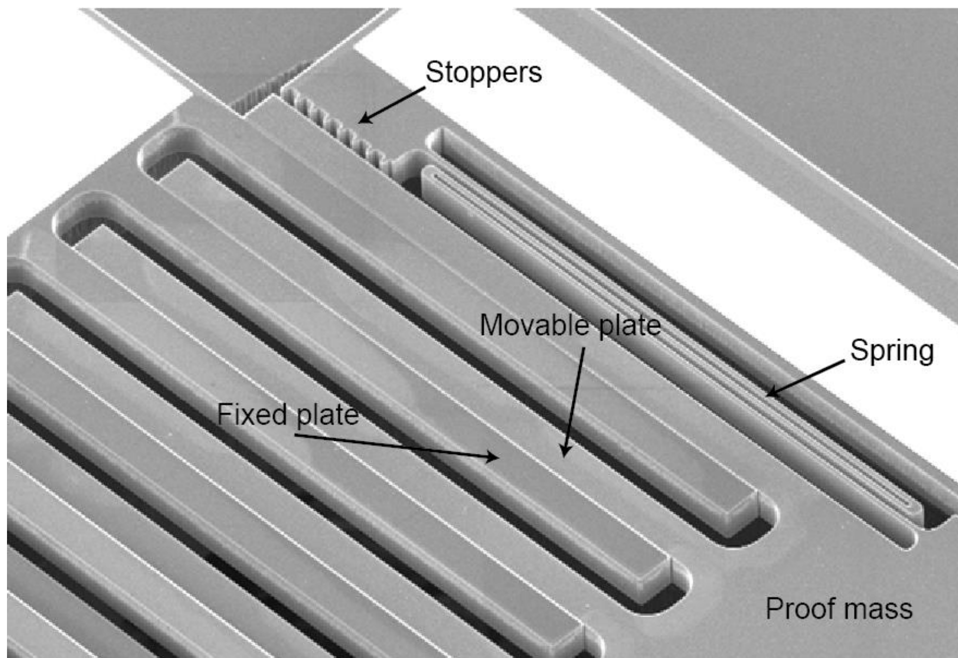

Figure 3.9: SEM picture of microstructure S0 detail showing spring and stoppers.

Table 3.1 presents the main design parameters obtained through analytical modeling of the microstructures (considering standard atmospheric conditions: pressure of 101 kPa and temperature of 293 K). Structure S0 comprises 12 beams for actuating and 46 for sensing, on each side (left and right). The beams are 530 µm long and 30 µm wide. Each one establishes a capacitance in an overlapping area of 500 µm (along length of the beams) by 25 µm (the thickness of the SOI wafer; beam height). Table 3.2 presents the damper channels dimensions. Matlab was used for the analytic modeling, with a full dynamic model being implemented on Simulink that includes squeeze-film damping with border and rarefaction effects (the damper model is presented in detail in Chapter 4). The expected pull-in voltages were calculated using a numerical method similar to the one described in [3.5], which accounts for the nonlinear behavior of the electrostatic and mechanical domains. Although in Chapter 2 an analytical solution for the pull-in voltage has been found, this method is more accurate as it accounts the electrostatic force generated between subsequent electrodes of different parallel-plates sets (gap d_{02}). This method consists of sweeping the voltage from an initial value towards increasing positive values while computing the stability points for each iteration, until a critical deflection solution is found beyond the full gap displacement.

Table 3.1: Main modeled (analytic model) design parameters of the structures S0, S1 and S2.

Design parameters		S0	S1	S2
Mass (m)		0.249 mg	0.159 mg	0.155 mg
Spring coefficient (k)		3.31 N/m	4.46 N/m	4.46 N/m
Natural resonance frequency (f_0)		580 Hz	842 Hz	853 Hz
Zero-displacement gap (d_0)		2.25 µm	2.25 µm	2.25 µm
Zero-displacement second gap (d_{02})		20 µm	20 µm	20 µm
Beams length		530 µm	530 µm	530 µm
Beams width		30 µm	30 µm	30 µm
Number of actuation capacitors in each direction		2×6 [a]	2×2 [a]	2×4 [a]
Number of sensing capacitors in each direction		2×23 [a]	2×10 [a]	2×20 [a]
Number of dampers in each direction		2×29 [a]	2×12 [a]	2×24 [a]
Zero-displacement actuation capacitance(C_{A0})		0.52 pF	0.175 pF	0.324 pF [b]
Zero-displacement sensing capacitance (C_0)		2.53 pF	1.10 pF	2.08 pF [b]
Low frequency damping coefficient (b)	gap=d_0	1.54 mNs/m	0.639mNs/m	0.825 mNs/m
	gap=(2/3)d_0	2.62mNs/m	1.08 mNs/m	1.38 mNs/m
Pull-in voltage (V_{PI})		2.916 V	5.846 V	4.310 V

[a] The total number of capacitors/dampers is twice these values since the structures are symmetrical (left and right sides)
[b] Minimum capacitance values considering only parallel facing surfaces

Table 3.2: S2 air channel damper geometry values.

Damper Parameters	Value
L_A	4 µm
L_B	10 µm
W_A	3 µm
W_B	6 µm
Damper length (l_0)	500 µm
Damper width (w_0, beam height)	25 µm
Beam width	30 µm
Number of channels (N_c)	5+5
Channel pitch	50 µm

3.2.2. Elastic spring model

The folded beams elastic coefficients were calculated by applying elementary elasticity equations. Considering a beam (one end fixed and one guided) with a concentrated load applied perpendicular to its length l_b, the linear stiffness coefficient is given by [3.6]:

$$k = \frac{12EI}{{l_b}^3} \tag{3.1}$$

where E is the elastic modulus of the material, Young's modulus, and I is the momentum of inertia of the cross-sectional area of the beam for the specific bending direction which is given by:

$$I = \frac{h_b {w_b}^3}{12} \tag{3.2}$$

where w_b and h_b are the beam width and height (rectangular shape) respectively, and considering the bending in the direction of the width, as illustrated in Figure 3.10. As the SOI wafer device layer surface orientation is (100), the Young's modulus of silicon in the direction parallel to the surface is 169 GPa.

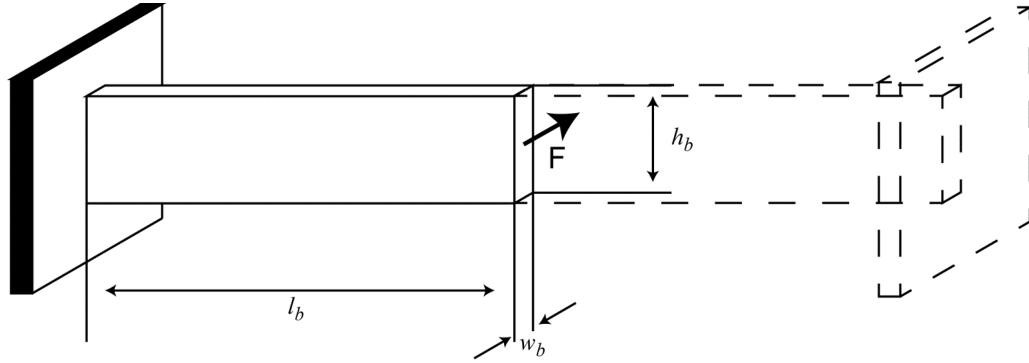

Figure 3.10: Applied force on beam with one fixed and one guided end.

As the structures have bi-folded springs, if the elbow features / trusses are considered rigid, the deflection of the bi-folded spring is shared by the three beams, adding the compliances:

$$\frac{1}{k_s} = \frac{1}{k_{b1}} + \frac{1}{k_{b2}} + \frac{1}{k_{b3}} \tag{3.3}$$

As the inertial mass is suspended on 4 bi-folded springs, the total stiffness coefficient of the structure is $k=4k_s$. The maximum structure displacement allowed, 2 µm, is within the spring's natural range and the spring is operating in the linear region (obeying Hooke's law).

3.3. Fabricated capacitive readout **circuit**

The goal in terms of readout is providing a signal that is proportional to the capacitance variation of the actuated structures. At rest position, when the proof-mass is centered in respect to the symmetrical electrodes on each side, both sensing capacitances are 2.53 pF. As the proof-mass moves to one of the sides, one of the capacitances decreases while the other decreases (Figure 3.11). The resulting differential capacitance increases nonlinearly up to approximately 20 pF at the maximum deflection.

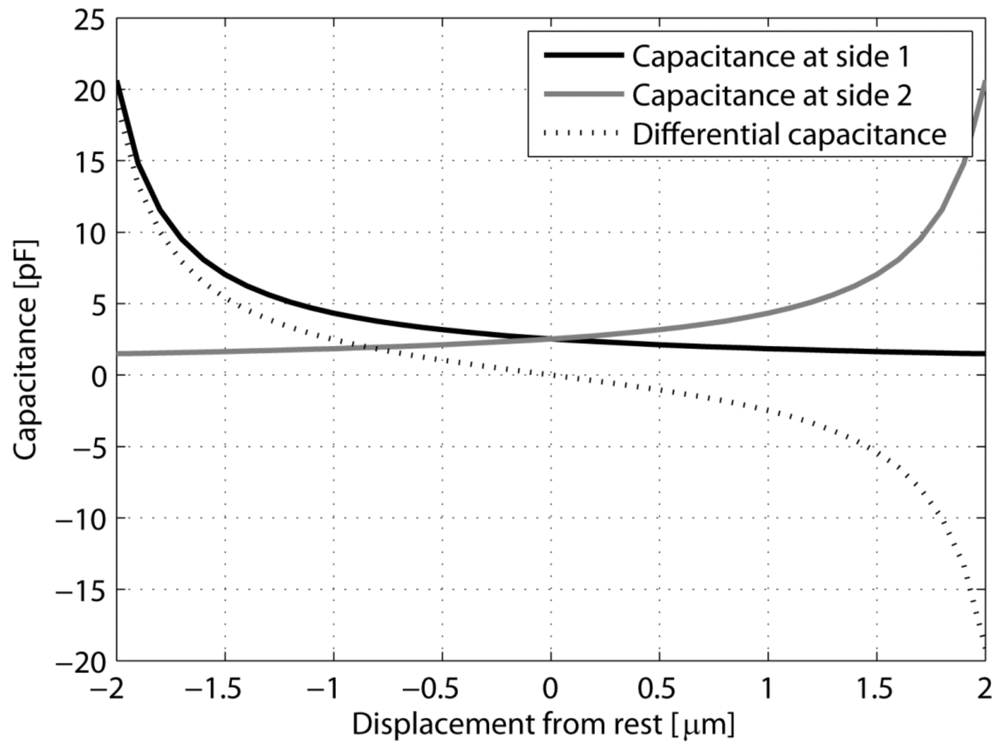

Figure 3.11: Sensing capacitance variation of microstructure S0 with displacement from rest position.

A single-ended approach was chosen for the capacitive readout circuit for simplicity. A capacitive circuit based on a charge amplifier was used for the readout of the MEMS structures (Figure 3.12). The output from the charge amplifier is an amplitude-modulated (AM) signal. The AM-demodulation is performed by multiplying the signal with the frequency carrier and low-pass filtering. The readout does not comprise mechanisms to guarantee that the carrier is in-phase with the signal from the charge amplifier (synchronization / phase adjustment), but an additional high pass filter was added, with a pole matching the charge amplifier, and using the same IC operational amplifier, LME49710, in order to produce equivalent delay. The circuit was implemented on a PCB (printed circuit board).

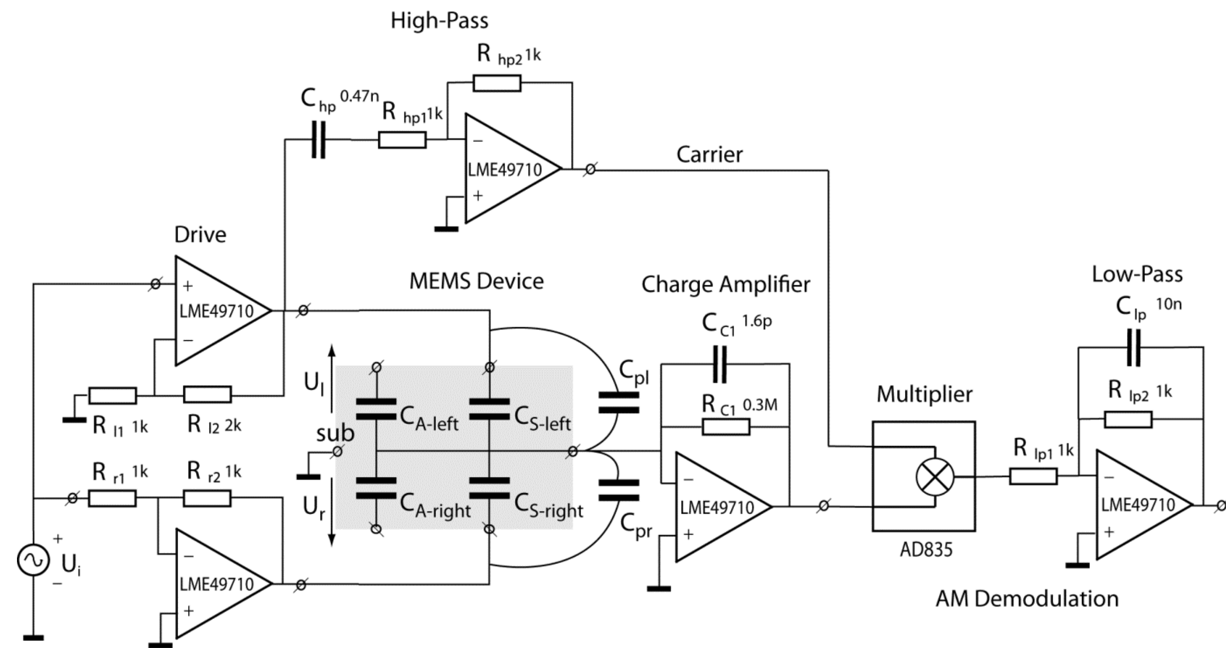

Figure 3.12: Displacement detection circuit with charge amplifier and AM demodulation stage.

The LME49710 is a low noise amplifier with high bandwidth, high slew rate and low input bias current of 7 nA. This feature is important as the input bias current creates an input offset voltage that is amplified along with the signal. A low input voltage guarantees that the circuit does not saturate during operation.

The readout circuit was implemented in Multisim for simulation prior to fabrication. Figure 3.13 presents the DC circuit output as a function of differential capacitance (nominal capacitor value of 2.53 pF), using a 1 MHz 500 $mV_{p\text{-}p}$ signal at U_i (carrier modulation signal). The simulation results show a linear behavior of 160 mV/pF until it saturates at about 6 pF. At the critical pull-in displacement the expected differential capacitance is 1.679 pF for S0 and 0.73 pF for S1 and therefore the readout circuit can be used with the designed microstructures. Nevertheless, please note that the gain is determined by both the capacitor C_{C1} and the amplitude of the carrier modulation signal. In fact, the carrier modulation signal was changed throughout the work, so the simulated curve can only serve as a guide, and a different calibration curve was later obtained experimentally (in Chapter 4). In addition, this simulation assumed an ideal multiplier, while in the actual implementation, the multiplier AD835 was used, which limited the output signal amplitude (due to saturation of the input signals).

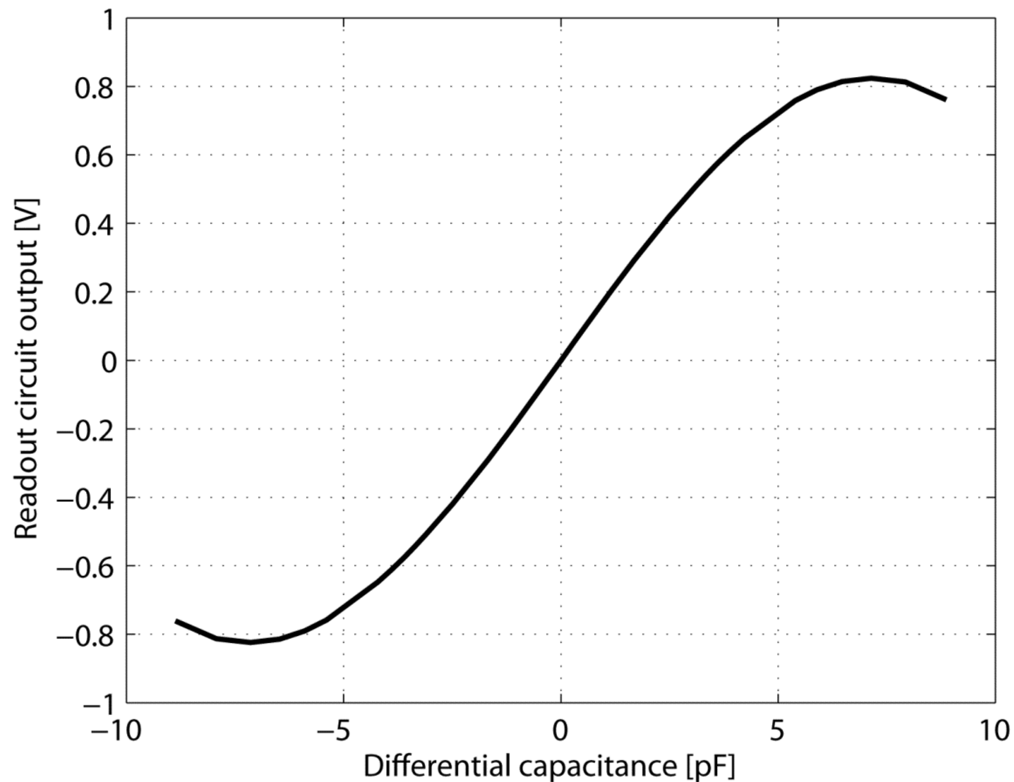

Figure 3.13: Readout circuit output as a function of sensed differential capacitance.

3.4. Conclusions

In this chapter, the SOIMUMPs micromachining process has been described and the fabricated MEMS structures were presented. This process allows fabrication of devices with movable parts attached/anchored by thin compliant silicon beams acting as springs. The substrate/handle wafer silicon is completely removed below the movable parts, leaving them suspended in the air. The springs are compliant in the in-plane direction, along the proof-mass length, and much stiffer in the out-of-plane direction. Three different and independent parallel-plate microstructures were fabricated on each die, differing in dimensions and parallel-plate geometry. Structure S0 has the largest proof-mass and capacitance. Structure S2 has a different parallel-plate geometry comprising small flow channels and structure S1 is similar to S2, but comprises conventional parallel-plate geometry. Structures S1 and S2 are used in Chapter 4 for the damping study and structures S0 are used in the following chapters for the pull-in time accelerometer and viscosity sensor studies.

The capacitive readout circuit used for the experimental work described throughout this thesis has also been described in this chapter. It is based on a single ended approach using a charge amplifier. Simulations (comprising a realistic model of the operational amplifier used, an

ideal multiplier and accounting for parasitic capacitances) have shown a linear response of 160 mV/pF up to 5 pF differential capacitance. This does not correspond to the experimental calibration performed later (in Chapter 4) due to the non-idealities of the multiplier used and the gain manipulation as convenient by adjusting the carrier modulation signal amplitude.

References

[3.1] A. Cowen, G. Hames, D. Monk, S. Wilcenski, and B. Hardy, *SOIMUMPs Design Handbook*, 8.0 ed. MEMSCAP Inc., 2011, pp. 0–25.

[3.2] "Europractice Homepage." [Online]. Available: http://www.europractice-ic.com/. [Accessed: 07-Nov-2012].

[3.3] J. Chae, H. Kulah, and K. Najafi, "An in-plane high-sensitivity, low-noise micro-g silicon accelerometer with CMOS readout circuitry," *Journal of Microelectromechanical Systems*, vol. 13, no. 4, pp. 628–635, 2004.

[3.4] J. Collet, *MEMSOI Design Rules Manual*, 1.2 ed. Tronics Microsystems, 2007.

[3.5] L. A. Rocha, E. Cretu, and R. F. Wolffenbuttel, "Analysis and analytical modeling of static pull-in with application to MEMS-based voltage reference and process monitoring," *Journal of Microelectromechanical Systems*, vol. 13, no. 2, pp. 342–354, 2004.

[3.6] J. J. Allen, *Micro Electro Mechanical System Design*. Boca Raton: CRC Press, 2005.

4.

Squeeze-film damper design

Squeeze-film damping plays a very important role on the dynamic performance of micro movable devices. When the distances between moving parts are just a few micrometers, fluid (usually air) is trapped, resulting in damping forces acting on the device during its motion that cannot be neglected. These forces are highly nonlinear and depend on the surrounding gaseous medium, geometry and device movement. The gas film forces obey to nonlinear partial differential equations that can be analytically solved for the simplest movements and geometries, such as movement in the direction perpendicular to the capacitor area (1-DOF). In the case of inertial MEMS devices, the damping forces are not only determining the dynamic response but also the mechanical-thermal noise of the system [4.1], [4.2].

When designing movable capacitive structures (either for sensing, electrostatic actuation, or both), squeeze-film damping becomes even more dominant on the system performance and therefore typical damper design involves a trade-off between sensitivity, response time and noise. In the case of a capacitive accelerometer, higher capacitive sensitivity is desirable; adding extra capacitor plates or increasing the plate area can be the solution, however, the extra parallel plates result in higher mechanical-thermal noise and, if the system is critically damped or overdamped, extended response time. In some cases, where high quality factors are desirable (case of gyroscopes), high vacuum encapsulation is used at the expense of more complex fabrication processes and higher cost.

This chapter focuses on damper design and modeling: the typical design approach for squeeze-film damping in parallel-plates is addressed and also a design improvement is introduced and experimentally verified. The design improvement for gap-varying in-plane parallel-plate

devices consists of a geometry comprising flow channels that enables reducing the damping coefficient while maintaining capacitive sensitivity (or increasing capacitance while maintaining the damping coefficient). In other words, a geometry that allows increasing the capacitance/damping ratio is studied. Design solutions addressing the trade-offs between capacitance increase and damping reduction in in-plane moving parallel-plates are not available in literature, although perforations in parallel-plates moving out-of-plane have already been used and studied [4.3]–[4.5]. The alternative to traditional damper design discussed in this chapter consists of flow channels, or wells, placed in the parallel-plates geometry, improving the gas flow between the parallel-plates. This geometry can be particularly useful in the design of capacitive inertial sensors, since it allows improving current devices with extra sensitivity and better noise performance.

In this chapter, both analytic and CFD (Computational Fluid Dynamics) models are initially used to study the damping forces acting on fabricated structures with conventional damper geometry and with damper comprising flow channels. Next, the damping coefficients are measured and compared to the analytic model and CFD simulations. Finally, a few CFD simulations are performed in an attempt to verify the influence of each of the new design geometry parameters on the overall damping reduction.

4.1. Parallel-plates MEMS design

4.1.1. Conventional plate configuration

A good capacitive MEMS design aims at obtaining the maximum electrical capacitance value in order to improve the detection capabilities. Electrical capacitance in parallel-plates is defined as [4.6]:

$$C_0 = \varepsilon_0 \varepsilon_r \frac{A}{d_0} \tag{4.1}$$

where ε_0 is the free space permittivity, ε_r is the relative permittivity of the material between the plates (air is considered in this work), A is the area of the plates and d_0 is the distance between the plates. In MEMS devices, the use of parallel-plates has proven to be an effective solution [4.6], however, while the capacitance increases, the damping coefficient also increases. The viscous damping coefficient is a measure of the damping forces in a system. One of the consequences of this damping increase is the raise of the noise floor. For instance, in an accelerometer the equivalent acceleration noise due to Brownian noise is described as [4.7]:

$$a_{noise,b} = \frac{\sqrt{4k_B T b}}{9.8m} \ [g/\sqrt{Hz}] \tag{4.2}$$

where k_B is the Boltzmann constant ($1.38.10^{-23}$ J/K), m the movable mass, T the absolute temperature in Kelvin and b is the damping coefficient in N.s/m.

The typical approach when designing capacitive parallel-plates devices is to find equilibrium between the damping coefficient and the capacitor value. Clearly, in a parallel-plate configuration, extra plates or increased plate area will increase both capacitance and damping coefficient and vice-versa. For those situations where it is desirable to increase capacitance and reduce damping, a design conflict exists. One possibility is to try to arrive to the desired capacitance using different parallel-plates length configurations (while the capacitance is the same the damping coefficient changes). As an example, consider a capacitor of 1 pF, with a parallel-plate configuration where the plates are 2 µm apart and the width of the plate is 10.6 µm (see inset on Figure 4.1). The length of the arms (i.e. plate length) and the number of parallel-plate dampers can be changed (in Figure 4.2, two sets of parallel-plates can be seen). If one computes the different possible combinations between length of arms and number of movable arms (to get 1 pF capacitance) along with the corresponding damping coefficient (at low frequencies, with the models described further in this chapter), the graph of Figure 4.1 is obtained. Both the damping coefficient and the arm length are normalized to the maximum values (100%).

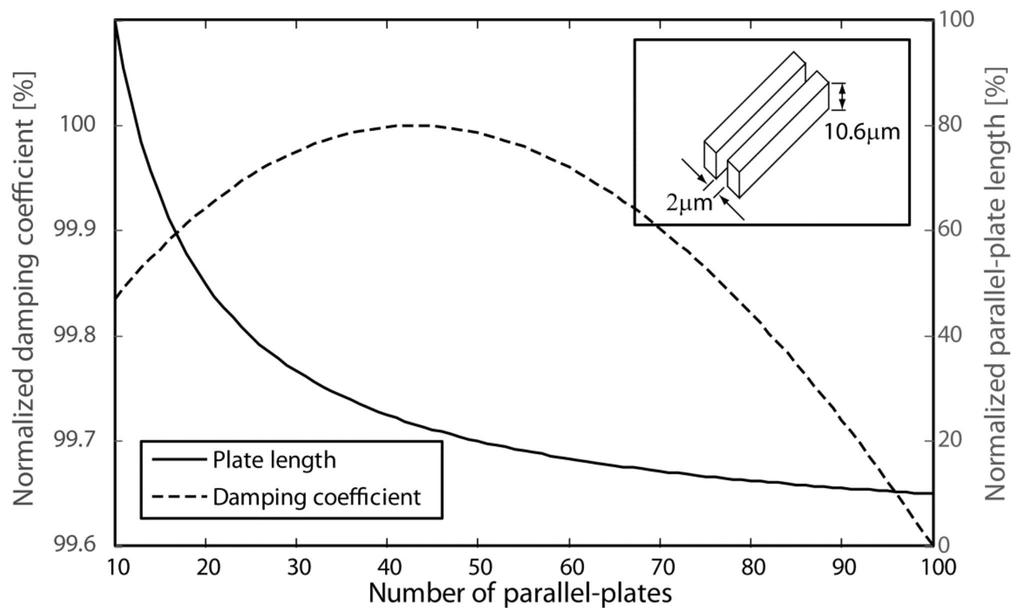

Figure 4.1: Change in damping coefficient as function of number of parallel-plates in a 1 pF total capacitance.

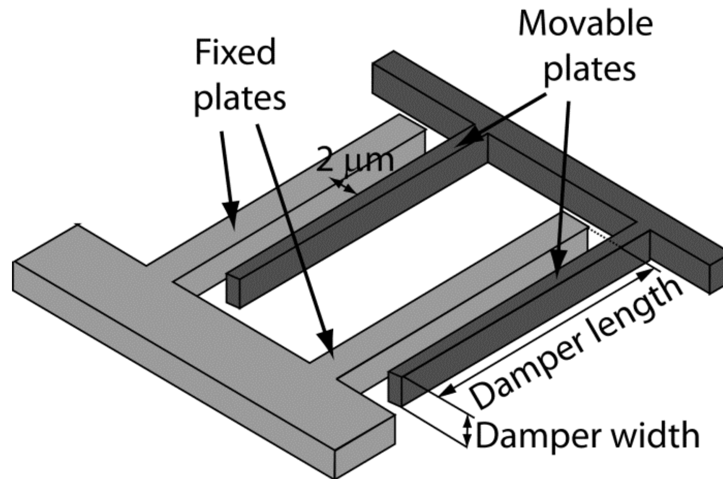

Figure 4.2 : Example of two sets of parallel-plates (dampers) of an in-plane device without substrate, with a sensing gap of 2 µm.

This small example is indicative of the existing limitations of a parallel-plate configuration to properly address both capacitance and damper design. A quick analysis of the graph demonstrates that the damping coefficient variation is just 0.4%, despite the large variation on the arm length and number of arms. It is evident that the traditional geometry used in parallel-plates cannot address this problem. In the next sub-section, a new geometry for parallel-plates MEMS is presented, that can be used as a tool to address this conflict.

4.1.2. Improved damper geometry – channels

During capacitor oscillations, the gas trapped between the parallel-plates gives origin to damping forces that depend not only on the gas pressure and viscosity, but also on the geometry. It seems intuitive that if gas channels are introduced along the length of the parallel-plates, in the direction of motion, the pressure differences caused by the trapped gas will be smaller, resulting in a controlled decrease of the damping forces. Hole introduction is a well-known approach for electrodes acting parallel to the substrate, i.e. out-of-plane devices in which the parallel-plates moves in the direction normal to the die [4.3]–[4.5] (see Figure 4.3). Although perforated parallel-plates is a commonly used and well-studied solution, so far it has not been applied to in-plane devices (Figure 4.2) since it is not possible to etch horizontal holes in a vertical plate with available microfabrication techniques. Therefore, a new geometry for in-plane devices, based on channels is proposed.

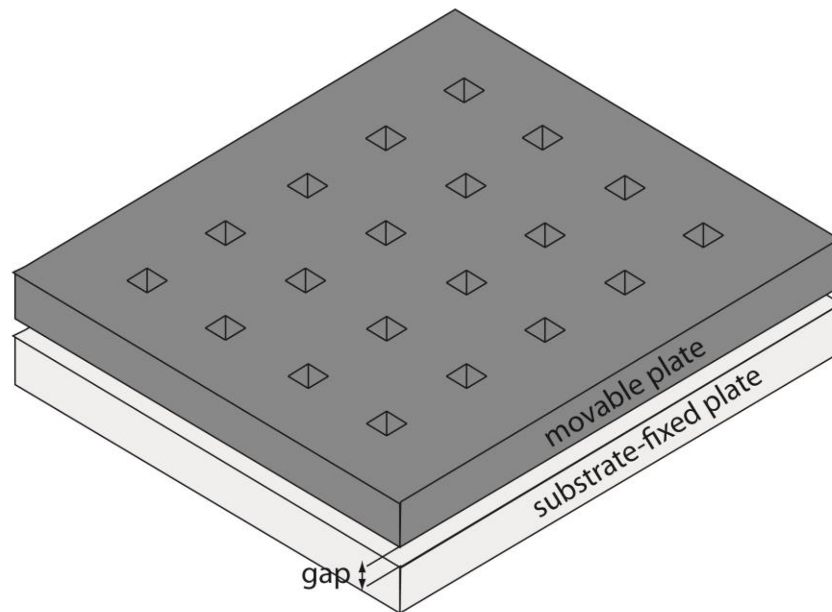

Figure 4.3: Design of square damping reducing holes on parallel plate moving out-of plane.

The new improved geometry for parallel-plate dampers is presented in Figure 4.4 showing a small section of a parallel-plate configuration. The underlying idea is to introduce small channels within the capacitor arms to improve the gas flow. As the flow is improved, less gas is trapped during oscillations, leading to a reduction of the damping coefficient. Since these gas channels are small, as compared to the arm length, they can effectively reduce the damping forces without significantly affecting the capacitance value.

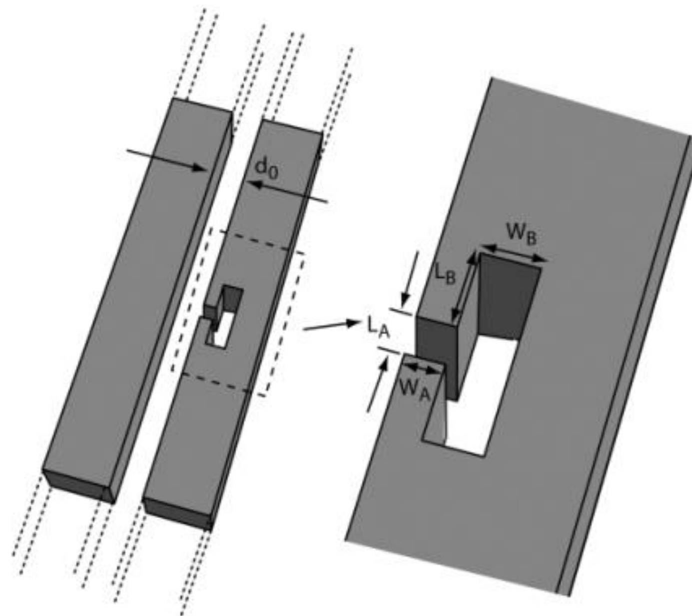

Figure 4.4: Proposed improved geometry for parallel-plates dampers: schematic of a flow channel in a parallel-plate.

This improved geometry is fully characterized by the number of channels (N_c), the distance between channels (pitch), and the dimensions of the channels, given by L_A, L_B, W_A and W_B as indicated in Figure 4.4.

The fabricated structures (described in Chapter 3) used in this work have thick electrodes (30 μm) to guarantee that arms do not bend after pull-in is reached. Depending on the application, it might be desirable to have thinner electrodes to decrease the size of the sensor (or fit more parallel-plates). In this case, the introduction of air channels limits how much the electrodes thickness can be reduced, which can limit the total number of arms per area, resulting in a smaller capacitance per die area. In summary, for a specific application it is necessary to reach a trade-off between mass/area, capacitance/area, damping/noise, electrostatic actuation voltage, etc.

The new approach introduced here might decrease the total device mass since silicon is etched from the arms. However, if the mass is large enough, this will not cause a significant reduction in sensitivity. Alternatively, the channels can also be implemented solely in the fixed arms. Simulations have been performed to check the dependence of damping coefficient on the location of the cavities, 10 on movable arm vs. 5 on movable plus 5 on fixed, and the differences are not significant (0.3% less damping on distributed cavities). For a better understanding of the damping mechanisms in parallel-plate MEMS devices, squeeze-film damping models are described in the next section.

4.2. Squeeze-film damping analytic model

4.2.1. Squeeze-film damping

The movement of a parallel-plate device, where the gap size between the plates changes in an oscillatory manner, squeezing the trapped fluid out and sucking it in, gives origin to squeeze-film damping. Fluid trapped between the movable electrode and the fixed one, results in major squeeze-film forces acting on the MEMS device.

The relation between velocity, pressure, density and viscosity for an isotropic Newtonian fluid with a laminar gas flow between two moving plates can be calculated by using the Navier-Stokes equations and the continuity equation. With a few assumptions (uniform film thickness; isothermal conditions – no temperature gradients within the gas film and density proportional to pressure; and small Reynolds number allowing to ignore gas inertia), the Navier-Stokes equations and the continuity equation can be simplified into the compressible-gas-film Reynolds equation for the two-dimensional case [4.8], [4.9]:

$$\frac{\partial}{\partial x}\left(\frac{d^3\rho}{\eta}\frac{\partial p}{\partial x}\right)+\frac{\partial}{\partial y}\left(\frac{d^3\rho}{\eta}\frac{\partial p}{\partial y}\right)=12\frac{\partial}{\partial t}(\rho d) \tag{4.3}$$

where p is the pressure, η the gas dynamic viscosity, ρ is density, d is the gap between the surfaces, and x and y are the directions of the damper width and length.

4.2.2. Analytic model with rarefaction and compressibility effects

For structures in which only the size of the small gap between two parallel-plates changes in time, the pressure changes Δp relative to the wall velocity can be described by the Reynolds equation (4.3) reduced to [4.10]–[4.12] (considering an isothermal process, neglecting gas inertia and assuming $\Delta p \ll P$):

$$\frac{d^3 Q_{pr}}{12\eta}\left(\frac{\partial^2 \Delta p}{\partial x^2}+\frac{\partial^2 \Delta p}{\partial y^2}\right)=\frac{d}{P}\frac{\partial \Delta p}{\partial t}+\frac{\partial d}{\partial t} \tag{4.4}$$

where P is the ambient pressure, and Q_{pr} describes the relative flow rate coefficient as:

$$Q_{pr}=1+9.638(K_n)^{1.159} \tag{4.5}$$

for transitional flow regime, $0.1 < K_n < 10$ [4.10], [4.13]; or:

$$Q_{pr}=1+6\sigma_p K_n \tag{4.6}$$

for slip regime $0.001<K_n<0.1$ [4.13]–[4.15]; where σ_p is the slip coefficient [4.16] (σ_p =1.016 for diffuse scattering) and K_n is the Knudsen number. For gases, the Knudsen number relates the gas specific mean free path (λ) and the film thickness, $K_n=\frac{\lambda}{d}$. $K_n<0.001$ defines continuum flow regime and $Q_{pr} = 1$. The relative flow rate coefficient is a compact way to include the boundary effects of rarified gas and these approximations are valid in the specific flow regimes mentioned (transitional and slip flow regimes respectively).

An analytical solution for the forces acting on the surfaces can be found if some conditions are assumed ($\Delta p \ll P$ and $\Delta d \ll d$) [4.10]. The solution is frequency dependent and is not suitable for transient analysis. A very suitable approach is presented in [4.10] where the damping force can be represented by a network of frequency independent spring-damper elements, which have the same transfer function of the initial solution. The resulting solution for the total damping force on rectangular parallel plates includes a component in-phase with the velocity ($G_{m,n}$) and an out-of-phase component ($C_{m,n}$) expressed as [4.10], [4.15], [4.17]:

$$F_{b\ M,N} = \sum_{m=1,3,\dots}^{M} \sum_{n=1,3,\dots}^{N} \frac{-v}{Q_{pr} G_{m,n} + j\omega C_{m,n}}$$

$$G_{m,n} = \frac{\pi^6 d^3 (mn)^2}{768 \eta w l} \left(\frac{m^2}{w^2} + \frac{n^2}{l^2} \right) \tag{4.7}$$

$$C_{m,n} = \frac{\pi^4 d (mn)^2}{64 w l P}$$

where m and n are odd integers, v is the velocity of the plates, l and w are the parallel-plate length and width respectively. In this work $M = N = 45$ was used, and considered accurate enough (increasing this value hundred-fold, to 4501, yields an increase in the results of just 0.05%). $C_{m,n}$ models the compressibility (spring force), $G_{m,n}$ models the viscous losses (viscous damping force) and Q_{pr} includes the rarefaction effects of the gas. As the total damping force is defined as $F_b = -b\ v$, the damping coefficient becomes:

$$b_{M,N} = \sum_{m=1,3,\dots}^{M} \sum_{n=1,3,\dots}^{N} \frac{1}{Q_{pr} G_{m,n} + j\omega C_{m,n}} \tag{4.8}$$

For low frequencies, the total damping force depends linearly on the velocity of the plate and the film behaves as a pure damper. At higher frequencies, the relation becomes nonlinear and the spring force increases. At very high frequencies the film acts like a spring. The squeeze number is the ratio between spring force due to gas compressibility and force due to viscous flow, and the cut-off frequency, for which the squeeze number is 1 (i.e. the damping force is equal to the spring force), is defined as:

$$f_c = \frac{\pi P d^2}{24\eta} \left(\frac{1}{w^2} + \frac{1}{l^2} \right) \tag{4.9}$$

Incorporation of rarefaction effects in squeeze-film damping models is very important. For instance, for a 1.50 µm gap in air, corresponding to a Knudsen number of $K_n = 69\times10^{-9}/1.5\times10^{-6} = 0.046$, the rarefaction effects are included in the model by introducing an effective viscosity instead of the nominal dynamic viscosity (defined as the ratio between nominal dynamic viscosity and relative flow rate coefficient). The effective viscosity for a 1.5 µm gap is $1.85\times10^{-5}/(1+6\sigma_p K_n) = 1.44\times10^{-5}$ Pa s, i.e., 78% of the nominal viscosity of air (1.85×10^{-5} Pa s). For smaller gaps the effect is even more pronounced and therefore, rarefaction effects must be taken into consideration for proper modeling of squeeze-film damping.

4.2.3. Border effects

It is often the case that the damper height has a significant effect on the damping coefficient due to the small dimension, i.e., the width of the damper is comparable with the gas thickness (gap size) [4.13]. This is often referred to as the border effect and can significantly change the damping coefficient. The border effects can be included in the squeeze-film model using a modified surface width, $w=w_0+\Delta w$, which is the actual width of the plate with an added elongation. Veijola et al. derived the surface elongations for a parallel-plate configuration with linear movement, including rarefaction effects, by extracting the elongations from FEM simulation results. The resulting approximation for the elongated plate width with nonsymmetrical outlets is valid up to $K_n < 0.1$ [4.13], [4.15]:

$$w = w_0 + 1.3\left(1 + 3.3\sigma_p K_n\right)d \tag{4.10}$$

The work focused on nonsymmetrical outlets (see Figure 4.5) but also provided an approximation for symmetrical outlets:

$$w = w_0 + 0.81\left(1 + 0.94\sigma_p K_n\right)d \tag{4.11}$$

Equation (4.11) is in better agreement with the relative elongation for a symmetrical outlet considering the continuum flow regime, known to be $8/(3\pi) \approx 0.8488$, and the expected inferior dependence on rarefaction in comparison to a nonsymmetrical outlet [4.13], [4.16], hence it will be adopted in this study.

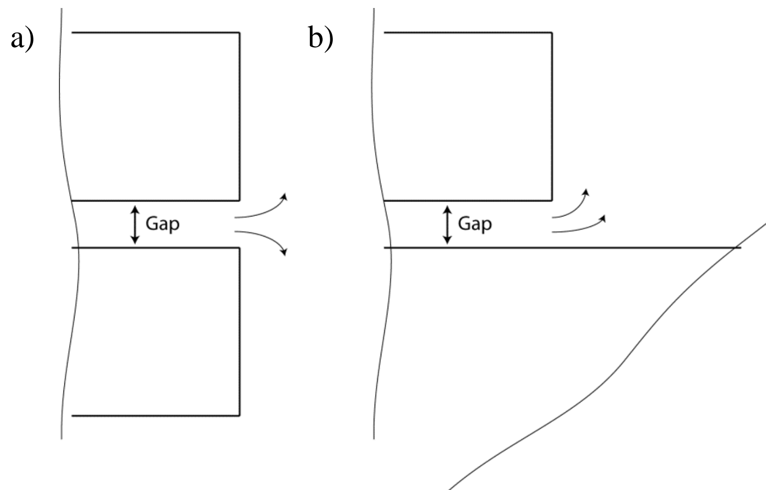

Figure 4.5: (a) Symmetrical and (b) nonsymmetrical outlets on parallel-plates.

For the structures considered in this work, the length of the damper is big enough so that the border effects can be safely neglected. That is not the case for the damper width, since the ratio width/gap can be relatively small (6<width/gap<100).

4.2.4. Inertial effects

The Reynolds equation introduced before assumes that the gas inertial forces are small when compared to the viscous forces and the gas inertia is neglected. However, for large gaps and high oscillation frequencies, the inertial effects increase and need to be considered when modeling squeeze-film damping. The gas inertia can be included in the model by modifying the flow rate coefficient as proposed in [4.14]:

$$Q_{pr} = \frac{1 + 6\sigma_p K_n}{1 + j\omega \dfrac{\rho d^2\left(1 + 10\sigma_p K_n + 30(\sigma_p K_n)^2\right)}{10\eta\left(1 + 6\sigma_p K_n\right)}} \tag{4.12}$$

This is an approximation for the slip flow regime and it is not suited for very high frequencies, i.e. above $10f_i$, where f_i is the cut-off frequency for which the Reynolds number (ratio between inertial and viscous forces) Re equals 1:

$$f_i = \frac{\eta}{2\pi\rho d^2} \tag{4.13}$$

At frequencies well below f_c the compressibility of the gas can be disregarded and the same applies for inertial effects in respect to f_i. For low frequencies, where both the inertia and compressibility effects can be ignored, the damping coefficient reduces to:

$$b_{M,N} = \sum_{m=1,3,\dots}^{M} \sum_{n=1,3,\dots}^{N} \frac{1}{Q_{pr} G_{m,n}} \tag{4.14}$$

4.2.5. Damping in parallel-plates with channels

The introduction of channels in the parallel-plates creates regions where the relative pressure approaches zero. Assuming the channels, equally distributed, are appropriately designed and ambient pressure P is achieved at the channels location, the parallel plate with channels, with length l_0 and width w_0, can be regarded as a sum of smaller parallel plates with width w_0 and length $l_c=(l_0-N_c \times L_A)/(N_c+1)$, where N_c is the number of channels. Elongations are in this case included also on the plate length, using the approximation for nonsymmetrical outlets and $K_n < 0.1$ [4.13]:

$$l_c = \frac{l_0 - N_c L_A}{N_c + 1} + 1.3\left(1 + 3.3\sigma_p K_n\right)d \tag{4.15}$$

For low frequencies where the inertia and compressibility effects can be ignored, the damping coefficient of the parallel plate with channels can be approximated by:

$$b_{c_{M,N}} = \sum_{m=1,3,\ldots}^{M} \sum_{n=1,3,\ldots}^{N} \frac{1}{(1+6\sigma_p K_n) G_{c_{m,n}}} \times (N_c + 1)$$
$$G_{c_{m,n}} = \frac{\pi^6 d^3 (mn)^2}{768 \eta w l_c} \left(\frac{m^2}{w^2} + \frac{n^2}{l_c{}^2} \right) \qquad (4.16)$$

Inertial and compressibility effects can also be included in the damping force expression, using the relative flow rate coefficient presented in equation (4.12) and the compressibility coefficient recalculated with the new length l_c:

$$F_{b\,M,N} = \sum_{m=1,3,\ldots}^{M} \sum_{n=1,3,\ldots}^{N} \frac{-v}{Q_{pr} G_{c_{m,n}} + j\omega C_{c_{m,n}}} \times (N_c + 1)$$
$$C_{c_{m,n}} = \frac{\pi^4 d (mn)^2}{64 w l_c P} \qquad (4.17)$$

4.3. Fabricated devices damper analysis

The MEMS structures used in this work to experimentally validate the proposed damping reduction geometry were S1 and S2; its main characteristics have been already presented in Chapter 3 (Figure 4.6). The inertial proof-masses can move up to 2 µm to each lateral direction, which yields gaps ranging from 0.25 µm to 4.25 µm. The main difference between the two structures is the squeeze-film damper design – with and without flow channels. The structures have a different number of comb fingers (parallel-plates are doubled in S2 as compared to S1), which does not impair direct comparison since damping in conventional parallel-plates is proportional to the number of comb fingers. The main structures parameters and dimensions are presented in Tables 3.1 and 3.2.

a)

b)

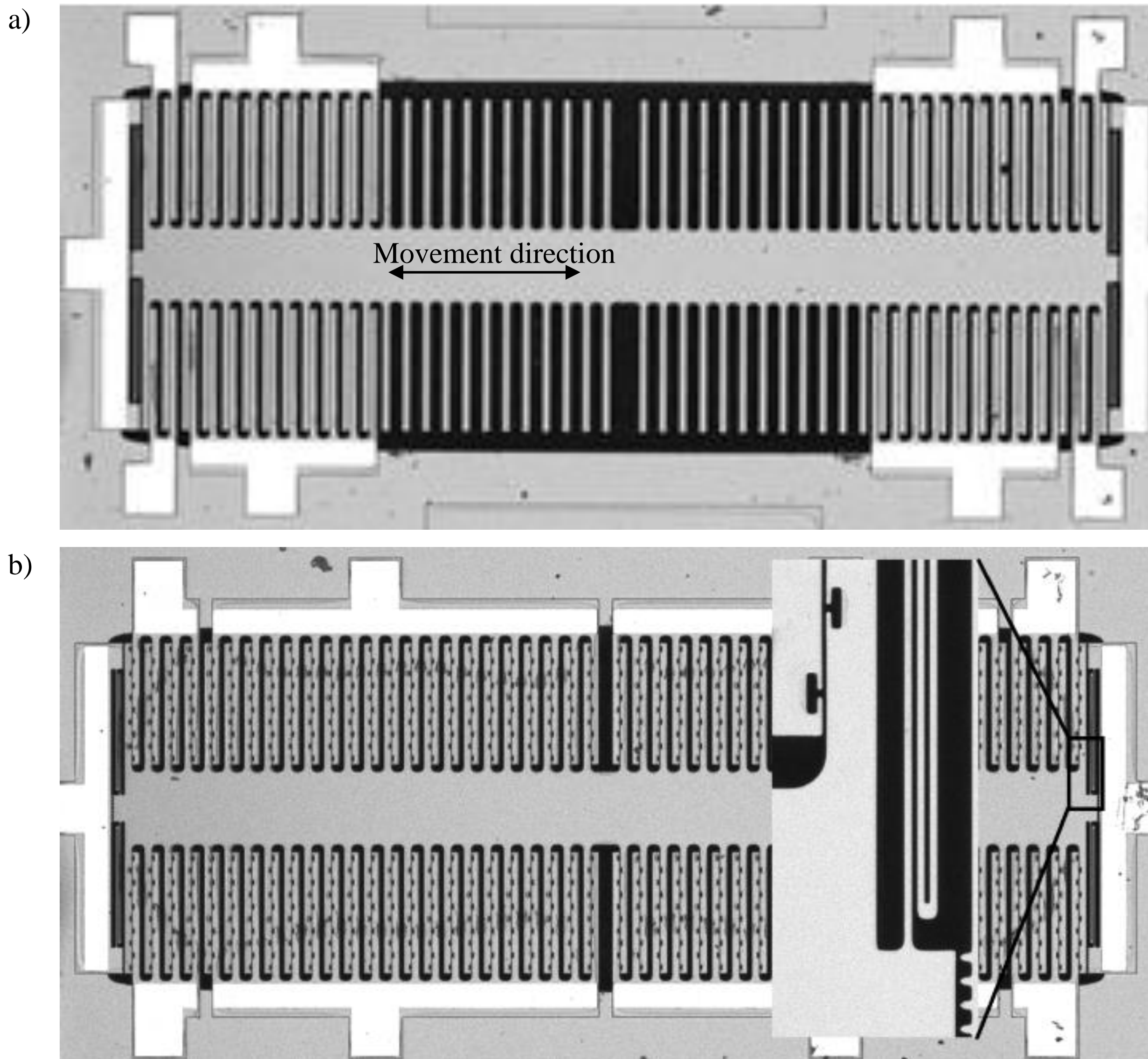

Figure 4.6: Microscope pictures of the fabricated structures (a) S1 and (b) S2 with detail showing air channels, folded spring and stoppers.

As the possible gap values range from 0.25 µm to 4.25 µm, the flow in these gaps corresponds to Knudsen numbers between 0.276 and 0.0162 respectively (Figure 4.7), positioning the gas flow in the slip regime ($0.001 \leq K_n \leq 0.1$) and in the transitional region ($0.1 \leq K_n \leq 10$). At zero displacement position (2.25 µm gap) the Knudsen number is 0.0307, and at the critical pull-in deflection (1.5 µm gap) is 0.046.

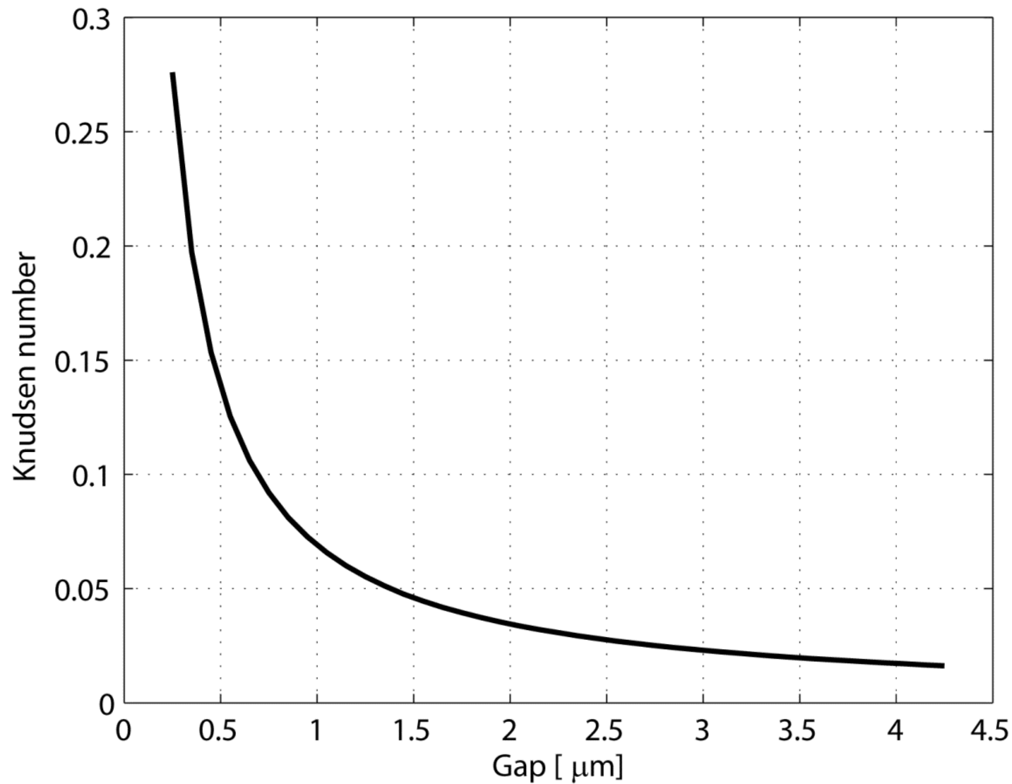

Figure 4.7: Knudsen number as a function of gap for the geometry of S1.

4.4. CFD modeling

Both analytical models and CFD (Computational Fluid Dynamics) models are extensively used to study the damping effect in MEMS [4.5], [4.10], [4.13]. There are several analytic models available in the literature, including models addressing both rarefaction and border effects that can describe reasonably well the damping effect. The analytic models are particularly useful to understand the underlying fundamentals of the damping mechanisms and are good indicators, to a first approximation, of the damping effects. CFD however provides more realistic and precise values at the expense of extra computational costs.

CFD models have been implemented for both S1 and S2 geometries and several different gaps, and results have been compared with experimental and analytical models.

A structured mesh was used. Figure 4.8a presents the schematic of the damper, highlighting the volume of air considered in the 3D model used in CFD simulations (very coarse mesh version shown in Figure 4.8b). The model dimensions are the same as the fabricated structures. The damping contribution of the movement of the air within the larger gap (20 μm), is negligible in comparison with the forces originated by the movement of the air within the smaller

2.25 μm gap, but this configuration was chosen as it represents one parallel-plate set, that is repeated 48 and 96 times in the fabricated S1 and S2 structures respectively.

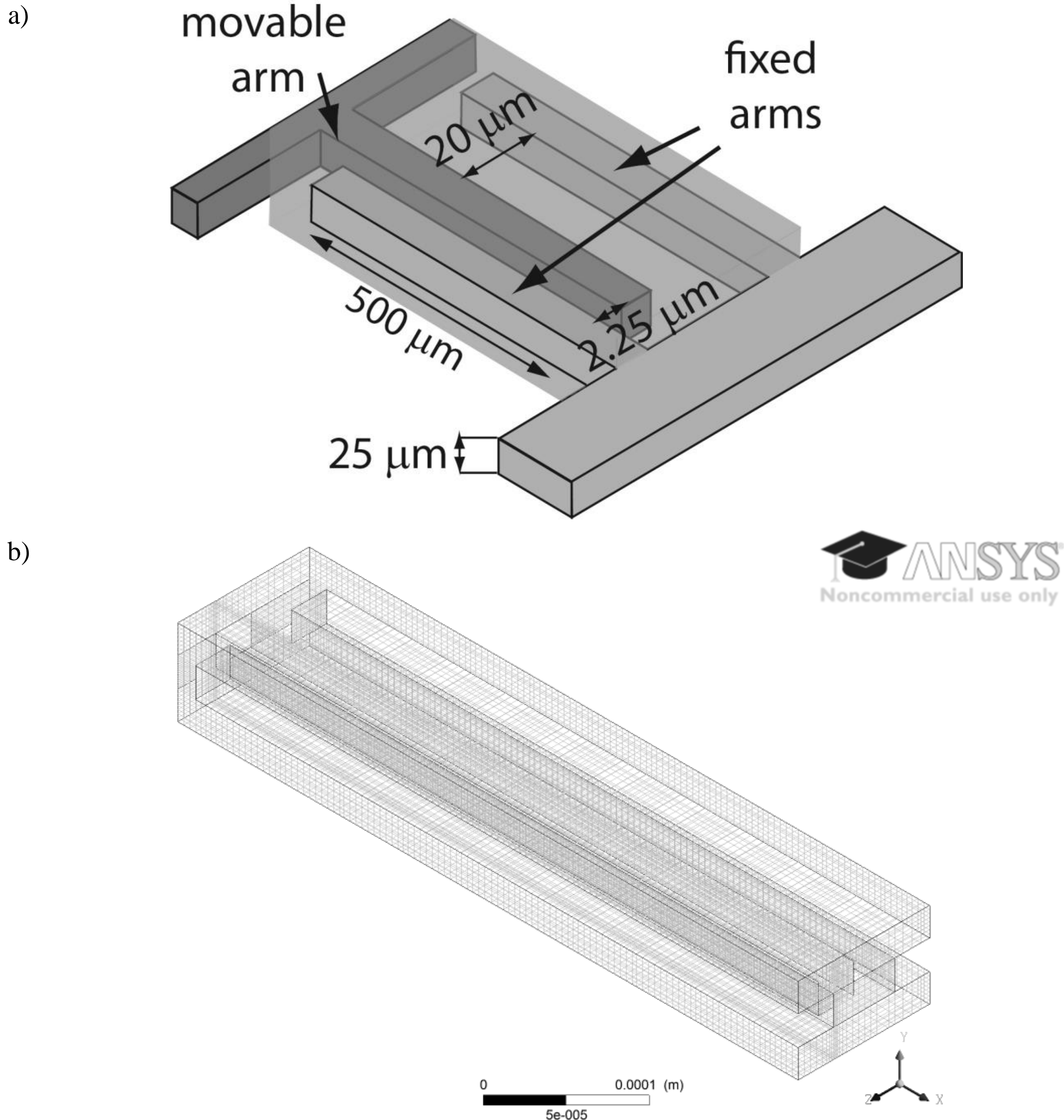

Figure 4.8: a) Schematic of the damper highlighting the volume of air modeled by CFD and b) 3D CFD meshed model.

The model in Figure 4.8b includes three types of boundary conditions. The fixed arms have zero velocity (wall), the moving arm has defined displacement (moving wall) and the remaining areas have zero relative pressure applied (opening) where gas can freely flow in and out.

Rarefaction effects have been included by defining wall velocity different from zero, thus considering slip-flow boundary conditions [4.18] at the electrodes walls. Considering isothermal conditions, the gas velocity at the wall can be found to be [4.18]–[4.20]:

$$v_{slip} = \frac{2 - TMAC}{TMAC} \lambda \left(\frac{\partial v_{gas}}{\partial n} \right)_{wall} \tag{4.18}$$

where v_{gas} is the gas streamwise velocity and n is the direction normal to the wall. The tangential momentum accommodation coefficient, *TMAC*, relates the amount of streamwise tangential momentum which is transferred to the wall upon collision; it is a physical characteristic based on surface and gas properties.

The Stokes boundary layer thickness [4.21], i.e. the distance perpendicular to the movement of the arm at which the fluid maximum velocity has been reduced to approximately 0.2 % of the arm maximum velocity, was considered in the model. The Stokes boundary layer depends on the fluid viscosity and the oscillation frequency and is defined as $\delta = 2\pi\sqrt{2\eta/\omega}$. The height of the extra air used in the 3D damper model, on top and underneath the parallel-plates, exceeds the Stokes layer and therefore zero relative pressure can be assumed at this boundary.

The models were built and meshed in ANSYS Multiphysics and then imported to ANSYS CFX, where the damping force simulations were performed. ANSYS CFX solves the unsteady Navier-Stokes equations in their conservation form and considers both compressible flow and inertia of the air [4.22]. The solver uses a conservative finite-element-based control volume method and 2nd order convection and transient schemes.

A grid density dependency study has been performed, ranging approximately from 1 to 80 elements/μm^3 at the critical regions (gap), with mesh-independent results having been achieved. Available computational capacity and simulation time tolerance were considered for the mesh selection. Several meshes were tested and a mesh was selected for which further increments in number of elements did not yield significant changes (doubling the number of elements per axis yielded a change in damping coefficient of about 3%). The simulation timesteps have also been regarded, and the initial oscillatory behavior (due to the velocity step input) being observed on the transient simulation.

4.4.1. Parallel-plates with channels – CFD

The validation of the proposed channel method for damping reduction was initially done by comparison of CFD simulation results of the improved geometry with those of the conventional parallel-plate configuration. The fabricated structures dimensions were the guidelines to build the model: 25 µm-thick layer (25 µm-high parallel-plates), arm length of 500 µm and gap within the range 0.25 µm to 4.25 µm (defined by the maximum proof-mass displacements). The geometry parameters of the cavities used in the model are coherent with the fabricated structure S2. The 3D meshed model for N_c = 10 (10 air channels) is shown in Figure 4.9 (half the model is illustrated, since a symmetry plane in the y-direction was defined). In the following set of simulations, a 1 nm harmonic oscillation at a frequency of 10 kHz is applied in the movable arm, and air at atmospheric pressure is used as the gas medium.

a)

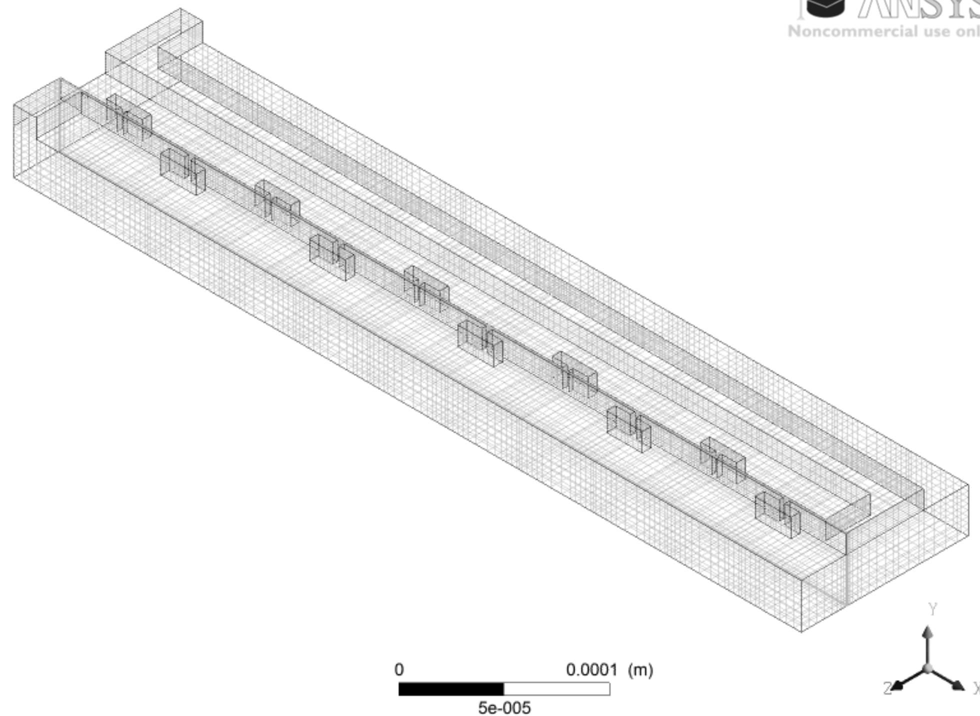

b)

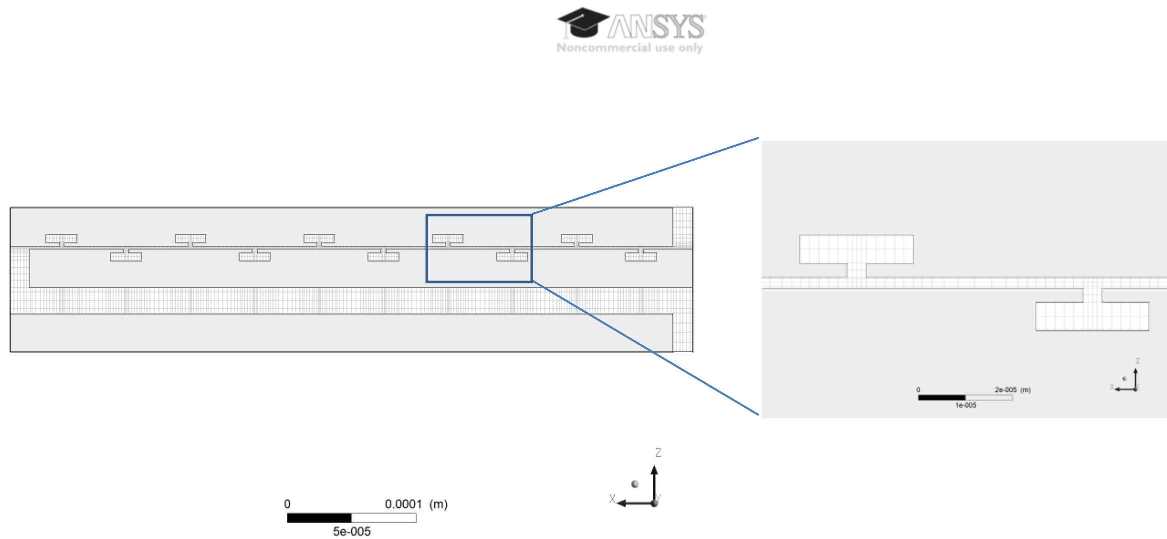

Figure 4.9: 3D CFD model with 10 air channels (channels are included both on the moving and fixed arms).

Simulation results presented in Figure 4.10 and Figure 4.11 illustrate the pressure distribution and the flow velocities on both dampers under study (with and without channels). The introduction of the channels create an alternative route for the gas to flow (Figure 4.11), leading to a much lower pressure at the locations of the channels (Figure 4.10). These smaller pressures contribute to a substantial reduction of the total damping coefficient.

a)

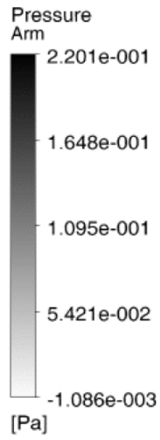

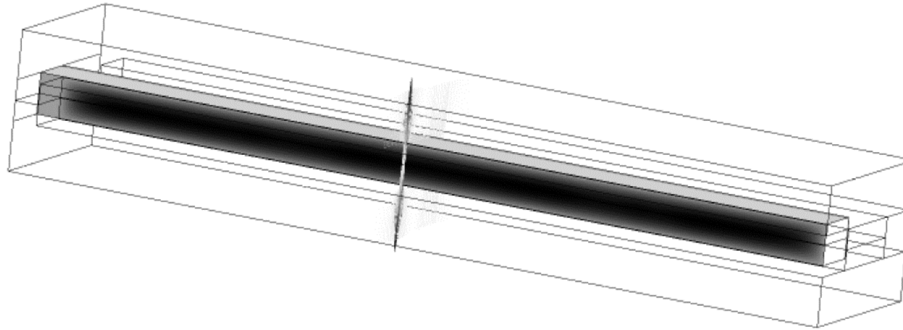

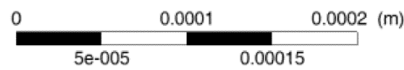

b)

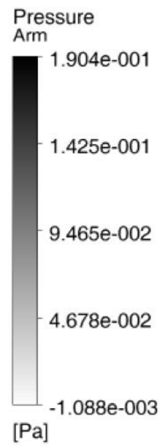

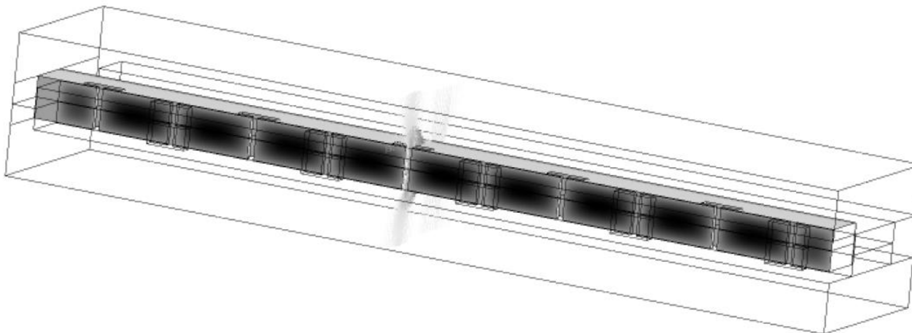

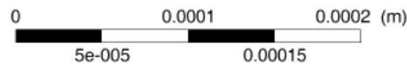

Figure 4.10: Pressure distribution on the gas medium for a) normal and b) improved geometry.

a)

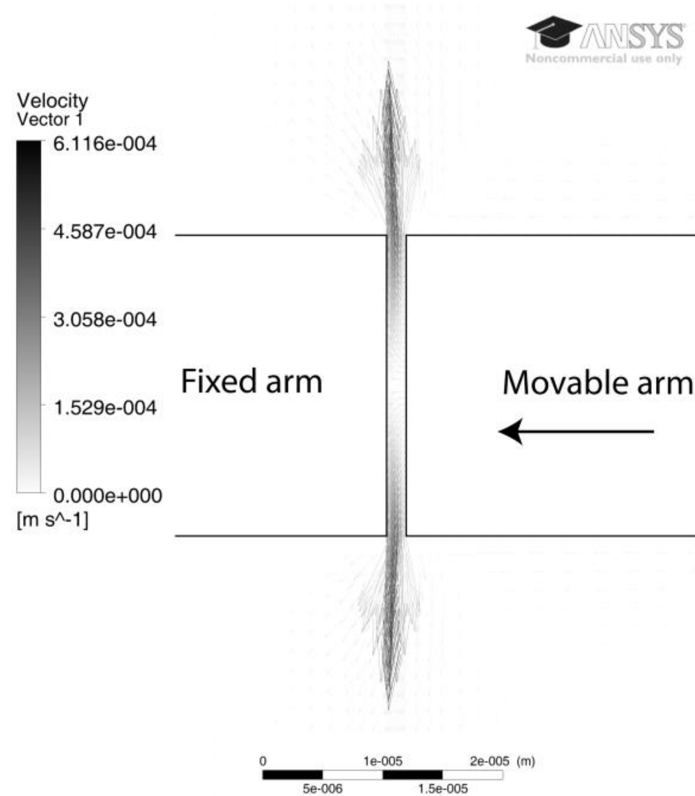

b)

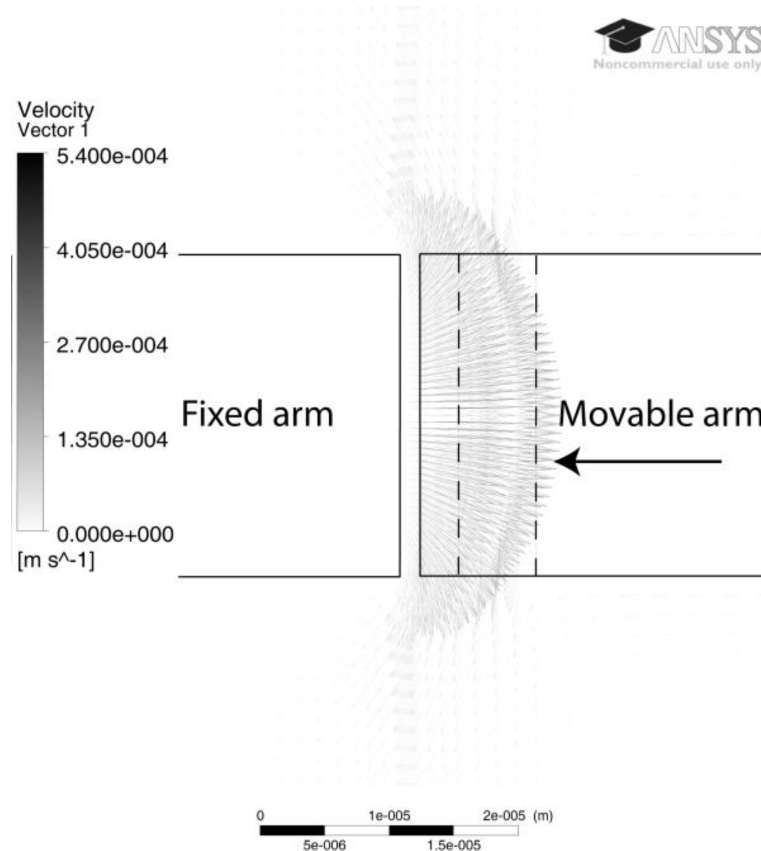

Figure 4.11: CFD modeled flow velocity profiles in cross sections (indicated in Figure 4.10) of a) conventional parallel-plates and b) parallel-plates with air channels.

Next, the model was tested for different number of air channels (ranging from 0 to 10). The damping coefficients were obtained for a 1.5 µm gap. At the simulated frequency (10 kHz), inertial and compressibility effects can be neglected. The damping coefficient values were also calculated using the analytic model for the channels described in Chapter 3. In order to compute the parallel-plate capacitance, the same model geometries, as used in the CFD simulations, were used in electrostatic FEM simulations performed on ANSYS. The expected capacitance reduction was also computed analytically considering the area $w_0*(l_0-N_c*L_A)$ of the electrodes at a 1.5 µm distance and the area N_c*L_A at the distance 1.5 µm+W_A+W_B, which translates to approximately a 6% capacitance decrease for 10 channels. This is a very simplistic model for the capacitors that overestimates the reduction since it does not take into account capacitance between perpendicular areas of the channel and fringe fields. The results from these several simulations are shown in Figure 4.12.

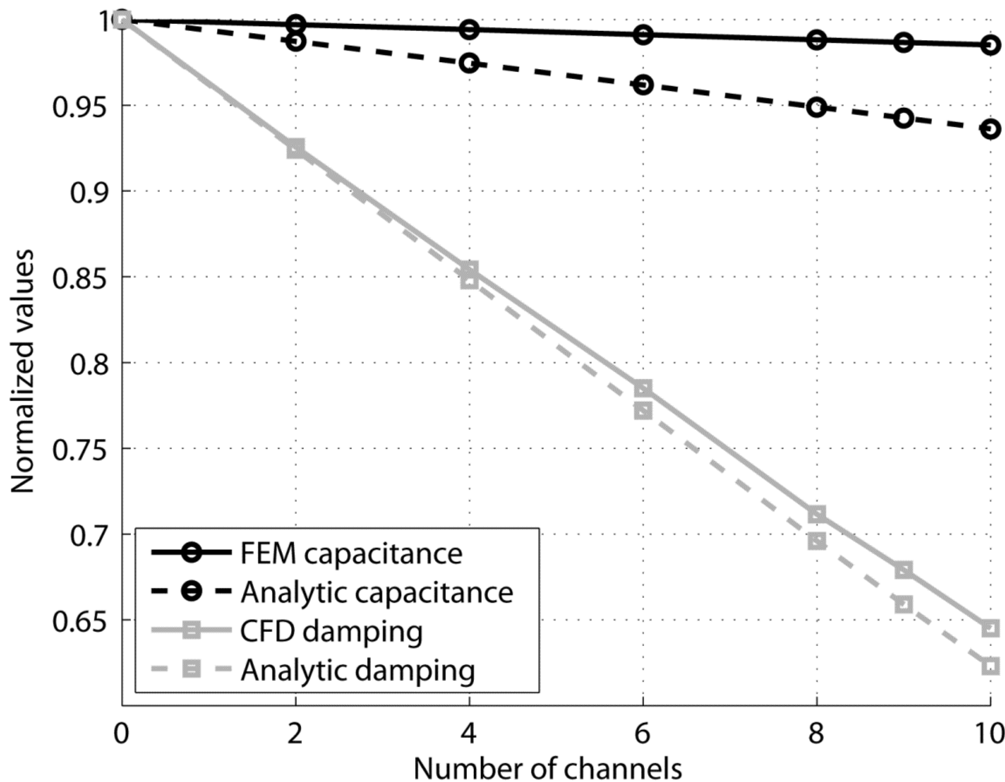

Figure 4.12: Capacitance and damping coefficient (normalized to the maximum values) changes with air channels at a 1.5 µm gap.

Initial results presented based on CFD and analytical models clearly demonstrate that the new improved geometry for parallel-plate electrodes can be effectively used to reduce the damping coefficient without changing the capacitance value. Introduction of 10 channels in the

electrodes leads to a damping coefficient reduction of about 35% while the capacitance reduction was less than 2% (CFD results).

4.5. Experimental procedure and results

The total damping force is defined as $F_b = -b\ v$ and since the damping coefficient cannot be measured directly by imposing a velocity while measuring the damping force, an alternative way to measure damping coefficient is required. When the structure is not electrostatically actuated and no other external forces act on the system, the dynamics governing the device's movement is described by a 2nd order differential equation:

$$m\frac{d^2x}{dt^2} + b\frac{dx}{dt} + kx = 0 \tag{4.19}$$

If one knows the spring constant, the mass of the movable parts, and the trajectory over time it is possible to retrieve the damping coefficient using equation (4.19). Assuming the differences between the mass of the fabricated structures and the expected values are negligible, the spring constant can be obtained by measuring the resonance frequency of the device in vacuum. The displacement of the structures over time is given by a properly calibrated capacitive readout circuit.

For the experimental validation of the damping reduction geometry, the circuit based on a charge amplifier presented in Chapter 3 was used for capacitive readout. The output was acquired with a data acquisition board (NI USB-6281) and the data was posteriorly processed and analyzed in Matlab. Initially the capacitive readout circuit was calibrated (Figure 4.13) by applying increasing acceleration values and monitoring the circuit output. A shaker was used to apply sinusoidal accelerations at a 30 Hz frequency. The acceleration was measured using sensor of the shaker. At such low frequencies the elastic component of damping can be disregarded, and the maximum displacement of the inertial mass is directly proportional to the acceleration applied to it (the readout circuit unsaturated output stops when the mass reaches the stoppers at 2 μm displacement). The resonant frequencies were also measured by placing the devices in a vacuum chamber while measuring the free oscillation frequency. The spring constants where then computed assuming that the mass is as designed, i.e., it is not significantly affected by micromachining process parameters like overetching. The measured natural frequencies of S1 and S2 were 768 Hz and 850.5 Hz respectively, which indicates spring coefficients of k_{S1}=3.71 N/m and k_{S2}=4.43 N/m.

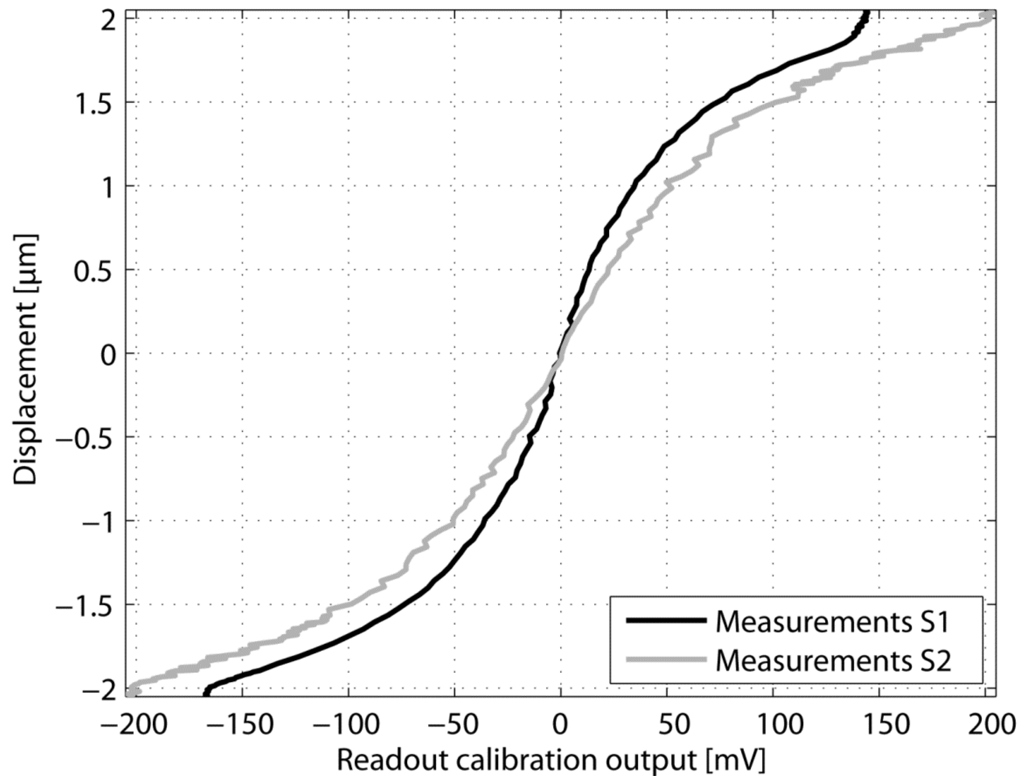

Figure 4.13: Capacitive readout circuit calibration results.

From the measured pull-in voltages of the structures S1 and S2 ($V_{PI,S1}$=5.457 V and $V_{PI,S2}$=4.290 V) the actuation capacitances can be computed (assuming a conventional electrostatic force model for the structure with channels). With these assumptions a value of $C_{A0,S1}$=0.167 pF is retrieved for S1 and $C_{A0,S2}$ =0.319 pF for S2, indicating that the inclusion of the channels decreased the capacitance value of S2 in approximately 4% ($C_{A0,S2} \approx 96\% \times 2 \times C_{A0,S1}$) only.

Afterwards, the structures were electrostatically actuated to induce full-gap displacement of the inertial mass. The applied voltage was then removed and the trajectory of the proof mass back to its rest position was monitored. Using the calibration curves, the time series of voltage measurements of the capacitive readout circuit output were translated to time series of position values (through 2nd order spline interpolation). From the time series of position measurements, the velocities at each point are calculated, as well as the accelerations. Using equation (4.19) with the initial conditions calculated from the previous positions, the damping forces are computed.

Inertial and compressibility effects were neglected in the calculation of the damping coefficient using the experimental data. To verify the validity of this assumption, the experimentally measured velocities at each position were used to calculate the oscillation frequencies for which the corresponding maximum velocities match the measured velocities

(assuming 1 nm of oscillation amplitude). These velocities were compared to the cut-off frequencies (Table 4.1) (f_c for compressibility and f_i for inertial effects) and it is noticeable that, for large gaps, the oscillating frequencies are above the inertial cut-off frequency. Hence, a new set of CFD simulations, using the calculated oscillating frequencies (amplitude of 1 nm), were performed to evaluate the contribution of the inertial effects. The results indicated a neglegible error (variation on the damping coefficient less than 3% as compared to the previous simulations at 10kHz) and therefore, inertial and compressibility effects can effectively be neglected on the damping coefficient retrieved from the measurements.

Table 4.1: Measured velocities, corresponding frequencies (for 1 nm oscillation amplitude), and cut-off frequencies, at different gaps for both structures S1 and S2.

	S1		S2			
Gap (µm)	Measured velocity (mm/s)	Equivalent frequency (kHz)	Measured velocity (mm/s)	Equivalent frequency (kHz)	f_i (kHz)	f_c (kHz)
3.75	1.302	207.3	1.909	303.8	176.9	16131
3.00	2.628	418.2	2.869	456.6	276.3	10324
2.25	2.445	389.2	1.883	299.8	491.3	5807
1.50	2.628	418.2	2.869	456.6	1105	2581
0.75	1.302	207.3	1.909	303.8	4421	645.3

The damping coefficients retrieved from the experimental measurements were compared to the expected values computed with the compact analytic models for micromechanical squeeze-film dampers described previously (equations (4.14) and (4.16)), that include inertia, compressibility, rarefaction and border effects, and the CFD simulations performed on ANSYS CFX with 1 nm oscillation at the experimental frequencies (Figure 4.14).

a)

b)

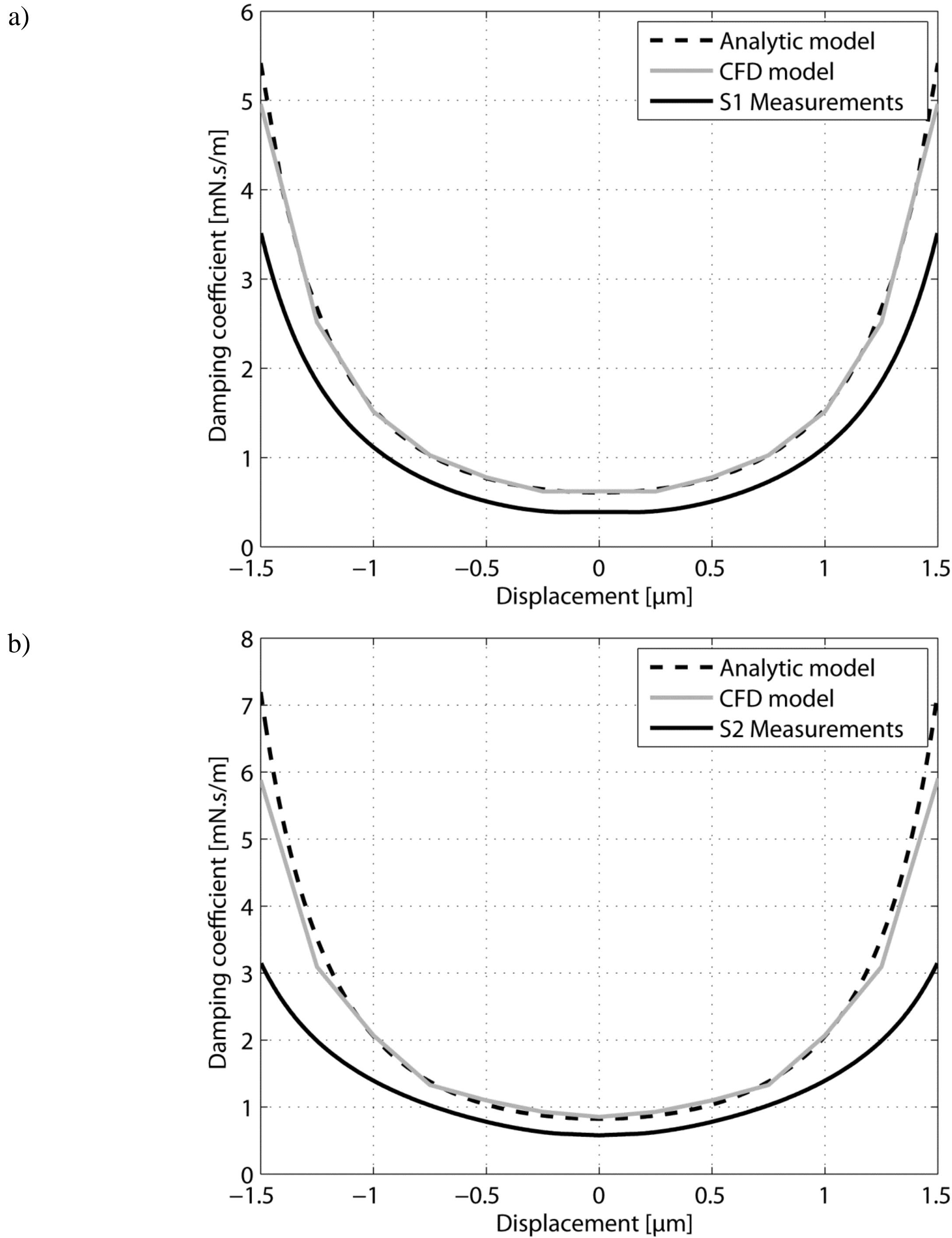

Figure 4.14: Comparison between damping coefficients obtained from experimental measurements, analytic (equations (4.14) and (4.16)) and CFD modeling for structures a) S1 and b) S2.

Displacements larger than 1.5 μm have been disregarded due to uncertainties arising from saturation of the readout circuit. Within the range of displacements plotted, K_n does not exceed 0.1, i.e. the structure operates in the slip regime.

The results presented in Figure 4.14 show that both the analytic model and CFD simulations overestimate the damping force considering layout dimensions for the models. The

structures were observed under SEM (Scanning Electron Microscope) and a vertical misalignment was detected between de movable parallel-plates of the inertial mass and the fixed parallel plates (Figure 4.15). The deflection of the inertial masses, measured by laser profilometry, describes a parabolic curve, with maximum misalignment. The maximum deflection is approximately 3.96 μm for S1 and 3.4 μm for S2 at the center of the inertial mass and almost inexistent at the parallel-plates near the anchoring springs (note that S1 does not have parallel-plates in the central area, hence the maximum plate misalignment is smaller). Hence, the cause of misalignment is not vertical deflection of the bi-folded springs, but deflection of the 4 mm long silicon proof mass. This deflection is due to intrinsic stress of the SOI active layer and surface stress caused by the doping process [4.23]. Vertical displacement translates to a decrease in the damper width (below the expected 25 μm).

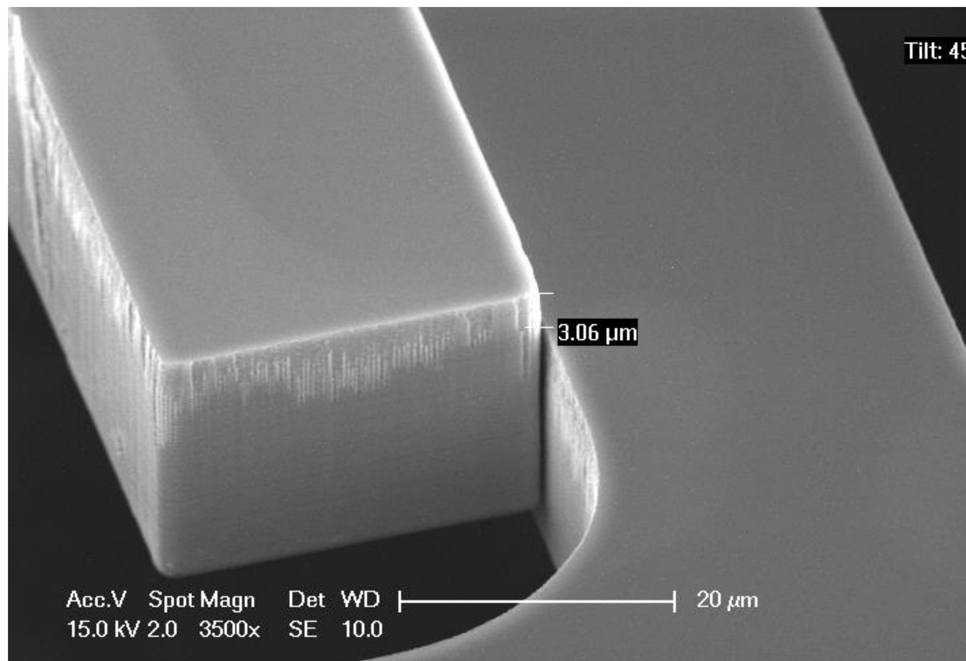

Figure 4.15: SEM picture of the structure S1, evidencing the vertical misalignment.

The vertical deflection found on the structures can justify the decrease of the measured damping coefficient in relation to the CFD expected values. In fact, if a damper height of 22 µm is introduced in the analytic model, instead of the expected 25 µm, a much better agreement is found with the experimental results, as can be observed in Figure 4.16. This fact validates the analytic modeling approach, and its use to model the fabricated structures, as long as a damper height correction is included.

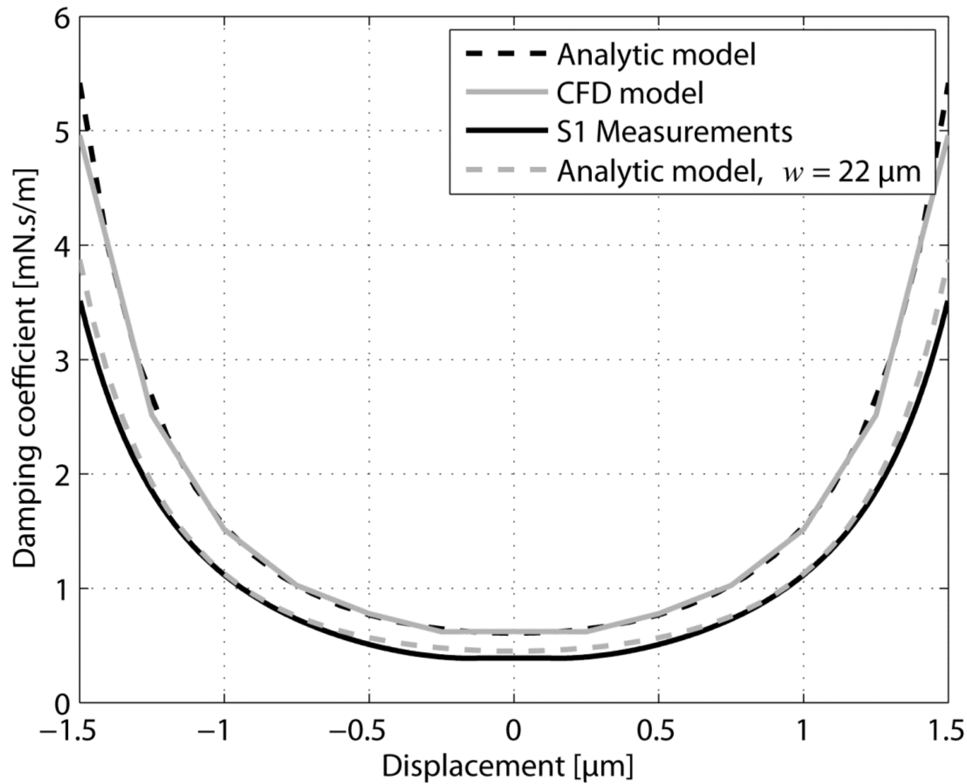

Figure 4.16: Comparison between S1 damping measurements with damping values obtained by analytic modelling with correction for deflection.

Finally, a comparison between the damping coefficients of the two structures, as a function of the displacement, was performed (Figure 4.17). Since S2 has the double of the arms of S1, and if no channels were introduced, the damping coefficient of S2 should be doubled as compared to S1. Assuming the vertical misalignment affects the damping coefficient of S1 and S2 equally, any decrease in S2 damping coefficient can be attributed to the introduction of the channels.

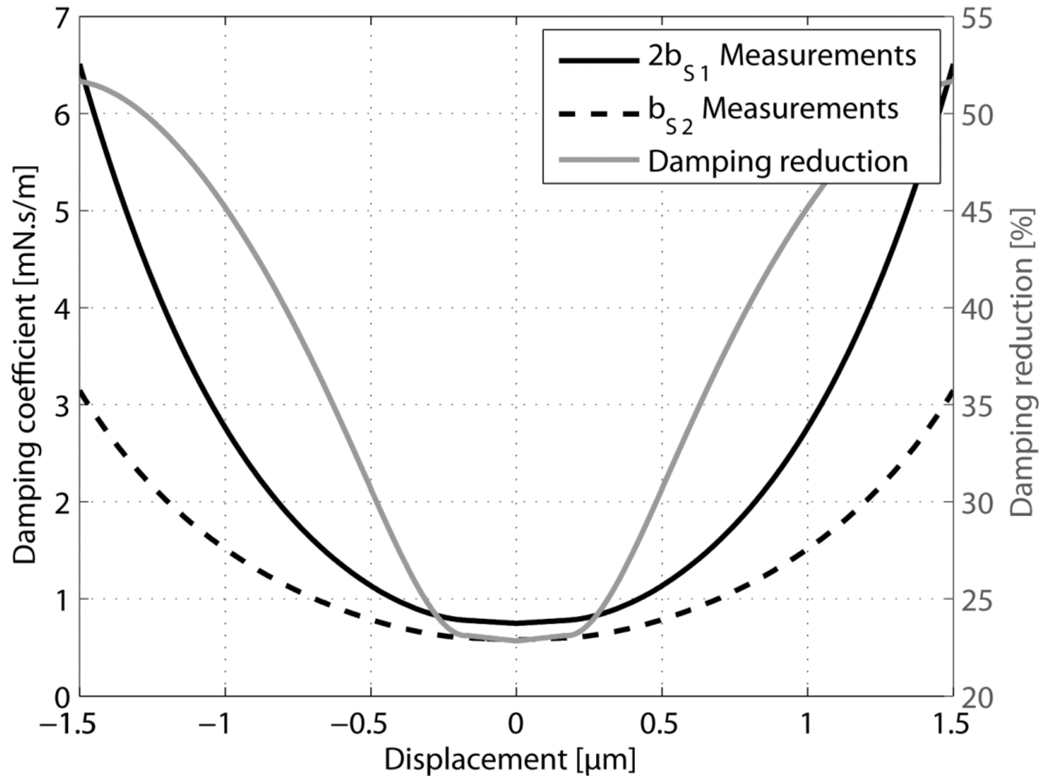

Figure 4.17: Damping coefficient results comparison, for the structures with conventional damper and with air channels.

Comparative experimental data shows an effective reduction of the damping coefficient of S2 (b_{S2}) as compared to the double of the damping coefficient of S1 ($b_{S2}<2b_{S1}$). The total damping reduction depends on the gap size and is more pronounced for smaller gaps. The mechanisms behind the damping reduction channels still need to be studied more deeply, in order to justify the improved performance of the channels for smaller gaps.

When a global comparison between structures S2 and S1 is performed, there is a capacitance gain on the actuation electrodes from 0.167 pF to 0.319 pF (similarly gain on the sensing capacitance from 0.939 pF to 1.814 pF at zero-displacement can be assumed), which represents approximately a 96% capacitance gain. The gain in capacitance is useful to achieve higher readout performance. This almost doubled capacitance brought no additional increase in the damping coefficient of S2 for large displacements (smaller gaps), and an increase in damping coefficient of about 50% at zero-displacement. These results validate experimentally that the flow channels method is a suitable design approach to increase the capacitance/damping coefficient ratio.

The improved damper geometry studied in this chapter can be implemented in parallel-plate capacitive sensors, allowing increasing the number of parallel-plates, hence improving

capacitive detection / readout capabilities, without increasing thermal-mechanical noise (proportional to damping) in the same proportion. In the case of the pull-in time accelerometer, where damping conditions are crucial for the device's behavior and performance (namely sensitivity and noise), this solution can be particularly useful as it makes the damping coefficient design less dependent on the capacitance design, allowing optimization of both characteristics more independently.

4.6. Channels geometry parameters – preliminary assessment

Although the first results of the new parallel-plate geometry prove the reduction mechanism concept, more insight is needed to properly understand the influence of the channels dimensions on the total damping reduction. Some preliminary CFD simulations were performed for several sizes of L_A, W_A, L_B and W_B, using a thickness of 25 μm and a capacitor gap of 1.5 μm. The goal was to evaluate how each individual parameter affects the damping coefficient when is changed between five levels: L_A=[1, 2, 3, 4, 5] μm, W_A=[1, 2, 3, 4, 5] μm, L_B=[2, 6, 10, 14, 18] μm and W_B=[2, 4, 6, 8, 10] μm. Since a total of 625 simulations would be required, the Taguchi method was adopted to reduce the number of simulations [4.24]. This method does not however provide any insights on the interactions between parameter.

According to the Taguchi method, evaluation of four parameters with five levels each requires 25 simulations. The damping force results for the 25 simulations performed are presented in Table 4.2. For this set of simulations, a 3D model with one single channel within a 100 μm long arm was implemented. The Taguchi analysis results are presented in Table 4.3.

Table 4.2: Channel parameters (in μm) and results of the 25 simulations performed.

Simulation	L_A	W_A	L_B	W_B	Force (N)	Simulation	L_A	W_A	L_B	W_B	Force (N)
1	1	1	2	2	3.87E-10	13	3	3	18	4	3.52E-10
2	1	2	6	4	3.87E-10	14	3	4	2	6	3.53E-10
3	1	3	10	6	3.92E-10	15	3	5	6	8	3.52E-10
4	1	4	14	8	3.95E-10	16	4	1	14	4	3.43E-10
5	1	5	18	10	3.98E-10	17	4	2	18	6	3.43E-10
6	2	1	6	6	3.57E-10	18	4	3	2	8	3.43E-10
7	2	2	10	8	3.61E-10	19	4	4	6	10	3.43E-10
8	2	3	14	10	3.64E-10	20	4	5	10	2	3.48E-10
9	2	4	18	2	3.71E-10	21	5	1	18	8	3.37E-10
10	2	5	2	4	3.70E-10	22	5	2	2	10	3.36E-10
11	3	1	10	10	3.47E-10	23	5	3	6	2	3.43E-10
12	3	2	14	2	3.56E-10	24	5	4	10	4	3.39E-10
						25	5	5	14	6	3.38E-10

Table 4.3: Rank results according to the Taguchi analysis.

Level	L_A	W_A	L_B	W_B
1	188.14	189.03	188.94	188.86
2	188.76	188.97	188.97	188.93
3	189.07	188.91	188.95	188.97
4	189.27	188.89	188.90	188.95
5	189.41	188.86	188.89	188.95
Range	1.27	0.17	0.09	0.11
Rank	1	2	4	3

The Taguchi analysis indicates that for the ranges studied, all four dimensions should be maximized to decrease damping, and that the L_A dimension is clearly the most important (in agreement with the expected). Nevertheless, further studies are required to evaluate the relation between the parameters in order to achieve an optimum design.

4.7. Pull-in accelerometer damper considerations

In the following chapters, the structure S0 is used for implementation of the accelerometer operated in open-loop and closed-loop, and also for the viscosity measurement study. Since this structure's main goal was the proof-of-concept of the time-based accelerometer, for sake of simplicity, the damping-reducing geometry was not implemented in S0. Nevertheless, it is worth noting that the pull-in accelerometer studied on this thesis requires a certain level of damping and that the damping-reduction mechanism can be an important tool to obtain high capacitance changes and low pull-in voltages without an increase in the mechanical-thermal noise.

The desirable damping level range is related, on one hand, to the sensitivity / Brownian noise trade-off, and on the other, to the step voltage (α in $V_{step}= \alpha V_{PI}$) required to achieve sufficient pull-in travel time. Figure 4.18 illustrates the noise and sensitivity variation in an open-loop operated pull-in accelerometer for different quality factors ($Q = \frac{\sqrt{km}}{b}$). The sensitivity/noise compromise becomes obvious when observing Figure 4.18 while keeping in mind that the goal is to maximize sensitivity while minimizing noise. In Chapter 2 it was also concluded that for higher quality factors a lower α (in $V_{step} = \alpha V_{PI}$) is necessary in order for the metastability to be observed, which requires more control over the actuation voltage source. In these conditions, actuation voltage noise/sensitivity gains increasing importance, so this situation is undesirable. Finally, increasing damping while maintaining all other parameters constant, also increases response time. In conclusion, the trade-offs required for an optimum damping value are not trivial.

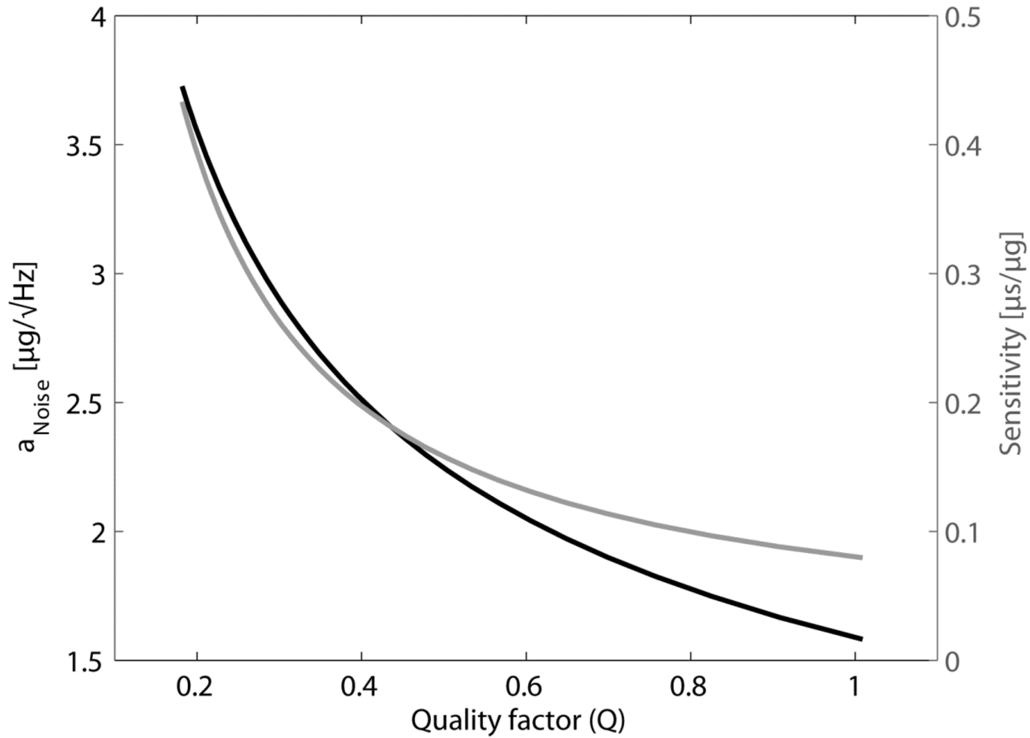

Figure 4.18: Variation of the brownian noise and the sensitivity with the quality factor of a pull-in accelerometer.

4.8. Conclusions

In this chapter, the damper modeling approach used in this thesis has been described. The damping mechanism considered is squeeze-film damping, and both analytical models and FEM/CFD simulations were used to evaluate its effect.

The analytic model used is derived from the linearized Reynolds equation and its solution for small parallel-plates displacements. It consists of a simplified damping model with a high degree of accuracy along the full film extension. Border effects are accounted for in the squeeze-film damping model, by using modified surface elongations.

A new geometry for parallel-plates MEMS has been introduced and studied. This geometry, suitable for in-plane devices, is based on the placement of channels in the electrodes wall and aims to increase the capacitance/damping ratio, thus addressing an existing conflict when designing parallel-plates devices. The microstructures used to experimentally validate the novel approach, with both conventional and improved parallel-plate geometries, presented an unwanted out-of-plane deflection which, while not compromising the damping measurement, impaired to some extent the correlation with the expected values from the analytic and CFD models. Still, both CFD simulations and the experimental results validate the air channel

geometry for capacitive parallel-plates as a method to decrease damping. Moreover, the analytic damping model results are satisfactorily in agreement with the experimental damping measurement results if a corrected damper height (accounting device deflection) is used instead of the full 25 μm wafer thickness.

The air channels geometry can improve current limitations of conventional parallel-plates design, by increasing the achievable capacitance/damping ratio. The damper geometry with air channels proved effective not only on reducing damping, but also showed no significant reduction of the actuation and sensing capacitance values. The experimental data shows a 25 to 50% reduction for the damping coefficient on structures with 10 air channels on 500 μm long dampers. By introducing air channels, the capacitance was reduced approximately 4% (in comparison to the expectable without air channels). In addition, a simple analytical model to predict the reduction of the damping with the incorporation of the channels was derived and compares well with the CFD model.

The results obtained validate the approach and open the door for further improvements on inertial sensor design and others. The proposed geometry can be particularly useful in the design of capacitive inertial sensors, since it allows improving current devices with extra sensitivity and better noise performance.

In many SOI processes (for instance MEMSOI [4.25]), a substrate is present below the movable parts of the microstructures, unlike in the SOIMUMPs process where the full thickness of the handle wafer is etched from the backside. Since the distance to the substrate is defined by the thickness of the buried oxide layer, that is usually very small (2 μm in the case of MEMSOI), it contributes significantly with additional damping. Inclusion of the channels in this case can be very advantageous, since it provides additional paths for the gas flow from/to the damper. The preliminary study on the geometry of the air channels revealed that the air channel width (L_A) is the most important parameter and its value must be properly chosen for effective damping reduction. However, additional tests are needed to investigate more deeply how the channels dimensions affect damping.

Since the analytic damping model is in agreement with the experimental results, if a corrected damper height is used, the damping model described in this chapter is adopted for modeling also the structure S0 used for the experimental work featured in the following chapters of this thesis. This analytic model is included in the Simulink model used for the dynamic pull-in behavior simulations that the following experimental results are compared to.

References

[4.1] N. Yazdi, F. Ayazi, and K. Najafi, “Micromachined inertial sensors,” *Proceedings of the IEEE*, vol. 86, no. 8, pp. 1640–1659, 1998.

[4.2] L. A. Rocha, E. Cretu, and R. F. Wolffenbuttel, “Measuring and interpreting the mechanical–thermal noise spectrum in a MEMS,” *Journal of Micromechanics and Microengineering*, vol. 15, no. 7, pp. S30–S38, Jul. 2005.

[4.3] M. Bao and H. Yang, “Squeeze film air damping in MEMS,” *Sensors and Actuators A: Physical*, vol. 136, no. 1, pp. 3–27, May 2007.

[4.4] T. Veijola, “Analytic damping model for an MEM perforation cell,” *Microfluidics and Nanofluidics*, vol. 2, no. 3, pp. 249–260, Dec. 2006.

[4.5] S. S. Mohite, V. R. Sonti, and R. Pratap, “A compact squeeze-film model includinginertia, compressibility, and rarefaction effects for perforated 3-D MEMS structures,” *Journal of Microelectromechanical Systems*, vol. 17, no. 3, pp. 709–723, Jun. 2008.

[4.6] S. D. Senturia, *Microsystem Design*. Dordrecht: Kluwer Academic Publishers, 2001.

[4.7] T. B. Gabrielson, “Mechanical-thermal noise in micromachined acoustic and vibration sensors,” *IEEE Transactions on Electron Devices*, vol. 40, no. 5, pp. 903–909, May 1993.

[4.8] J. J. Blech, “On isothermal squeeze films,” *Journal of Lubrication Technology*, vol. 105, no. 4, pp. 615–620, 1983.

[4.9] W. A. Gross, *Fluid Film Lubrication*. John Wiley & Sons Inc, 1980.

[4.10] T. Veijola, H. Kuisma, J. Lahdenpera, and T. Ryhanen, “Equivalent-circuit model of the squeezed gas film in a silicon accelerometer,” *Sensors and Actuators A: Physical*, vol. 48, pp. 239–248, 1995.

[4.11] S. Fukui and R. Kaneko, “Analysis of ultra-thin gas film lubrification based on linearized boltzmann equation: First report - Derivation of a generalized lubrication equation including thermal creep flow,” *Journal of Tribolology*, vol. 110, pp. 253–262, 1988.

[4.12] S. Fukui and R. Kaneko, “Database for interpolation of poiseuille flow rates for high Knudsen number lubrication problems,” *Journal of Tribolology*, vol. 112, pp. 78–83, 1990.

[4.13] T. Veijola, a Pursula, and P. Råback, “Extending the validity of squeezed-film damper models with elongations of surface dimensions,” *Journal of Micromechanics and Microengineering*, vol. 15, no. 9, pp. 1624–1636, Sep. 2005.

[4.14] T. Veijola, “Compact models for squeezed-film dampers with inertial and rarefied gas effects,” *Journal of Micromechanics and Microengineering*, vol. 14, no. 7, pp. 1109–1118, Jul. 2004.

[4.15] V. Lindroos, M. Tilli, A. Lehto, and T. Motooka, *Handbook of Silicon Based MEMS Materials and Technologies*. William Andrew, 2010.

[4.16] F. Sharipov and V. Seleznev, "Data on internal rarefied gas flows," *J. Phys. Chem. Ref. Data*, vol. 27, pp. 657–706, 1998.

[4.17] T. Veijola, "Simple but accurate models for squeeze-film dampers," *EEE Sensors*, vol. 4, no. 4, pp. 83–86, 2007.

[4.18] F. La Torre, "Gas flow in miniaturized nozzles for micro-thrusters," Delft University of Technology, 2011.

[4.19] J. Maxwell, "On stresses in rarefied gases arising from inequalities of temperature," *Philosofical Transactions of the Royal Society of London*, vol. 170, pp. 231–256, 1878.

[4.20] W. Steckelmacher, "Knudsen flow 75 years on: the current state of the art for flow of rarefied gases in tubes and systems," *Reports on Progress in Physics*, vol. 49, no. 10, pp. 1083–1107, Oct. 1986.

[4.21] C. Pozrikidis, *Introduction to Theoretical and Computational Fluid Dynamics*, vol. 2011. Oxford University Press, 2011.

[4.22] ANSYS Inc., "ANSYS CFX-Solver Theory Guide," in *ANSYS CFX*, 12th ed., 2009.

[4.23] A. Cowen, G. Hames, D. Monk, S. Wilcenski, and B. Hardy, *SOIMUMPs Design Handbook*, 8.0 ed. MEMSCAP Inc., 2011, pp. 0–25.

[4.24] R. K. Roy, *A primer on the taguchi method*, 2nd ed. Michigan: Society of manufacturing engineers, 2010.

[4.25] J. Collet, *MEMSOI Design Rules Manual*, 1.2 ed. Tronics Microsystems, 2007.

5.

Open-loop accelerometer operation and characterization

A promising approach for the realization of μg-resolution accelerometer, introduced in [5.1], uses the pull-in time measurement of microfabricated structures as the detection mechanism. Basically, repeatedly bringing the microstructure to pull-in (actuating with a voltage step $V_{step} = \alpha V_{PI}$, $\alpha > 1$) while measuring the pull-in time, enables the measurement of external accelerations. The non-mechanical noise is set primarily by the resolution of the time measurement (which can be made very high, up to few nanoseconds), and therefore, the main noise source is the mechanical-thermal noise. This low-noise feature is a key advantage of this approach, as well as the low requirements for the capacitive sensing circuit [5.2]. Moreover, micromachined structures to implement this accelerometer concept can be fabricated using standard commercially available fabrication processes. The main disadvantages are the increase in the system complexity, as compared to other open-loop operated accelerometers that use direct capacitance/acceleration transduction, and the low system bandwidth and dynamic range.

A very important characteristic on the performance of a pull-in-based accelerometer is the damping. Squeeze-film damping forces dominate the dynamic pull-in behavior of capacitive parallel-plates MEMS devices [5.3], [5.4] and are setting the total mechanical-thermal noise.

Noise is a very important factor to consider in accelerometers, and it must be kept as low as possible in order to achieve a high signal-to-noise ratio. In a typical sensor using a mechanical system, electronic circuits are used for readout and processing of the electrical signal provided by the sensing element [5.5]. The uncertainty (usually total noise level) of the measurement is therefore due to the combined effect of the mechanical-thermal noise in the mechanical domain [5.6], the electrical noise of the (resistive) mechanical sensing element and the input referred noise of the readout circuits.

The pull-in dynamic transition, which is the basis of the operation principle, the fabricated MEMS structures, and the damper design have been described in the previous chapters. In this chapter, the pull-in time open-loop operation is described and the dynamic behavior is simulated taking in consideration the characteristics of structure S0. Since noise is a key feature in this approach, a study of the noise sources affecting the system is performed. Fabricated microstructures (S0) are then characterized and used for the implementation of the time-based µg-accelerometer, enabling the evaluation of both the pull-in time accelerometer concept and the analytic models. This accelerometer was designed for high resolution measurement with low bandwidth. Therefore, the accelerometer was tested for small accelerations (up to a few mg), applied in DC and AC mode (1 Hz). The experimental results are presented and compared against simulations from the analytical models. Since a noise level much higher than expected was observed in the measurements, an additional experiment was conducted to investigate the possibility of this noise having origin in the actuation voltage. The study of the noise sources affecting the system and the results support the low noise characteristics of the pull-in time approach.

5.1. Open-loop operation description

The underlying physical principle for the transduction approach is the high sensitivity of the pull-in time to external forces in electrostatically operated micromechanical devices [5.1]. A detailed study of the pull-in dynamic transition [5.2] has been presented in Chapter 2 and the existence of a metastable region during a pull-in transition has been demonstrated in overdamped micromechanical devices. A very important feature of the meta-stability and associated pull-in time is its high sensitivity to external forces. In fact, the presence of very small forces can change the overall pull-in time and this characteristic has already been used in [5.4] to measure and characterize the mechanical-thermal noise in MEMS devices.

Using the pull-in time as the sensing mechanism requires for the implementation of functionalities in the mechanical domain, rather than conventional direct transduction, and signal processing in the electrical domain. The time measurement can be performed with a very high resolution by simply using a fast clock: for instance if a 100 MHz frequency is used, the resolution of the time measurement will be 10 ns. Since the non-mechanical noise is set primarily by the resolution of the time measurement, there is a huge potential for the realization of high sensitivity, low-noise accelerometers.

A block diagram of the proposed time-based accelerometer is shown in Figure 5.1. The core of the microsystem is a parallel-plate microstructure with separate sensing and actuation electrodes. The microdevice is actuated by a square wave generator. The actuation voltage must be applied for a long enough period of time in order to guarantee the measurement of the full pull-in transition time (the time taken by the device to travel from the rest position to a position beyond critical pull-in displacement).

The capacitive changes of the microdevice are converted to a voltage by the front-end readout circuit. Since the changes in capacitance are quite large (considering nearly full gap displacements), the capacitive readout specifications are low in terms of resolution and noise, which is a competitive advantage to the conventional direct transduction and signal processing in the electrical domain approach.

Following the capacitive transduction, the signal is fed to a comparator, and as soon as a known threshold is reached (nearly full gap), the time counting mechanism is stopped and ground is applied to prevent the movable electrode to reach the counter-electrode (or the physical stoppers). Using this preventive measure, the movable electrode returns to its rest position increasing the system's reliability (the movable structure does not reach the counter-electrodes or protective stoppers).

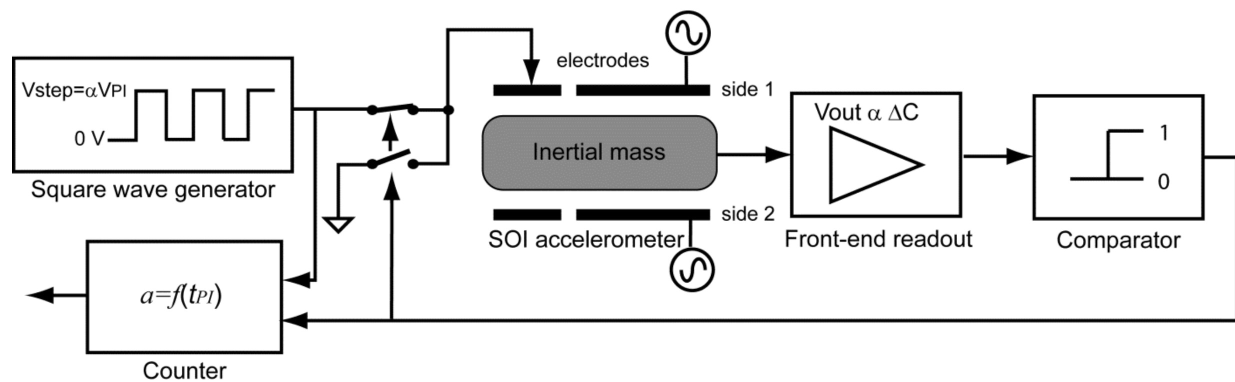

Figure 5.1: Microaccelerometer block diagram.

Finally, a time counting mechanism is used to measure the pull-in time, counting the time elapsed from rising edge of square wave to rising edge of comparator output. If acceleration is present in the direction of the mass movement, pull-in will be faster and, likewise, if the acceleration opposes the pull-in movement, the pull-in time will be longer. The pull-in time changes in respect to the nominal (at 0 g) pull-in time are proportional to the external acceleration sensed by the accelerometer.

Other methods, rather than capacitive, have been reported in literature for pull-in detection. In [5.7], [5.8], piezoresistive elements placed in flexible stoppers are used to detect when contact occurs while in [5.9] hard electrical contacts are used in the stoppers. Although capacitive detection is a more complex approach than the two other methods, the shock between the proof mass and the stoppers can be avoided in this case, increasing system's reliability.

Operation of the microstructure in the meta-stable region raises some design constraints. Since the micromechanical structure should be sufficiently damped (to present the meta-stable behavior) and the mechanical-thermal noise depends on the damping coefficient, the damping conditions are critical. Therefore, design of the damper is very important as it will define the main characteristics of the accelerometer, namely sensitivity and noise [5.4], [5.10]. The design constraints are discussed next.

5.2. Microstructure design and dynamic behavior simulation

For the implementation of the pull-in time accelerometer the fabricated microstructure S0 has been used. The microstructure geometry design has been carried out simultaneously with its dynamic behavior simulation, in order to achieve the desired characteristics for the sensor. In other words, the structure dimensions have been defined aiming to obtain the desired device behavior.

The main structure parameters that must be defined for the microstructure design are the movable parts size (that defines the proof-mass), spring dimensions (that define the stiffness coefficient) and gap, length and number of parallel-plates (which will define damping and capacitances). Concerning the pull-in time accelerometer design and considering these changeable parameters, six general goals can be outlined:

1. Maximizing pull-in time sensitivity to external acceleration:

   a. Maximizing damping (lower quality factor) in order to obtain large metastable region when pulling-in, for high sensitivity (achived by adding/increasing parallel-plates and decreasing gap);
2. Minimizing thermal-mechanical noise:
   a. Maximizing the proof-mass in order to reduce the Brownian noise;
   b. Minimizing damping since Brownian noise increases with damping (removing/decreasing parallel-plates and increasing gap);
3. Maximizing readout capabilities:
   a. Maximizing sensing capacitances to achieve large variations when pulling-in and enable straightforward readout (adding/increasing parallel-plates and decreasing gap);
   b. Minimize parasitic capacitances (increasing the spacing between different capacitances);
4. Minimizing voltage requirements for actuation (for compatibility with low power interfaces and digital circuitry):
   a. Increasing actuation capacitances (adding/increasing parallel-plates and decreasing gap);
5. Maximizing operation range (and dynamic range):
   a. Maximum measurable acceleration mustn't lead the proof-mass to travel full-displacement (this is defined by mass, gap size and spring stiffness), and
6. Minimizing response time (and increasing bandwidth).

As can be concluded from the constraints featured in this list, some compromises must be met. The most obvious trade-off is related to damping design: minimizing thermal-mechanical noise requires minimizing damping while improving pull-in time sensitivity requires higher damping. Microstructure S0 has been design to meet following goals in terms of pull-in accelerometer characteristics:

1. Target sensitivity >0.1 μs/μg,
2. Target noise <10 μg/√Hz,
3. Nominal sensing capacitance higher than 2 pF,
4. Pull-in voltage lower than 3 V,
5. ±2 g operation range and
6. Nominal pull-in time shorter than 20 ms.

The dynamic behavior modeling approach has been previously presented for a generic device (Chapter 2). The full dynamic model of the pull-in accelerometer was implemented in Matlab/Simulink, similar to the normalized model from Chapter 2, but including the designed parameters of microstructure S0 (movable mass, parallel-plates / gap geometry and spring stiffness coefficient) and the analytic squeeze-film damping model described in Chapter 4 that includes rarefaction, border effects and compensation for the out-of-plane deflection (also present in this structure). Figure 5.2 presents the modeled system response to a voltage step $V_{step} = \alpha V_{PI}$. A nominal pull-in time (t_{PI}) of 10.2 ms is found when actuating with α=1.01, with a metastability region clearly observable. Simulations were also performed using different α values in order to verify the influence of the actuation voltage on the pull-in time (Figure 5.3). In agreement with the simulations performed for a generic device in Chapter 2, pull-in time is longer for lower actuation voltage values, with the time increments being increasingly larger for *α* closer to 1.

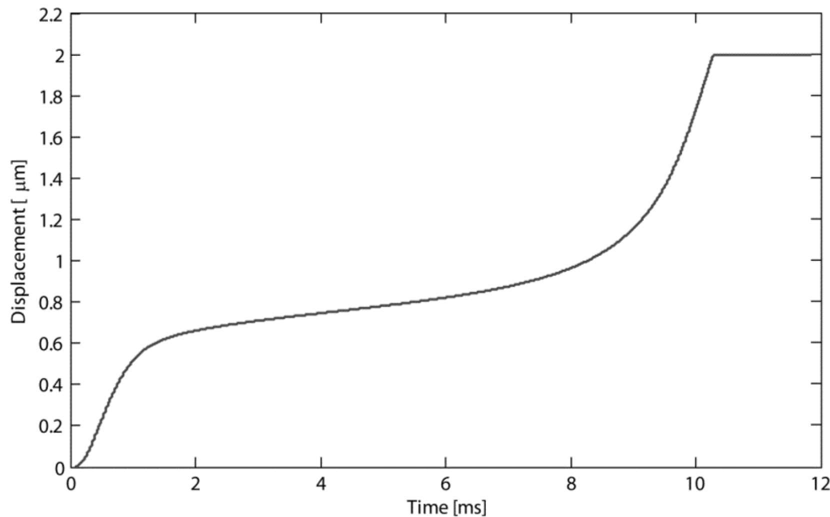

Figure 5.2: Simulated pull-in dynamic transition using α = 1.01.

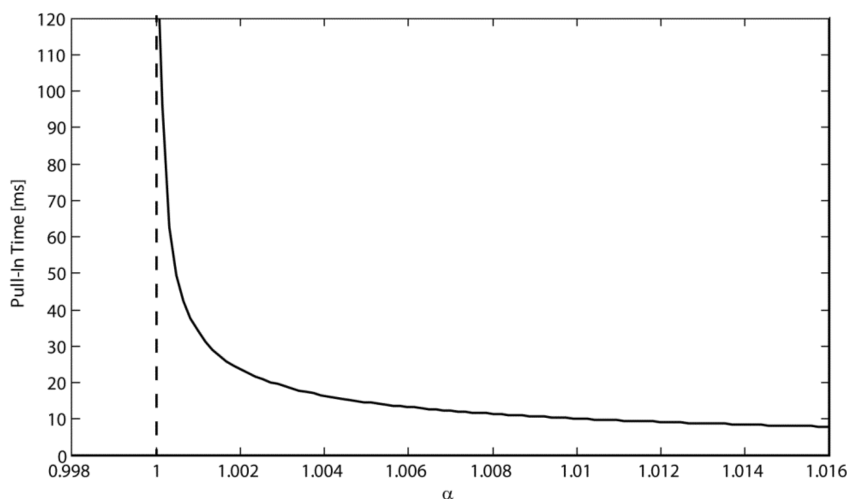

Figure 5.3: Simulated pull-in time variation with α.

Simulations have been performed including small external accelerations and using an actuation voltage $\alpha = 1.01$. The results are presented in Figure 5.4. It can be observed that the pull-in variation with acceleration is slightly non-linear within this range of a few milli-g. The pull-in time sensitivity to external acceleration at 0 g is 0.2646 μs/μg. If only the range of ±1 mg is considered, the best-fit sensitivity is 0.269 μs/μg, with a non-linearity of less than 1.3%, while for the range of ±5 mg, a non-linearity of 3.9% is found for a best-fit sensitivity of 0.276 μs/μg.

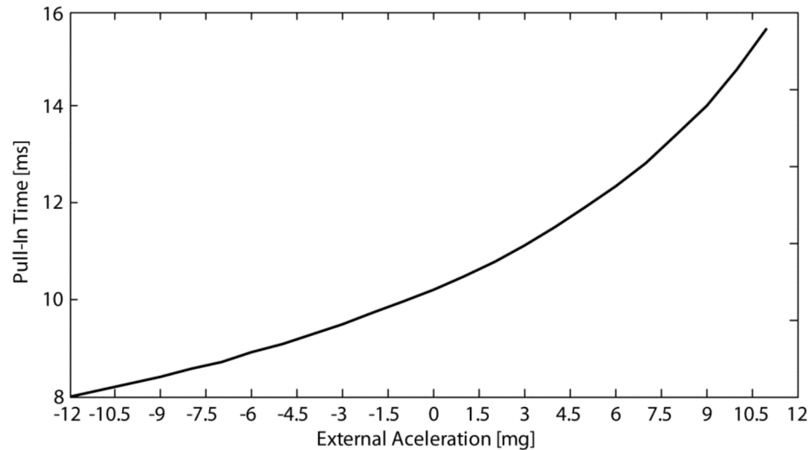

Figure 5.4: Pull-in time variation with external acceleration, for α = 1.01.

It can be concluded that the design parameters of structure S0 meet the pull-in time accelerometer specifications in respect to sensitivity and response time. The expected pull-in voltage is also lower than 3 V and the nominal sensing capacitance is higher than 2 pF. For the designed mass and spring stiffness, a 2 g acceleration moves the proof-mass displacement $2\,[\mathrm{g}]\times 9.8\,[\mathrm{m/s^2}\,/\,\mathrm{g}]\times m\,/\,k = 1.48\,\mu\mathrm{m}$. The remaining specification is the mechanical-thermal noise. As the mechanical-thermal noise is expected to be the main noise source of a pull-in time accelerometer, a detailed noise analysis is performed in the next section.

5.3. Noise analysis

The noise sources affecting the system can have mechanical or electrical origin [5.11]. Damping is a well-known source of mechanical noise, referred to as mechanical-thermal noise. The electrical noise sources are at the signal readout level and on the actuation voltage. Due to the fact that the time measurement can be performed with a very high resolution, the pull-in time accelerometer concept is expected to have the mechanical-thermal noise as the dominant noise source.

One well-known mechanism for mechanical-thermal noise is Brownian motion. Here, an agitation of the mechanical structure is caused by molecular collisions from the surrounding air

and the agitation is directly related to the viscosity (damping) [5.6]. This noise source is particularly important for this time-based accelerometer since it is expected to set the resolution limit, as opposed to other systems in which the measurement principle is usually the limiting factor. The damping characteristics are therefore crucial for the final sensitivity, pull-in time and total mechanical-thermal noise characteristics of the pull-in time based accelerometer.

The pull-in time is very dependent, however, on the actuation voltage. While the readout circuit is not expected to significantly affect the noise performance, care must be taken regarding the actuation voltage, and a low noise source is desirable. In order to evaluate the several noise sources contribution, a deep noise analysis was conducted.

5.3.1. Mechanical-thermal (Brownian) noise

The random movement (Brownian motion) of the gas molecules surrounding the mechanical structure leads to random fluctuations in the energy transfer between structure and damping gas [5.6]. This mechanical-thermal noise corresponds to an equivalent acceleration noise spectral density of [5.6], [5.12]:

$$a_{noise,b} = \frac{\sqrt{4k_B T b}}{9.8m} \; [g/\sqrt{Hz}] \tag{5.1}$$

where m is the mass of the movable structure, k_B is the Boltzman's constant, T is the temperature in Kelvin, and b is the damping coefficient in N.m/s.

Since the metastable region occurs at a gap value of 2/3 d_0, the damping coefficient can be linearized at this gap in the (low) frequency range of interest [5.13]. The computed linearized damping coefficient for the fabricated structure, at a gap size of 2/3 d_0, is $b = 2.62$ mN.s/m. Thus, an equivalent acceleration noise of $a_{noise,b} = 2.7$ µg/√Hz is obtained at room temperature. This method for determining the white noise floor due to damping, as well as the damping theory supporting it, has been previously validated by experimental white noise measurements on parallel plates MEMS devices [5.4].

Pull-in time measurements exhibit time averaging of high-frequency components of the equivalent mechanical-thermal noise due to the zero-mean property of noise [5.4]. Since noise at high frequencies is integrated during the pull-in transition, it does not contribute to variations in the displacement and therefore only frequencies lower than $2/t_{PI}$ are present during the full pull-in transition [5.4]. This property limits the noise spectral frequency range (bandwidth) measured to $BW = 2 / t_{PI}$. Operation with $V_{step} = 1.01 \times V_{PI}$, yields a t_{PI} of 10.2 ms and therefore the bandwidth

of interest is $BW = 2/t_{PI} \approx 200$ Hz. At this bandwidth, the mechanical-thermal noise contribution is expected to be $N_b = 2.7\ \mu g/\sqrt{Hz} * \sqrt{2/t_{PI}\ Hz} \approx 38\ \mu g$.

5.3.2. Readout circuit noise

The front-end amplifier of the electronic circuit used in this work for the capacitive readout (described in Chapter 3) has an input noise density specification of 2.5 nV/√Hz. Considering an operation bandwidth of 1 MHz results in a total noise of the readout circuit of about 2.5 µV.

The pull-in time is obtained by measuring the time elapsed from the moment the square signal is applied, until the structure passes through about 75% of the original gap. From the characteristic dynamic pull-in curve (Figure 5.2) it can be seen that in this position the structure is moving rapidly at about 0.71 µm/ms. The differential capacitance at this position is approximately 5 pF for S0, changing 10 pF/µm with displacement (from Figure 3.11). At this position the capacitive readout gain has decreased to approximately 90 mV/pF, corresponding to a voltage change rate of approximately 644 µV/µs, which allows disregarding the front-end readout electronic noise.

In addition to the front-end capacitive readout noise, another readout noise source exists, concerning the actual time measurement. Given the sensitivity of 0.26 µs/µg, uncertainty in the time measurement is directly translated into acceleration measurement uncertainty (quantization noise), and the time measurement resolution is set by the resolution of the counter or other time counting mechanism. In order to the quantization noise to not exceed, for example 50% of the expected mechanical-thermal noise ($N_b = 38$ µg), a time resolution of approximately 4.9 µs is required on the time counting mechanism: $N_r = 4.9$ µs / 0.26 µs/µg ≈ 19 µg.

5.3.1. Actuation voltage source noise

In this pull-in time accelerometer a MEMS structure is actuated with $V_{step}=\alpha V_{PI}$, α=1.01. The sensitivity of pull-in time to the actuation voltage variation (α) has been analyzed in Chapter 2 for a generic device and is illustrated in Figure 5.3 for the microstructure S0 specifically. Noise present in the actuation voltage will be reflected in pull-in time noise. From Figure 5.3 a t_{PI} change rate of -0.5394 s/α can be retrieved for α = 1.01 (slope at α = 1.01). Given the actuation voltage inserted in the model $V_{step}=\alpha V_{PI}$ and for an expected pull-in voltage of 2.916 V, the change rate is 0.5394/(2.916*1.01) =0.183 µs/µV, which is the t_{PI} sensitivity to actuation voltage

variation. Given this sensitivity, if one wants the acceleration-referred actuation noise not to exceed 50% of the expected mechanical-thermal noise (N_b = 38 μg), the voltage generator must present a noise performance better than approximately 1.9 μV/√Hz, i.e. 27 μV given the noise bandwidth of $BW = 2/t_{PI} \approx 200$ Hz: 27 μV*0.183 μs/μV = 4.9 μs; N_a= 4.9 μs / 0.26 μs/μg ≈ 19 μg. The DC stability of the actuation voltage source is a very important factor on the performance of the device.

5.3.1. Total noise

The total noise is a contribution of all the noise sources existing in the microsystem $N_t^2 = N_a^2 + N_b^2 + N_r^2 + N_{ext}^2$, where N_{ext} is external acceleration noise. Assuming there is no external noise contribution and considering the exemplificative noise values calculated in the previous sections, N_a = 19 μg, N_b = 38 μg, and N_r = 19 μg, the total system noise is expected to be: $N_t^2 = (19\ \mu g)^2 + (38\ \mu g)^2 + (19\ \mu g)^2 \rightarrow N_t \approx 46.5\ \mu g$, or $N_t \approx 3.29\ \mu g/\sqrt{Hz}$.

5.4. Experimental evaluation

5.4.1. Experimental setup

For the implementation of the accelerometer, the structure S0 (defined in Chapter 3) was used. The structure main parameters and dimensions are presented in Table 3.1.

Initially, the micromechanical structures were characterized using the Polytec's micro system analyzer MSA-500 (Figure 5.5), which uses stroboscopic video microscopy and image processing for in-plane motion detection [5.14]. Next, the pull-in voltage and nominal pull-in time were measured. The front-end readout circuit (seen in Figure 5.6b), consisting mainly in charge amplification and filtering, was used to detect the capacitive changes. It outputs a voltage signal proportional to the differential capacitance variation occurred on the MEMS structure. This signal is acquired by a NI USB-6281 (625 kHz sampling frequency) data acquisition board (DAQ) [5.15] and later processed on Matlab to retrieve the pull-in time (thus performing the time measurement). As the full pull-in transition (until the proof-mass reaches the stoppers) is acquired and the comparison is done posteriorly in Matlab, the threshold used was approximately 95 % hence the pull-in time results presented are very close to the full pull-in time.

The experiments with external acceleration were performed on a setup comprising a platform with one fixed end and a free end controlled by a vibration exciter (Figure 5.6a). The

shaker changes the horizontal level (angle ϕ) of the platform (where the sensor was placed horizontally). Since the sensor's motion is in-plane and the sensitivity axis was aligned with the platform's tilting direction, the setup allowed the generations of small accelerations ($a_{ext} = sin(\phi)$ [g]) ranging from as low as 300 µg up to a 10 mg. The generated angle was calibrated using a very sensitive optical sensor (based on a fiber bragg grating sensor). All experiments were performed under ambient pressure and temperature.

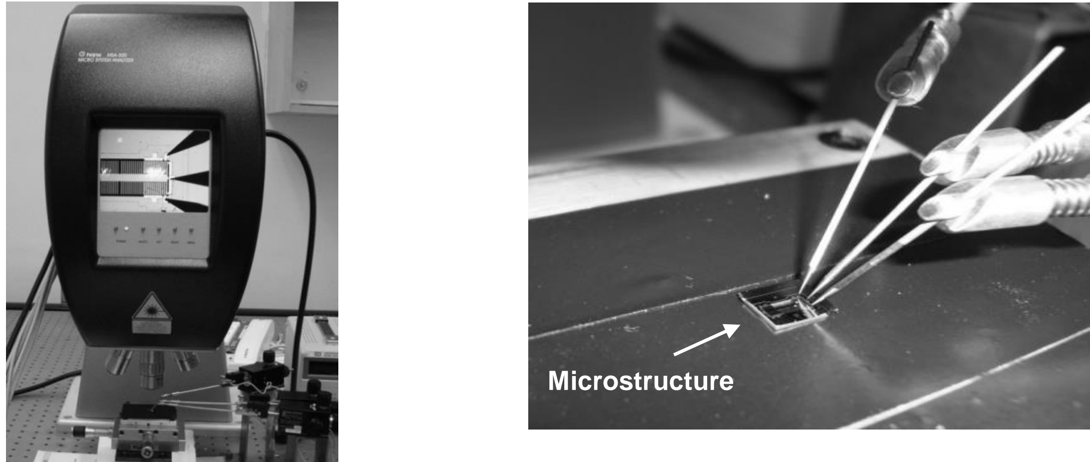

Figure 5.5: Picture of the Polytec microsystem analyzer MSA-500, the setup used for frequency analysis.

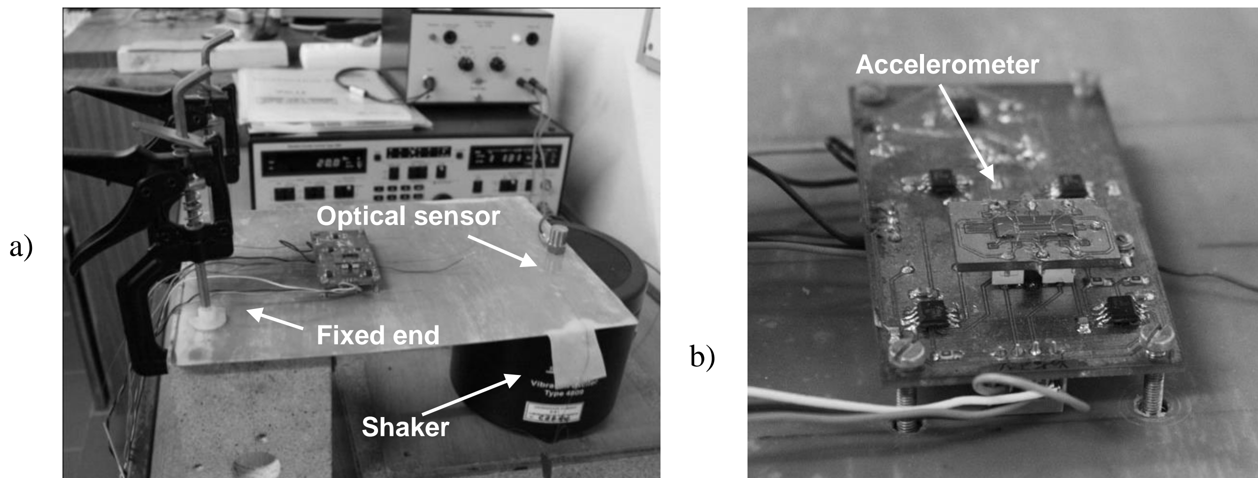

Figure 5.6: Experimental setup a) overview and b) detail of the microstructure mounted on the front-end readout circuit.

5.4.2. Results

The microdevice frequency response obtained with the Polytec's micro system analyzer MSA-500 is depicted in Figure 5.7. A resonance frequency of 515 Hz (582 Hz expected) is retrieved from the phase plot while a quality factor Q=0.7 is found through transfer function curve fitting of the bode plot data. The curve fitting yielded a correlation factor of $R^2 = 0.98$. The

noise of the measurements is due to the in-plane mode measurement of the equipment – the motion is evaluated through image processing, which is not as accurate as analyzing in the out-of-plane mode.

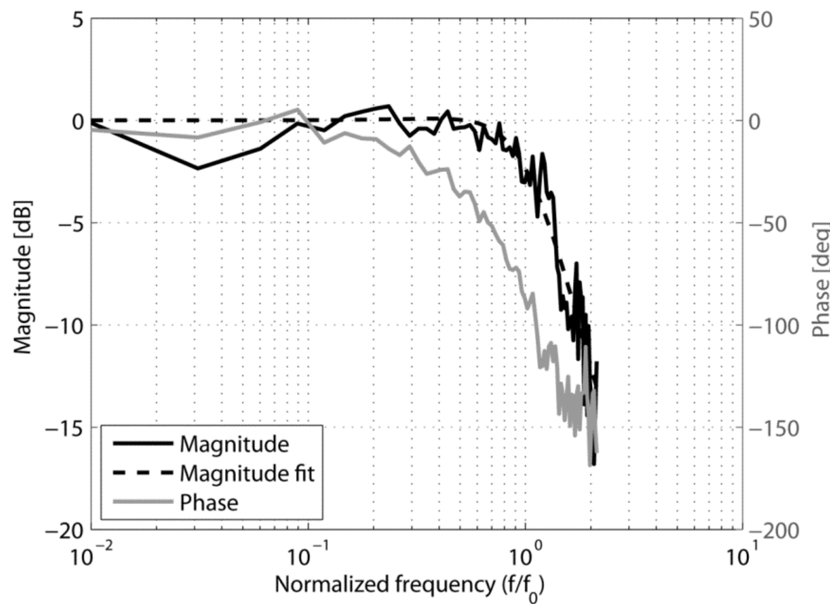

Figure 5.7: Bode analysis performed with MSA-500 using sinusoidal actuation of amplitude 1 V and 1 V offset.

Next, dynamic behavior experiments were performed. Initially, the pull-in voltage was measured, and the experimental value found was 2.931 V which is in very good agreement with the predicted value of 2.916 V. The difference between experimental and expected values can be easily understood when considering micromachining process variations, such as overetching, which affect mainly the spring stiffness coefficient of the microstructure. Then, the structure was actuated with voltage step inputs with an amplitude slightly higher than the pull-in voltage, $V_{step}=\alpha V_{PI}$, α=1.01 in order to analyze its dynamic behavior. The simulated and measured nominal (0 g) pull-in time (t_{PI}) was 10.2 ms with α=1.01 (Figure 5.8). The microstructure was also actuated with different step voltages $V_{step} = \alpha V_{PI}$, the results are presented in Figure 5.9. In both experiments very good agreement with the predicted results (from the dynamic Matlab/Simulink model) was achieved, which validates the modeling approach.

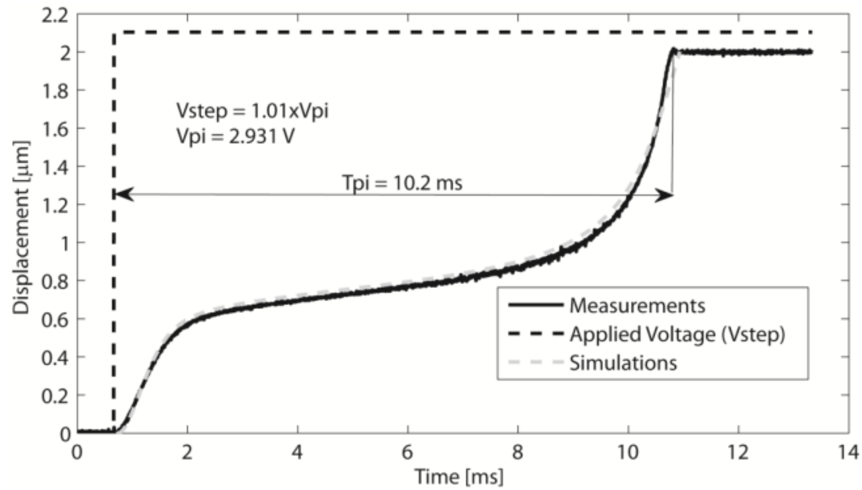

Figure 5.8: Simulated and experimental nominal (0 g) pull-in time.

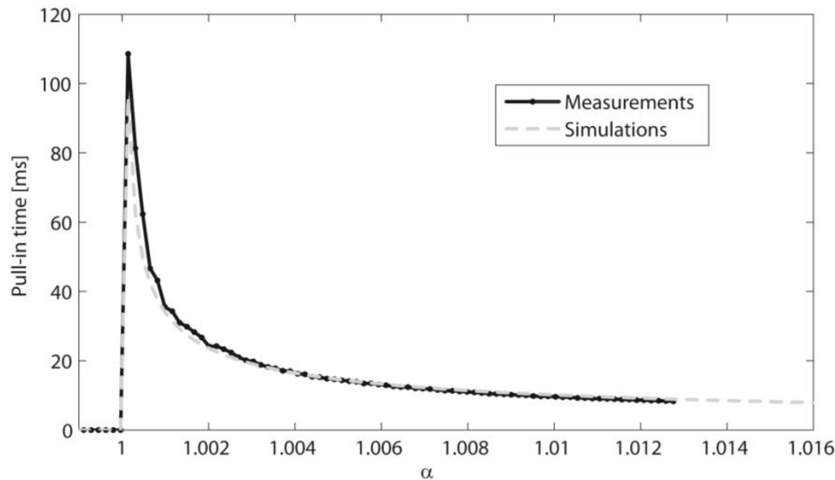

Figure 5.9: Simulated and experimental pull-in time values for different values of α (α=V_{step}/V_{PI}).

Finally, the device was tested using accelerations smaller than 10 mg (Figure 5.10). The response curve of the accelerometer was computed, using the Matlab/Simulink model, for small accelerations and the sensitivity is expected to be approximately 0.26 µs/µg in the vicinity of 0 g acceleration. Experimental measurements of the pull-in time with external acceleration inputs were performed using the previously described setup and the results show a pull-in time variation proportional to the acceleration in close agreement with the predicted results (Figure 5.10a). A sensitivity of 0.26 µs/µg was measured along with a noise floor of approximately 400 µg (105 µs). Due to the non-linear behavior of both electrostatic and damping forces, the sensitivity of the pull-in time accelerometer can only be considered linear within a limited range of a few mg (Figure 5.10a). If an operation range of ±10 mg is considered along with the resolution limit of 2.7 µg (due to mechanical-thermal noise), a maximum dynamic range of approximately 77 dB is achieved. This is a disadvantage of this approach that can be compensated by an effective use of

the differential pair of electrostatic actuators. In fact, the use of counter-balance electrostatic forces is expected to improve both linearity and dynamic range, improving the limitations of the open-loop operation (Chapter 6).

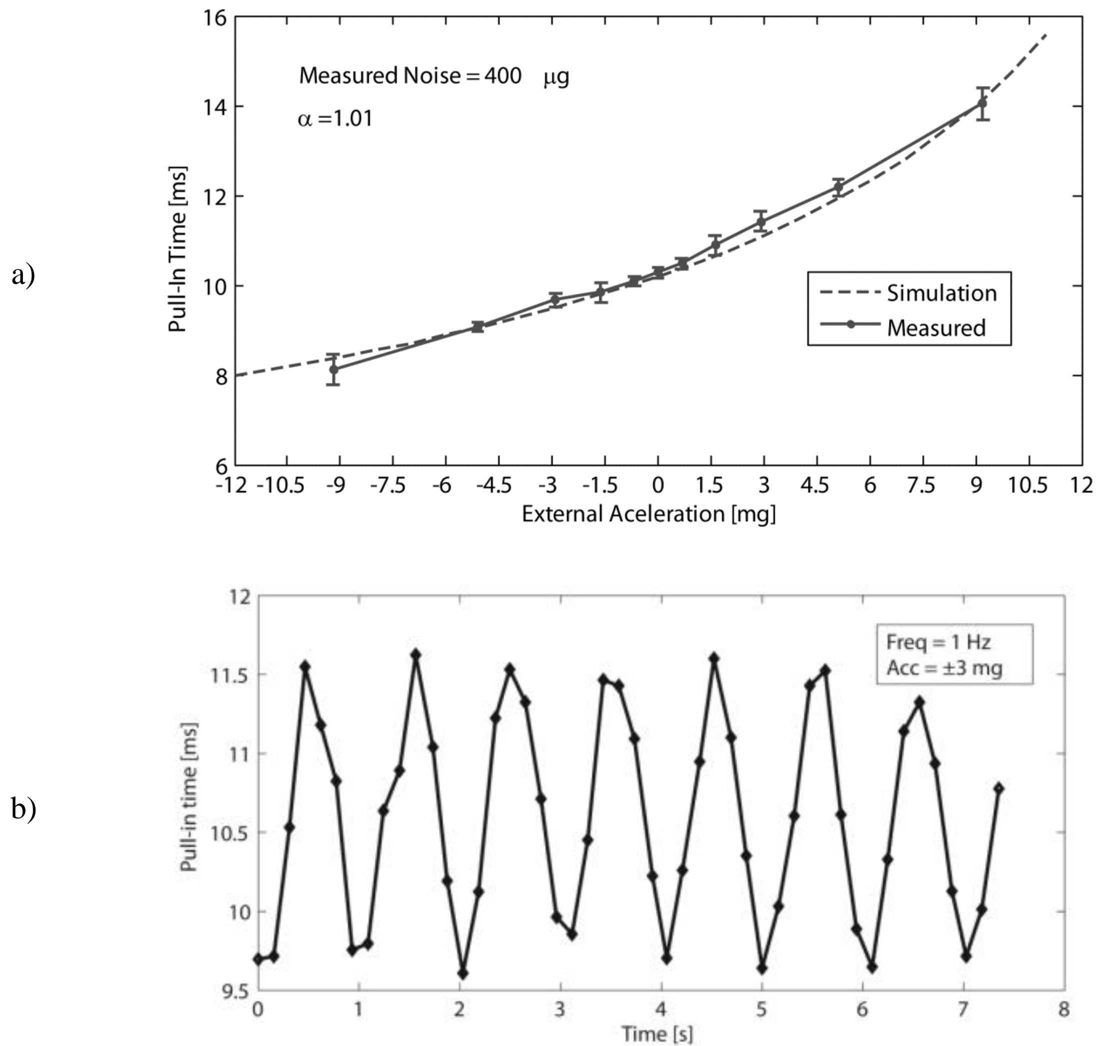

Figure 5.10: a) Simulation and experimental results of pull-in time variation with external acceleration and b) accelerometer response to ±3 mg external acceleration (6 mg$_{p-p}$) applied at 1 Hz.

The 400 µg acceleration noise found experimentally is much higher than expected, justifying an additional noise analysis of the pull-in time accelerometer and setup.

5.4.3. Readout noise

At the displacement of approximately 95% of the original gap, the structure is moving rapidly and the experimentally measured voltage change rate is higher than 300 µV/µs, which allows disregarding the front-end readout electronic noise.

In these measurements, rather than using a real time counting method, the analog output of the front-end readout circuit is acquired by the DAQ and later processed in Matlab. The DAQ allows a 625 kHz sampling frequency, corresponding to a time resolution of 1.6 μs, hence to an acceleration noise due to readout noise of N_r = 1.6 μs / 0.26 μs/μg = 6.2 μg. To facilitate data processing and taking into account that the noise floor level is much higher than this value, a sampling frequency of 150 kHz was used instead, which translates to a time measurement resolution of about 7 μs. Higher resolutions are possible but this DAQ measurement uncertainty is already much lower than the measured noise level. Since this uncertainty in the pull-in time measurement is quantization noise and thus can be interpreted as readout noise, for a given sensitivity of 0.26 μs/μg, the resolution of 7 μs corresponds to a readout circuit noise contribution of N_r = 27 μg. The data is then processed on Matlab (the signal is digitally filtered and the time elapsed is calculated) with no further noise addition.

5.4.4. Actuation voltage noise

For the work featured in this chapter, the actuation voltage was provided by the analog output of the same DAQ used for readout. The analog output, with a 500 kHz update rate, was monitored with a high resolution multimeter at 10 kHz, and a standard deviation of 68 µV was found. The samples were filtered with a 200 Hz (the noise bandwidth) low-pass filter yielding a standard deviation of 11.9 µV. From the t_{PI} sensitivity to actuation voltage of 0.183 μs/µV, the measured noise of 11.9 µV yields a pull-in time noise of 11.9 µV*0.183 μs/µV = 2.2 μs which corresponds to an acceleration-equivalent noise of N_a= 2.2 μs / 0.26 μs/μg = 8.4 μg

Since the pull-in time is highly dependent on the actuation voltage, simulations and experiments were performed to further evaluate the influence of actuation voltage noise on the pull-in time. Noise with different values at a 500 kHz bandwidth was added to the actuation voltage and the pull-in time noise was measured at a frequency of approximately 50 Hz (Figure 5.11). Linear curve fitting was applied to the experimental data and it was found that the pull-in time noise varies linearly with the actuation voltage noise, for actuation voltage noises above approximately 30 mV, according to the function t_{PI_noise} [μs] = 2.8 × V_{step_noise} [mV]+50 (R^2=0.987 correlation factor). For lower actuation voltage noise, the data does not follow the linear trend and the t_{PI} noise does not reduce below approximately 100 μs. This suggests that the measured noise floor (100 μs) is not due to the actuation voltage noise.

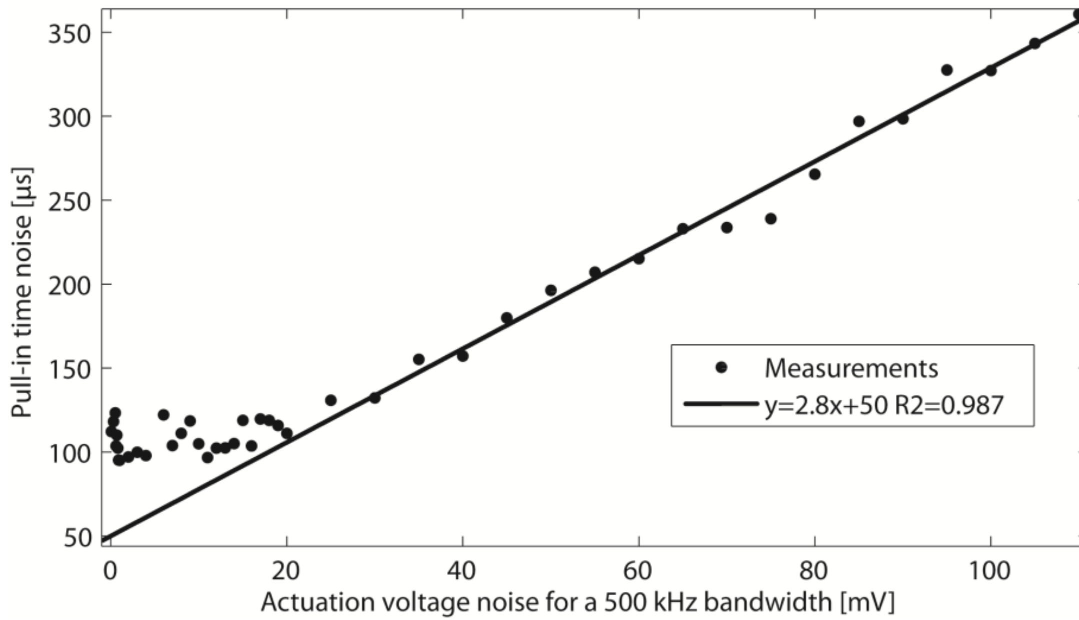

Figure 5.11: Measured t_{PI} rms noise using actuation voltages with added rms noise. The data was fitted excluding the actuation voltage rms noise values below 30 mV and yielded a correlation factor R^2= 0.987.

To better understand these results, several actuation voltage noise values were introduced in the Simulink dynamic model. The resulting t_{PI} noise values showed a linear dependence on the actuation noise following the expression t_{PI_noise} [µs] = 3.02× V_{step_noise} [mV]. According to these values, the actuation voltage noise of 68 µV at 500 kHz would yield a t_{PI} noise of 0.20 µs, which corresponds to N_a = 0.20 µs / 0.26 µs/µg = 0.77 µg acceleration noise due to actuation voltage noise.

5.4.5. External noise

Assuming that an external noise is present, N_{ext}, yielding the unexpectedly high total noise N_t=400 µg, its contribution can be found through $N_t^{\ 2} = N_a^{\ 2} + N_b^{\ 2} + N_r^{\ 2} + N_{ext}^{\ 2}$ considering the noise sources calculated in the previous sections, N_a = 0.77 µg, N_b = 38 µg, and N_r = 27 µg: $(400\ \mu g)^2 = (0.77\ \mu g)^2 + (38\ \mu g)^2 + (27\ \mu g)^2 + (N_{ext})^2 \rightarrow N_{ext} = 397\ \mu g$.

This external noise was attributed to environmental disturbances since no measures were taken to isolate the experimental setup from building vibrations. The magnitude of these external vibrations is in reasonable accordance with values found in literature [5.16], [5.17].

In addition to these calculations, the readout circuit noise, the mechanical-thermal noise and the assumed-environmental noise were subtracted to the measured values for increasing actuation voltage noise (isolating the actuation voltage noise) and the results were compared to

the expected actuation voltage noise dependence obtained with the analytic model (Figure 5.12). The linear fittings of both series show approximately the same slope, and good correlation factors, which supports the conclusions taken concerning the actuation voltage noise and the presence of external environmental noise.

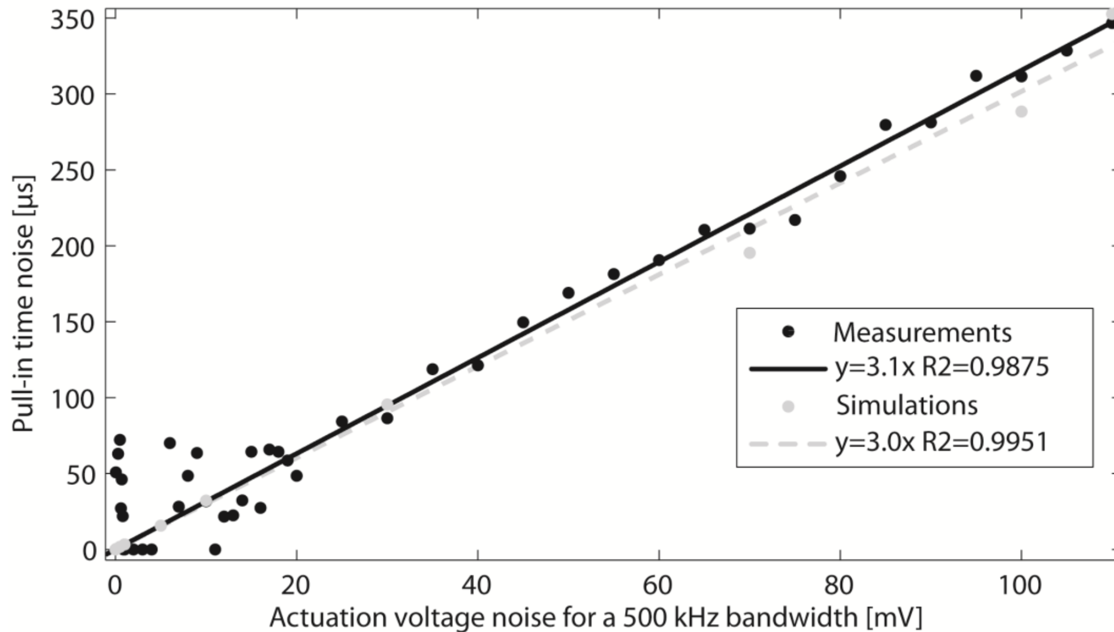

Figure 5.12: Comparison between normalized experimental and modeled results for pull-in time noise as a function of the actuation voltage noise.

5.4.6. Discussion

The accelerometer has a measured sensitivity of 0.26 µs/µg and a bandwidth that is directly related to the pull-in time, $BW = 1/2t_{PI} \approx 50$ Hz. A sensitivity of 0.26 µs/µg is a very good feature since it is very easy to accurately measure time. A simple 4 MHz crystal would enable a 0.25 µs time measurement resolution corresponding to an acceleration resolution better than 1 µg. A mechanical-thermal noise of 2.7 µg/√Hz is expected for these devices, which places them reasonably near the state-of the art devices (refer to Table 1.2 in Chapter 1). It should be noted that the microstructure design aimed the proof of concept, and the approach can be implemented using structures with larger proof-masses, i.e. with lower thermal-mechanical noise, so that these high resolutions can effectively be measured.

The DC stability of the actuation voltage source is a very important factor on the performance of the device. The structure is actuated with $V_{step}=\alpha V_{PI}$. For α = 1.01, the t_{PI} change rate is -0.5394 s/α (slope of graph in Figure 5.9b at α = 1.01). If a pull-in voltage of 2.931 V is considered, the change rate is 0.5394/(2.931*1.01) =0.182 µs/µV. This means that a relatively

small DC drift (in the order of magnitude of a few microvolt), yields a significant t_{PI} change. From this perspective it is useful to increase the pull-in voltage of the structures (for instance by reducing the actuation capacitance) since the sensitivity to actuation voltage noise is decreased. This low frequency sensitivity is not present in the analysis performed in section 5.4.4 because no long-term noise evaluation was performed.

5.5. Conclusions

The open-loop operation of the μg accelerometer based on pull-in time measurement has been described and implemented in this chapter. The experimental results from the microstructures fabricated in the SOIMUMPs process are in agreement with the simulations obtained with the dynamic model of the accelerometer implemented in Matlab/Simulink. The pull-in time accelerometer concept and the models used are thus validated by the results obtained.

The measured noise floor was much higher than expected and this is attributed to environmental vibrations, due to lack of vibration isolation of the measurement setup. An in-depth study of the noise sources was performed which supports this conclusion. This situation made impossible to measure the expected mechanical-thermal noise of 2.7 μg/√Hz which is very close to the state-of-the-art accelerometers noise found in literature, as shown in Table 1.2 in Chapter 1 (0.23 μg/√Hz [5.18], 1.6 μg/√Hz [5.19] and 0.85 μg/√Hz [5.20], [5.21]). Further experimental work must be performed in a more controlled environment (to reduce the environmental noise), in order to evaluate the low noise specifications of the accelerometer.

This approach presents a high sensitivity of the pull-in time to DC drift on the actuation voltage, 0.182 $\mu s/\mu V_{DC}$. Methods to compensate this problem, by means of closed-loop control, could be implemented to minimize this effect.

In comparison to the traditional approach of high-resolution capacitive accelerometers found in literature, the main advantage is the huge potential of the measurement method in terms of resolution. Since a time measurement is performed, rather than just direct transduction of capacitance into acceleration, increasing the measurement resolution only requires a faster clock of the time counting mechanism (to detect smaller changes in the pull-in time). For instance, if a sampling frequency of a few nanoseconds is used, nano-g can easily be measured with this readout approach, as opposed to direct capacitive transduction approaches where very small capacitance changes are difficult to detect. The sensitivity is not therefore dependent on technology developments. The capacitance change in the gap of interest is very large (pF) and the

voltage increase at the front-end readout circuit output is straight-forward to detect. Thus, the requirements of the front-end readout circuit are very low since there is no need to detect small capacitance variations as in the case of the traditional capacitive approach. For instance, the accelerometer presented in [5.18] (noise of 0.23 μg/√Hz) needs a sensitivity of 35 aF/μg. These specifications for the readout circuits are much more demanding in terms of circuit design and implementation, than the measured sensitivity of 0.26 μs/μg presented in this work.

As opposed to conventional displacement detection techniques, in which often attofarad capacitance changes need to be sensed, this accelerometer concept main limitation is the mechanical-thermal noise of the mechanical structure, with almost no constraints on the readout circuit. Another key advantage of the presented pull-in time based approach is the potential to easily realize very high resolution accelerometers using simple electronics on the readout circuit and standard, readily available, commercial micromachining processes for the MEMS structures fabrication, as opposed to state-of-the-art devices which require dedicated and modified fabrication processes.

The main disadvantages of the current implementation are the non-linear response and the low dynamic range. Nevertheless, both the linearity and the dynamic range can be improved by an effective use of the differential pair of electrostatic actuators. Techniques to compensate the nonlinearities and improve dynamic range using electrostatic forces are the subject of the next chapter. The presented high-sensitivity high-resolution accelerometer can find applications in tilt control, platform stabilization, space applications (microgravity measurement), structural monitoring, seismography, and others.

References

[5.1] L. A. Rocha, L. Mol, R. F. Wollfenbuttel, and A. Lage, “A time based micro-g accelerometer,” in *Proceedings of Eurosensors XXII*, 2008, pp. 1565–1568.

[5.2] L. A. Rocha, E. Cretu, and R. F. Wolffenbuttel, “Behavioural analysis of the pull-in dynamic transition,” *Journal of Micromechanics and Microengineering*, vol. 14, no. 9, pp. S37–S42, 2004.

[5.3] N. Yazdi, F. Ayazi, and K. Najafi, “Micromachined inertial sensors,” *Proceedings of the IEEE*, vol. 86, no. 8, pp. 1640–1659, 1998.

[5.4] L. A. Rocha, E. Cretu, and R. F. Wolffenbuttel, “Measuring and interpreting the mechanical–thermal noise spectrum in a MEMS,” *Journal of Micromechanics and Microengineering*, vol. 15, no. 7, pp. S30–S38, Jul. 2005.

[5.5] R. F. Wolffenbuttel, "Silicon Sensors and Circuits," in *On-Chip Compability*, London: Chapman and Hall, 1996.

[5.6] T. B. Gabrielson, "Mechanical-thermal noise in micromachined acoustic and vibration sensors," *IEEE Transactions on Electron Devices*, vol. 40, no. 5, pp. 903–909, May 1993.

[5.7] V. Rajaraman, B. S. Hau, L. A. Rocha, P. J. French, and K. A. A. Makinwa, "Design and modeling of a flexible contact-mode piezoresistive detector for time-based acceleration sensing," *Procedia Engineering*, vol. 5, pp. 1063–1066, Jan. 2010.

[5.8] V. Rajaraman, B. S. Hau, L. A. Rocha, R. A. Dias, K. A. A. Makinwa, and R. Dekker, "A novel SOI-MEMS ' micro-swing' time-accelerometer operating in two time-based tranduction modes for high sensitivity and extended range," in *Proceedings of Transducers*, 2011, pp. 2066–2069.

[5.9] H. Lang, L. S. Pakula, and P. J. French, "A novel pull-in accelerometer," in *Proceedings of Eurosensors XVII*, 2003, pp. 204–207.

[5.10] R. A. Dias, L. Mol, E. Cretu, R. F. Wolffenbuttel, and L. A. Rocha, "Improved damper geometry for parallel-plate MEMS," in *Proceedings of MME*, 2009, pp. 20–23.

[5.11] B. V. Amini and F. Ayazi, "Micro-gravity capacitive silicon-on-insulator accelerometers," *Journal of Micromechanics and Microengineering*, vol. 15, no. 11, pp. 2113–2120, Nov. 2005.

[5.12] M. Lemkin and B. E. Boser, "A three-axis micromachined accelerometer with a CMOS position-sense interface and digital offset-trim electronics," *IEEE Journal of Solid-State Circuits*, vol. 34, no. 4, pp. 456–468, Apr. 1999.

[5.13] L. A. Rocha, E. Cretu, and R. F. Wolffenbuttel, "Analytical model for the pull-in time of low-Q MEMS devices," in *Proceedings of Nanotech*, 2004, vol. 2, pp. 271–274.

[5.14] Polytec Inc., "MSA-500 Micro System Analyzer: Measuring 3-D Dynamics and Topography of MEMS and Microstructures," 2009.

[5.15] National Instruments, "NI USB-6281 Datasheet," 2012.

[5.16] Y. Cao and H. Xia, "Experimental study of railway traffic induced environmental vibrations," *Proceedings of MACE*, pp. 1850–1853, 2010.

[5.17] S. Hunaidi, J. H. Rainer, and G. Pernica, "Measurement and analysis of traffic-induced vibrations," in *Proceedings of Second International Symposium - Transport Noise and Vibration*, 1994, pp. 103–108.

[5.18] R. Abdolvand, B. V. Amini, and F. Ayazi, "Sub-micro-gravity in-plane accelerometers with reduced capacitive gaps and extra seismic mass," *Jounal of Microelectromechanical Systems*, vol. 16, no. 5, pp. 1036–1043, 2007.

[5.19] J. Chae, H. Kulah, and K. Najafi, “An in-plane high-sensitivity, low-noise micro-g silicon accelerometer with CMOS readout circuitry,” *Journal of Microelectromechanical Systems*, vol. 13, no. 4, pp. 628–635, 2004.

[5.20] Y. Dong, M. Kraft, and W. Redman-White, “Force feedback linearization for higher-order electromechanical sigma–delta modulators,” *Journal of Micromechanics and Microengineering*, vol. 16, no. 6, pp. S54–S60, Jun. 2006.

[5.21] H. Kulah, J. Chae, N. Yazdi, and K. Najafi, “Noise analysis and characterization of a sigma-delta capacitive microaccelerometer,” *IEEE Journal of Solid-State Circuits*, vol. 41, no. 2, pp. 352–361, 2006.

6.

Closed-loop operation

In Chapter 2, damped movable parallel-plate capacitive devices actuated electrostatically have been demonstrated to show a metastable behavior during the pull-in transition, located at a critical deflection x_{PI} = (1/3)gap for 1-DOF devices, which is very sensitive to small external accelerations when actuated with voltages at a specific range. This characteristic has been explored for the realization of a high resolution accelerometer in the previous chapter 5, operating in open-loop mode within an acceleration range of a few milli-g, $< \pm 10$ mg. The main limitation of this approach is the non-linear response and the low dynamic range [6.1], [6.2]. This chapter focuses on closed-loop operation of the pull-in time accelerometer, aiming to improve response linearity and extend dynamic range.

6.1. Open loop response limitations

Electrostatically actuated parallel-plated devices, show longer pull-in times for actuation voltages closer to the pull-in voltage, $\alpha \approx 1$, (as long as $\alpha > 1$). In addition, the longer the pull-in time, the more sensitive to external accelerations (a_{ext}) the device is. Nevertheless, an overly long pull-in time is not desirable (due to consequent measurement frequency limitations), and therefore a step voltage $V_{step} = \alpha\ V_{PI,n}$ with $\alpha = 1.01$ was used in previous chapter for open-loop operation. From Chapter 2, the analytical solutions for the nominal pull-in voltage and critical displacement in the presence of external acceleration are:

$$V_{PI,a} = \sqrt{\frac{8}{27}\frac{d_0 k - ma}{k}\sqrt{\frac{d_0 k - ma}{d_0 C_0}}} \quad (6.1)$$

$$x_{PI,a} = \frac{d_0 k + 2ma}{3k} \tag{6.2}$$

Figure 6.1 shows the modeled S0 microstructure response for a large range of accelerations (pull-in time as a function of acceleration) with two different actuation conditions. Taking into account the microstructure's parameters, the maximum measurable acceleration is approximately 2.7 g, since accelerations larger than this value bring the proof mass to the stoppers. The positive acceleration values correspond to acceleration in the direction of pull-in. When using $V_{step} = \alpha V_{PI,n}$ (where $V_{PI,n}$ is the nominal V_{PI}, at a_{ext} =0 g), t_{PI} tends to infinity with accelerations opposite to pull-in, which is due to the fact that the critical pull-in voltage in the new conditions ($a_{ext} \neq 0$ g), $V_{PI,a}$, has increased and the fixed V_{step} value being used ($\alpha\ V_{PI,n}$) is no longer enough to induce pull-in.

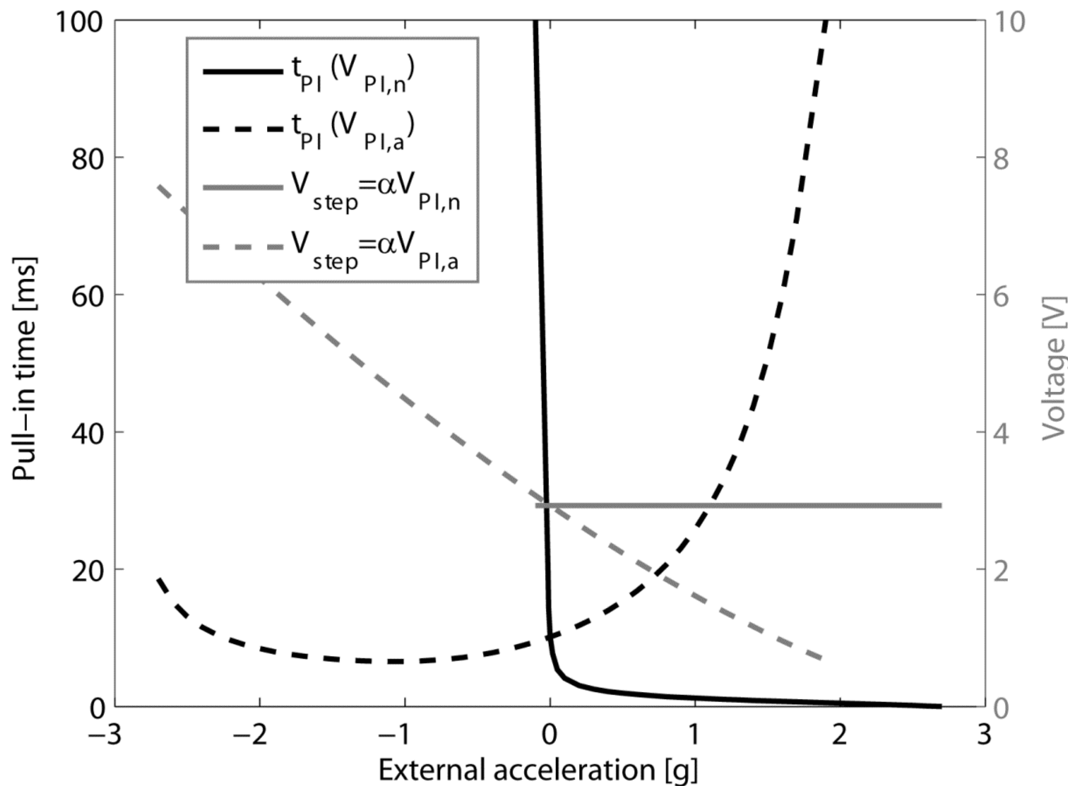

Figure 6.1: Accelerometer model response using $V_{step} = \alpha V_{PI,n}$ and $V_{step} = \alpha V_{PI,a}$.

On the other hand, if one actuates with $V_{step} = \alpha V_{PI_a}$, the modeled response, as plotted in Figure 6.1, shows a pull-in time increase when acceleration is present in the direction of pull-in. This is due to fact that the critical deflection x_{PI} is no longer at (1/3)d_0, but shifted to a larger displacement – smaller gap. This smaller gap is associated with higher damping coefficient, thus making pull-in slower. On the opposite direction, accelerations higher than approximately 1 g show a slight t_{PI} increase, since the travel distance increases. This behavior is due to the fact that

the damping for this large gap range is much smaller and pull-in no longer presents the metastable behavior. Operating the accelerometer in this way would require continuous pull-in voltage monitoring which would decrease the pull-in time measurement frequency significantly.

Pull-in time open-loop operated accelerometers are suitable for low-g acceleration sensing. Experimental results on fabricated devices showed a nominal (0 g) t_{PI} of 10.2 ms with a sensitivity of 0.26 μs/μg, which is in agreement with simulations. However, the sensitivity can only be considered linear without major error over a limited range of ±10 mg (non-linearity of approximately 7.6 $\%_{\pm 10mg}$ and 3.9 $\%_{\pm 5mg}$). For larger accelerations, the t_{PI} change rate is highly nonlinear. This feature clearly limits operation of the accelerometer for larger accelerations.

6.2. Electrostatic feedback compensation

In order to improve the dynamic range, the sensitivity must be kept constant over a large acceleration range and feedback techniques are required. As demonstrated in Chapter 2, the pull-in time sensitivity to acceleration depends on the quality factor (thus on the damping coefficient) and on α (in $V_{step}=\alpha V_{PI}$). Previous discussion showed that a constant α, i.e. actuating with $V_{step} = \alpha V_{PI_a}$, is not enough to keep the pull-in time sensitivity to external acceleration constant since the critical pull-in voltage occurs at a different gap (with a different damping coefficient associated).

Ideally, to achieve constant sensitivity over an extended operation range, both t_{PI} (directly related to sensitivity), and the critical pull-in deflection x_{PI} (so that the damping coefficient at the critical deflection is maintained) should be kept constant [6.3]. In this section, methods to increase dynamic range are pursued, using not only the main pull-in drive voltage, V_{step}, but also applying voltage to the counter-actuation electrodes (as the microstructure is symmetrical), V_{EF} – electrostatic feedback voltage, as illustrated in Figure 6.2.

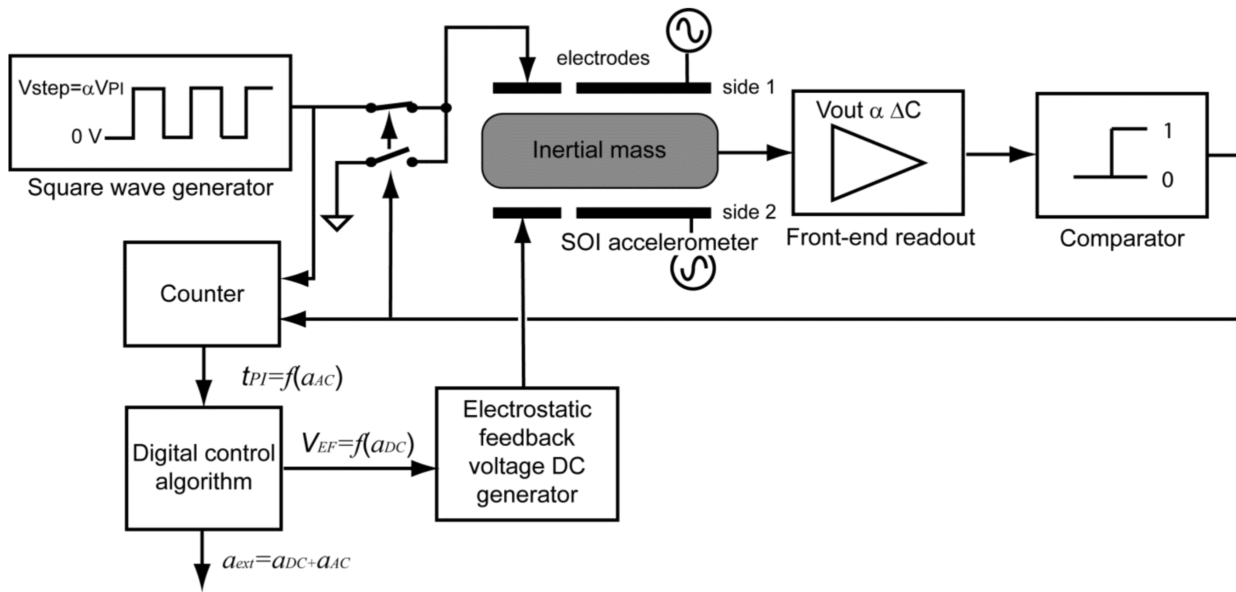

Figure 6.2: Pull-in accelerometer setup with electrostatic counter-actuation.

The main idea behind closed-loop operation is to use the voltage V_{EF} to compensate for large DC accelerations present in the direction of pull-in, while smaller AC accelerations can be measured by monitoring the pull-in time changes, with the sensitivity of 0.26 µs/µg, similarly to the open-loop approach on the previous chapter. For accelerations in the opposite direction, the same method can be used by changing the roles of the electrodes at which V_{step} and V_{EF} are applied (considering symmetrical MEMS structure). Several alternative ways to compensate the DC acceleration using the compensation electrodes are discussed next.

6.2.1. Constant pull-in critical displacement

Sensitivity in the pull-in time accelerometer concept depends on the pull-in time duration and therefore it is also dependent on the damping forces (higher damping coefficients yield longer pull-in times). Keeping the critical deflection constant at *1/3* d_0, has the advantage of maintaining the same damping coefficient during metastability (damping is a function of the gap), which is determinant to the overall pull-in duration. When acceleration is present in the direction of pull-in, the critical displacement $x_{PI,a} = \frac{d_0 k + 2ma}{3k}$ becomes larger than *1/3* d_0, i.e. occurs at a smaller gap, to which a larger damping coefficient is associated. An electrostatic force applied in the direction opposite to pull-in can compensate this external acceleration effect and maintain the critical displacement at *1/3* d_0. The voltages, V_{step} and V_{EF}, required to keep the critical displacement at *1/3* d_0 can be computed analytically by solving the equation system:

$$\begin{cases} |F_{elas}| + |F_{elect,V_{EF}}| = |F_{elect,V_{PI}} + F_a| \\ \dfrac{d|F_{elas}| + |F_{elect,V_{EF}}|}{dx} = \dfrac{d|F_{elect,V_{PI}} + F_a|}{dx} \\ x = \dfrac{1}{3}d_0 \end{cases} \tag{6.3}$$

in respect to the voltages V_{PI} and V_{EF}:

$$V_{PI,xPI} = \sqrt{\frac{8}{27}\frac{{d_0}^2k - ad_0m}{C_0}}$$
$$V_{EF,xPI} = 8\sqrt{\frac{ad_0m}{27C_0}} \tag{6.4}$$

Keeping x_{PI} at $1/3\ d_0$ requires applying an electrostatic actuation voltage $V_{EF,xPI}$ on the compensation electrodes. In this new force equilibrium there is also a new pull-in voltage value, $V_{PI,xPI}$. Maintaining the same α requires actuating with V_{step} = α $V_{PI,xPI}$. A Simulink model of microstructure S0 (parameters in Table 3.1) has been used to model the system pull-in time response to external acceleration, when being actuated with the voltages V_{step} = 1.01 $V_{PI,xPI}$ and $V_{EF,xPI}$. The results are shown in Figure 6.3. The analytical pull-in voltages at both sides $V_{PI,a}$ and $V_{PI,a,op}$, in the presence of external acceleration (equation (6.1)), are also plotted in this figure.

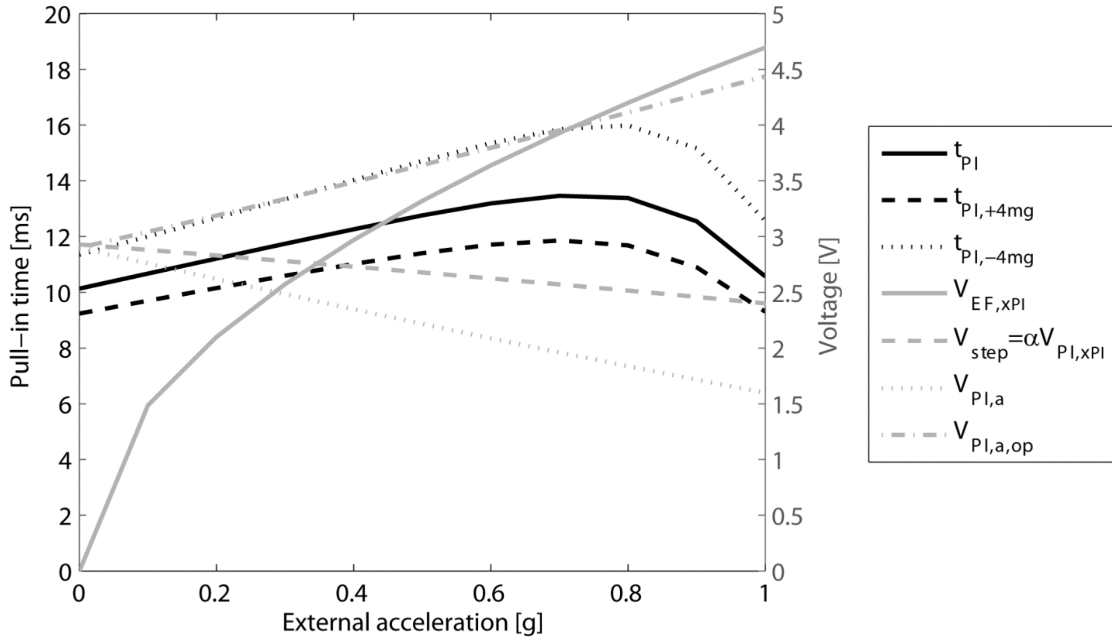

Figure 6.3: Simulation pull-in time results when actuating with $V_{step} = \alpha V_{PI,xPI}$ and $V_{EF,xPI}$ and corresponding voltages, over large DC acceleration range and ± 4 mg.

Simulations show that the pull-in time compensated for large accelerations is not maintained at the nominal value $t_{PI,n} \approx 10.2$ ms (the pull-in time changes linearly up to 600 mg at 5.1 ms/g, approximately), hence the sensitivity is not kept constant, as it is shown by the system's response to ± 4 mg. The pull-in time variation $\Delta t_{PI} = t_{PI,a}\text{-}t_{PI}$ increases slightly as the DC-compensated pull-in time increases, which occurs up to approximately 800 mg.

Accelerations larger than 1 g cannot be compensated by this method because the initial displacement caused by the acceleration is already beyond 1/3 of the initial gap.

Although the applied voltage, $V_{EF,xPI}$, is larger than the pull-in voltage on the side it is being applied, $V_{PI,a,op}$, pull-in keeps occurring to the side that V_{step} is being applied because the ratio $V_{step} / V_{PI,a}$ is larger than the ratio $V_{EF,xPI} / V_{PI,a,op}$ and both voltages are applied at the same time on the model. If an experimental implementation using the configuration from Figure 6.2 was considered, however, the maximum measurable acceleration would be approximately 700 mg because beyond that value, once V_{step} is turned off, the structure would be pulled-in to the opposite side.

Note that the voltages analytic expressions do not account for the parasitic capacitances of the actuation electrodes so these were also not accounted for in the model.

6.2.2. Constant pull-in time

6.2.2.1. Keeping $V_{step} = \alpha\, V_{PI,n}$, changing V_{EF}

Extension of the useful dynamic range by keeping the nominal t_{PI} constant at 10.2 ms can be achieved by using the actuation counter-electrodes, enabling the generation of a counter-force when the pull-in-driving voltage is applied. Acceleration forces present in the direction of pull-in can thus be compensated for, enabling a constant nominal t_{PI} for higher accelerations. The voltage V_{EF} (for electrostatic compensation feedback) required on the opposite side electrodes to keep the pull-in time at 10.2 ms increases with higher accelerations (in the direction of pull-in). Simulations have been performed with different acceleration values. Iteratively, the voltage V_{EF} required to keep t_{PI} constant was determined and fitted to a polynomial function $V_{EF} = f(a_{ext})$. Following, smaller accelerations of - 1 mg and - 4 mg were added (not compensated by V_{EF}). Figure 6.4 shows the modeled system's response and corresponding voltages. The results show that the sensitivity is maintained throughout the entire range of accelerations tested and therefore it is possible to extend the pull-in time with accelerations up to 600 mg with a voltage $V_{EF}\,[V] \approx \sqrt{30.98\, a_{ext}[g]}$. DC accelerations up to 600 mg have been considered. It is possible to

extend pull-in time for larger accelerations, but the experimental implementation is already limited to approximately 400 mg, for which V_{EF} exceeds $V_{PI,a,op}$.

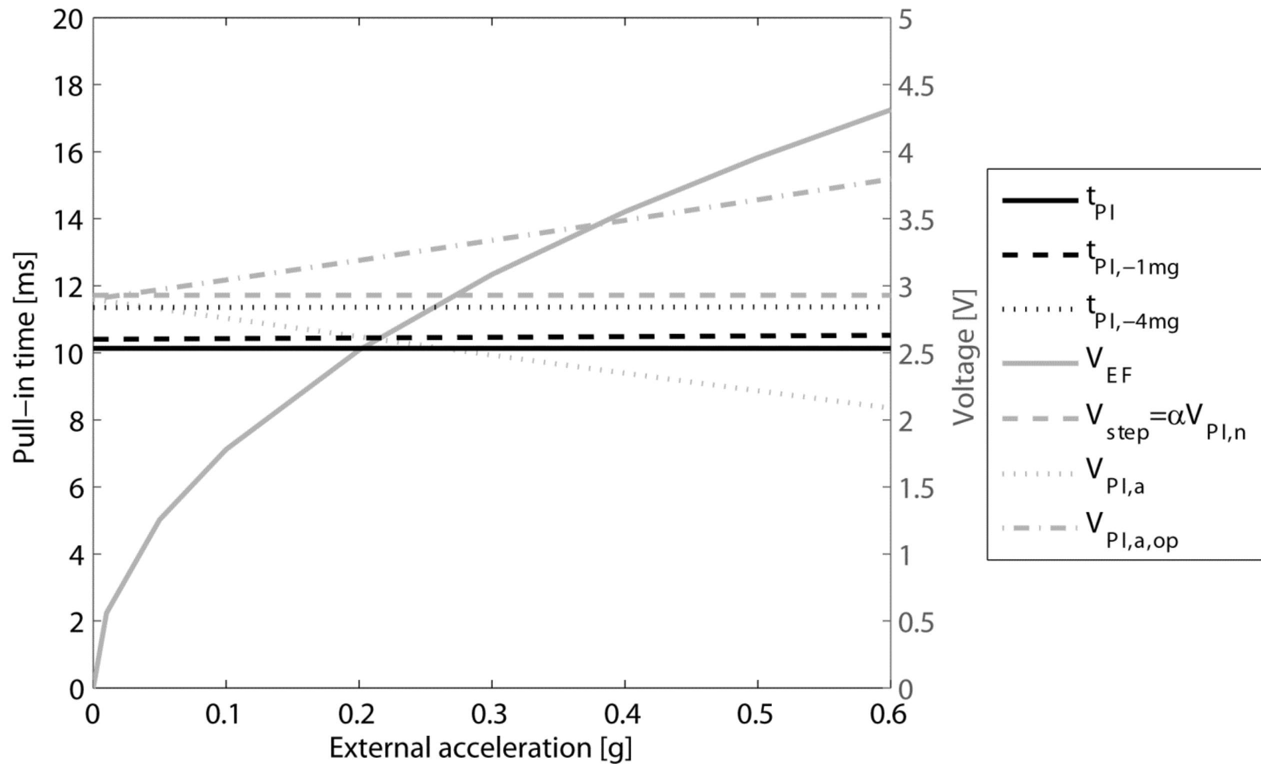

Figure 6.4: Simulation pull-in time results when actuating with constant $V_{step} = \alpha V_{PI,n}$ and $V_{EF} = f(a_{ext})$ and corresponding voltages, over large DC acceleration range and - 1 mg - 4 mg.

6.2.2.2. Other possibilities

Changing α (in $V_{step} = \alpha V_{PI,n}$ or $V_{step} = \alpha V_{PI,a}$), without using V_{EF}, may also allow compensating t_{PI} at large acceleration offsets. With accelerations occurring in the direction of pull-in (faster pull-in), the pull-in time can be extended by using a smaller α, and vice-versa, but the sensitivity depends nonlinearly on α, hence (it's expectable that) it is not kept constant.

Keeping t_{PI} constant with a DC acceleration offset may also be achieved by using different combinations of V_{EF} and V_{step}. This method has not been completely explored.

6.2.3. Model study conclusions

Two methods to extend the dynamic range of pull-in operated accelerometers have been thoroughly studied. Simulations show that keeping x_{PI} constant at $1/3\ d_0$ (in 6.2.1), does not yield a constant pull-in time or sensitivity, and therefore is not suitable for the accelerometer

closed-loop operation. In addition, this method is difficult to implement since both actuation voltages (V_{step} = 1.01 $V_{PI,xPI}$ and $V_{EF,xPI}$) depend on external acceleration.

The second presented method, pulling-in with constant $V_{step} = \alpha\ V_{PI,n}$ while compensating with V_{EF} (6.2.2.1), seems to be effective in extending the dynamic range while maintaining sensitivity, according to the simulations performed. Next, the experimental implementation of this approach is presented.

6.3. Sensitivity verification over an extended operation range

The proposed sensitivity linearization technique using electrostatic feedback (V_{EF} manipulation while pulling-in with $V_{step} = \alpha V_{PI,n}$) was verified experimentally. The MEMS structure S0 has been used for the implementation of the closed-loop approach. The structure possesses parallel-plate capacitors separated in different groups for actuation and for sensing on each side. The inertial mass can be pulled-in to either side, by using one of the two sets of symmetrical actuation electrodes.

The use of the S0 structure Simulink model enabled to derive an expression for the feedback voltage, $V_{EF} = f(a_{ext})$, necessary to keep pull-in time constant at 10.2 ms, as a function of the external DC acceleration. The squared electrostatic feedback voltage is linear with acceleration and can be approximated to $V_{EF}^2 \approx 30.98\ a_{ext}$ (a_{ext} in g), i.e., $V_{EF} \approx 5.57\ a_{ext}^{0.5}$, with R^2=0.9994.

According to the simulations, this method is usable with accelerations up to 400 mg, the limit for which the compensation voltage does not exceed the pull-in voltage on the side it is being applied ($V_{EF} = V_{PI,a,op}$). Beyond that value, pull-in occurs to the opposite side.

Small AC accelerations in the order of a few milli-g (up to 4 mg) were measured over larger DC acceleration offset up to 400 mg, in order to verify if the nominal sensitivity can be observed over such large acceleration offsets.

6.3.1. Experimental verification

The experiments with external acceleration were performed on a setup comprising a platform with one fixed end and a free end controlled by a vibration exciter (Figure 6.5, left). A shaker changes the horizontal level (angle ϕ) of the platform (where the sensor was placed), which allows the generation of small accelerations ($a_{ext} = \sin\phi$ [g]). The DC accelerations are set

using the screws that hold the readout circuit PCB in which the sensor is placed (tilting the accelerometer).

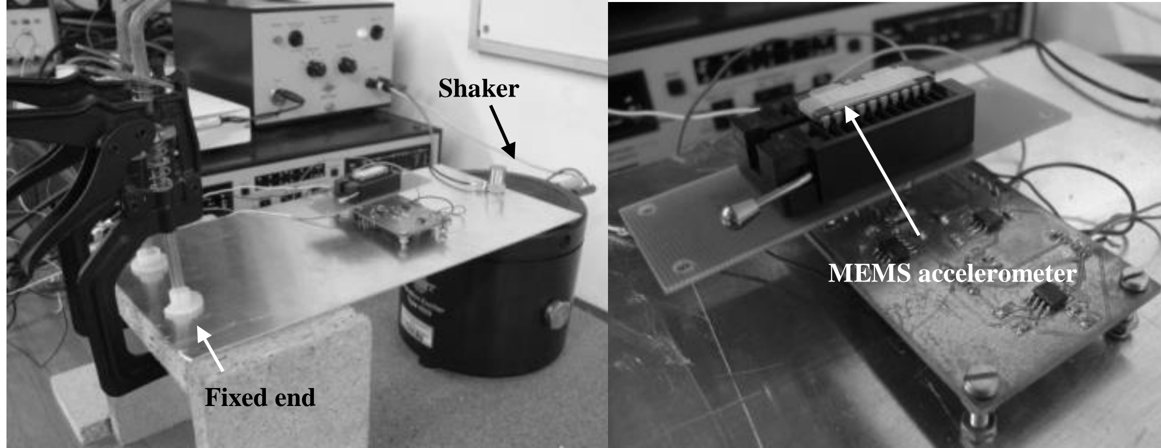

Figure 6.5: Photograph of the experimental setup used and detail of the accelerometer mounted on the PCB readout circuit.

The actuation voltages were provided by the NI USB-6281 data acquisition board (DAQ) [6.4]. The capacitive readout analog output was also acquired by the same DAQ and later processed on Matlab to retrieve the pull-in time (thus performing the time measurement). In this operation mode, the full pull-in time, taken by the structure to reach the stoppers, is measured.

Initially, a calibration step was performed to determine the pull-in voltage for each side ($V_{PI,a}$ and $V_{PI,a,op}$). The acceleration due to tilt is retrieved from the calibration results as $a_{ext} = f(V_{PI,a}, V_{PI,a,op})$ (function obtained through Simulink modeling).

The analytic expression for the feedback voltage $V_{EF} = f(a_{ext})$ is used to calculate the V_{EF} to be applied experimentally, while inducing pull-in with $V_{step} = \alpha V_{PI,n}$. The starting V_{EF} value is posteriorly fine-tuned iteratively to yield a t_{PI} of 10.2 ms over a determined acceleration offset due to tilt, while the AC acceleration is off.

Figure 6.6 presents the sensor output with AC accelerations ranging from ±1 to ±4 mg, applied at 1 Hz, and a DC acceleration (tilt) of 200 mg, while being compensated with the corresponding V_{EF}. The t_{PI} measurements were performed at approximately 50 pull-ins per second. The same procedure was repeated for several DC acceleration values between 0 and 400 mg. The results for the measured pull-in voltages and applied feedback voltages are gathered in Figure 6.7. Figure 6.8 shows the accelerometer response to ±4 mg AC acceleration, and the measured sensitivity.

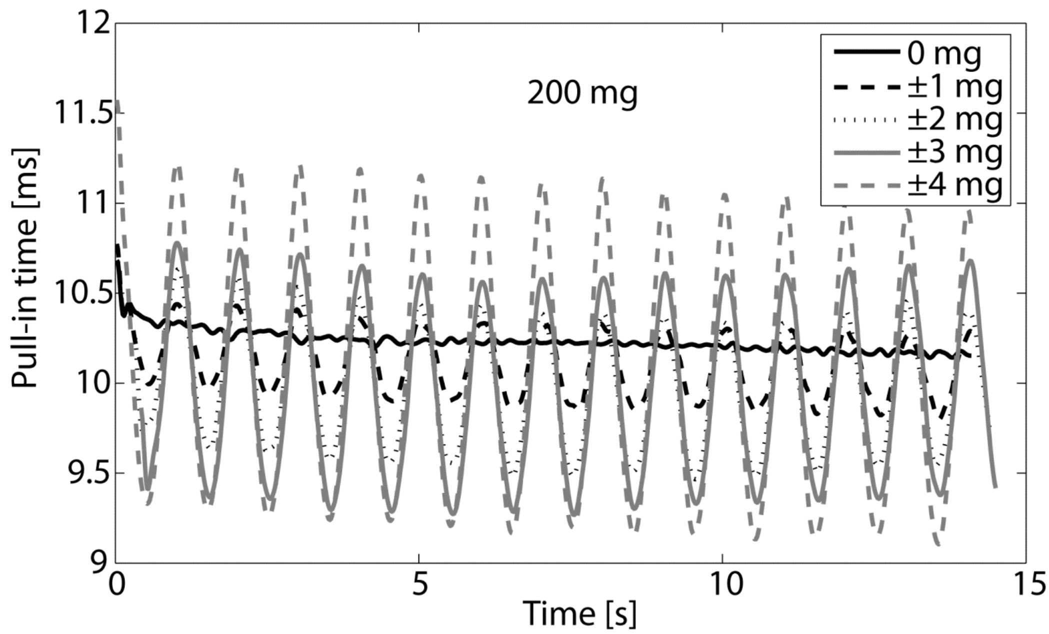

Figure 6.6: Pull-in time results for AC acceleration values of ± 1 to ± 4 mg, at 1 Hz, over a 200 mg DC acceleration.

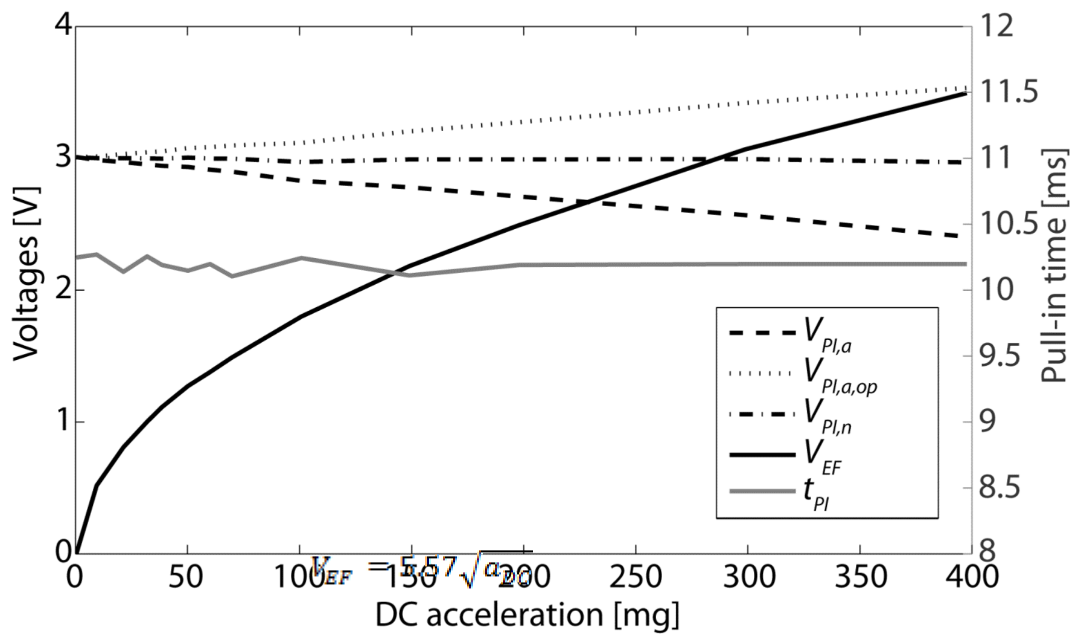

Figure 6.7: Pull-in voltages results and electrostatic compensation voltage applied.

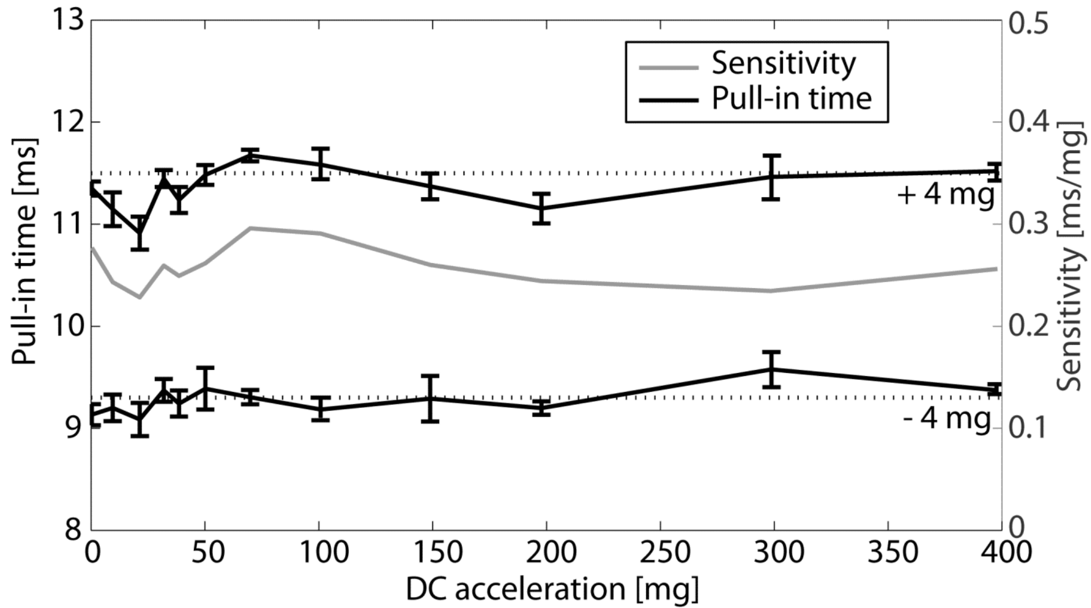

Figure 6.8: Accelerometer response to ± 4 mg AC acceleration, with DC accelerations compensated electrostatically, and resulting sensitivity.

6.3.2. Discussion

The results show that t_{PI} can be compensated, i.e. extended up to its nominal value of 10.2 ms, while keeping sensitivity constant, over an extended acceleration range of ± 400 mg. If the resolution limit of 2.7 µg is considered, a dynamic range of 109 dB is obtained. The $V_{EF} = f(a_{ext})$ necessary to be applied in order to maintain the t_{PI} constant is in very good agreement with the simulations $\left(V_{EF} = 5.57\sqrt{a_{DC}} \leftrightarrow V_{EF} = \sqrt{31\, a_{DC}}\right)$.

If an algorithm is implemented to set the required V_{EF} to keep pull-in time at the nominal value, the total acceleration acting on the system can be defined as $a_{ext} = a_{DC} + a_{AC}$ where a_{DC} is a function of V_{EF}, $a_{DC} \approx \left(\frac{V_{EF}}{5.57}\right)^2$, and a_{AC} is a function of Δt_{PI}, $a_{AC} \approx \frac{t_{PI}-10.2\times10^{-3}}{0.26}$.

If the time measurement is performed with a resolution of 0.1 µs (10 MHz clock), corresponding to an AC acceleration resolution of 0.38 µg, a 120 dB dynamic range can be obtained with the pull-in time accelerometer sensing approach (if larger inertial masses are used with an acceleration mechanical thermal noise lower than 0.38 µg). In order to guarantee that the voltage noise is not the resolution limiting factor (the acceleration-referred V_{EF} voltage noise does not exceed 0.38 µg), V_{EF} must be controlled with a resolution better than $5.57 \times \sqrt{0.38\ \mu g} = 3.4\ mV$, which is feasible.

These results demonstrate that high-resolution pull-in time accelerometers can be operated on an extended range, preserving the characteristic high resolution due to the time-based transduction method. For real-time operation an effective feedback electrostatic compensation controller is required that is capable to set V_{EF} based on the measured pull-in time, $\Delta V_{EF} = f(\Delta t_{PI})$.

6.4. Closed-loop real time operation

In this section, rather than the t_{PI} measurement per se, the counter-actuation voltage (V_{EF} - electrostatic feedback), necessary to keep t_{PI} constant at the nominal value is used as the transduction mechanism. A control algorithm was implemented digitally to calculate and update V_{EF} through the DACs (digital-to-analog converters) connected to the actuation electrodes of the microstructure (Figure 6.9). The pull-in time accelerometer is therefore closed-loop operated, yielding an increased dynamic range and largely improving linearity.

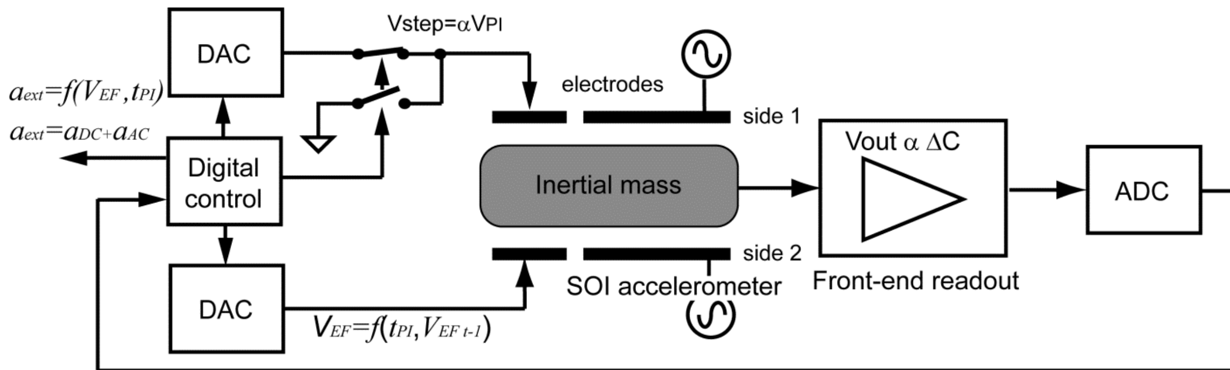

Figure 6.9: Closed-loop pull-in accelerometer setup.

6.4.1. Control algorithm

The existing Simulink model was extended to include the controller for closed-loop operation. A reference t_{PI} value of 9.89 ms, instead of 10.2 ms, has been used to calculate Δt_{PI} because it's the time taken by the structure to travel 1.8 µm (90% of the gap) with no external acceleration. The voltage V_{step} is turned off before the structure reaches the stoppers. The model was used to study the best function $\Delta V_{EF} = f(\Delta t_{PI})$ that updates V_{EF}, $V_{EF\ \mathbf{t}} = V_{EF\ \mathbf{t-1}} + \Delta V_{EF}$, and enables operation in the acceleration range ± 400 mg while minimizing the response time, overshoot and oscillations around the target value.

Firstly, a proportional control algorithm was tested: $\Delta V_{EF} = -50\Delta t_{PI}$, where $\Delta t_{PI} = t_{PI} - 9.89\times10^{-3}$. A measured t_{PI} lower than 9.89 ms yields a negative value of Δt_{PI} and the negative proportionality constant makes the V_{EF} voltage increase (and vice-versa). Figure 6.10

presents the response to acceleration steps of 50 mg and 300 mg. From the results, it is evident that a higher proportionality constant is more adequate to smaller acceleration values while for higher values of acceleration, a smaller proportionality constant is desirable.

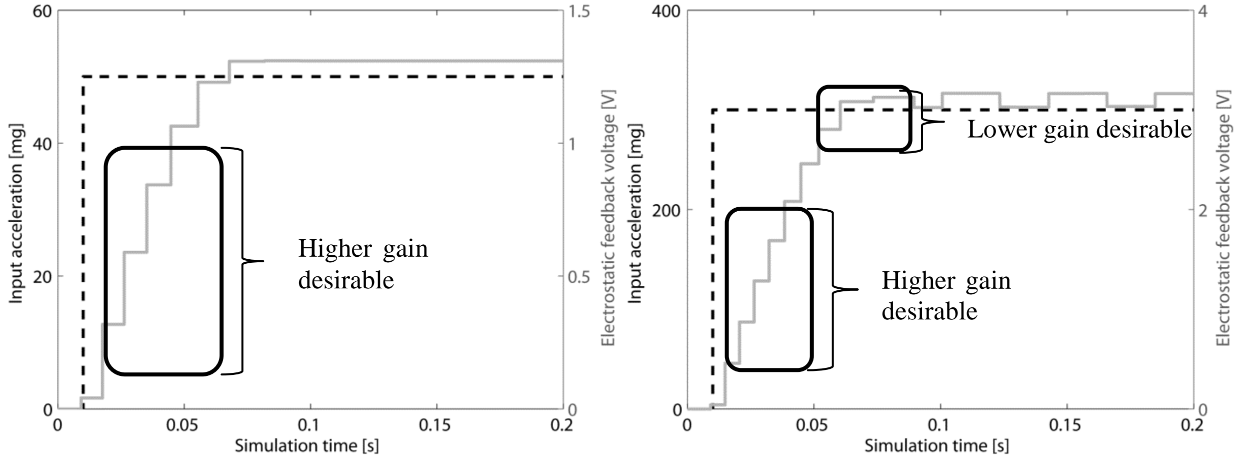

Figure 6.10: Response of proportionality constant (50) algorithm.

For 300 mg a lower gain is required when the voltage approaches the vicinity of the target value, in order to enable V_{EF} to stabilize, while for 50 mg this proportional gain allows stabilization. This can be achieved by implementing a non-linear gain that decreases with V_{EF}, such as $e^{-V_{EF}}$. To improve response time, the gain should also be higher for larger Δt_{PI} values.

The following control law was defined and tested on the Matlab/Simulink model:

$$V_{EF} = V_{EF} + gain\left(1.5\Delta t_{PI}^{\ 2} - 30\Delta t_{PI}\right) - 20\Delta t_{PI}$$
$$gain = 7e^{-V_{EF}} \qquad (6.5)$$
$$\Delta t_{PI} = t_{PI} - 9.89 \times 10^{-3}$$

This control law comprises a proportional term - $20\ \Delta t_{PI}$ and a variable gain term. The variable gain term is larger for smaller V_{EF} voltages ($gain_{V_{EF}\to 0} = 7$ and $gain_{V_{EF}=3.5} \approx 0.2$) since the V_{EF} change rate in respect to acceleration is higher for smaller accelerations and therefore V_{EF} must change faster. For higher V_{EF} values, the variable gain is almost negligible. V_{EF} should also change faster for larger Δt_{PI} values, which is included through the use of a squared term $\Delta t_{PI}^{\ 2}$.

According to the simulations, this control algorithm is capable of compensating for sinusoidal accelerations spanning the entire measurement range of the accelerometer, ±400 mg, at 1 Hz. Figure 6.11 shows the response of this control algorithm to different amplitude acceleration

steps and Figure 6.12 shows the simulation results with sinusoidal accelerations. Although it is clear there is room for improvement, this algorithm has been implemented and experimentally tested. It should be noted that the development of a proper controller is not a trivial issue and would require a lot of time. Since the controller was not the focus of the thesis, a more empiric approach was taken here.

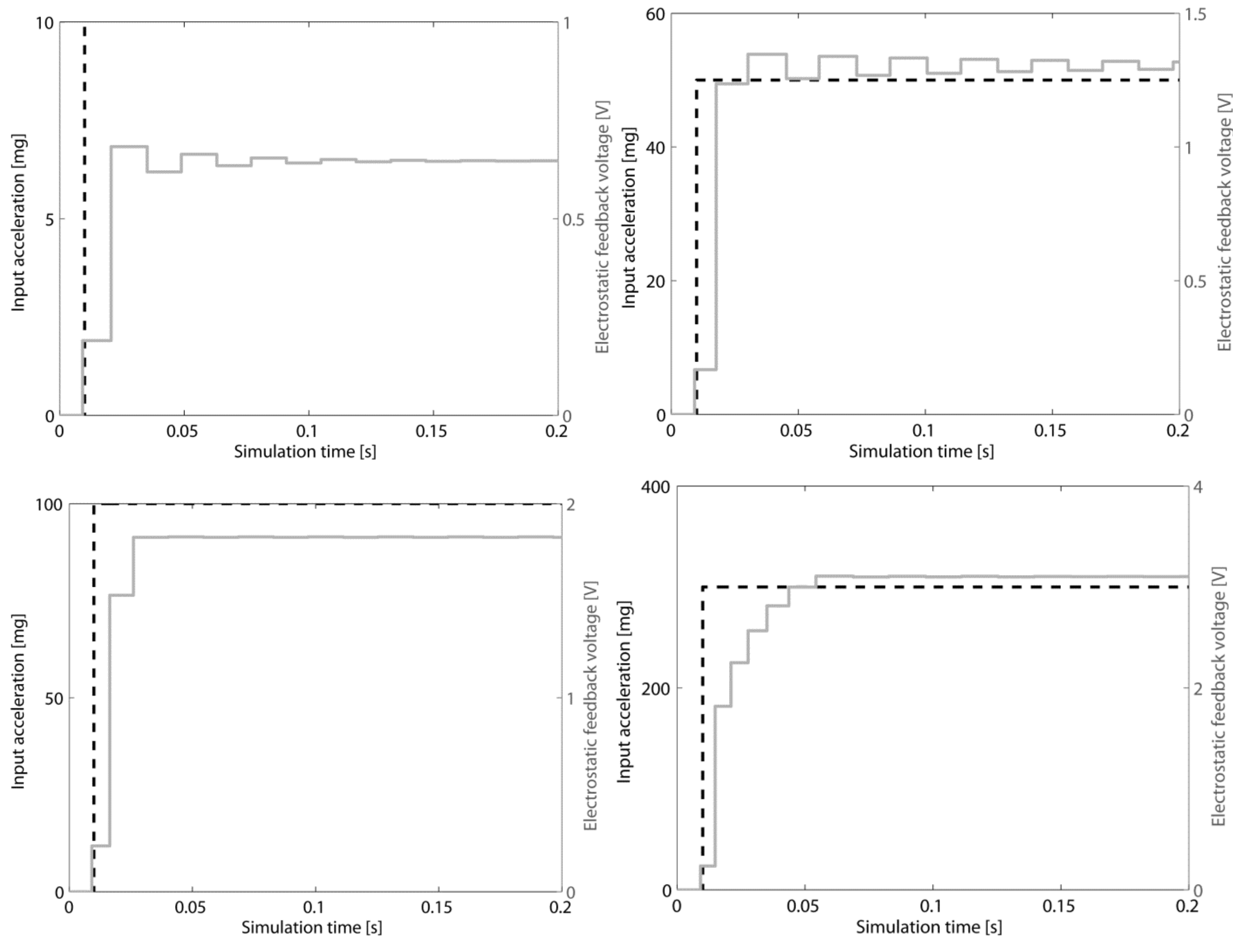

Figure 6.11: Control algorithm response to acceleration steps of 10, 50 100 and 300 mg.

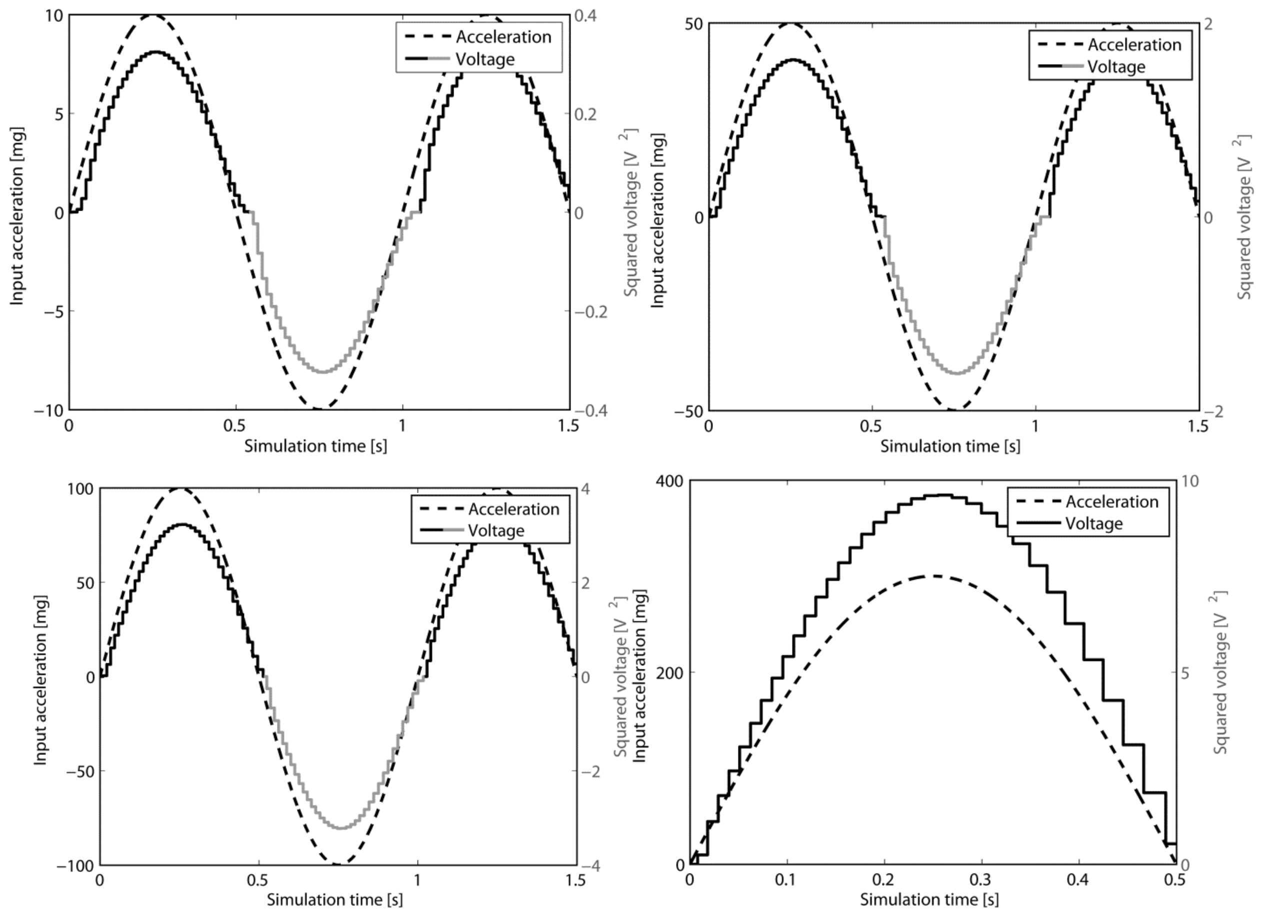

Figure 6.12: Control algorithm response to sinusoidal acceleration of amplitude 10, 50 100 and 300 mg.

6.4.2. Experimental setup

The fabricated devices S0 were used to experimentally verify the closed-loop operation. The control algorithm was implemented in a Cyclone II FPGA (Field Programmable Gate Array) from ALTERA [6.5], working at 50 MHz (enabling a 20 ns resolution for the pull-in time measurement). Two 16 bits digital to analog converters (DAC) were used to generate the required V_{step} and V_{EF} voltages. A limit value for V_{EF} of 3.5 V was set at the FPGA program in order to avoid pulling-in with the compensation voltage.

Initially, the sensor plus PCB were mounted on the elevator platform depicted in Figure 6.13. A high-precision laser distance meter was used to measure the angle of the platform (to calculate the input acceleration). This setup was used to calibrate the system. Afterwards, another setup was used to generate external sinusoidal accelerations, consisting of the accelerometer PCB mounted on the shaker, (attaching one extremity and fixing the other (Figure 6.14). The shaker changes the horizontal level (angle ϕ) of the sensor which allows the generation of sinusoidal accelerations ($a_{ext}=sin(\phi)$ [g]).

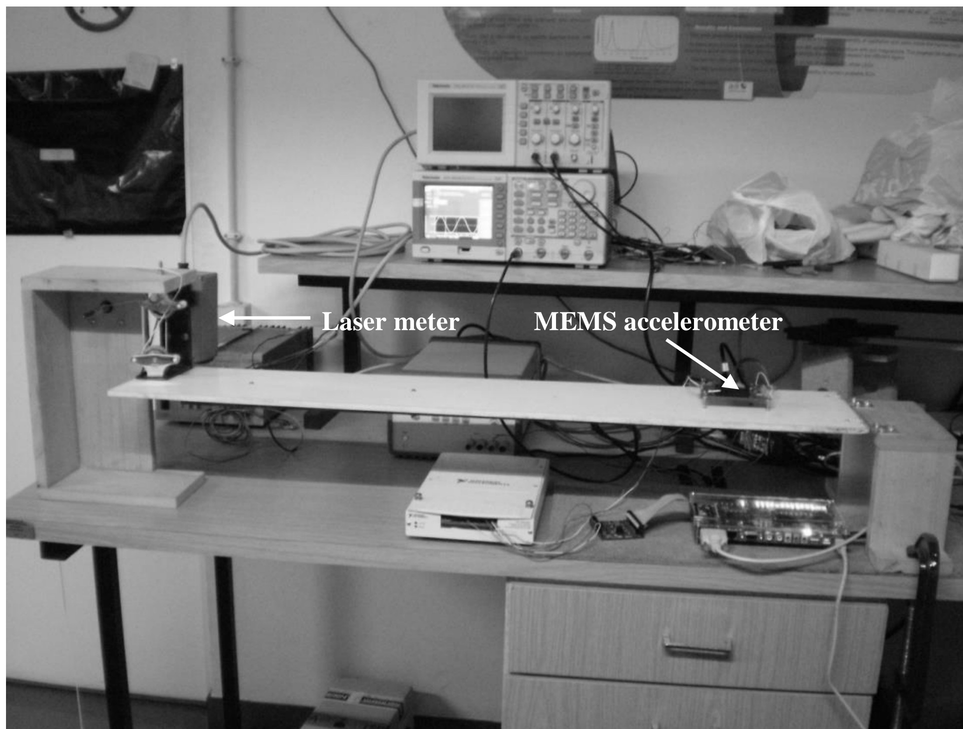

Figure 6.13: Photograph of the accelerometer and the readout circuit PCB mounted on the elevator structure.

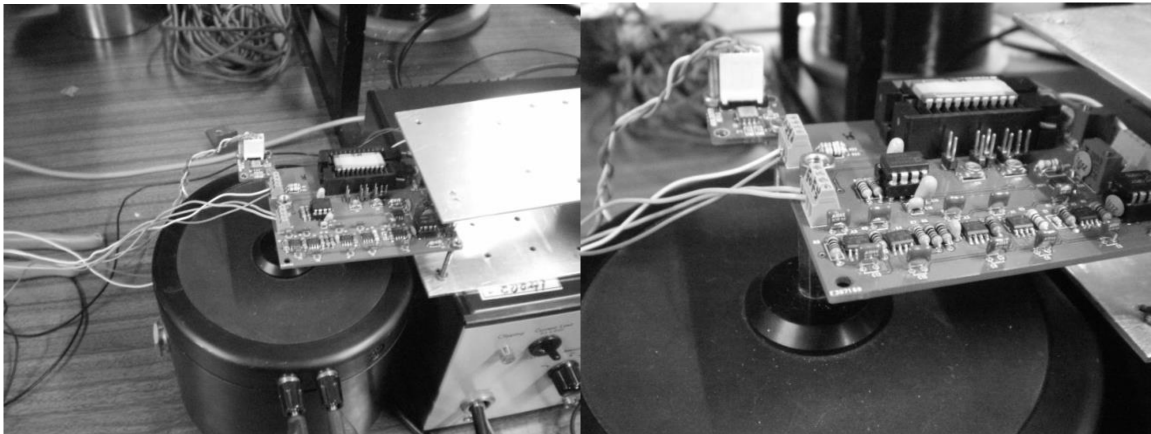

Figure 6.14: Photograph of the accelerometer and the readout circuit PCB mounted on the shaker.

6.4.3. Results

Some experimental results are presented in Figure 6.15-Figure 6.18. Figure 6.15 presents two constant AC acceleration for which the control algorithm can compensate the pull-in time reasonably well. Figure 6.16 shows increasing AC acceleration values at constant offset, and it is clear that the efficiency of the control algorithm decreases as the acceleration magnitude increases. Figure 6.17 shows that as the AC acceleration increases, the voltage switching actuates compensating also for accelerations in the opposite direction.

Figure 6.18 presents the sensor or a 1 Hz input acceleration of 110 $mg_{p\text{-}p}$ over a 15 mg offset, showing the control switching effectiveness more clearly. The pull-in time measurement was performed at a frequency of approximately 50 pull-ins per second. These results clearly show the effectiveness of the control algorithm and the capability of the controller to shift the voltages between left and right electrodes.

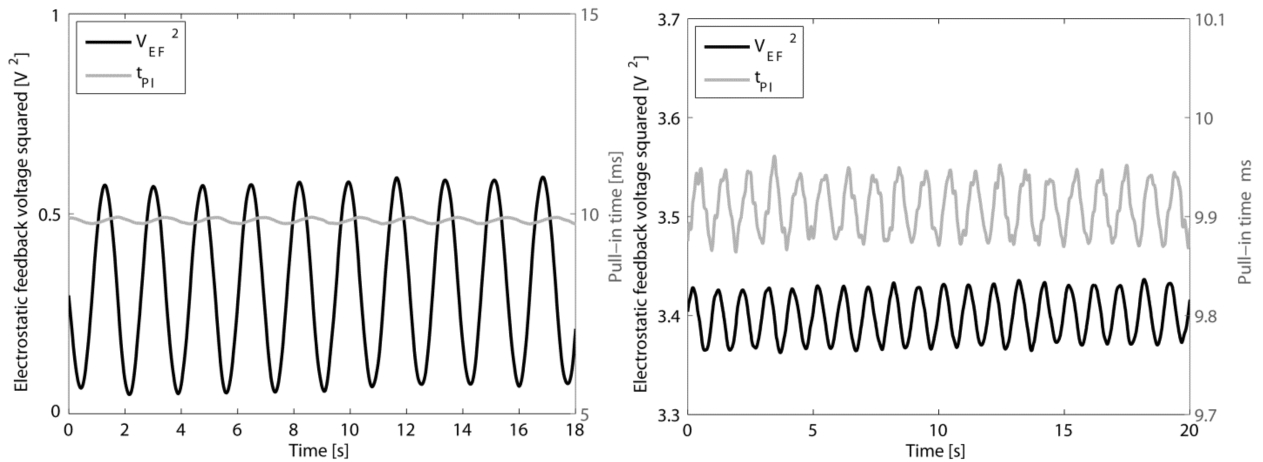

Figure 6.15: Experimental pull-in time and V_{EF} results under (left) an AC acceleration of 8 $mg_{p\text{-}p}$ at 1 Hz, over a 13 mg offset and (right) an AC acceleration of 2 $mg_{p\text{-}p}$ at 1 Hz, over a 110 mg offset.

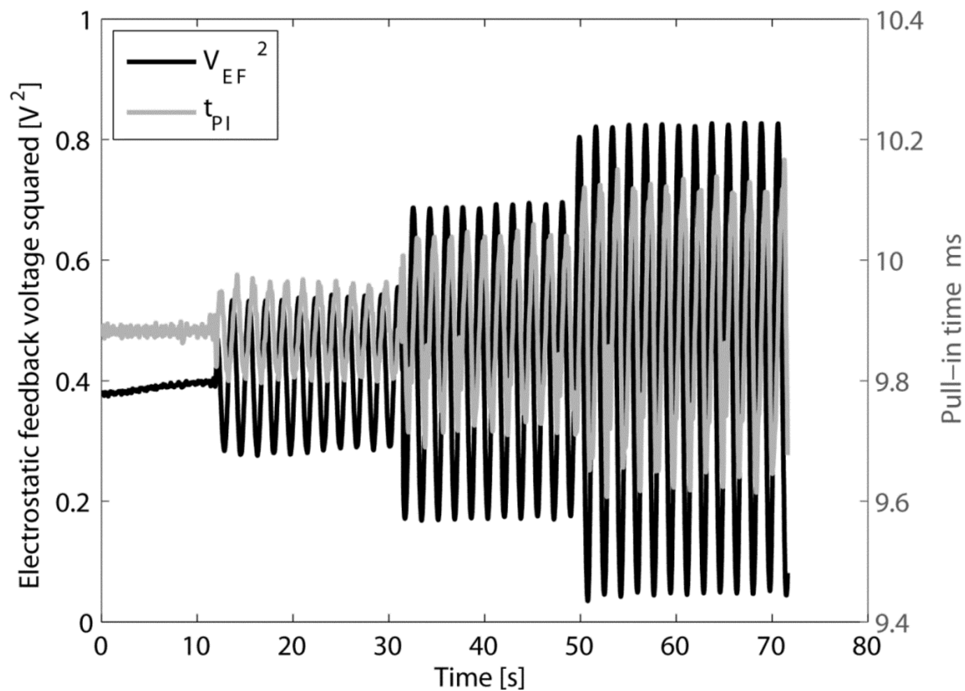

Figure 6.16: Experimental pull-in time and V_{EF} results under an increasing AC acceleration of 26 $mg_{p\text{-}p}$ over a 14 mg offset.

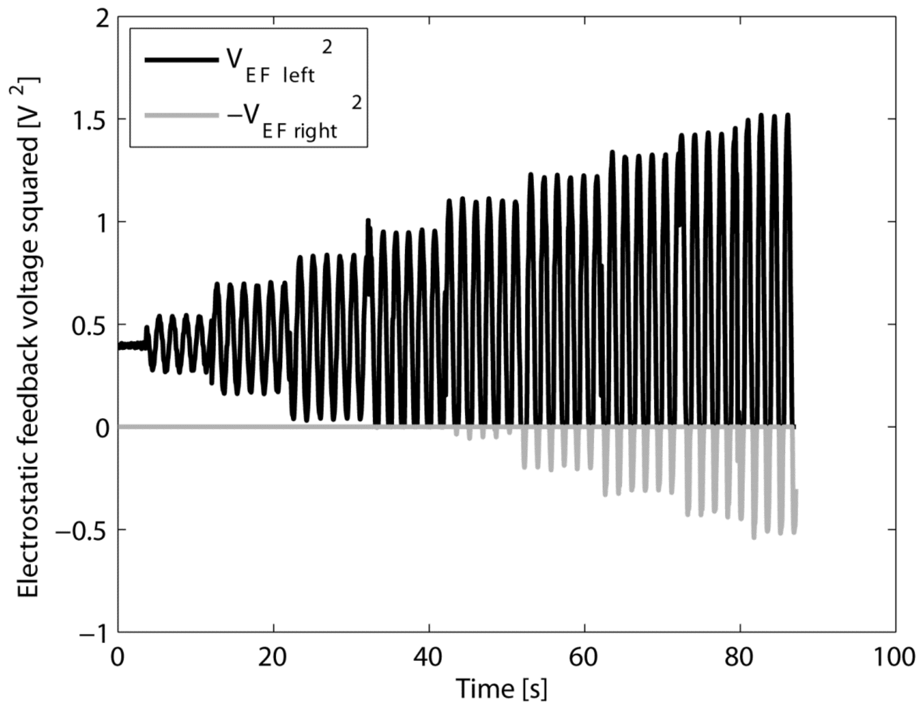

Figure 6.17: Experimental V_{EF} results under an increasing AC acceleration of 66 mg_{p-p} maximum over a 14 mg offset.

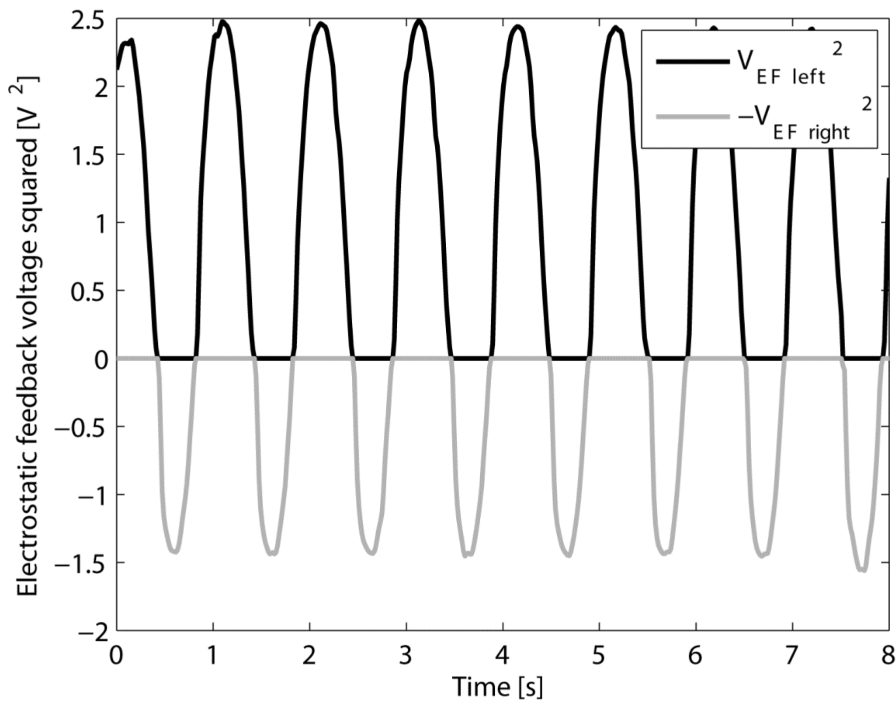

Figure 6.18: Electrostatic feedback voltage results for 125 mg_{p-p} acceleration, at 1 Hz, over a 14 mg offset.

Figure 6.19 shows the closed-loop accelerometer response to the different applied accelerations where the high sensitivity of this approach is demonstrated. Further increase in

sensitivity is possible by designing the electrostatic feedback electrodes with smaller capacitance (higher feedback voltages required). This closed-loop accelerometer approach presents good linearity over the full operation range with a sensitivity of 30.9 V^2/g. If the resolution limit of 2.7 µg (set by the mechanical-thermal noise of this specific microstructure) is considered, a dynamic range of 109 dB is obtained.

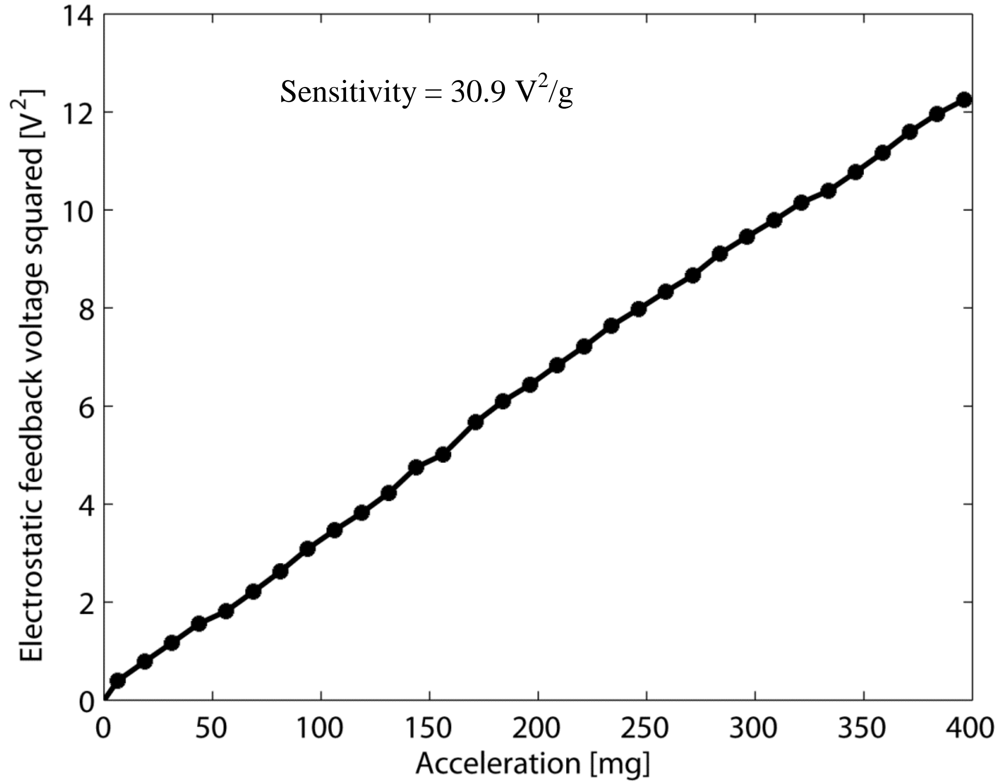

Figure 6.19: Electrostatic feedback voltages for the different external accelerations applied.

Within the range of accelerations tested, it was found that t_{PI} can be compensated, i.e. extended up to its nominal value, demonstrating high-resolution closed-loop real-time operation of pull-in time accelerometers. The high sensitivity has been preserved and the total acceleration acting on the system is defined as $a_{ext} = a_{V_{EF}} + a_{t_{PI}}$ where $a_{V_{EF}}$ is a function of V_{EF}, $a_{V_{EF}} \approx \left(\frac{V_{EF}}{5.56}\right)^2$,

and $a_{t_{PI}}$ is a function of Δt_{PI}, $a_{t_{PI}} \approx \frac{t_{PI} - 9.9\times10^{-8}}{0.26}$.

The FPGA 20 ns time measurement resolution corresponds to an acceleration resolution limit of 77 ng. The total acceleration measurement resolution would be limited not by the measurement resolution, as it is most frequent, but by the mechanical-thermal noise of the MEMS structures used (as it is the case of this study). Table 6.1 presents the main characteristics of this accelerometer.

With the control law implemented, the bandwidth is limited to 1 Hz. Overcoming this aspect requires optimizing the control, which is not a trivial task and requires an extensive study.

Table 6.1: Main accelerometer parameters.

Device parameters	Value
Natural resonance frequency (f_0)	515 Hz
Sensor bandwidth (BW=1/2 t_{PI})	50 Hz
Control-loop bandwidth	1 Hz
Sensitivity	30.9 V^2/g and 0.26 µs/µg
Operation range	± 0.4 g (minimum)
Time measurement input-referred resolution	77 ng (clk 50 MHz)
Dynamic range	110 dB
Mechanical-thermal noise	2.7 µg/√Hz (38 µg @ 200 Hz)

6.5. Conclusions

A high-resolution, high-sensitivity capacitive accelerometer based on pull-in time measurement has been described. Non-linearity is the main characteristic compromising performance of high-sensitivity pull-in time operated open-loop accelerometers. An electrostatic compensation technique that addresses the non-linearity problem, based on the control of the pull-in time duration, has been presented and its implementation in a real time closed control loop has yielded an accelerometer with 30.9 V^2/g sensitivity, over a dynamic range of approximately 109 dB. Capacitive parallel-plates MEMS structures were used and the measured sensitivities for different acceleration ranges confirm the potential of this technique and the overall accelerometer concept.

The pull-in time accelerometer concept enables very high resolutions since the transduction method relies on time measurements, and the verified sensitivity of the electrostatic feedback voltage to external acceleration is very high.

The limitations of the closed-loop pull-in time accelerometer implemented are still considerable, and further efforts are required to improve it, namely optimization of the feedback electrostatic compensation circuit in order to allow its use over the current limited bandwidth.

One possible problem affecting the accelerometer is the sensitivity to low frequency noise on the pull-in drive voltage. Although this subject was not studied in this chapter, similarly to the open-loop operation it is likely that it will also be present in closed-loop operation. Means to

improve this feature, possibly requiring implementation of functionalities in the mechanical domain, should be studied in the future.

In conclusion, it has been shown that closed-loop operation method can improve linearity and enable the use of high-sensitivity, high-resolution pull-in time accelerometers to measure acceleration over a much larger dynamic range than in open-loop operation.

References

[6.1] R. A. Dias, L. Mol, R. F. Wolffenbuttel, E. Cretu, and L. A. Rocha, "Design of a time-based micro-g accelerometer," *IEEE Sensors Journal*, vol. 11, no. 8, pp. 1677–1683, 2011.

[6.2] R. A. Dias, E. Cretu, R. Wolffenbuttel, and L. A. Rocha, "Pull-in-based μg-resolution accelerometer: Characterization and noise analysis," *Sensors and Actuators A: Physical*, vol. 172, no. 1, pp. 47–53, Dec. 2011.

[6.3] R. A. Dias, R. F. Wolffenbuttel, E. Cretu, and L. A. Rocha, "Sensitivity linearization technique for a time based MEMS accelerometer," in *Proceedings of Transducers*, 2011, pp. 715–718.

[6.4] National Instruments, "NI USB-6281 Datasheet," 2012.

[6.5] Altera Corporation, "Cyclone II Device Handbook , Volume 1," 2008.

7.

Gas viscosity sensing based on pull-in time

In this chapter, a viscosity sensing application using pull-in time is introduced. The nonlinear dynamic analysis performed in Chapter 2 demonstrated the influence of damping conditions on the pull-in time of devices operated at metastability while in Chapter 4 an analysis to squeeze-film damping in parallel-plate MEMS was performed. The fundamentals of pull-in behavior suggest that pull-in can be used for the implementation of a gas viscosity sensor.

This chapter starts by introducing the currently existing viscosity measurement methods applied to gases, both using conventional instruments and microsystems, and its applications. The idea of using the electrostatically operated microstructures for gas viscosity sensing is not new [7.1]–[7.5], but so far the pull-in transition has not been explored for this purpose. The proposed approaches that use MEMS structures either use frequency resonance shift to detect changes in damping characteristics [7.1], [7.2], phase lag between electrostatic actuation and motion of a microstructure [7.3], or an actual fluid flow measurement method [7.4], [7.5]. A brief description of these approaches is given in the next section.

For a proper use of the pull-in time as a measure of the viscosity, the full system configuration must be considered. The nonlinear analysis performed in Chapter 2 is used here since it provides the right insight on the device dynamics regarding quality factor and damping. Also, the damping model studied in Chapter 4 is used to analyze the system. Finally, experimental verification is performed and the approach validated.

7.1. Viscosity measurement

Viscosity is the main parameter that characterizes the flow behavior of fluids. Frictional forces between molecules occur if a fluid is subjected to an applied force. The dynamic or absolute viscosity coefficient for Newtonian fluids is defined as the ratio of the shear velocity and the shear rate [7.6] expressed in the units Pa.s (Pascal.second) or Poise (10 μP = 1 μPa.s). Some instruments measure kinematic viscosity, which is the ratio between viscosity and density (units are m^2/s or Stokes) and absolute viscosity is generally referred to as dynamic viscosity. Sometimes viscometer manufacturers also provide specifications in term of acoustic viscosity, which is defined as absolute viscosity × density [7.7]. Viscosity measurement tools are widespread in industries for quality control of liquids, pastes and gases, dealing with products such as paints, lubricants, adhesives, fuels or food [7.8]–[7.11].

7.1.1. General viscosity measurement techniques

There are many types of viscometers available for liquids, generally classified by the actuation method, such as capillary, orifice, high temperature shear rate, rotational, falling ball, rising bubble, moving piston, vibrational or ultrasonic viscometers [7.12]. Most equipment on the market are laboratory instruments since samples have to be prepared and processed manually [7.6].

Due to the much lower viscosity of gases in general, in comparison to liquids, the forces involved are small and at the moment only a few measurement techniques developed for liquids viscosity sensing are capable of measuring viscosity in gases. As a consequence, the use of on-line gas viscosity sensing equipment is still not widely spread. Gas viscosity measurement is much more difficult due to the much lower viscosity of gases, typically in the range $\eta = 10^{-5}$ Pa.s as compared to 10^{-3} Pa.s for water and 10^{-1} Pa.s for oil. Only a few measurement techniques, such as the capillary tube [7.13], the vibrating wire and the moving-piston principle have been used in commercial gas viscometers [7.14]. As an example, the Cambridge Viscosity Inc. VISCOpvt moving-piston viscometer modified for gases has a measurement range of 10^{-4} Pa.s to 10^{-3} Pa.s with an accuracy of 1% [7.14]. In [7.15] a modified perturbation viscometer has been used to measure the gradient of viscosity of non-ideal binary gases mixtures as function of composition, but obtaining the absolute viscosity requires previous knowledge of one of the pure gases viscosity.

Great challenges exist in the design of new gas viscometers. Using new technology such as MEMS (Micro-Electro-Mechanical Systems) techniques may enable new opportunities for gas sensing because they are more suitable to measure the small frictional forces involved.

7.1.2. Viscosity measurement based on MEMS techniques

Most of the work reported in literature on gas viscosity measurements using microsystems use vibrating beams. There are a few exceptions that focus on the measurement of flow and pressure gradient to obtain viscosity. Characteristic parameters, such as resonance frequency, quality-factor and phase-shift depend on pressure and viscosity of the trapped gas and thus can be used for sensing these gas properties [7.1].

In [7.3], gas viscosity measurements using damping of a microstructure are demonstrated. The method uses the phase lag between the motion of a microstructure (Figure 7.1) and its actuation signal to measure the damping of a gas. The effective viscosities (normalized to the free gas viscosity) of some gases, with viscosities ranging from 8 to 22 μPa.s, were measured in the molecular and transitional flow regions, with an accuracy of 1% [7.3]. In this study, only the ration between viscosities is measured, not allowing the measurement of absolute values.

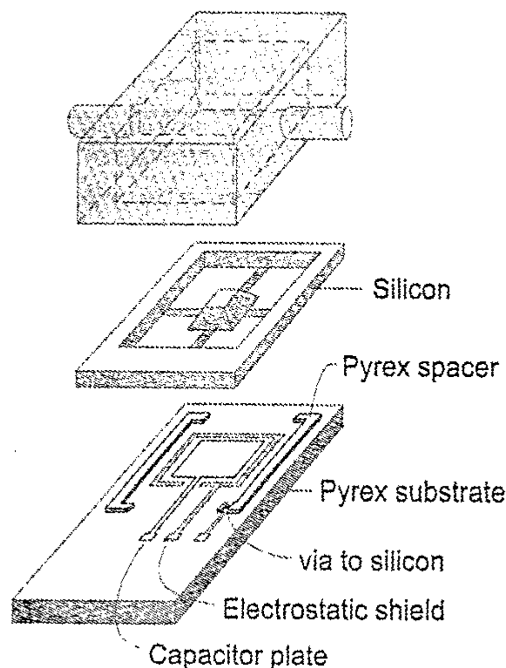

Figure 7.1: Beam-supported, mass-loaded plate, Pyrex substrate and gas-flow cap comprising the test structure [7.3].

In [7.4] a micromachined two dimensional resistor array has been used to measure temperature distribution, allowing measurement of flow velocity of heated gases and kinematic viscosity. Argon, carbon dioxide and nitrogen were used in the experimental validation, yielding an accuracy in the order of 5%.

A gas density and viscosity measurement system has been developed in [7.5], using flow and pressure gradient measurements. It comprises a commercial differential pressure sensor, a laminar flow rate MEMS sensor (micro hot wire anemometer chip) and a bi-cylindrical flow channel. Air and carbon dioxide have been tested with an uncertainty of less than 3% [7.5].

The work reported in [7.1], uses squeeze-film damping to measure the viscosity of gases. Satisfactory experimental results are not however available as measurements were performed at low pressures and the authors concluded that in these conditions the changes in quality factor and resonance frequency were gas independent.

More recently, quartz tuning fork resonators (32.768 kHz resonance frequency) have been used to measure simultaneously the density and the viscosity in gases at a measurement frequency (density/viscosity sampling frequency) of 1 Hz, using a frequency tracking method (measuring motional resistance due to viscous damping and resonance frequency shift due to mass loading) and fitting data in an equivalent circuit model [7.2]. The deviations/errors obtained in the viscosity measurements were less than 2% for densities above 3 kg/m^3 (achieved by performing the measurements at high pressures).

The resonating beams used for measuring viscosity reported in literature can be fabricated in the same technology as the device presented here. However low gas damping is required for operation of these structures in resonance, and low damping cannot always be achieved at atmospheric pressure levels, when designing large capacitances, required for increased signal levels. Moreover, at higher frequencies, the effects of compressibility and inertia of the gas become significant and the relation between viscosity and damping force becomes non-linear. Resonance operation, at standard conditions in most gases, is generally only possible in very small microstructures. In general, these devices operate at a much higher motion frequency than the microsystem described here.

Using the pull-in event for the measurement of viscosity as presented here is new and has several advantages. Firstly, the critical pull-in displacement of a lateral comb microstructure is well defined, since it depends mainly on the geometry of the structure. Secondly, pull-in operation enables the largest possible displacement of the structure, which is an advantage in relation to conventional electrostatic actuators where pull-in is avoided and displacement is

limited to 1/3 of the total gap and is also an advantage in terms of readout capabilities (larger sensing capacitance). Thirdly, the large increase of the displacement signal when pull-in occurs enables accurate detection of the pull-in time of the structure and measurement of the damping. Finally, as the operating frequency is low, for the gap dimensions used and viscosities measured, the gas inertia (and gas density) plays a negligible role (frequencies much lower than the inertial cut-off frequency).Therefore, absolute (not kinematic) viscosity is measured.

7.1.3. Application areas for gas viscosity sensors

Knowledge of the rheological characteristics of a gas is valuable in predicting the flow and pumpability of gas distribution systems or the flame properties and performance in the nozzles of gas burners. Viscosity gas sensors can therefore be used for monitoring of the quality of combustible gas e.g. in burners. Another challenging application is the detection of the composition of a gas mixture by the measurement of viscosity and several other physical parameters of the gas mixture. Quality control of natural gas is another target application for composition measurement using viscosity sensors. Conversely, if the gas temperature and composition is known, the gas density can be calculated from the measured viscosity coefficient [7.16]. New applications can arise if small, portable and low-cost systems are developed.

7.1.4. Gas viscosity theory

The simplest version of the kinetic theory of gases (molecules treated as hard spheres of diameter d_m) allows a qualitative analysis of the viscosity coefficient. It can be shown that the viscosity coefficient is proportional to both the mass density ρ, the mean free path λ and the mean velocity, $\bar{u}$, of the atoms in gas [7.17], [7.18];

$$\eta = \frac{1}{3}\rho\bar{u}\lambda \qquad (7.1)$$

The mean velocity is defined as

$$\bar{u} = \sqrt{\frac{8k_B T}{\pi M_m}} \qquad (7.2)$$

where M_m is molecular mass. The mean free path is defined by the same model as [7.19]:

$$\lambda = \frac{k_B T}{\pi\sqrt{2} p {d_m}^2} \tag{7.3}$$

where k_B is the Boltzmann constant (at pressure p and temperature T). By combining these three expressions, the viscosity of an ideal gas can be rewritten:

$$\eta = \frac{1}{3}\rho\sqrt{\frac{8k_B T}{\pi M_m}}\frac{k_B T}{\pi\sqrt{2} p {d_m}^2} = \frac{2\sqrt{M_m k_B T \pi}}{3{d_m}^2\pi^2} \tag{7.4}$$

From this expression, viscosity is independent from pressure. Experimentally this behavior has been confirmed up to approximately 10 atm, above which it is no longer verified. The assumption that viscosity is roughly independent of pressure [7.20], [7.21] is valid for dilute gases, at low pressures, not for gas at high pressures. The predicted temperature dependence is less satisfactory. A good approximation of the temperature dependence of the viscosity in gases has been given by Sutherland [7.21], [7.22]:

$$\eta = \eta_{T0}\left(\frac{\mathrm{T}_0 + C_S}{\mathrm{T} + C_S}\right)\left(\frac{T}{\mathrm{T}_0}\right)^{3/2} \tag{7.5}$$

with η_{T0} the viscosity at a reference temperature T0 and CS the gas-specific Sutherland's constant.

This work aims the viscosity measurement of pure gases as well as viscosity of gaseous mixtures. The viscosity of a mixture of gases depends nonlinearly on the composition and viscosity of each gas. The viscosity of mixtures of n gases can be calculated using the equation (7.6) [7.23]:

$$\eta_n = \sum_{i=1}^{n} \frac{\eta_i}{1 + \frac{1.385\eta_i}{x_i \rho_i}\sum_{\substack{j=1 \\ j\neq i}}^{n}\frac{x_i}{D_{ij}}} \tag{7.6}$$

where ρ_i is density, x_i is molar fraction of gas i in the mixture and D_{ij} is the diffusion coefficient of gas i in gas j [7.19], [7.24], [7.25].

7.2. Principle of operation of the viscosity sensor based on pull-in time

The gas viscosity sensing method studied here uses the pull-in effect of electrostatically actuated, capacitive microstructures as the sensing mechanism, thus not requiring operation in

resonance. The pull-in time (t_{PI}) of a microstructure is measured, under well-defined electrostatic actuation conditions. The pull-in time is very sensitive to the damping conditions (as seen in Chapter 2), which depends on the viscous characteristics of the gas that fills the gap (according to the analytical damping model described in Chapter 4). In this mode of operation, at low frequencies, the effects of the mass or density of the gas on the overall tPI are negligible.

The pull-in time, the time required for the structure to move from the zero-displacement / rest position to (nearly) full-gap displacement, depends on the characteristics of the fluid filling the gap, such as viscosity. The basic topology of the viscosity sensor is the parallel-plate configuration considered throughout this thesis, shown in Figure 7.2. Gas fills the small gap between two rigid parallel surfaces, (with one 1-DOF plate anchored by a spring). During electrostatic operation the movable surface moves towards the fixed one with a displacement of almost the full gap distance and the gas will be squeezed out of the gap. Contact between the plates is prevented by physical stoppers that limit displacement.

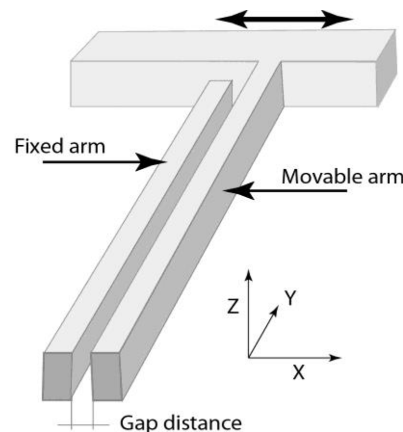

Figure 7.2: Basic topology of the viscosity sensor.

The length of the parallel-plates (squeeze-film damper) is much larger than the width and height dimensions justifying a 2D gas flow in the cross-section. The squeeze-film damping model [7.26]–[7.29] described in section 4.2 has been used for analysis of the structure. At low beam velocities a viscous gas flow in the gap can be assumed and the mass (density) of the gas can be neglected. The damping of the system is therefore proportional to the gas viscosity. The micro-scale sensor structure and co-integration of the electronic circuits enable this solution to be very small, light-weight, low-power and low-cost.

The pull-in is a very sensitive phenomenon and small changes in the intervenient forces, such as damping, affect greatly the overall duration of the event. This damping is determined by the geometry of the squeeze-film damper and the gas properties. Hence, variations in gas

properties (such as viscosity) are reflected in variations in pull-in time. It is worth noting that the electrostatic force depends on the dielectric permittivity of the medium, but as can be seen from Table 7.1, the variations in the relative permittivity value (and consequently in the capacitance and electrostatic force) for these common gases, taking air as reference, are negligible.

Table 7.1: Physical constants of a few common gases at standard conditions (1 atm and T= 293 K) [7.17], [7.19], [7.24], [7.30], [7.31].

Gas	Molecular weight	Density ρ (kg/m^3)	Viscosity η (μPa.s)	Mean free path λ (μm)	Thermal conductivity (mW/m.K)	Dielectric permittivity ε_r	$(\varepsilon_r-\varepsilon_{rair})/\varepsilon_{rair}$
Air	28.96	1.20	18.4	66.4	24.1	1.00054	0.00%
CH_4	16.00	0.67	11.0	51.6	30.01	1.00081	0.03%
CO_2	44.00	1.84	14.7	41.9	14.5	1.00092	0.04%
CO	28.00	1.17	17.4	62.9	24.6	1.00065	0.01%
N_2	28.02	1.17	17.6	63.1	24.3	1.00055	0.00%
H_2	2.02	0.08	8.8	118.7	168.4	1.00025	-0.03%
O_2	32.00	0.74	20.2	67.9	24.4	1.00049	0.00%
He	4.03	0.17	19.6	186.3	146	1.00007	-0.05%

7.2.1. Damping coefficient viscosity dependence

The squeeze-film damping model described in Chapter 4 is adopted for this study [7.26]–[7.29]. Inertial effects have been disregarded as they are negligible at the frequencies used in this approach. The compressibility effects are also significant only for velocities much higher than those used in these experiments. Moreover, in this approach the structures are designed for increased damping, i.e., the system will be overdamped for most gases, and in such cases the overall pull-in time is dominated by the metastable region characterized by slow movement which results in a t_{PI} insensitive to high frequency effects [7.32]. Considering slip flow regime ($0.001<K_n<0.1$), the damping coefficient reduces to:

$$b_{M,N}(\eta,\lambda) = \sum_{m=1,3,\dots}^{M}\sum_{n=1,3,\dots}^{N}\frac{1}{Q_{pr}(\lambda)G_{n,m}(\eta)} = \sum_{m=1,3,\dots}^{M}\sum_{n=1,3,\dots}^{N}\frac{768\eta wl}{\left(1+6\sigma_p\,{}^{\lambda}/_{d}\right)\pi^6 d^3(mn)^2\left(\frac{m^2}{w^2}+\frac{n^2}{l^2}\right)} \quad (7.7)$$

where w and l are the parallel plates width and length respectively, separated by a gap d. m and n are odd integers. σ_p is the slip coefficient, which depends on the plate surface characteristics (roughness, contamination) and gas nature [7.33].

Equation (7.7) shows the damping coefficient a function of the viscosity and the mean free path of the gas. However, while the damping is directly proportional to the viscosity, it is only inversely proportional to $1+6*\sigma_p \lambda/d$. While a change of, for example, 25% in viscosity, η, translates to the same 25% change in damping coefficient, a similar increase of 25% in the mean free path, λ, if one considers, for instance, a gap of 1.5 µm and a slip coefficient of 1.016, yields a damping coefficient decrease of just 5.2%. This dependence decreases for larger gaps, as rarefaction effects become negligible. Thus, the damping coefficient, for the gaps considered in this work, is much more sensitive to viscosity variations than mean free path changes. Table 7.2 presents the viscosities and mean free paths of a few common gases in comparison to air, and the resulting variation in the damping coefficient.

Table 7.2: Comparison between damping coefficient sensitivity to viscosity and mean free path changes, using different gases and taking in account a 1.5 µm damper width, at standard conditions (1 atm and T= 293 K) [7.17], [7.24], [7.30], [7.31].

Gas	η (µPa.s)	$(\eta-\eta_{air})/\eta_{air}$	$[(b-b_{air})/b_{air}]_\eta$	λ (µm)	$(\lambda-\lambda_{air})-\lambda_{air}$	$[(b-b_{air})/b_{air}]_\lambda$
Air	18.4	0.0%	0.0%	66.4	0.0%	0.0%
CH_4	11.0	-40.1%	-40.1%	51.6	-22.3%	+5.0%
CO_2	14.7	-20.2%	-20.2%	41.9	-37.0%	+8.5%
CO	17.4	-5.3%	-5.3%	62.9	-5.3%	+1.1%
N_2	17.6	-4.5%	-4.5%	63.1	-5.0%	+1.1%
H_2	8.8	-52.1%	-52.1%	118.7	+78.8%	-14.3%
O_2	20.2	+9.6%	+9.6%	67.9	+2.3%	-0.5%
He	19.6	+6.6%	+6.6%	186.3	+180.6%	-27.7%

Changes in the damping coefficient are reflected in t_{PI} variations and for low frequencies the damping coefficient is directly proportional to the viscosity of the gas in the gap (7.7).

7.2.2. Pull-in time viscosity dependence

Previous section showed a linear variation of the damping coefficient with viscosity. Nevertheless, this aspect does not necessary imply that the pull-in time variation will also be linear with viscosity changes. To evaluate the pull-in time dependence on damping, let's consider the differential equation $m\frac{d^2x}{dt^2} + b\frac{dx}{dt} + kx = \frac{V_{step}{}^2 C_0 d_0}{2(d_0-x)^2}$, which describes the displacement of the device. A local linearization of this equation around the critical pull-in displacement ($x_{PI} = 1/3\ d_0$) results in the transfer function of the metastable regime (derivation in [7.32]). Considering a few

assumptions such as a sufficiently damped system (low quality factor Q), small α, and neglecting the negative pole of this transfer function, an expression for the metastable transition time can be obtained (equation (2.24) rewritten) [7.32]:

$$t_{PI} = C_1\left(b + \sqrt{b^2 + C_2}\right)$$
$$C_1 = \frac{\log\left(\frac{(d_0 + \Delta x)^2}{{d_0}^2}\right)}{4k(\alpha^2 - 1)} \quad (7.8)$$
$$C_2 = 4km(\alpha^2 - 1)$$

where C_1 and C_2 are constants that depend on the mass, m, spring stiffness, k, gap d_0 and α (V_{step}/V_{PI}). Δx is the small displacement during the metastable transition. From this expression it can be concluded that for $b >> C_2$, $t_{PI} = 2C_1 b$, hence t_{PI} changes linearly with b.

The pull-in time is a function of damping and MEMS structure mechanical parameters. According to this linearized pull-in model, the device is operating in the linear region of pull-in time in respect to damping. Since the damping coefficient at low frequencies is directly proportional to damper geometry and viscosity, in other words, the t_{PI} of the fabricated structures changes linearly with the viscosity of the gas medium. The assumptions made to obtain this model, however, limit its applicability (underdamped contitions were excluded and Δx actually changes with quality factor). Although care must be taken concerning the applicability and accuracy limitations of that model, it can be useful in predicting the trend in pull-in time sensitivity to interfering parameters.

7.3. Experimental setup

7.3.1. Microstructure electrostatic operation and readout

The MEMS device used for the experimental verification was microstructure S0 which presents low quality factor given its compliant springs and high damping level.

Initially, an accurate voltage step, higher than the nominal pull-in voltage, $V_{step} = \alpha V_{pi}$, $\alpha>1$, applied on the actuation electrodes creates the electrostatic force that moves the structure from the original position (zero displacement) to a position beyond the critical pull-in displacement. As the gap decreases, the gas between the parallel-plates is squeezed out.

By measuring the electrical capacitance between the fixed and moving arms, the displacement of the structure is detected. As a very large change in capacitance occurs when the device is pulled-in, (from 3.7 pF at the critical displacement up to 20pF at the maximum displacement / full gap travel) the pull-in event is accurately detected as a sudden large increase in the displacement signal from the front-end readout. The capacitive readout circuit based on a charge amplifier described in Chapter 3 is used for the readout, with the MEMS structure mounted on the same PCB (printed circuit board). With a high frequency carrier on the sensor electrodes, the readout circuit outputs a voltage proportional to the differential capacitive variation that is acquired by a NI USB-6251 data acquisition board at a sample rate of 100 kS/s (providing a time resolution of the measured pull-in time of 10 µs) and later processed on Matlab to retrieve the pull-in time.

The time elapsed from the start of the actuation (at zero-displacement) until the end of the pull-in event (near full displacement) is recorded. When the actuation voltage is removed, the structure returns to the rest position (by the elastic force). Repeatedly bringing the microstructure to pull-in enables continuous t_{PI} sampling. Each measurement takes a few milliseconds and t_{PI} can be sampled at a frequency up to approximately 50 Hz for a nominal pull-in time around 10 ms.

The actuation signal is a square wave, also provided by the NI USB-6251 data acquisition board (with an analog output voltage resolution of 300 µV). The high level voltage of the square (step) wave is $V_{step}=1.01\times V_{PI}$, and the low level is 0 V. In these experiments an off-time in the actuation voltage of 50 ms was used to decrease charge effects affecting the measurements, at the expense of lowering sampling frequency to 12.5 Hz (value used for most experiments except N_2-H_2 mixtures where a 15 Hz sample frequency was used instead).

7.3.2. Gas testing experimental setup

The MEMS chip was packaged in a 20-pin DIL (dual-in-line) package and fitted in a gas-tight housing (Figure 7.3) that allows mounting on the electronic readout PCB (Figure 7.4). The gas tight housing was then connected to the gas supply of the EDGaR installation as illustrated in Figure 7.4. Accurate mass flow controllers can deliver mixtures of up to 5 different gases each at a flow rate of 20 cm^3/min maximum.

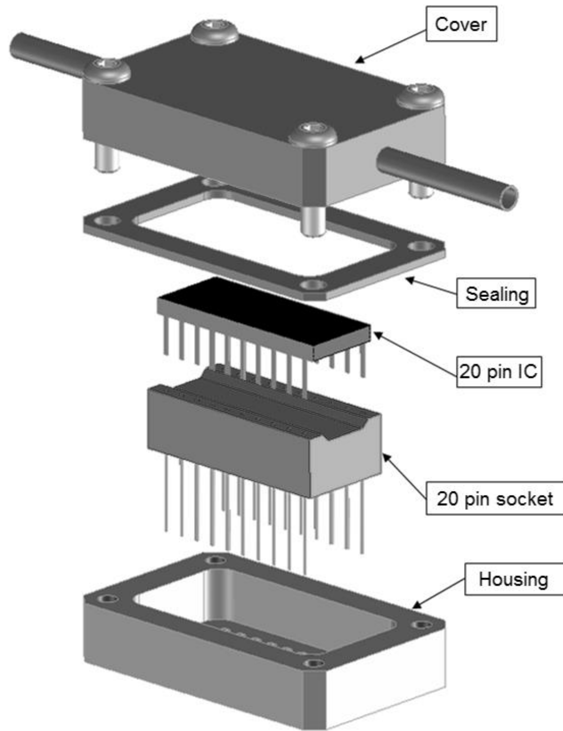

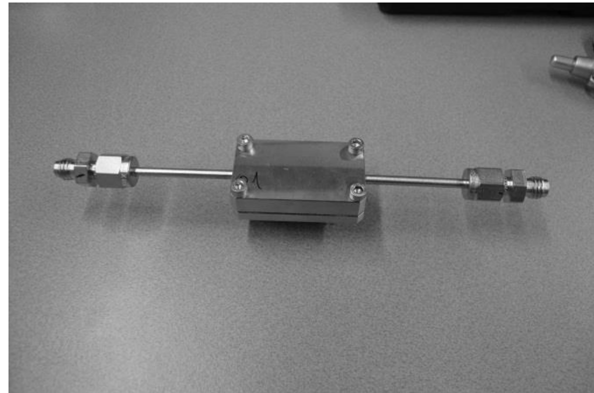

Figure 7.3: a) Schematics and b) picture of the fabricated sensor housing.

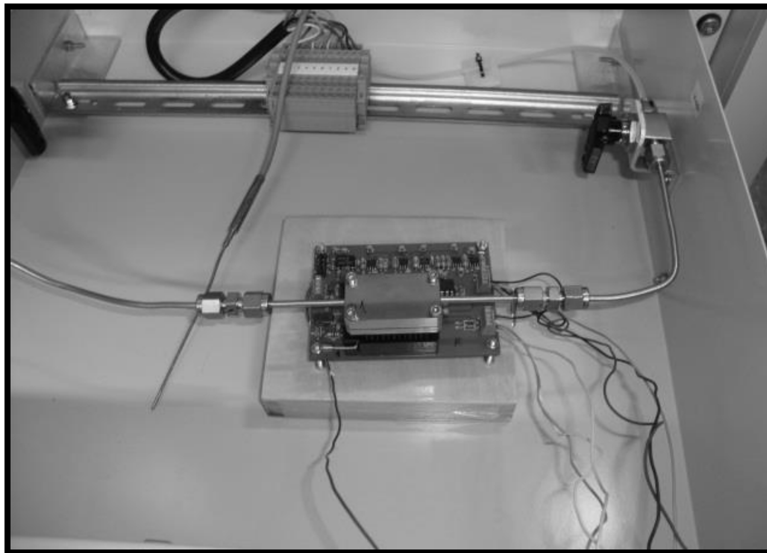

Figure 7.4: Sensor in housing connected to gas supply of the EDGaR installation.

Several tests were performed including viscosity measurement of pure gases (H_2, CH_4, CO_2, CO and N_2) and H_2-N_2, CH_4-N_2 and CH_4-N_2-CO_2 mixtures.

7.4. Test procedure

Firstly the pull-in voltage V_{PI} was measured in air. The actuation step voltage used was $V_{step}=\alpha \times V_{PI}$ with α=1.005 for the experiments with N_2-H_2 mixtures (section 7.4.1) and α=1.001 for the experiments with pure gases and other mixtures, while in section 7.4.4 the dependence of t_{PI} on the actuation voltage was tested. The results obtained under different actuation conditions cannot be directly compared. Moreover, since the measurements were performed while gas was flowing in the housing, the measured pull-in times on air do not correspond to the nominal values measured in previous chapters.

For each measurement, t_{PI} was sampled for a few seconds and the data featured in the charts is the mean value (and standard deviations). The experiments were conducted at ambient pressure (101 kPa) and temperature (293 K). The measurements were performed at a gas flow of 10 cm^3/min, except the results presented in section 7.4.3 which were obtained at stop flow. The overpressure in the gas vessels in these conditions is below 0.05 mbar.

7.4.1. H_2-N_2 mixtures

The viscosity of mixtures was calculated using equation (7.6) with data from Table 7.1 and [7.17]. Table 7.3 presents the resulting viscosity values and the corresponding measured t_{PI} values. Pull-in time decreases with increasing H_2 concentration, i.e. with decreasing viscosity and a clear correlation is observed (Figure 7.5).

Table 7.3: Pure gas and mixture calculated viscosities and pull-in time results.

Gas composition	H_2(vol%)	η (µPa.s)	Mean t_{PI} (ms)	t_{PI} standard deviation (ms)
100%N_2	0	17.6	14.24	0.974
75%N_2+25%H_2	25	17.5	13.67	0.712
50%N_2+50%H_2	50	16.9	12.71	0.754
25%N_2+75 H_2	75	15.2	10.57	0.833
100%H_2	100	8.8	4.489	0.141

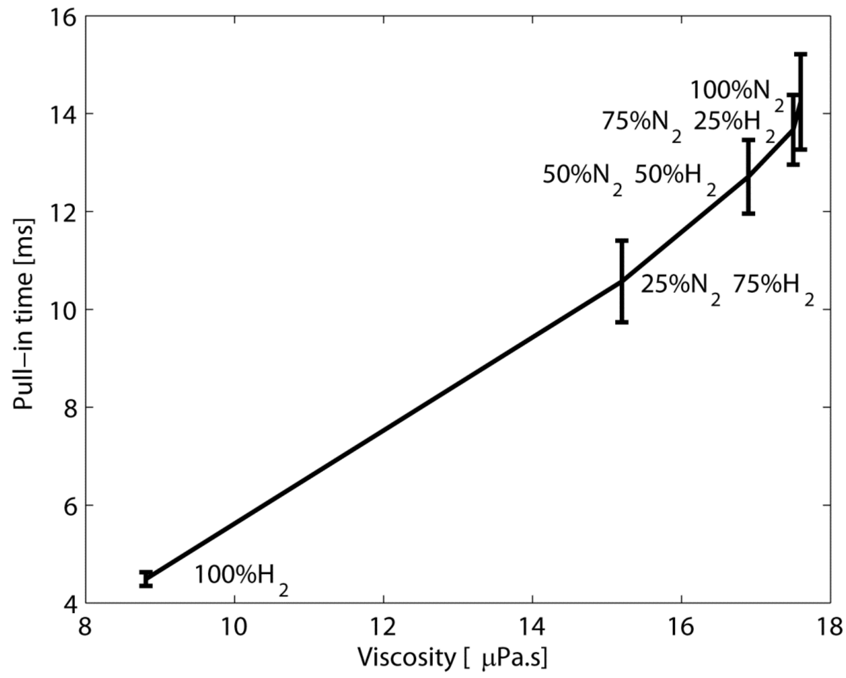

Figure 7.5: Pull-in times measured for different N2-H2 compositions.

7.4.2. Pure gas viscosity measurements

Figure 7.6 presents the t_{PI} measured for different gases, plotted against viscosity values in Table 7.1. For the linear polynomial fitting, the inverse of the standard deviation was used as weights.

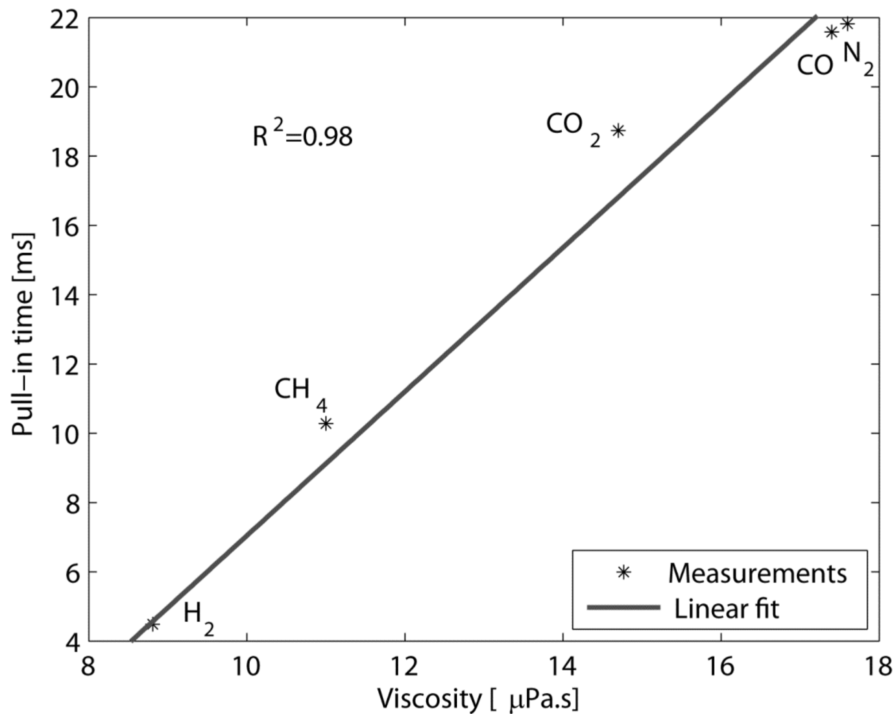

Figure 7.6: t_{PI} measurement results for pure gases.

For the pure gases tested, a good correlation between viscosity and t_{PI} was found. The sensor demonstrates a high t_{PI} sensitivity to viscosity, around 2 ms / (µPa.s). As predicted, no correlation between the gas density and measured t_{PI} was observed.

7.4.3. CH_4-N_2 and CH_4-N_2-CO_2 mixtures

These gas combinations have been chosen since they may represent different types of synthetic (SNG – Synthetic Natural Gas) and natural gas from gas fields (Table 7.4).

Table 7.4: Compositions of natural and synthetic gases reported in literature [7.34]–[7.37].

Gas	Worldwide natural gas from gas fields [7.34] (%)	Different SNGs compositions from literature (vol%)		
		[7.35] (mol%)	[7.36] (vol%$_{dry}$)	[7.37] (vol%$_{dry}$)
CO	n.a.	n.a.	0.06	0
H_2	n.a.	2.5-4.1	4.22	9.8
CO_2	0-8	1.8-5.1	4.68	8.3
CH_4	70-90	89.9-90.7	90.4	81.9
C_2H_6+C_3H_8+C_4H_{10}	0-20	n.a.	n.a.	n.a.
N_2	0-5	1.7-3(Ar+N_2)	0.64	n.a.
O_2	0-0.2	n.a.	n.a.	n.a.
H_2S	0-5	n.a.	n.a.	n.a.

n.a. – not available

Table 7.5 presents the measured pull-in times in different gas mediums. Although a tendency is observed for the pull-in time to increase with decreasing methane content, which is the less viscous gas in the mixtures, if the results are plotted together with all other measurements performed in this work (Figure 7.7), it can be noted that these pull-in time variations are within the measurement uncertainy due to noise. So in order to be able to distinguish between these relatively small viscosity variations, the overall noise must be reduced.

Table 7.5: t_{PI} results for different gas mixtures.

Gas composition	CH_4(%)	η(µPa.s)	Mean t_{PI} (ms)	t_{PI} standard deviation (ms)
75%CH_4+25%N_2	75	1.24E-05	13.5	1.469
80%CH_4+20%N_2	80	1.22E-05	12.98	1.531
85%CH_4+15%N_2	85	1.19E-05	12.67	1.558
75%CH_4+10%N_2+15%CO_2	75	1.23E-05	13.37	1.421
80%CH_4+10%N_2+10%CO_2	80	1.21E-05	13.29	1.565
85%CH_4+10%N_2+5%CO_2	85	1.18E-05	12.47	1.505

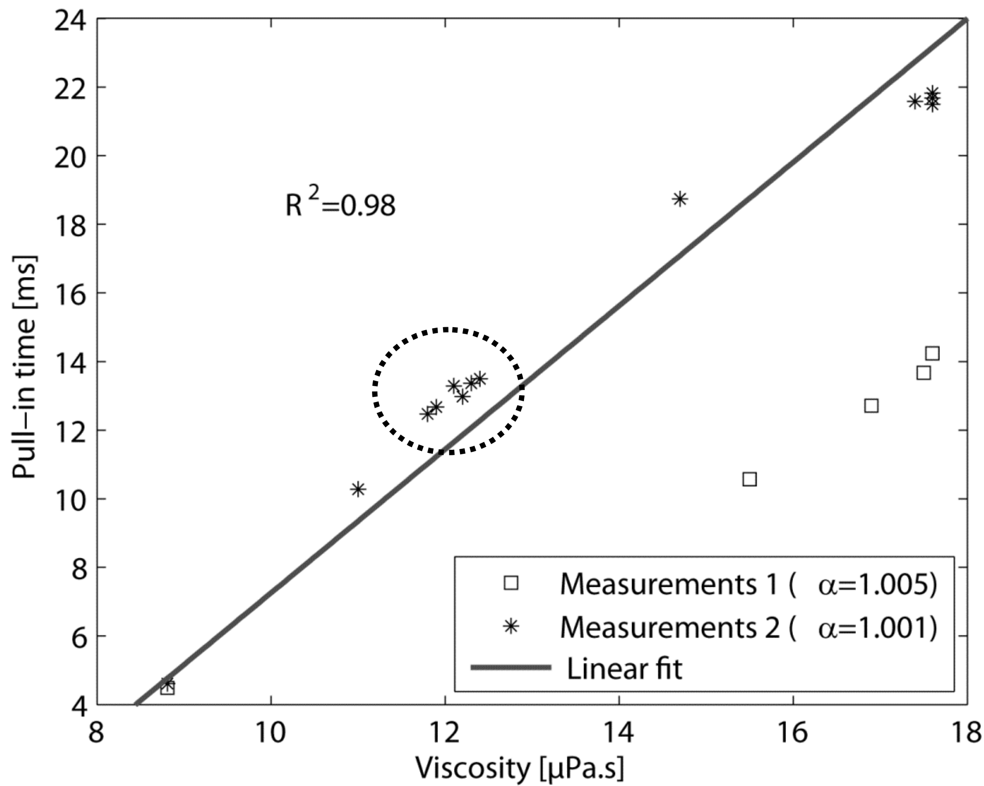

Figure 7.7: All the pull-in times measured. Those of mixtures with methane are inside the circle.

Figure 7.7 presents a linear polynomial fitting of the data from measurement group 2. The results for H_2-N_2 mixtures are separated in measurement group 1.

A few additional measurements were performed with nitrogen and air and a repeatability error smaller than 3% with an accuracy of the mass-flow controllers in the setup of around 1%. Further efforts however, are necessary to evaluate performance parameters such as reproducibility and stability. These will depend greatly on the implementation of calibration procedures.

7.4.4. Actuation voltage dependence

The experiment realize to check the actuation voltage dependence was performed at zero flow. For this experiment, a different set of actuation voltages was used instead of the fixed value used throughout the previous experiments. Figure 7.8 shows that the sensitivity increases for lower actuation voltages. The noise however, also increases, and the SNR (signal-to-noise ratio) was not improved. This noise amount might be mostly due to setup vibrations and if these are controlled in a future improved setup/sensor, then it might be an advantage to actuate at lower voltages.

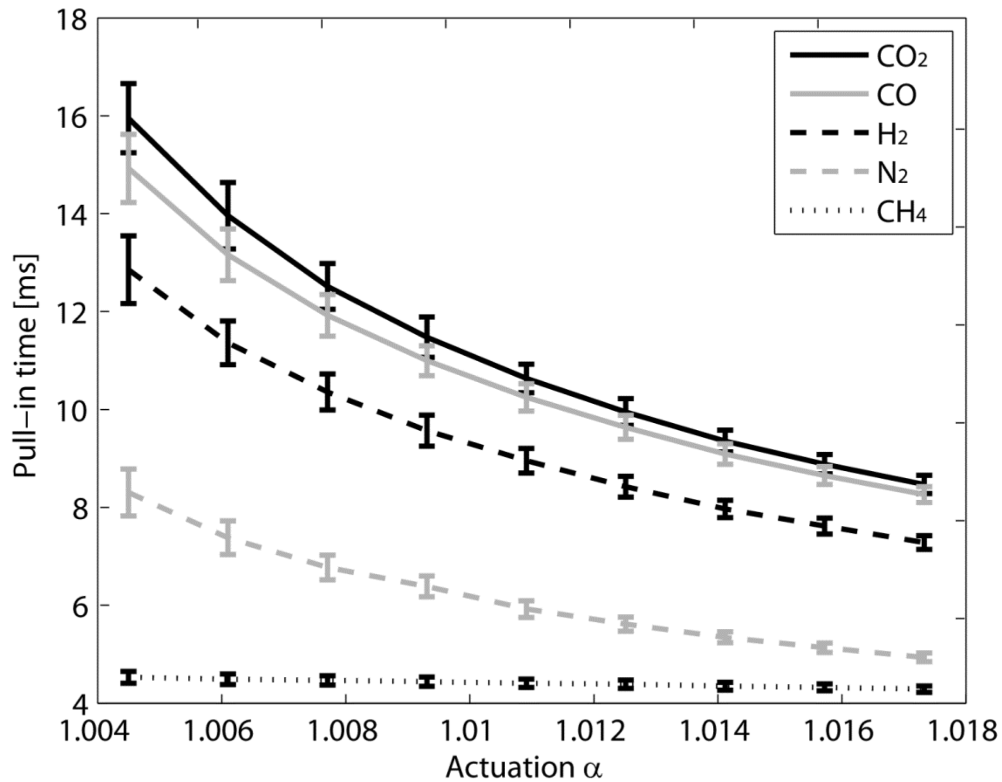

Figure 7.8: Pull-in time variation as a function of the actuation voltage, for the different pure gases tested.

7.4.5. Performance discussion and future improvements

The prototype used in this work is very sensitive to external acceleration (shocks and/or vibration). This is partially due to the relatively large mass of the movable parts: external acceleration acting on the system creates forces ($F_a = m \times a$, where a is the external acceleration) to which pull-in time is very sensitive, as seen in previous chapters. Decreasing the mass of the movable parts is a direct way of decreasing the sensitivity to external acceleration/vibrations.

The noise magnitude observed (~1.4 ms for N_2 and α=1.005) is mostly due to vibrations of the measurement apparatus that are transmitted to the MEMS sensor by the housing / gas tubing. This rms (root mean square) noise value is very high compared to previous measurements (noise study in Chapter 5) using the same structures and electronic equipment, but not the gas setup, where rms noise of approximately 100 μs was measured without vibration control measures (in an electronics laboratory environment) [7.38] . This leads to the conclusion that most of the noise at the gas measurements comes from vibrations from the gas setup that were transmitted to the sensor.

In future experiments the sensor should be isolated from external vibrations by placing layers of a vibration-absorbing material (such as elastic foam or rubber) under the electronic

board to isolate it from the vibrations from the building and specially from the EDGaR instalation (that are transmitted through the contact with the drawer), and use accessories in the gas tubing to absorb vibrations transmitted through it.

Most importantly, the MEMS design can be optimized for viscosity measurement, minimizing noise due to external acceleration. New structures can be designed to be less sensitive to mechanical vibrations (smaller inertial mass, stiffer springs) and more sensitive to viscosity/damping (designed with higher damping). A new design may explore pull-in between two movable parallel-plate structures, making the whole system insensitive to external acceleration. Additional damping increases sensitivity to viscosity.

In respect to the electrostatic actuation and readout, a few improvements have already been implemented towards real time monitoring and actuation (posterior to these results). A comparator is used to detect the voltage threshold that corresponds to the completion of the pull-in event (almost full gap displacement), and a microcontroller performs the time counting and switches the actuation voltage on and off in real time, preventing the movable structure from hitting the stoppers (increasing the lifespan of the structures) and optimizing the sampling time. The existing electronic circuits may also be improved, including digital signal processing for averaging, filtering, compensation of tilt and auto-calibration.

7.5. Conclusions

In this chapter a novel gas viscosity sensor has been studied. The working principle based on pull-in time measurement has been presented. Fabricated MEMS structures and dedicated electronic circuits for controlling and readout of the device have been used for experimental verification. The first experimental results with several different gases (pure gases and gas mixtures) already show a very high sensitivity to viscosity. A sensitivity of approximately 2 ms/(μPa.s) was observed, as well as a preliminary repeatability error smaller than 3%, which make this a very promising approach for gas viscosity sensing. Further efforts are however needed to reduce noise, improve accuracy and evaluate stability and reproducibility.

Given the sensitivity of 2 ms/(μPa.s) the measured rms noise of 1.4 ms in the pull-in time (mainly due to vibration of the measurement setup) corresponds to a viscosity equivalent rms noise of 0.7 μPa.s. So far viscosity has been measured in the small range of approximately 9 – 18 μPa.s. For the structure used, these viscosity values (and corresponding damping coefficients) are within the linear operation range of the sensor. Higher viscosity values can be

measured (at the expense of higher response times), but for lower viscosities the sensitivity will decrease exponentially until the pull-in time reaches approximately 2 ms (particularly for this structure). In other words, for high quality factors the quadratic factor of equation (7.8) makes the response constant. The factor determining the upper range limit will eventually be actuation voltage noise and external acceleration, since the sensitivity to these factors increases with pull-in time. A more thorough analysis is required in the future to properly evaluate this limitation.

The prototype used in these experiments is sensitive to external accelerations (vibration or tilt). This sensitivity can be reduced by a new design and/or compensation techniques, probably up to negligible levels. A new design has already been studied and fabrication of new MEMS structures is scheduled. This new design explores pull-in between two movable parallel-plate structures, making the whole system almost insensitive to external acceleration. Additionally damping was further increased. The microscale sensor structure and co-integration of the electronic circuits may enable the fabrication of very small, portable, low-power, low-cost and high performance gas viscosity sensors.

References

[7.1] P. Schwarz, D. Feili, R. Engel, N. Pagel, and H. Seidel, "Vacuum pressure and gas detection with a silicon based micromechanical squeeze film sensor," *Procedia Engineering*, vol. 5, pp. 750–753, Jan. 2010.

[7.2] J. K. Sell, a. O. Niedermayer, and B. Jakoby, "Simultaneous measurement of density and viscosity in gases with a quartz tuning fork resonator by tracking of the series resonance frequency," *Procedia Engineering*, vol. 25, pp. 1297–1300, Jan. 2011.

[7.3] M. K. Andrews and P. D. Harris, "Damping and gas viscosity measurements using a microstructure," *Sensors and Actuators A: Physical*, vol. 49, pp. 103–108, 1995.

[7.4] J. van Baar, W. A. Verweij, M. Dijkstra, R. J. Wiegerink, and M. Elwenspoek, "Micromachined two dimensional resistor arrays for determination of gas parameters," in *Proceedings of Transducers*, 2003, pp. 1606–1609.

[7.5] K. Igarashi, K. Kawashima, and T. Kagawa, "Development of simultaneous measurement system for instantaneous density, viscosity and flow rate of gases," *Sensors and Actuators A: Physical*, vol. 140, no. 1, pp. 1–7, Oct. 2007.

[7.6] A. Dinsdale and F. Moore, *Viscosity and its measurement*. Published on behalf of the Institute of Physics and the Physical Society by Chapman and Hall, 1962, p. 67.

[7.7] "Solid-state Viscometer for Oil Condition Monitoring." [Online]. Available: http://www.machinerylubrication.com/Read/675/solid-state-viscometer-oil. [Accessed: 11-Dec-2012].

[7.8] A. I. Malkin, A. Y. Malkin, and A. I. Isayev, *Rheology: Concepts, Methods, And Applications*, vol. 1. ChemTec Publishing, 2006.

[7.9] M. A. Rao, *Rheology of Fluid and Semisolid Foods: Principles and Applications (Google eBook)*, vol. 2007. Springer, 2007.

[7.10] N. & Chaudhry and B. C. N. K. K. Chaudhry, *Instrumentation, Measurement and Analysis,2e*. Tata McGraw-Hill Education, 2004, p. 632.

[7.11] R. McKay, M. L. McMillan, and T. W. Selby, *Viscometry and its application to automotive lubricants*. Society of Automotive Engineers, 1973.

[7.12] D. S. Viswanath, T. K. Ghosh, D. H. L. Prasad, N. V. K. Dutt, and K. Y. Rani, *Viscosity of Liquids: Theory, Estimation, Experiment and Data*. Springer, 2010.

[7.13] J. J. Singh, G. H. Mall, and H. Chegini, *Measurement of viscosity of gaseous mixtures at atmospheric pressure*. NASA Technical Paper, 1986.

[7.14] A. Viswanathan, "Viscosities of natural gases at high pressures and high temperatures," Texas A&M University, 2007.

[7.15] P. A. Russell, B. A. Buffham, G. Mason, and K. Hellgardt, "Measurement of the gradient of viscosity with composition of mixtures of non-ideal gases," *Chemical Engineering Science*, vol. 61, no. 19, pp. 6604–6615, Oct. 2006.

[7.16] A. L. Lee, M. H. Gonzalez, and B. E. Eakin, "The viscosity of natural gases," *Journal of Petroleum Technology*, vol. 37, pp. 997–1000, 1966.

[7.17] J. O. Hirschfelder, C. F. Curtiss, R. B. Bird, and U. of W. T. C. Laboratory, "Molecular theory of gases and liquids," 1954. [Online]. Available: http://books.google.com/books?id=HQtRAAAAMAAJ&pgis=1. [Accessed: 11-Dec-2012].

[7.18] R. B. Bird, W. E. Stewart, and E. N. Lightfoot, *Transport Phenomena*, 2nd ed. John Wiley & Sons, 2007.

[7.19] D. R. Lide, Ph.D., and T. J. Bruno, *CRC Handbook of Chemistry and Physics 2012-2013*. CRC Press, 2012.

[7.20] J. C. Maxwell, "The bakerian lecture: On the viscosity or internal friction of air and other gases," *Phil. Trans. R. Soc Lond.*, vol. 156, 1866.

[7.21] J. C. Maxwell, E. Garber, S. G. Brush, and C. W. F. Everitt, *Maxwell on Molecules and Gases*. MIT Press, 1986.

[7.22] W. Sutherland, "The viscosity of mixed gases," *Phil. Mag.*, vol. 40, pp. 421–432, 1895.

[7.23] J. W. Buddenberg and C. R. Wilke, "Calculation of gas mixture viscosities," *Industrial & Engineering Chemistry*, vol. 41, no. 7, pp. 1345–1347, Jul. 1949.

[7.24] NIST, "Thermophysical Properties of Fluid Systems." [Online]. Available: http://webbook.nist.gov/chemistry/fluid/. [Accessed: 11-Dec-2012].

[7.25] H. Li, Ø. Wilhelmsen, Y. Lv, W. Wang, and J. Yan, "Viscosities, thermal conductivities and diffusion coefficients of CO2 mixtures: Review of experimental data and theoretical models," *International Journal of Greenhouse Gas Control*, vol. 5, no. 5, pp. 1119–1139, Sep. 2011.

[7.26] R. A. Dias, L. Mol, R. F. Wolffenbuttel, E. Cretu, and L. A. Rocha, "Design of a time-based micro-g accelerometer," *IEEE Sensors Journal*, vol. 11, no. 8, pp. 1677–1683, 2011.

[7.27] T. Veijola, H. Kuisma, J. Lahdenpera, and T. Ryhanen, "Equivalent-circuit model of the squeezed gas film in a silicon accelerometer," *Sensors and Actuators A: Physical*, vol. 48, pp. 239–248, 1995.

[7.28] T. Veijola, "Compact models for squeezed-film dampers with inertial and rarefied gas effects," *Journal of Micromechanics and Microengineering*, vol. 14, no. 7, pp. 1109–1118, Jul. 2004.

[7.29] V. Lindroos, M. Tilli, A. Lehto, and T. Motooka, *Handbook of Silicon Based MEMS Materials and Technologies*. William Andrew, 2010.

[7.30] P. Kulkarni, P. A. Baron, and K. Willeke, *Aerosol Measurement: Principles, Techniques, and Applications*. John Wiley & Sons, 2011, p. 704.

[7.31] J. W. Schmidt and M. R. Moldover, "Dielectric permittivity of eight gases measured with cross capacitors," *International Journal of Thermophysics*, vol. 24, no. 2, pp. 375–403, 2003.

[7.32] L. A. Rocha, E. Cretu, and R. F. Wolffenbuttel, "Measuring and interpreting the mechanical–thermal noise spectrum in a MEMS," *Journal of Micromechanics and Microengineering*, vol. 15, no. 7, pp. S30–S38, Jul. 2005.

[7.33] T. Veijola, H. Kuisma, and J. Lahdenpera, "The influence of gas-surface interaction on gas-film damping in a silicon accelerometer," *Sensors and Actuators A: Physical*, vol. 66, pp. 83–92, 1998.

[7.34] Maclain Marshall Holton, "Autoignition delay time measurements for natural gas fuel components and their mixtures," University of Maryland, 2008.

[7.35] C. M. van der Meijden, H. J. Veringa, and L. P. L. M. Rabou, "The production of synthetic natural gas (SNG): A comparison of three wood gasification systems for energy balance and overall efficiency," *Biomass and Bioenergy*, vol. 34, no. 3, pp. 302–311, Mar. 2010.

[7.36] R. W. R. Zwart, H. Boerrigter, E. P. Deurwaarder, C. M. van der Meijden, and S. V. B. van Paasen, *Production of synthetic natural gas (SNG) from biomass*. ENC Report, 2006.

[7.37] U. Zuberbuhler, "Adjusting methanation stoichiometry via AER process," in *Proceedings of BioSNG*, 2009.

[7.38] R. A. Dias, E. Cretu, R. Wolffenbuttel, and L. A. Rocha, "Pull-in-based μg-resolution accelerometer: Characterization and noise analysis," *Sensors and Actuators A: Physical*, vol. 172, no. 1, pp. 47–53, Dec. 2011.

8.

Conclusions

The work presented in this thesis deals with acceleration sensing using pull-in operated devices. The pull-in nonlinear behavior of microelectromechanical structures has been analyzed (from both static and dynamic perspectives) and has been experimentally used for open and closed-loop accelerometers with high resolution and sensitivity. Squeeze-film damping is of outmost importance when designing parallel-plates movable devices, and specially pull-in accelerometers due to the high sensitivity of metastable pull-ins to small changes in the intervenient forces such as damping. Modeling, simulation and experimental verification have been used to study damping and acceleration sensing based on pull-in time measurement and also enabled a new application that explored the pull-in sensitivity to viscosity of the damping gas medium.

8.1. Conclusions

The main conclusions to be drawn from the work are as follows:

1. **Damper modeling/design:** An accurate and easy to implement analytic damping model is essential for both design and behavior prediction of MEMS structures, since FEM and Fluid dynamics simulation tools are not straight-forward to use and present very high computational costs in order to obtain accurate results. The squeeze-film damping model used in this thesis was compared against ANSYS CFX simulation results and experimental damping measurements on fabricated MEMS structures, and it has been used throughout this work proving to be adequate to model the fabricated micromachined devices dynamic behavior.

A new damper geometry has been studied for use in in-plane parallel-plate devices. It consists of introducing flow channels in the parallel-plate structures, similarly to holes etched in out-of-plane devices. The method is very useful to increase the capacitance / damping ratio, which is a limitation and a common difficulty encountered when designing in-plane movable parallel-plates capacitive devices.

2. Pull-in time accelerometer performance:

a. **High sensitivity:** Open-loop operation of the µg accelerometer based on pull-in time measurement has been described and implemented. The measured sensitivity of 0.26 µs/µg presented in this work is a very good feature since microseconds can very easily be measured with high frequency time-counting mechanisms available. This is a great advantage in comparison to state-of-the-art capacitive accelerometers where very small capacitance variations must be detected, in the order of few attofarads, which presents a technical challenge.

b. **Low noise:** The mechanical-thermal noise is expected to be the main noise source in this approach. The mechanical-thermal noise could not be experimentally measured due to insufficient isolation from external vibration sources, but the noise study performed supports the assumptions made and the low noise characteristics of a pull-in time accelerometer. The main drawback discovered in this study concerns the approach's vulnerability to low frequency actuation voltage noise, or DC drift, which can be overcome by actuation conditions reassessment.

c. **High resolution:** The main advantage of this approach in comparison to other high-resolution capacitive accelerometers is the huge resolution potential of the measurement method. Since a time measurement is performed, rather than just direct transduction of capacitance into acceleration, increasing the measurement resolution only requires a faster clock of the time counting mechanism (to detect smaller changes in the pull-in time) as opposed to direct capacitive transduction approaches where very small capacitance changes (aF) are required (and difficult) to be detected. The capacitance change in the gap of interest is very large (pF) and straight-forward to be detected with low front-end readout circuit requirements

d. **Large dynamic range:** Closed-loop operation approaches have been studied in order to decrease the response non-linearity and thus increase dynamic range, which are the main features limiting the performance of the pull-in time accelerometer. An electrostatic compensation technique that addresses the non-linearity problem, based on pull-in time duration control, has been presented and its implementation in a real time closed control loop has yielded

an accelerometer with 31 V^2/g sensitivity, over a dynamic range of approximately 109 dB. The main problem encountered was the response time of the control law, that requires optimization.

It has been shown that closed-loop operation method can improve linearity and enable the use of high-sensitivity, high-resolution pull-in time accelerometers to measure acceleration over a much larger dynamic range than in open-loop operation.

3. **Viscosity measurement:** From the study of the nonlinear pull-in behavior and the squeeze film damping mechanism/model, a new application for gas viscosity sensing has evolved. The novel working principle based on pull-in time measurement has been presented and preliminary experimental results with several different gas mixtures, using the fabricated microstructures and electronic readout, have already shown a very high sensitivity to viscosity (approximately 2 ms / µPa.s).

8.2. Future work

In respect to the pull-in time accelerometer, which is the main subject of this thesis, the main remaining problem is the closed-loop control algorithm, which limited the usable bandwidth in comparison to open-loop operation. Developing an optimized algorithm is not a trivial task, and much work is still required. Several control algorithms must be explored in order to control the MEMS structure in the three regions of pull-in. Since the structure must be brought repeatedly to pull-in in order to precisely measuring the time and thus determining the acceleration, allowing navigation grade quality parameters, the control system should be fully implemented in hardware. Additionally, methods to reduce the pull-in drive voltage noise sensitivity are needed, especially when aiming to miniaturize and integrate the whole system.

The realization of such a microsystem raises several challenges. Of particularly importance is the integration in the same platform (MEMS/sensor plus electronic circuits) of different functions to allow the control and sensing on one side, and calibration, diagnosis and thermal compensation on the other. These desirable features are only possible if the micromechanical device is integrated with analog readout electronic circuits and with a digital controller. This integration is a key aspect for a proper microsensor, requiring a multi-disciplinary approach that can deliver new control algorithms for the closed-loop operation, new sensor architectures and improved accelerometer performance.

An improved accelerometer requires long-term stability and therefore the system should have auto-calibration and thermal compensation mechanisms. Non-idealities of the micromachining process (such as overetching or internal material stresses) are reflected on the fabricated microstructures as deviations from the nominal gap and varying spring dimensions, yielding capacitances and spring stiffness coefficients different from designed/expected. These affect the pull-in voltage directly. If a differential scheme is adopted, using symmetrical structures, fabrication process parameters non-idealities affect both pull-in voltages equally. Differential pull-in voltage measurements (combined with a single resonance frequency measurement) can be used to quantify deviations from ideal conditions/parameters [8.1], thus allowing compensating for those effects. This approach can be used to implement auto-calibration techniques (if the measurements and the actuation voltage updates are performed automatically).

The pull-in voltage depends solely on the geometry of the structure and material properties. Changes in temperature affect the mechanical properties and the pull-in voltage has a negative temperature coefficient [8.2] due to the combined effect of the changes in Young's modulus and in the spring's dimensions. In a differential scheme, temperature changes affect both pull-in voltages equally, hence the nominal pull-in voltage can be found from the differential measurement. In [8.3] it is shown that the thermal effects (expansion of the spring and stiffness coefficient drift) on the differential pull-in voltage sensitivity to tilt (acceleration) are compensated when considering a normalized differential measurement. Temperature changes also affect damping, through changes in viscosity. By the same logic, differential pull-in voltage measurements can be used to quantify that effect allowing calibration.

Compensation of physical changes such as thermal expansion and resulting shift of the Young's modulus of the material can be accomplished through changes in the actuation voltages. Pull-in time operation relies on electrostatic actuation with a voltage proportional to the pull-in voltage. Using the calibrated pull-in voltage, the actuation conditions (namely the proportionality constant α) are kept constant/calibrated. These auto-calibration and thermal compensation capabilities can only be possible by actuating the structures to pull-in.

In respect to the viscosity sensor, the most prominent task is the design and fabrication of an optimized, viscosity-sensing-oriented microstructure, with sensitivity maximized for viscosity instead of acceleration. The same issues remaining in respect to the accelerometer can also be applied to the viscosity sensor, namely concerning long-term stability of the system, auto-calibration and thermal compensation mechanisms. Design and simulation of the full

microsystem is also a challenge. The full-system simulation involves the integration on the same simulation platform of several physical domains (all interacting at the micro domain) including the mechanical (the MEMS structure), electrical (actuation and readout analog circuit), fluidic, and digital components (digital controller for closed loop-operation), which is not a trivial task.

References

[8.1] L. A. Rocha, R. A. Dias, E. Cretu, L. Mol, and R. F. Wolffenbuttel, “Auto-calibration of capacitive MEMS accelerometers based on pull-in voltage,” *Microsystem Technologies*, vol. 17, no. 3, pp. 429–436, Feb. 2011.

[8.2] L. A. Rocha, E. Cretu, and R. F. Wolffenbuttel, “Analysis and analytical modeling of static pull-in with application to MEMS-based voltage reference and process monitoring,” *Journal of Microelectromechanical Systems*, vol. 13, no. 2, pp. 342–354, 2004.

[8.3] F. M. S. Alves, “Micro inclinómetro eletromecânico,” Universidade do Minho, 2012.

ANNEX 1 – LIST OF PUBLICATIONS

Journal publications:

R. A. Dias, E. Cretu, L. Mol, R. F. Wolffenbuttel and L.A. Rocha – Design of a time-based micro-g accelerometer, Sensors Journal: Volume 17, Issue 3 (2011), pp. 1677-1683. http://dx.doi.org/10.1109/JSEN.2010.2103938

R. A. Dias, E. Cretu, R. F. Wolffenbuttel and L.A. Rocha – Pull-in based μg-resolution accelerometer: characterization and noise analysis, Sensors and Actuators A: Volume 172, Number 1,(December 2011), pp. 47-53. http://dx.doi.org/10.1016/j.sna.2011.01.027

R. A. Dias and L.A. Rocha – Improving capacitance/damping ratio in a capacitive MEMS transducer, Journal of Micromechanics and Microelectronics (Submitted)